# FLOW PAST DIMPLED SURFACES

## TAY CHIEN MING JONATHAN
*(M. Eng., NUS)*

## A THESIS SUBMITTED FOR THE DEGREE OF

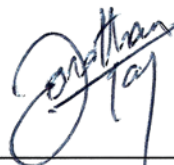## DOCTOR OF PHILOSOPHY

## DEPARTMENT OF MECHANICAL ENGINEERING

## NATIONAL UNIVERSITY OF SINGAPORE

## 2016

# Declaration

I hereby declare that this thesis is my original work and it has been written by me in its entirety. I have duly acknowledged all the sources of information which have been used in the thesis.


This thesis has also not been submitted for any degree in any university previously.




Tay Chien Ming Jonathan

9 April 2016

# Acknowledgements

I would like to express my deep gratitude to my supervisors Professor Khoo Boo Cheong and Professor Chew Yong Tian for their patient guidance, encouragement and very helpful and valuable advice during the course of this work. I would also like to thank the staff at the Fluid Laboratory, particularly Mr. Yap Chin Seng and Mr. Tan Kim Yah for their generous practical help when running the experiments, as well as Dr. Wang Junhong at the NUS computer centre for his patience and help in the running of the DES code.

Special thanks also go to Airbus Operations Ltd. for providing much of the funds that make this work possible.

Finally, I wish to thank my parents as well as my loving wife for their endless support, understanding and encouragement throughout this project.

# Table of Contents

# Summary

The present study investigates the effect that an array of dimples has on turbulent drag reduction. Although dimples have shown drag reduction in some cases, this drag reduction is usually of the order of a few percent, making quantifying the drag reduction accurately a challenging task. For this purpose, a channel flow is used to allow accurate control of the flow over an array of dimples. A novel method involving the use of measuring relative changes in the mean streamwise pressure gradients within the different sections of the channel was developed to obtain the accuracy required to quantify the effect that the dimples have on drag.

Arrays of shallow axisymmetric circular dimples with depth to diameter ratios of 1.5% and 5% are studied in a turbulent channel flow at Reynolds numbers between 3,300 and 37,000. Pressure measurements show that drag reduction of up to 3% is possible at a Reynolds number of 37,000. Single element hot-wire velocimetry is also carried out to measure the streamwise velocity of the flow over the dimple array. Investigation of the flow was further carried out using Detached Eddy Simulation (DES) of the same dimple geometry as the experiments. This allowed the DES and the experiments to compliment as well as validate each other's findings.

The most significant finding of the study is that the mechanism of skin friction drag reduction with dimples is the same as that observed using active methods such as spanwise wall motions or transverse wall jets over flat plates. The three dimensional dimples introduce streamwise vorticity into the flow which results in spanwise flow components near the wall. The DES shows that although the streamwise vorticity introduced is weak, it is concentrated near the dimple surface, and generates

significant spanwise flow components near the dimple surface. The result is that the normal energy cascade to the smaller scales is suppressed, which leads to a reduction in turbulent skin friction drag because of the stabilized flow. This suppression is supported by the spectral analysis of the hot-wire velocimetry as well as the turbulent budget and Reynolds stress analysis of the DES. Peaks in the spectral distribution are observed to shift towards the lower frequencies, and reductions in the peaks of the various energy budget terms and Reynolds stress terms are observed with drag reduction. Increasing the dimple depth from 1.5% to 5% of its diameter increases the streamwise vorticity introduced, which leads to a greater reduction in skin friction. However, increasing the dimple depth also results in flow separation which increases pressure or form drag. The DES shows that flow separation is dependent on both the dimple depth and flow Reynolds number. The net effect to the total drag depends on the relative dominance between the drag reducing streamwise vorticity and the drag increasing flow separation. The region of flow separation can shrink with increasing Reynolds number, so that at sufficiently high Reynolds numbers, the flow separation region can shrink and may disappear completely, consequently leading to a larger drag reduction.

# List of Tables

# List of Figures

ix

# List of Symbols

$A_w$ — surface area of upper and lower walls of DES domain

$a$ — first coefficient for best fit quadratic curve for hot-wire signal output

$b$ — second coefficient for best fit quadratic curve for hot-wire signal output

$CR$ — dimple coverage ratio

$C_f$ — mean skin friction of oscillating wall

$C_{f0}$ — mean skin friction of stationary smooth flat wall

$c_1$ — constant for best fit quadratic curve for hot-wire calibration signal output

$c_2$ — constant for best fit quadratic curve for hot-wire detection signal output

$D$ — dimple diameter

$D_f$ — skin friction

$D_p$ — pressure friction

$\text{Dimple}_{\text{total drag}}$ — total drag from dimple surface

$\text{Dimple}_{\text{skin friction}}$ — total drag from dimple surface

$\text{Dimple}_{\text{form drag}}$ — total drag from dimple surface $d$ dimple depth

$E_c$ — corrected hot-wire voltage signal

$E_m$ — measured hot-wire voltage signal

$h$ — channel height

$h_d$ — height of domain in DES simulation

$i$ — vector in the streamwise direction

$j$ — vector in the vertical direction

$k$ — vector in the spanwise direction

$L_D$ — length of dimpled test section

| | |
|---|---|
| $l_d$ | length of domain in DES simulation |
| $m$ | hypothetical mean streamwise pressure gradient |
| $N$ | number of cells in each direction in the DES domain |
| $P_g$ | mean streamwise pressure gradient |
| $P_1$ | vertical intercept of hypothetical pressure variation before channel test section |
| $P_2$ | vertical intercept of hypothetical pressure variation after channel test section |
| $p$ | pressure |
| $R$ | dimple edge radius |
| $Re$ | Reynolds number based on half channel height and channel centreline velocity |
| $Re_\tau$ | Reynolds number based on friction velocity and half channel height |
| $St$ | Strouhal number |
| $s$ | riblet spacing |
| $T_a$ | ambient temperature |
| $T_r$ | reference temperature |
| $T_w$ | hot-wire temperature |
| $t$ | time |
| $t_{ij}$ | subgrid-scale stresses |
| $U$ | mean streamwise velocity component |
| $u$ | streamwise velocity component |
| $u_{rms}$ | root-mean-square of streamwise velocity fluctuations |
| $u_\tau$ | friction velocity $u_\tau = \sqrt{\dfrac{\tau_w}{\rho}}$ |
| $V$ | hot-wire mean voltage signal |
| $v$ | vertical velocity component |
| $w_d$ | width of domain in DES simulation |

| | |
|---|---|
| $w$ | spanwise velocity component |
| $w_{osc}^+$ | nondimensional spanwise velocity of oscillating wall, |
| $x$ | streamwise coordinate from dimple center |
| $x_i$ | streamwise coordinate from channel inlet |
| $y$ | vertical coordinate |
| $z$ | spanwise coordinate |
| $\beta^*$ | dimensional mean streamwise pressure gradient |
| $\alpha$ | Deflection angle of hot-wire probe die to flow induced deformation |
| $\Delta$ | change in quantity, largest grid spacing in the $x$, $y$ and $z$ directions in DES |
| $\delta$ | small change in quantity |
| $\delta_e$ | Error due to flow induced deformation of hot-wire probe |
| $\delta_{ij}$ | Kronecker delta |
| $\lambda$ | distance between dimple centres |
| $\rho$ | fluid density |
| $\sigma$ | $\Delta V/\Delta y$, vertical hot-wire voltage signal gradient |
| $\tau$ | shear stress |
| $\tau_w$ | wall shear stress |
| $\nu$ | fluid kinematic viscosity |

Superscripts

| | |
|---|---|
| $*$ | dimensional quantity |
| $+$ | quantity expressed in wall coordinates |

Subscripts

| | |
|---|---|
| $d$ | quantity downstream of test section for hypothetical pressure variation |

*u*  quantity upstream of test section for hypothetical pressure variation

# Chapter 1
# Introduction

Fluid drag is most commonly encountered in two forms, pressure drag and skin friction drag. Pressure drag, also known as form drag refers to the drag encountered when a solid body moves fluid apart and around it as it is moves through the fluid. The energy required to do this is experienced as drag and is the dominant form of drag for bluff bodies. To minimise this form of drag, the body moving through the fluid can be made more streamline in shape. Through streamlining, the fluid is moved apart and around the solid body as smoothly as possible, thus minimizing the associated energy losses. For streamlined bodies, the dominant form of drag comes from skin friction drag. While form drag can be reduced significantly by simply streamlining a body, no such simple method exists to reduce skin friction drag by a comparable amount. Vast amounts of time and resources have been channelled over the past century to the study of the problem of skin friction drag reduction, and in particular turbulent skin friction drag reduction since many practical engineering applications involve the turbulent flow regime. For aircraft, as much as 48% of its total drag arises from skin friction alone (Dean and Bushan 2010). There is much gain from its reduction, particularly when one considers that a 1% drag reduction can reduce the operating cost of a large transport aircraft by 0.2% or increase its carrying capacity by 1.6 tons, or 10 passengers (Reneaux 2004). Further benefits include reduced carbon emissions in the present environmentally conscious age. Considering also that overcoming skin friction forms a large portion of the energy expenditure in many other forms of transportation, including land and water transport systems, and many diverse industrial applications, one can only conclude the tremendous importance of any form of technology that reduces turbulent skin friction drag.

## 1.1 Near wall fluid motion

Although once thought to be completely random, studies of turbulent fluid flow has shown that organized structures do exist within the fluid, particularly in the viscous layer very near the wall (Kline et al. 1967). In a fully developed turbulent boundary layer, the fluid layer near the wall is covered with numerous high and low speed streaks spaced alternately along the spanwise direction. These unsteady near wall streaks are scaled with the wall unit length scale $v/u_\tau$, where $v$ is the kinematic viscosity and $u_\tau$ is the friction velocity. The streaks are observed to have average spanwise spacing $\Delta z^+ \approx 100$ (Kline et al. 1967), and streamwise extents $\Delta x^+ \approx 1000$ (Blackwelder 1978, Jimenez and Moin 1991). These streaks were later found to be the result of quasi-streamwise vortices bringing high speed fluid from above the wall downwards and low speed fluid from near the wall upwards (Blackwelder and Eckelmann 1979). Together with these streaks and quasi-streamwise vortices, another common observation in the flow region near the wall are what have been commonly called ejections and sweeps. Ejections denote events that involve the outward movement from the wall of low speed fluid and occur intermittently and violently. Sweeps refer to downward motions of high speed fluid towards the wall at relatively shallow angles and these usually accompany ejection events (Cantwell 1981). Sweeps in particular, are known to be responsible for causing high skin friction due to the increased velocity gradient that result from their bringing high speed fluid down towards the wall (Choi 1989, Orlandi and Jimenez 1994). Based on the quadrant-splitting scheme of Wallace et al. (1972) and Willmarth and Lu (1972), ejections and sweeps correspond to $(uv)_2$ and $(uv)_4$ motions respectively and contribute significantly to the Reynolds shear stresses. These ejections and associated sweep motions usually occur near the wall (Wallace et al. 1972), and are commonly referred to as bursting.

Further studies revealed that the streamwise vortices observed near the wall are part of hairpin vortices, or sometimes also referred to as horseshoe vortices based on its relative physical proportions (Head and Bandyopadhyay 1981). Much of these early vortex models are extensively reviewed by Robinson (1991). While these earlier models proposed were symmetric in nature, the advancement of computing power and the ability to carry out numerical simulations at higher Reynolds numbers shows that many of these hairpin vortices are often non symmetric, appearing more like a cane than a hairpin with two symmetric "legs" (Guezennec and Choi, 1989). Nonetheless, the concept of such hairpin structures populating the near wall flow explains much of the observations encountered in this flow region. Zhou *et al*. (1999) summarized this point very well: the long quasi-streamwise legs of such structures explain the cause of the high and low speed streaks observed near the wall. The rapid lifting of the hairpin head and the fluid in between the hairpin legs give rise to the observed violent ejection events. Even the characteristic spanwise spacing of the near wall streaks can be explained by the spanwise width of the hairpin legs. Another common observation of near wall turbulent structures, the 30º to 50º angle of inclination of these structures can be traced to the angle of inclination of the hairpin head as it is lifted and rises from the wall.

## 1.2    Review of drag reduction techniques

While there is some consensus in the existence of hairpin structures near the wall, the process by which they cyclically regenerate is still open to much debate. One thing that is agreed upon is that due to the $\overline{-u'v'}$ contribution of the ejections and sweeps in burst events observed with these near wall structures, and the mass and momentum transfer in the vertical wall normal direction that results, these structures contribute significantly to the production and distribution of turbulent energy in wall bounded flows. Lu and Willmarth (1973) estimate that up to 80% of turbulent energy is

produced by such bursting events. The increased production and distribution of turbulent energy manifests itself in increased turbulent drag.

One way to effectively reduce this turbulent drag over the wall is to suppress or interfere with the generation and sustainment of these near wall turbulent structures. Turbulent drag reduction technologies typically do this in broadly two ways: active and passive methods. In active drag reduction techniques, additional energy is required to reduce the turbulent drag. This may be achieved by some form of mass transfer or wall movement at the solid/fluid boundary. For the system to be effective, the added energy should be less than the energy saved from the reduced drag, so that the overall system requires less energy to operate than if the active drag reduction system is absent. Passive drag reduction methods achieve drag reduction without additional input of energy. This form of drag reduction usually employs surface contouring, modification of surface microstructure or compliance, or the addition of some surface attachments to perturb the flow favourably.

### 1.2.1 Active drag reduction

The most direct way to reduce turbulent drag is to target the near wall structures themselves. Various schemes employing closed-loop control attempt to do this with varying success. In such closed-loop systems, the location of the near wall structures are sensed in 3D space using chosen flow parameters associated with them, and the flow is acted upon using actuators or controls that are not necessarily located at the same position where the sensing is carried out. Most have only been carried out numerically (Choi et al. 1994, Bewley et al. 2001) due to the very small length and times scales of the turbulent structures.  As such, the physical actuators required for these control schemes are very small and prohibitively expensive to implement in the large numbers and high density required to cover a solid surface effectively. Physical

implementation of control schemes targeting such near wall structures, though implemented over a relatively small surface using a small number of sensors have shown these methods to be effective in reducing skin friction drag (Kerho 2002, Rathnasingham and Breuer 2003). Open-loop flow control for drag reduction overcomes part of the problem of closed-loop system by simply removing the sensor portion of the control system. This makes the system simpler to implement since the large number of sensors required for closed-loop control is simply done away with. Despite not sensing the presence of the individual streaks, this approach has also been shown to be successful in suppressing the streaky structures in the turbulent near-wall flow (Zhang et al. 2010). However, like the closed-loop system, this method still suffers from the need to have a very high density of very small control actuators to target individual streaks at moderate to high Reynolds numbers since the streaks scale with wall variables.

Instead of targeting individual streaks, it may be more practical to implement open-loop controls that affect a relatively large area which encompass many streaks. Not only does such a control system do away with the large number of sensors needed, it also does away with the large number of physically small actuators needed to target individual streaks. Such an approach was considered numerically by Schoppa and Hussain (1998) using counter-rotating vortices and colliding spanwise wall jets as actuators with spacings several times that of the near-wall streak spacing in a channel flow simulation. Using Direct Numerical Simulation (DNS) for a fully developed channel flow at Reynolds numbers of 1800 and 3200, they were able to show that with an actuator spacing of 400 wall units, about four times that of observed streak spacing, and with a control amplitude of only 6% of the channel centreline velocity, they were able to obtain a very significant 20% average drag reduction with the counter-rotating vortices and 50% for the colliding spanwise wall jets. The drag reduction ability of large scale streamwise vortices in a channel flow was confirmed

experimentally by Iuso et al. (2002) where local skin friction reductions of up to 30% were found. The large scale streamwise vortices, with their centers located along the channel centreline, produced significant spanwise fluid motions near the wall.

Many others have successfully demonstrated the use of spanwise forcing to reduce turbulent skin friction drag. While both Schoppa and Hussain (1998) and Iuso et al. (2002) used large scale streamwise vortices to introduce spanwise moving flow components near a stationary wall to achieve drag reduction, others have implemented spanwise forcing by using a spanwise oscillating wall in both channel flows (Quadrio and Ricco 2004, Choi et al. 1998, Choi et al. 2002) and pipe flows (Orlandi and Fatica 1997, Quadrio and Sibilla 2000) and obtained comparable levels of drag reductions. Similar results are also obtained using spanwise travelling waves (Du and Karniadakis 2000, Du et al. 2002) and spanwise forcing using Lorentz force (Lim et al. 1998, Berger et al. 2000). DNS studies show that with spanwise wall oscillations, a maximum drag reduction of up to 40% under optimised conditions can be achieved (Jung et al. 1992, Quadrio and Ricco 2004). In their oscillating wall experiment, Choi et *al*. (1998) obtained a maximum local drag reduction of 45% near the center of the oscillating section. They also showed that this decrease in the turbulent skin friction scales with the mean spanwise wall velocity $w_{ocs}^+$, the product of wall displacement amplitude $\Delta Z$ and circular oscillation frequency $\omega$, normalised by the friction velocity $u_\tau$, ($w_{ocs}^+ = \Delta Z \cdot \omega / 2u_\tau$) and that the skin friction decreases steadily as the wall velocity increases from zero as Figure 1 shows.
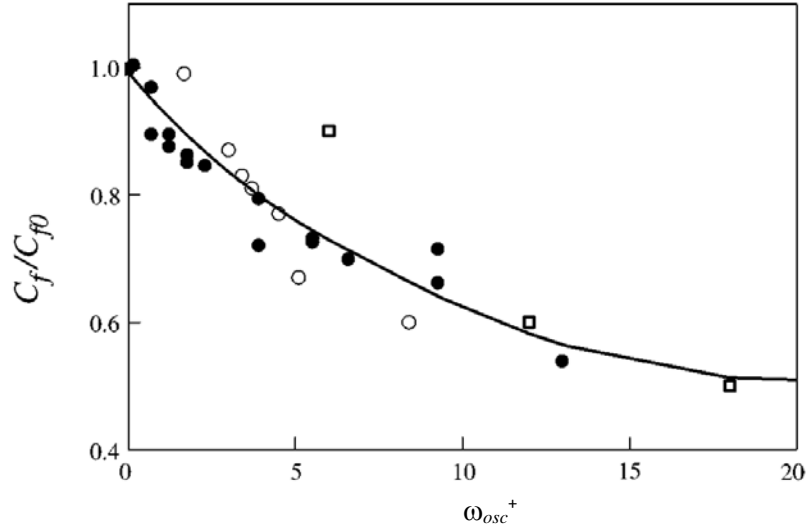
**Figure 1. Dependence of turbulent skin friction reduction on the non-dimensional wall velocity as shown in Karniadakis and Choi (2003).**

Based on the growth mechanism of the near wall streaks provided by Schoppa and Hussain (2002), Karniadakis and Choi (2003) suggest that such spanwise forcing may suppress the natural growth of the streamwise vortices by disrupting the phase locking of the near-wall streaks and regenerated near-wall streamwise vortices. By disrupting this natural growth and the subsequent generation of new near-wall streamwise vortices, the associated phenomena of bursting events near the wall, for which up to 80% of the total turbulent energy is attributed to (Lu and Willmarth 1973) is significantly reduced, and with it, the turbulent skin friction drag it results in.

While active systems boast levels of drag reductions as high as 40% or even more (Jung et al. 1992, Quadrio and Ricco 2004, Choi et *al.* 1998), some energy must be employed to operate the drag reduction system. In the case of an oscillating wall, when the energy used to oscillate the wall is taken into account, Quadrio and Ricco (2004) estimates a net energy saving of up to 7% in their DNS study of a turbulent channel flow. The use of an active system also adds significant complexity and cost into the design and operation of the device. With only about 10% net drag reduction

7

attainable after accounting for the energy required for the active system to operate, the alternative of passive drag reduction methods become attractive, particularly when one considers that passive methods have also demonstrated similar drag reduction levels, but without the added cost and complexity of active systems.

1.2.2   Passive drag reduction

As mentioned before, passive drag reduction methods do not require energy for the drag reduction to be active. The drag reduction is usually achieved by some modification to the surface geometry that targets and suppresses the near wall streamwise vortices and drag inducing burst events.

Several methods to do this passively exist, one of the earlier ones being via the use of Large Eddy Break Up (LEBU) devices (Savill and Mumford 1988). This involves positioning small stationary aerodynamic devices, usually in the form of a flat or airfoil shaped ribbon within the boundary layer. These are placed either in single or tandem configurations and their wakes interact with the turbulent boundary layer structure to effect a reduction in normal component of the velocity downstream of these devices (Balakumar and Widnall 1986, Graham 1998). This suppressed motion of the turbulent flow results in a reduction in the skin friction in the region immediately downstream of it. A large spread is observed in the skin friction measurements reported, with values of skin friction reductions of up to 40% reported (Sahlin et al. 1988). However, the difficulty and inaccuracies in measuring the skin friction through indirect methods at the relatively low Reynolds numbers studied cast some doubt on these measurements (Savill and Mumford 1988). This, together with the idea that if these devices reduce skin friction by breaking up the large scales, then their effectiveness should decrease at practically large Reynolds numbers, prompted Sahlin et al. (1986, 1988) to carry out direct force measurements of the skin friction

with LEBU devices at Reynolds numbers up to 260,000. Their investigation covered a wide range of parameters and included both single and tandem LEBU configurations. Although skin friction reductions as high as 8% were measured in regions downstream of the LEBU device, when the additional drag of the LEBU device was considered, no net drag reduction was found among the many cases considered. Despite significant differences in the drag of the LEBU device itself, the total drag obtained from all the configurations studied showed only a small variation, between about 0% to 3% more than the baseline case without the LEBU device. This led them to conclude that the use of LEBU devices for drag reduction at practical Reynolds numbers seem implausible.

One of the more notable methods of passive drag reduction is the use of riblets (Choi, 1989). These are small surface protrusions that are aligned in the streamwise direction with respect to the flow over the surface (Garcia-Mayoral and Jimenez, 2012). Walsh and his colleagues (Walsh 1980, 1982, 1990) at NASA Langley Research Center studied a variety of riblet geometries, and found that the effectiveness of riblets for drag reduction scales with the near-wall scales. The drag was observed to reduce when the riblet spacing $s^+ = su_\tau/v$, where $u_\tau = (\tau_w/\rho)^{1/2}$, is about 15. However, drag increase occurs when $s^+ > 30$ and when the riblet height $h^+$ ($= hu_\tau/v$) is greater than 25, possibly due to the increased wetted area that riblets introduce to the wall. Under optimal conditions, Walsh found that up to 8% drag reduction can be achieved with the riblets. While blade shaped riblets showed more favourable drag reduction (Berchet et al. 1997), they were less practical from a structural standpoint than shapes such as triangular and trapezoidal riblets, which are seen as more practical alternatives.

Both experiments (Bacher and Smith 1986, Choi 1989) and numerical simulations (Karniadakis and Choi 2003) show that the near-wall streaks that form above a riblet surface are wider and show significantly less lateral movement than those that form above a flat surface, while the flow between the riblets is slow and relatively quiet. Choi (1989) argues that this restriction of the lateral movement of the near wall streaks and their associated streamwise vortices is a prime reason for the reduction in drag. Significant wall shear stress is produced by the "sweeps" involving high momentum fluid being pushed towards the wall at the end of the burst cycle. As this occurs, the "legs" of the ejecting hairpin vortices experience streamwise stretching and lateral motion. The riblets restrict this lateral motion, subsequently hampering the streamwise stretching of the vortices, and ultimately reducing the intensity of the downward sweeps responsible for the high wall shear stress. In this way, riblets exert some kind of passive spanwise flow constraint to the near-wall flow over them to achieve the drag reduction. Similar mechanisms relating the reduced spanwise motion of the streamwise vortices above the riblets to the drag reduction that results have been proposed by Wallace (1982) and Berchert et al. (1986).

Unlike many other drag reduction methods, riblets have enjoyed greater success as a method of drag reduction outside of laboratories. Riblets have been successfully used in the U.S. men's rowing boat at the 1984 Olympic Games, as well as by the racing yacht Stars and Stripes to win the America's Cup in 1987. Airbus test flew a commercial jet with riblets covering its wings and fuselage and concluded that there was about 2% of drag reduction with the riblets. Swimsuits utilizing riblet technology was also successfully used in the 2008 Olympic Games in Beijing to set records and win many gold medals. The fact that their effectiveness scales with the near-wall parameters means that their physical size shrinks with increasing Reynolds number. For a fast commercial jet, the size of riblets typically needs to be between 30 to 50 $\mu$m to be effective for drag reduction (Karniadakis and Choi 2003). Their very small

physical size when used in such high Reynolds number applications introduces wear and maintenance problems that make them less practical for widespread application. The effectiveness of riblets is also dependent on the flow direction over the riblets. When the local flow is not parallel to the riblets, drag increase can result (Grüneberger and Hage 2011), making them unsuitable in applications where either the flow direction is unknown, or changes significantly over time.

### 1.2.3 Flow over dimples

Recently, there has been interest in the use of dimples for the purpose of drag reduction (Alekseev et al. 1998, Lienhart et al. 2008, Tay 2011). In the past, dimple geometries have been widely studied and used in heat transfer applications where they enhance heat transfer for a relatively small pressure drop when compared to other more traditional heat transfer devices (Won et al. 2005). For turbulent drag reduction applications however, much fewer studies have been published compared to those for heat transfer enhancement applications. Even among the few published works, there are inconsistencies in the reported results for the use of dimples for drag reduction. Some studies such as Alekseev et al.'s (1998) report drag reduction of up to 20% compared to flat surfaces, while others like Lienhart et al.'s (2008) report little to no drag reduction in their studies of dimples in both open and internal boundary layers. No clear reason has been found to explain such significant differences in the results.

Flows over dimpled surfaces are complex, and are influenced by a variety of dimple and flow parameters. Most significant of these parameters is the dimple depth, often non-dimensionalized by the dimple diameter. The effect of the dimple depth to diameter ratio has been well studied both experimentally (Won et al. 2005, Burgess and Ligrani 2005, Kovalenko et al. 2010, Ligrani et al. 2001, Kwon et al. 2011) and

numerically (Isaev et al. 2003, Wang et al. 2006), and typically range between 5% and 50% in most reported studies. Flow visualization experiments commonly show the generation of streamwise vortices, periodic in some cases, from the dimple depression (Ligrani et al. 2001, Won et al. 2005, Kovalenko et al. 2010, Tay et al. 2014), similar to that illustrated in Figure 2.
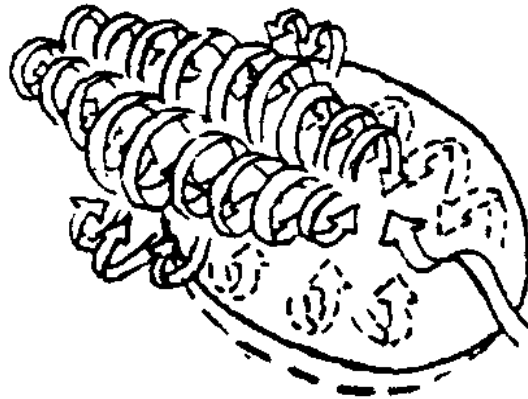


**Figure 2. Flow structures observed by Ligrani et al. (2001) for dimples with depth to diameter ratio of 20% in a channel flow.**

These flow structures are also observed in numerical studies (Isaev et al. 2000) and depend not only on the depth to diameter ratios of the dimples but also on the flow Reynolds number (Kovalenko et al. 2010, Tay et al. 2014, Isaev et al. 2003). Flow separation is observed for dimples with depth to diameter ratios greater than 10% (Kovalenko et al. 2010, Tay et al. 2014) with increased mixing and heat transfer (Burgess and Ligrani 2005). Dimples with sharp edges also encourage such flow separation, with its associated mixing and heat transfer enhancement (Tay et al. 2014). Most of the studies reported in the literature involve dimples in a channel flow environment, and many empirical relations have been proposed relating practically useful parameters such as Nusselt numbers and friction factors with the dimple depth to diameter ratio, Reynolds number, channel turbulent intensity, channel height and even the channel aspect ratio (Burgess and Ligrani 2005; Mahmood and Ligrani 2002; Ligrani et al. 2005; Isaev et al. 2010; Chen et al. 2013).

Although most reported studies focus on the heat transfer enhancement aspect of dimples and have limited direct application to the use of dimples for drag reduction, the results for friction factors in these studies may still serve as a useful guide for identifying possible trends for minimizing drag. There is a general consensus that increasing the dimple depth to diameter ratio increases the friction factor for the range of dimple depth to diameter ratios typically studied, usually greater than 10% (Burgess and Ligrani 2005, Isaev et al. 2010, Chen et al. 2012). For dimples with depth to diameter ratios of 30%, Burgess and Ligrani (2005) found that the friction factor increases with Reynolds numbers, though it shows little variation for dimple depth to diameter ratios of 10% and 20%. Numerical results and flow visualization both show that flow separation, which usually increases drag is minimised with decreasing dimple depth (Isaev et al. 2003, Tay et al. 2014). Isaev et al. (2003) found numerically that shallow dimples with depth to diameter ratios of less than 6% have no separated flow, though Tay et al. (2014) shows that the occurrence of flow separation within a dimple is dependent on both the depth to diameter ratio and the flow Reynolds number. Among the few studies relating dimples to drag reduction, both Veldhuis and Vervoort (2009) and Alekseev et al. (1998) reported drag reduction with dimples having depth to diameter ratios of about 5% and less. Dimples with depth to diameter ratio of 5% were also studied by Lienhart et al. (2008) for drag reduction both experimentally and numerically, one of the more comprehensive studies reported in the literature.

The extensive study carried out by Lienhart et al. (2008) included both experiments in a turbulent channel flow and zero pressure gradient open boundary layer flow over a flat plate, as well as DNS simulations of turbulent channel flow with dimples covering one wall and both walls of the simulated channel. The dimples studied had depth to diameter ratios of 5% and below with relatively sharp edges. The channel flow experiments were carried out over a range of Reynolds numbers from 10,000 to

65,000 based on the channel bulk velocity and half channel height, while the channel simulations were carried out at a Reynolds number of about 11,000 ($Re_\tau = 590$). The regularly staggered dimple arrangement used had an area coverage ratio of 22.5%, the area coverage ratio being defined as the horizontal area occupied by the dimples as a percentage of the total plan area of the dimpled wall. Interestingly, Wu and Yeo (2011) carried out DNS for arrangements of dimples with depth to diameter ratio of 10% in a channel flow with varying coverage ratios for a much lower Reynolds number ($Re_\tau = 180$) and found that dimple arrangements with coverage ratios of less than about 70% resulted in drag increase. Their results only showed drag reduction when the coverage ratio is greater than 70%.

Lienhart *et al.* (2008) used static pressure measurements to determine the pressure drop and flow resistance of the dimple with respect to a plane channel flow. A boundary layer rake downstream of the dimples was used to measure the velocity profile and determine the momentum thickness and skin friction coefficient for the open boundary layer case. Unfortunately, the changes in drag due to the dimples were so small that it fell within the margins of uncertainty for both the channel and open boundary layer flow experiments. Their numerical results confirmed these very small changes in drag, showing that the dimple arrangement when covering one wall of the channel increased the drag by 2% over a flat channel. When the dimples covered both the top and bottom walls of the channel, drag was increased by about 4%, suggesting minimal flow interaction with the opposite wall of the channel and that the drag increase due to the dimples varies proportionally to the area covered by the dimples. The simulations also showed that the dimples actually caused a 2% reduction in the spatially averaged skin friction, but caused a 4% increase in pressure drag, so that the total drag rises by about 2% for each of the channel walls covered with the dimples.

## 1.3    Objectives and scope

The objective of the present study is to investigate the effect of passive dimples for the purpose of drag reduction with the aim of understanding the mechanism behind it. Shallow dimples with smooth rounded edges and depth to diameter ratios of 1.5% and 5% and coverage ratios of 40% and 90% are investigated experimentally in a turbulent channel flow. Due to the streamwise vortices generated by the dimples, the flow component near the surface has a spanwise component imparted to it (Isaev et al. 2003, Mitsudharmadi et al. 2009). Schoppa and Hussain (1998) and Iuso et al. (2002) have demonstrated that drag reduction can be achieved by using streamwise vortices or transverse jets to introduce spanwise flow components into the near wall flow. The spanwise component required for drag reduction is found to be relatively small (Schoppa and Hussain 1998, Karniadakis and Choi 2003). The present study attempts to establish if the streamwise vortices generated by an array of regularly arranged dimples is sufficient to reduce the skin friction and produce a net drag reduction in a similar way.


Pressure measurements to determine the streamwise pressure gradient will be made to evaluate the change in drag due to the dimples, and hot-wire anemometry will be used to study the flow over the dimples in further detail. Single hot-wire anemometry is chosen over double and triple hot-wires because of the relatively narrow height of the channel as well as the poorer spatial resolution in the wall-normal direction of these double and triple wires. The spatial resolution in the wall normal direction is important since hot-wire measurements will be made at positions near the wall where the velocity gradient in the wall normal direction is high (Khoo et al. 1997; Chew et al. 1998). Unlike other popular measurement methods such as Laser Doppler Anemometry or Particle Image Velocimetry, the high temporal resolution of the hot-wire also allows the frequency spectra of the velocity signal to be accurately analysed. Turbulent drag reduction is usually accompanied by changes in the near

wall flow structures, which are too small to be effectively studied using most velocity measurement methods. However, their modification of the frequency spectra of the velocity signal near the wall (Iuso et *al*. 2002, Den Toonder et *al*. 1997, Li et *al*. 2004) can be detected using methods with high temporal resolution such as hot-wire anemometry.

Although Direct Numerical Simulation (DNS) can be used to study the flow in great detail, it is computationally very costly to resolve all flow features for such a channel flow with dimples. The main reason for this very high computational cost is due to the relatively high Reynolds number requiring a dense grid spacing to resolve the small flow features, and the minimum domain size required to contain a sufficient number of dimples in the domain to accurately simulate the flow over a dimple array. The dense grid spacing together with a large domain results in a very large number of simulation grid points that makes the DNS very costly. A reasonable compromise is to simulate the flow using Detached Eddy Simulation (DES). By modelling the near-wall flow using Reynolds Averaged Navier-Stokes (RANS) methods and resolving only the much larger vortices generated by the dimples higher above the wall, the requirement of a high mesh density can be relaxed, making the simulation of the turbulent flow over the dimpled channel more practical. The experiments compliments the DES, providing data to validate the DES, while the DES is able to provide quantitative data such as turbulent kinetic energy budgets, Reynolds stresses, skin friction and pressure data of which it is very difficult to measure experimentally, to give further insights into the flow development.

# Chapter 2

# Experimental details

## 2.1    The fully developed channel flow

When a viscous flow enters a duct, it begins to develop as the flow immediately next to the walls of the duct slow down due to the formation of the boundary layer and the no slip condition at the wall. This occurs while at the center of the duct, the flow is still free of the effects of viscosity. As the flow continues through the duct, the boundary layer along the walls of the duct continue to grow and thicken until their thickness reaches half the height of the duct and the boundary layer from the upper wall meets that of the lower wall. Eventually, the flow stops developing further and reaches what is called a "fully developed" state. When this happens, the streamwise pressure gradient becomes constant and is determined by the hydraulic resistance of the walls of the duct.

For a duct with flat walls, this hydraulic resistance is due to the skin friction acting on the walls of the duct. If the walls of the duct is not flat but vary in the vertical direction, then the hydraulic resistance comprises of both skin friction and form drag components. In both cases, the hydraulic resistance of the duct can be determined relatively easily and accurately by the measurement of the streamwise pressure gradient. In the case of a narrow channel where the spanwise dimension is much greater than its height, the flow at the center of the channel approaches that of a two dimensional flow and becomes relatively independent of the side walls of the channel. The study of the flow behaviour also becomes relatively easier since the effect of the side walls no longer need to be considered. Due to these characteristics of the fully developed channel, such a flow is chosen for the present study. Determination of the streamwise pressure gradient can be used to accurately quantify the hydraulic resistance, or drag due to the walls of the channel. To ensure that the

flow is fully developed within the channel, a relatively long channel is used. A narrow but wide channel is chosen to achieve relative two dimensionality of the flow at the center of the channel.

## 2.2    Test channel and dimple geometries

The channel flow experiments were conducted in an aluminum air channel measuring 20mm in height by 400mm wide, for an aspect ratio of 20. A bellmouth, honey comb, screens and a 16:1 contraction conditions the flow at the channel entrance. This is followed by a 3.2m long flat channel section, before a 2.4m long test section. The length of the flat section upstream of the test section is equivalent to $160h$, where $h$ is the channel height and allows the flow to become fully developed before it reaches the test section immediately downstream of it (Lien et al. 2004). The modular design of the channel allows the walls of the 2.4m ($120h$) long test section to be disassembled and flat or dimpled plates to be installed to form part of the channel wall. Immediately downstream of the test section is another 2.4m length of flat channel section before the downstream end to minimize any exit effects. The total length of the channel, at 8m or 400h in terms of channel height, is significantly longer than most used in the literature (Ligrani et al. 2005, Lienhart et al. 2008, Kwon et al. 2011). A centrifugal fan driven by a variable speed controller is located downstream of the channel to provide power to drive the flow over a range of Reynolds numbers. In the present study, the flow speed is varied to obtain Reynolds numbers ranging from about 3,000 to over 35,000. The Reynolds number is based on the half channel height $h/2$ and the channel centerline velocity. Figure 3 shows a schematic of the channel flow experimental set-up.
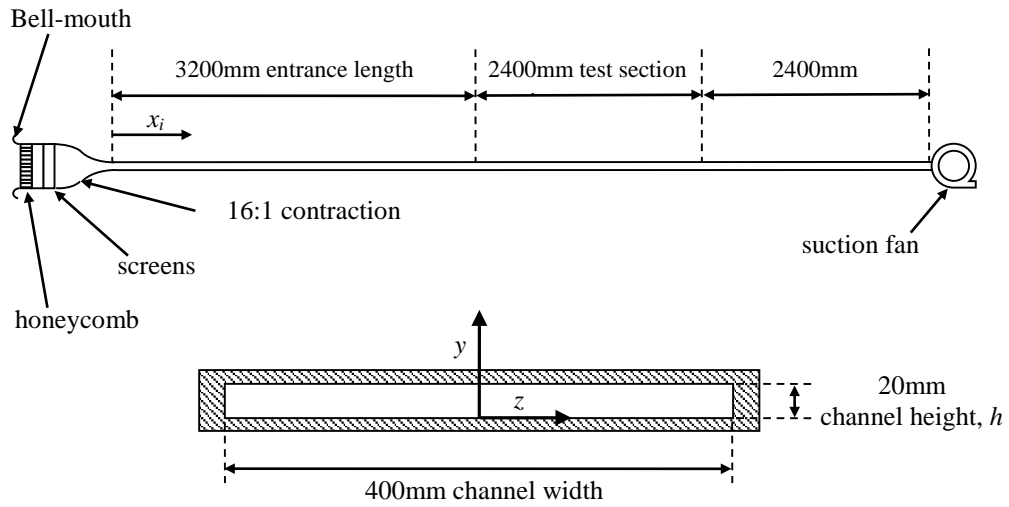
**Figure 3. Schematic of channel set-up with coordinate system used.**

Three different dimple array geometries are studied in the current work. Regularly arranged arrays of circular axisymmetric dimples are machined onto aluminum plates which form part of the channel test section floor when installed. The dimples cover the whole 2.4m of the test section floor, and have diameters, $D$ of 50mm, and depths, $d$ of 2.5mm and 0.75mm, giving dimple depth to diameter ratios of 5% for the deeper dimples, and 1.5% for the shallower ones. These dimples, when compared to those regularly studied in the literature are relatively shallow (Isaev et al. 2003, Burgess and Ligrani 2005, Won et al. 2005, Tay et al. 2014). The dimples have smooth rounded edges that meet the flat surfaces around it tangentially and are arranged so that the centers of adjacent dimples in the array form isosceles triangles with each other. This arrangement is shown in Figure 4, together with their cross section of the dimples across their diameter. The results of Veldhuis and Vervoort (2009) suggest that this configuration is more promising for drag reduction than one with the flow direction turned 90 degrees from that shown in Figure 4. The distance $\lambda$ between the dimple centers in Figure 4 determine the area coverage ratio, defined as the horizontal area occupied by the dimples as a percentage of the total plan area. When the coverage ratio is 90%, the adjacent dimple edges touch each other, and no further

19

increase in the coverage ratio is physically possible with such a dimple arrangement. Two different coverage ratios, 40% and 90% are investigated in the current work. A summary of the dimple parameters for the three cases is given in Table 1.
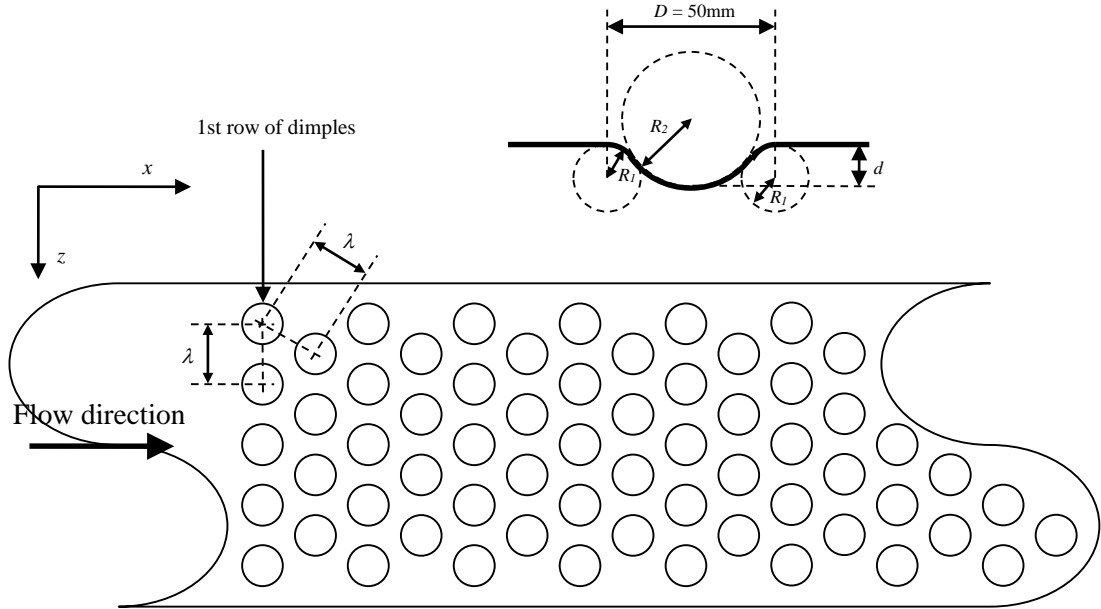


**Figure 4. Dimple cross section and arrangement**

**Table 1. Dimple parameters**

| Case | $D$ (mm) | $d$ (mm) | $R_1$ (mm) | $R_2$ (mm) | $d/D$ | $\lambda$ (mm) | Coverage ratio |
|------|----------|----------|------------|------------|-------|----------------|----------------|
| 1 | 50 | 2.5 | 42 | 84 | 5% | 75 | 40% |
| 2 | 50 | 2.5 | 42 | 84 | 5% | 50 | 90% |
| 3 | 50 | 0.75 | 150 | 267 | 1.5% | 50 | 90% |

## 2.3    Pressure measurements

In a fully developed channel flow, the flow is driven by a steady mean streamwise pressure gradient, and the drag on the solid walls exactly balance the driving force provided by the mean pressure gradient. Measurement of the mean streamwise pressure gradient allows the accurate determination of the total drag on the solid walls. For this purpose, static pressure taps of 1mm diameter are located along the length of the channel between $x_i/h = 27.5$ and $367.5$, where $x_i$ is the distance from the channel inlet, to allow the streamwise static pressure along the channel to be

20

measured. The pressure tapings are spaced at 50mm apart ($\Delta x/h = 2.5$), and line the length of the channel except within the test section located between $x_i/h = 160$ and 280. The static pressures are obtained using a multiplexer with a single Setra model 239 pressure transducer sampling at 1000Hz for about $2^{15}$ samples, giving a sampling time of about 33 seconds. The flow speed along the channel centerline is measured by a total pressure tube in conjunction with a static pressure tap, both located at $x_i/h = 367.5$, far downstream from the test section to minimize its effect on the flow in the test section. Besides the streamwise pressure tapings, pressure tapings are also available along the spanwise directions at $x_i/h = 147.5$ and 297.5, just upstream and downstream of the test section to ensure that the flow within the test section is relatively two-dimensional. All static pressure tapings are measured using a single pressure transducer connected via a computer controlled multiplexer. The use of a single pressure transducer ensures that no errors are introduced due to minor variations in the calibration of different separate pressure transducers used for pressure measurement.

## 2.4    Hot-wire velocimetry

While a fixed channel roof is used for pressure measurements, the modular design of the channel allows the installation of a sliding roof system and access for a hot-wire probe for velocity measurements within the channel. With the dimpled array installed on the channel floor, the computer controlled sliding roof system allows the positioning of a hot-wire probe at any point within the three-dimensional space over the dimple array for flow velocity measurement. A photograph of the 3-axis positioning system used is shown in Figure 5. Spanwise motion is provided for by the spanwise sliding roof, while a vertical actuator connected to the hot-wire probe controls the vertical position of the hot-wire probe. The hot-wire probe, together with its vertical position actuator rests on a rotating circular disc on the sliding roof. The

rotation of this disc, in conjunction with the spanwise motion of the sliding roof, allows the hot-wire probe to be moved in the streamwise direction. A computer controls the vertical motion actuator, spanwise motion actuator and rotation of the disc to position the hot-wire probe along all 3 axes within the sealed channel environment. An alignment bar keeps the hot-wire probe aligned along the coordinate axis at all times while the disc rotates to position the probe. While the vertical motion and spanwise motion actuators use lead screws with negligible backlash, the rotating disc uses a set of pinion and spur gears to control rotation and these have significant backlash, introducing inaccuracies in the positioning system if not accounted for. To eliminate the effect of this backlash, the last rotation made by the disk before measurements are made with the hot-wire probe is always clockwise. This means that if an anti-clockwise rotation is required to position the probe, the disc will be rotated anti-clockwise until it overshoots the desired position by an amount that is greater than the gear backlash. A final clockwise rotation is then made to bring the probe to the desired measurement position. A Dantec 55P15 boundary layer type probe was used to allow velocity measurements to be made very near the dimple surface. This probe uses a 5 micron tungsten wire with a length of 1.2mm as its sensing element. A overheat ratio of about 1.7 was used for all the experiments. Further details regarding the spatial resolution of such probes may be found in Khoo et al. (1997, 1998).
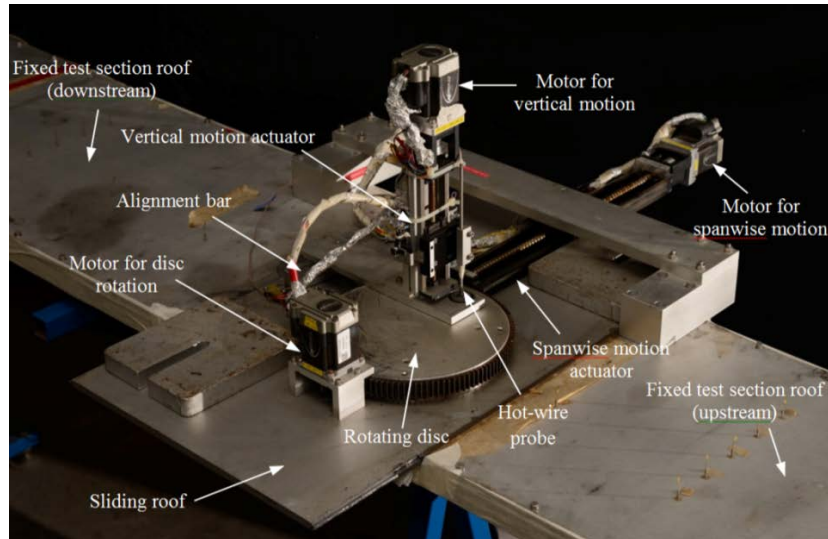
**Figure 5. 3-axis hot-wire probe positioning system.**

## 2.5    Wall detection with hot-wire

The channel was constructed out of aluminium to limit the channel deformation at high flow speeds due to the low pressure inside. It is estimated that the height of the aluminium channel reduces by about 0.8% at the test section location at the maximum Reynolds number of 35,000. The use of aluminium however, renders the channel opaque and makes the determination of the hot-wire probe distance from the wall impossible by direct optical means. An initial attempt was made to detect the position of the aluminium wall by monitoring the prongs for an electrical short across them. It was thought that when the prongs supporting the hot-wire element contacted the wall, the conductive aluminium wall will cause an electrical short across the prongs. Detection of this electrical short by monitoring the voltage across the prongs may be used to establish contact of the hot-wire probe with the wall. However, it was found that no electrical short resulted even when the hot-wire prongs were depressed against the wall, most likely due to the naturally occurring layer of non-conductive aluminium oxide on the aluminium surface.

To overcome this problem, the response of the hot-wire signal as the hot-wire probe approaches a solid wall was used to determine the distance of the hot-wire probe

23

from the wall instead. This method is described in Tay et al. (2012) and exploits the distinct change in the hot-wire voltage signal as the hot-wire probe comes into close proximity with a solid wall. Figure 6(a) shows the variation in the hot-wire mean voltage signal $V$ at various distances from the wall as measured on three separate occasions on three different days at zero flow speed. This variation is typical and well documented in the literature (Shi et al 2003, Chew et al, 1995, Khoo et al 1998, Turan and Azad 1987). The variation among the three curves also shows the effect of electronic drift, a common occurrence in the use of constant temperature hot-wire probes such as the one currently used (Bruun 1995). The drift significantly affects the repeatability of the hot-wire voltage signal variation with its distance $y$ from the wall. Figure 6(b) shows the same data, but plotted so that the spatial gradient of the voltage signal $\Delta V/\Delta y$ is plotted against the distance from the wall. The curves collapse together very well when plotted in this way.
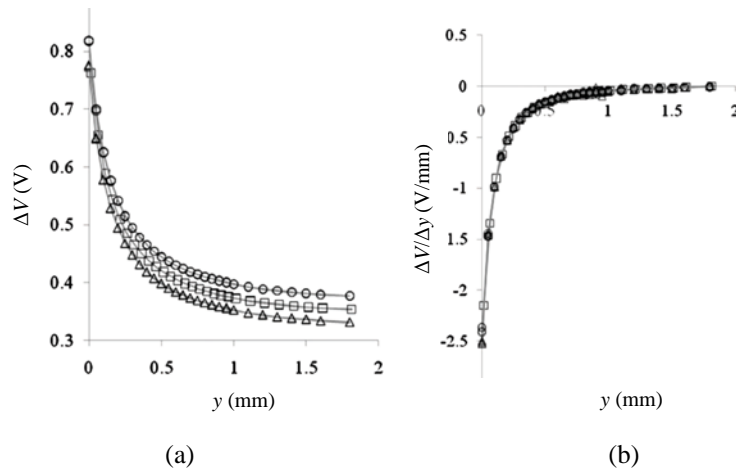


**Figure 6. Effect of a solid wall on the hot-wire voltage signal (a) and the spatial gradient of the hot-wire voltage signal (b). Circles: day 1, squares: day 3, triangles: day 5.**

The method described by Tay et al. (2012) relies on the use of this variation in the spatial gradient of the hot-wire voltage signal to determine the distance of the hot-wire probe from the wall. The output voltage response for a particular hot-wire probe is first determined and plotted in a similar manner to Figure 6(b) to obtain a calibration curve. This is done externally from the aluminium channel in a Perspex enclosure to ensure zero airflow around the hot-wire probe during the calibration

24

process. The transparent Perspex enclosure also allows optical access to visually determine the distance of the hot-wire probe from the wall using a travelling microscope. The wall material used in this calibration exercise is the same aluminium material that the channel is made from. During this calibration process, the hot-wire probe is lowered towards the wall in small steps and the mean signal from the hot-wire is recorded at each step until a curve similar to that in Figure 6(b) is obtained.

Once the external calibration of the hot-wire probe is done, the probe can be reinstalled into the aluminium channel for determination of the wall location and measurement of the flow velocity. The determination of the wall location is first carried out before the start of the experiment. This is done with the drive fan still off and with zero air flow. The detection process starts by the lowering of the hot-wire probe towards the wall in small steps similar to those carried out during the calibration procedure. Although the distance of the hot-wire from the wall can be visually determined during the calibration, its position from the wall when inside the aluminium channel has to be determined from the hot-wire voltage signal. During the wall distance detection procedure, the hot-wire is lowered towards the wall in the same manner as during the calibration procedure. A reference height is arbitrarily chosen and the movement of the hot-wire probe towards the wall is measured with respect to this reference height. To avoid the fragile hot-wire from coming into contact with the wall and possibly damaging it, an arbitrary reference value of $\Delta V/\Delta y$ is selected based on the calibration curve, and the movement of the hot-wire towards the wall is terminated when $\Delta V/\Delta y$ exceeds this selected value. This value of $\Delta V/\Delta y$ is chosen so that the hot-wire is very near the wall but not touching it when the procedure terminates.

The voltage signal from this detection procedure is then compared with that obtained from the calibration procedure. Figure 7 shows the comparison of $\Delta V/\Delta y$ obtained

from the calibration and detection procedure with a quadratic curve fitted to each. Because the variation in $\Delta V/\Delta y$ due to the response of the hot-wire as it moves towards the solid wall is identical for both the calibration and detection procedures, the two quadratic curves shares the same coefficients $a$ and $b$. Only the last coefficient, which determines the vertical intercept, or the distance of the reference height above the wall differs, is as shown in Figure 7. A least-squares fit of the points can be used to identify the values $a$, $b$, $c_1$ and $c_2$ of the quadratic curves shown in Figure 7.
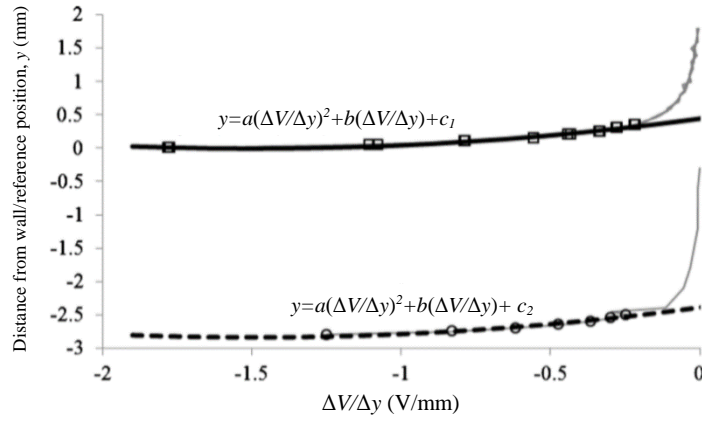


**Figure 7. Comparison of hot-wire voltage signal from calibration and detection procedures. Squares: data from calibration procedure, circles: data from detection procedure.**

Using a least-squares fit, the coefficients $a$, $b$, $c_1$ and $c_2$ can be shown to satisfy the following matrix:

$$
\begin{bmatrix}
\left( \sum_{i=0}^{n_{c_1}} \sigma_{c_1}^{4} + \sum_{i=0}^{n_{c_2}} \sigma_{c_2}^{4} \right) & \left( \sum_{i=0}^{n_{c_1}} \sigma_{c_1}^{3} + \sum_{i=0}^{n_{c_2}} \sigma_{c_2}^{3} \right) & \sum_{i=0}^{n_{c_1}} \sigma_{c_1}^{2} & \sum_{i=0}^{n_{c_2}} \sigma_{c_2}^{2} \\[2mm]
\left( \sum_{i=0}^{n_{c_1}} \sigma_{c_1}^{3} + \sum_{i=0}^{n_{c_2}} \sigma_{c_2}^{3} \right) & \left( \sum_{i=0}^{n_{c_1}} \sigma_{c_1}^{2} + \sum_{i=0}^{n_{c_2}} \sigma_{c_2}^{2} \right) & \sum_{i=0}^{n_{c_1}} \sigma_{c_1} & \sum_{i=0}^{n_{c_2}} \sigma_{c_2} \\[2mm]
\sum_{i=0}^{n_{c_1}} \sigma_{c_1}^{2} & \sum_{i=0}^{n_{c_1}} \sigma_{c_1} & n_{c_1} & 0 \\[2mm]
\sum_{i=0}^{n_{c_2}} \sigma_{c_2}^{2} & \sum_{i=0}^{n_{c_2}} \sigma_{c_2} & 0 & n_{c_2}
\end{bmatrix}
\times
\begin{bmatrix} a \\ b \\ c_1 \\ c_2 \end{bmatrix}
=
\begin{bmatrix}
\left( \sum_{i=0}^{n_{c_1}} y_{c_1} \sigma_{c_1}^{2} + \sum_{i=0}^{n_{c_2}} y_{c_2} \sigma_{c_2}^{2} \right) \\[2mm]
\left( \sum_{i=0}^{n_{c_1}} y_{c_1} \sigma_{c_1} + \sum_{i=0}^{n_{c_2}} y_{c_2} \sigma_{c_2} \right) \\[2mm]
\sum_{i=0}^{n_{c_1}} y_{c_1} \\[2mm]
\sum_{i=0}^{n_{c_2}} y_{c_2}
\end{bmatrix}
$$

where $\sigma = \Delta V/\Delta y$, $y$ is the distance from the reference height at which the mean voltage gradient $\sigma$ is obtained, and the subscripts $c_1$ and $c_2$ refer to the coefficients of

the quadratic curves shown in Figure 7 for the calibration and detection procedure respectively. The distance of the reference height above the wall is then the difference between the values of the vertical intercepts $c_1$ and $c_2$.

As mentioned before, the calibration and detection procedure is carried out under zero flow conditions before the actual experiments begin. There may be some concern that with a flow present, inaccuracies may be introduced due to the hot-wire probe bending in the presence of a flow. A simple analysis was carried out by modelling the hot wire probe holder as a hollow stainless steel tube with 4mm outside diameter and 0.1mm wall thickness. The internal components are assumed to have no contribution to the stiffness of the probe holder. A top hat profile is assumed of the velocity profile within the channel at maximum Reynolds number, and a 2D drag coefficient of 1.1 is assumed for the tube (Sumer and Fredsøe, 1997). Figure 8 shows the geometry considered, but with the deformation angle $\alpha$ greatly exaggerated. Even with these conservative assumptions giving an over-estimation of the resulting probe holder deflection in the presence of the flow, the resulting error $\delta_e$ introduced to the wall detection is only about 0.002mm at the maximum Reynolds number condition.
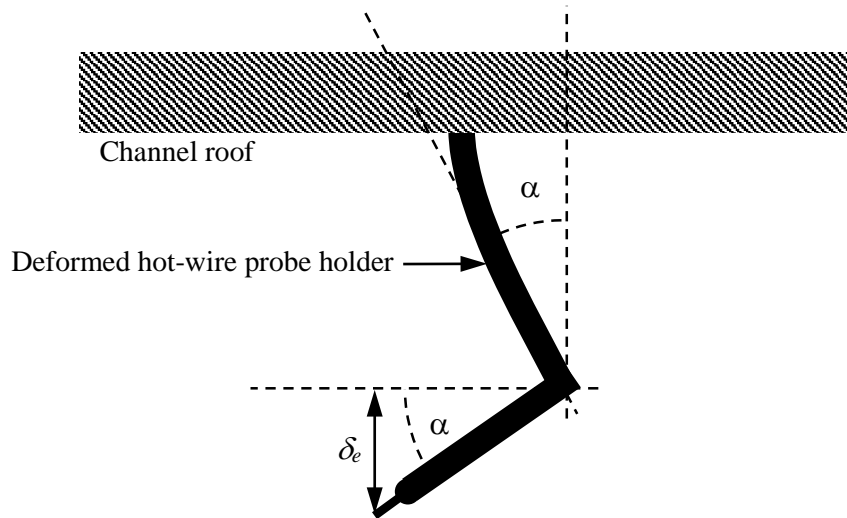
**Figure 8. Flow induced deflection of hot-wire probe holder. Angles are greatly exaggerated for illustration.**

## 2.6    Temperature compensation for hot-wire

As the experiment is not carried out in a temperature controlled air-conditioned environment, there is a concern that ambient temperature fluctuations can affect the accuracy of the hot-wire measurements. This is particularly so since hot-wire anemometry is well-known to be affected by changes in the fluid temperature (Bruun 1995, Abdel-Rahman et al. 1987). To reduce the errors due to ambient temperature changes, the ambient temperature was measured by a type T thermocouple in conjunction with a thermistor for cold junction reference temperature measurement. This ambient temperature measurement is done with the thermocouple located near but outside of the aluminium channel. Since the channel is an open type with a suction motor at the downstream end, and not the re-circulatory type, the ambient air temperature outside of the channel is representative of the fluid temperature inside the channel. The temperature measurements allowed the effect of any changes in the ambient temperature on the hot-wire measurements to be compensated according to equation (1) (Bruun 1995).

$$E_c = E_m \left[ \frac{T_w - T_r}{T_w - T_a} \right] \qquad (1)$$

where $E_c$ is the corrected voltage signal, $E_m$ is the measured voltage signal, $T_w$ is the wire temperature, $T_r$ is the reference temperature, taken as the temperature during the hot-wire calibration and $T_a$ is the ambient temperature at which the velocity measurement was carried out.

# Chapter 3

# Experimental results

## 3.1   Channel validation

Before experiments with the dimples began, the flow within the air channel was first validated with known results from the literature. A smooth flat channel floor was installed within the test section and pressure and velocity measurements were made for the validation. The static pressures measured with the various streamwise pressure taps are presented in Figure 9 for a range of Reynolds numbers. Figure 9(a) shows the streamwise variation in the static pressures referenced to that measured at $x_i/h = 27.5$, where $x_i$ is the length measured from the inlet of the channel. A solid line fitted over the linear portion of the streamwise pressure variation shows that the streamwise pressure gradient within the channel has reached a constant value well before the test section located at $x_i/h = 160$. Although there is some debate whether the constant streamwise pressure gradient implies that the flow is fully developed (Lien et al. 2004), the relatively long entrance length used in the present channel is beyond even the conservative estimation of $130h$ suggested by Lien et al. (2004) required to attain fully developed flow in a channel. The constant streamwise pressure gradients obtained with the current channel at various Reynolds numbers is also in excellent agreement with that predicted by the Colebrook-White equation (Mott, 1994) for fully developed flows in conduits, as shown in Figure 9(b).

Static pressure measurements obtained using the pressure taps at $x_i/h = 147.5$ and 297.5 distributed in the spanwise direction are shown in Figure 10. The measurements show that the flow is relatively 2-dimensional immediately upstream and downstream of the test section located between $x_i/h = 160$ and 280.

**(a)**

**(b)**
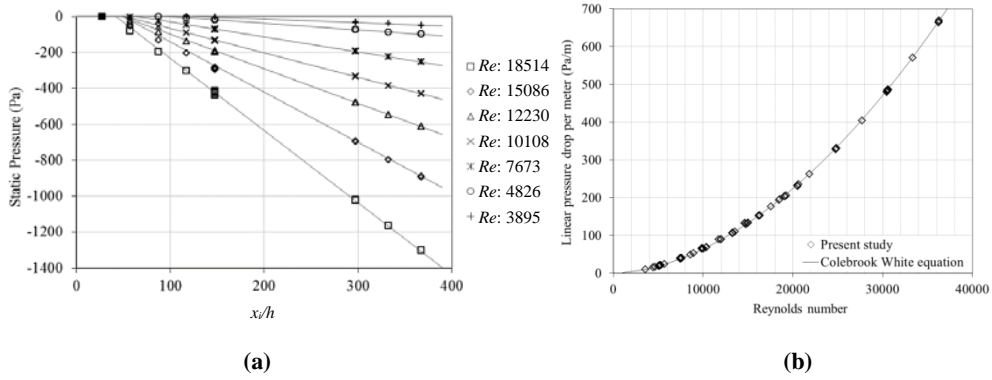
**Figure 9. Streamwise static pressure measurements without dimples.**



**(a)**

**(b)**
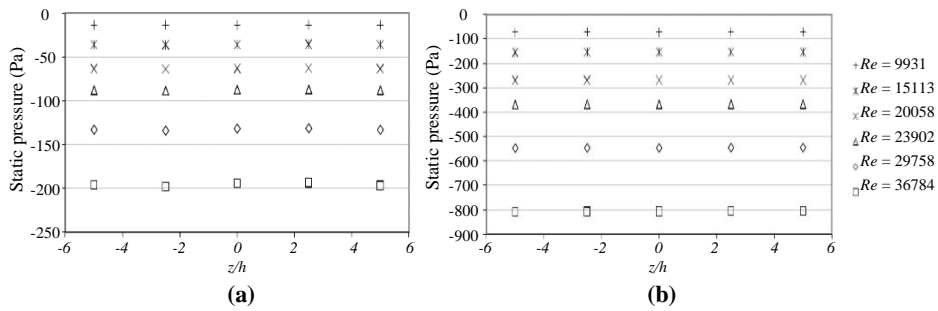
**Figure 10. Spanwise static pressure measurements without dimples. (a) $x_i/h = 147.5$, (b) $x_i/h = 297.5$.**

The profile of the streamwise velocity within the smooth flat test section without dimples was measured using hot-wire anemometry at various Reynolds numbers. Figure 11 shows that the results obtained compares favorably with that of Johansson and Alfredsson (1982). The good agreement further supports the accuracy of the wall detection method used in the present study even in the presence of the flow.
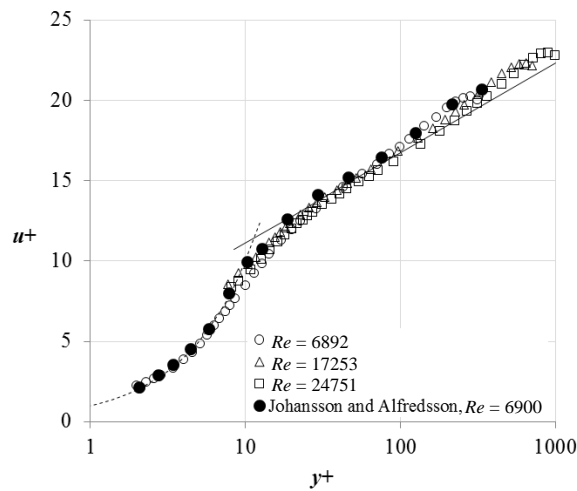
**Figure 11. Channel velocity profiles. Dashed line: $u^+ = y^+$, solid line:** $u^+ = \dfrac{1}{0.41}\ln(y^+) + 5.5$

## 3.2  Pressure measurements

### 3.2.1  Drag measurement detailed methodology

Traditionally, the determination of drag can be obtained by measuring the mean streamwise pressure gradient in the fully developed portion of a channel flow (Chen et al. 1986, Itoh et al. 2006). However, reports from the literature suggest that the drag reduction by circular dimples may be small and not easily determined by measurement of the mean streamwise pressure gradient (Lienhart et al. 2008). In the course of the experiments, whenever the channel configuration had to be changed from a dimpled to a non-dimpled one, the fan powering the channel flow had to be shut down as the very low pressure within the channel while the fan is running makes removal and installation of the test plates very difficult, particularly at high flow speed. The finite accuracy of the motor speed controller resulted in small changes in flow speed even for consecutive experimental runs, leading to a small but finite change in the flow Reynolds number. An example of such a change in Reynolds number that occurs can be observed in the two runs shown in Figure 12. A simple analysis was carried out to estimate the significance of this small change in the Reynolds number.
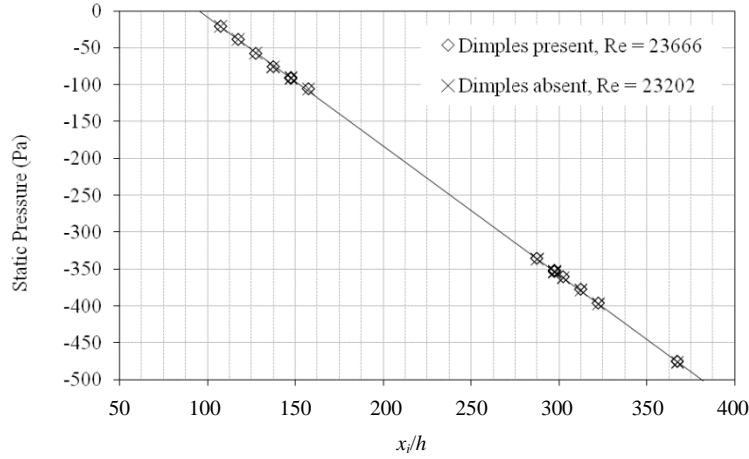
**Figure 12. Streamwise static pressure measurements with and without Case 1 dimples.**

As Figure 9(b) shows, the mean streamwise pressure gradient $P_g$ may be assumed to be a function of the Reynolds number $Re$ of the flow, and can be expressed as:

$$P_g = f(\text{Re}) \tag{2}$$

where the function $f$ is the Colebrook-White equation in Figure 9(b).

Differentiating with respect to the Reynolds number gives:

$$\frac{\delta P_g}{\delta \text{Re}} = f'(\text{Re}) \tag{3}$$

For a small change in the Reynolds number,

$$\frac{\delta P_g}{P_g} \approx \frac{f'(\text{Re})\delta \text{Re}}{P_g} \tag{4}$$

Figure 13 shows the percentage change in the mean pressure gradient when the Reynolds number changes by 500, ie. $\delta \text{Re} = 500$, which is approximately the difference in Reynolds number between the two cases presented in Figure 12. The effect varies with the Reynolds number, and is as high as 14% at a Reynolds number of 5,000, but decreases to 3.6% at a Reynolds number of 20,000. At a Reynolds number of 40,000, the effect on the mean pressure gradient reduces further to about 1.8%. These percentage changes are deemed to be significantly large as the expected changes in drag due to the dimples are very small and may be of the order of a few

33

percent (Lienhart *et al.* 2008). The analysis suggests that the traditional method of changing the test plates and comparing the drag results obtained is not possible due to the high accuracy required.
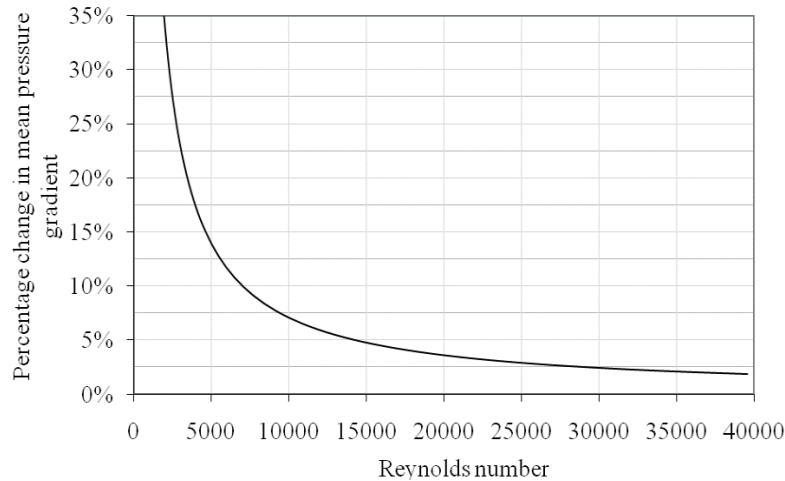


**Figure 13. Effect on mean pressure gradient with a Reynolds number change of 500.**

An alternative method needs to be found to determine any change in drag due to dimples. To overcome this difficulty, the method of Tay (2011) was employed since the channel used is sufficiently long. This method does not quantify the absolute drag due to the dimples in the channel, but gives the relative difference in the drag compared with that for a flat channel flow.

Consider again the mean streamwise pressure variation shown in Figure 12 for the cases with and without dimples installed in the channel test section at comparable Reynolds number. The pressure variation is practically indistinguishable for both these cases, showing that any change that the dimples have on the drag is indeed very small. Because the section after the test section in the channel is also flat, it is expected that the mean streamwise pressure in this section should be the same as that in the flat section upstream of the test section. It may be observed in Figure 9 that the streamwise pressure variation is already linear from $x_i/h = 100$ onwards, indicating that the fully developed mean streamwise pressure gradient has been attained.

34

Although some debate exist about the minimum length required for the flow to reach its fully developed state, and what "fully developed' actually entails (Lien et al. 2004), it is known that even before the flow reaches its fully developed state, the mean streamwise pressure gradient will reach its fully developed value first (Potter and Foss 1983). Barbin and Jones (1963) estimates that for a circular pipe, the mean streamwise pressure gradient reaches its fully developed state within 15 pipe diameters from the pipe entrance. The sections within the present channel are much longer in terms of the channel height $h$, which is analogous to the diameter of a circular pipe. The section upstream of the test section is $160h$ in length, the test section is $120h$ in length, and the section downstream of the test section is also $120h$ in length. Thus, it is assumed that for most of the flow within these three sections, the mean pressure gradients are those of the fully developed values.

Figure 14 illustrates this assumption graphically using a hypothetical case. In this hypothetical case, the measurement points are shown by crosses, and the dimpled test section is located between $x_i/h = 160$ and $x_i/h = 280$. The linear pressure variation of the flat sections upstream and downstream of the test section is represented by dashed lines in Figure 14 and share a common gradient $m$. Any change in the mean pressure gradient from that of the flat sections due to the dimples results in a vertical shift of the dashed lines so that they remain parallel but are not co-linear and have different intercepts on the vertical pressure axis given by $P_1$ and $P_2$. A vertical shift upward, or if $P_2 > P_1$ means a reduction in the mean pressure gradient in the dimpled test section signaling a decrease in drag by the dimples. A downward shift or $P_2 < P_1$ means a drag increase by the dimples. If the difference in $P_1$ and $P_2$ are known, the effect of the dimples on the drag compared to the flat sections can be determined quantitatively.
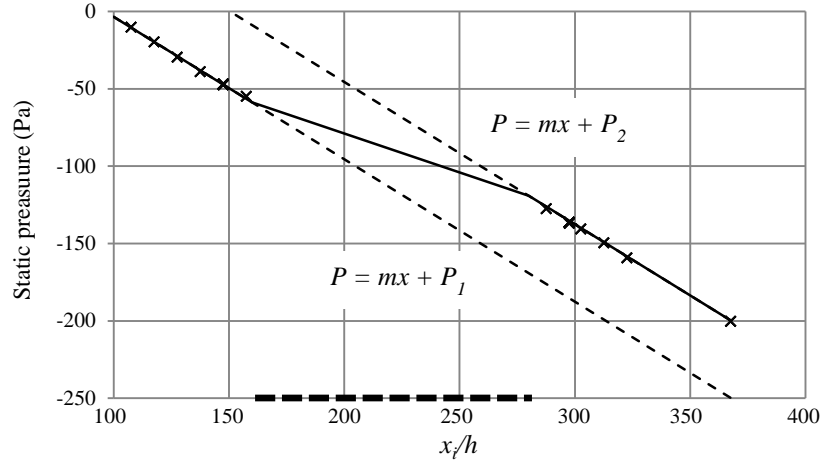
**Figure 14. Hypothetical static pressure distribution with dimples present. Bold dashed line: test section location.**

The equations for the dashed lines can be estimated from actual measurements by least squares fitting. The sum of the squares for the points upstream of the test section is given by:

$$\sum_{i=1}^{n_u}[P_u - (mx_u + P_1)]^2 \tag{5}$$

where the subscript $u$ refers to data points upstream of the test section. Similarly, the sum of the squares for the points downstream of the dimples is given by:

$$\sum_{i=1}^{n_d}[P_d - (mx_d + P_2)]^2 \tag{6}$$

where the subscript $d$ refers to data points downstream of the test section. The total sum of squares for all the data points is given by summing these two expressions. Minimizing this total sum yields the following:

$$m = \frac{n_u \sum_{i=1}^{n_u} x_u P_u - \sum_{i=1}^{n_u} x_u \sum_{i=1}^{n_u} P_u + n_d \sum_{i=1}^{n_d} x_d P_d - \sum_{i=1}^{n_d} x_d \sum_{i=1}^{n_d} P_d}{n_u \sum_{i=1}^{n_u}(x_u^2) - (\sum_{i=1}^{n_u} x_u)^2 + n_d \sum_{i=1}^{n_d}(x_d^2) - (\sum_{i=1}^{n_d} x_d)^2} \tag{7}$$

36

$$P_1 = \frac{\sum_{i=1}^{n_u} P_u - m \sum_{i=1}^{n_u} x_u}{n_u} \qquad (8)$$

$$P_2 = \frac{\sum_{i=1}^{n_d} P_d - m \sum_{i=1}^{n_d} x_d}{n_d} \qquad (9)$$

where $P$ is the measured static pressure, $n$ is the number of measurements and the subscripts $u$ and $d$ are defined as before. The change in drag $\Delta_d$ due to the dimple array is then given by:

$$\Delta_d = \frac{(P_1 - P_2)}{L_D m} \qquad (10)$$

where $L_D$ is the length of the dimple array. A negative value represents a drag reduction and a positive value represents a drag increase when compared to the smooth flat sections of the channel, used as the baseline for the comparison. Using this method, separate static pressure measurements for a flat wall case and a dimpled case is not required, as the comparison is done directly through the measurement of the streamwise pressure variation for a single channel configuration, using the flat sections of the channel upstream and downstream of the dimple array in the test section as the baseline for the comparison.

This method relies on the assumption that the channel sections are sufficiently long so that the mean streamwise pressure gradients in the flat sections upstream and downstream of the test section is the same. An investigation was carried out to find out if this is the case and so verify the assumption. With a flat wall installed in the test section, the difference between the actual measured static pressures and that given by their respective equations represented by the dashed lines in

Figure **14**, was normalised by the dynamic pressures and plotted in Figure 15 for a range of Reynolds numbers.
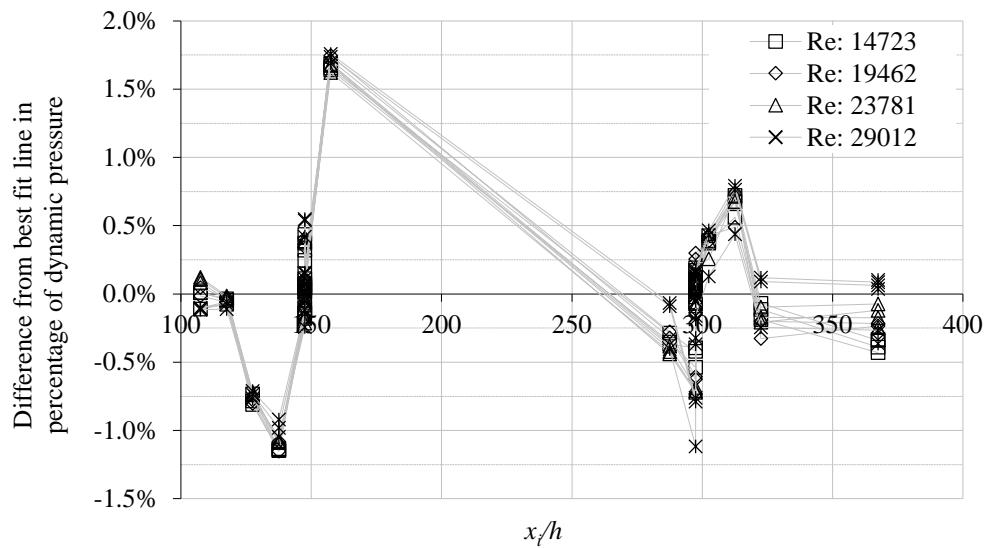


**Figure 15. Variation of difference in measured static pressures from least squares fit for flat wall case.**

Small deviations of the actual measurements from the best fit line described by the equations in Figure 14 are observed along the channel due to the imperfect nature of real physical channel flow facilities. The deviations are small and well within the experimental errors expected of real experiments, and may be caused by imperfections in wall smoothness, small changes in the channel height due to machining imperfections, finite accuracy of the measurement system and other factors of which are not possible to control. It is important to note that the deviations are not random with time, but are highly repeatable even as the Reynolds number varies. This allows the deviations to be corrected.

A similar plot was made with a dimpled section installed. This time a shift in the static pressure measurements downstream of the test section is expected, similar to that shown in Figure 14, and $P_1 \neq P_2$. Plotting only the difference with respect to the

equation $P = mx + P_1$ yields the plot in Figure 16. Note that for the flat wall case, it is expected that $P_1 = P_2$. It is obvious that for the dimpled wall case, all the points downstream of the dimpled test section are shifted vertically up in Figure 16, while the points upstream of the test section is hardly affected by the presence of the dimples. The upward shift of the points downstream of the test section is the same for all the points, thus preserving the trend in the streamwise variation. This means that the actual pressures are only shifted vertically due to the dimples in the test section, while the mean pressure gradient of the flat section downstream of the test section remains the same as the other flat sections of the channel. The value of the mean streamwise pressure gradients in the flat sections are also not affected by the presence of the dimples in the test section. The assumption that the channel is sufficiently long so that the mean streamwise pressure gradients of the flat sections before and after the test section are the same is thus valid.
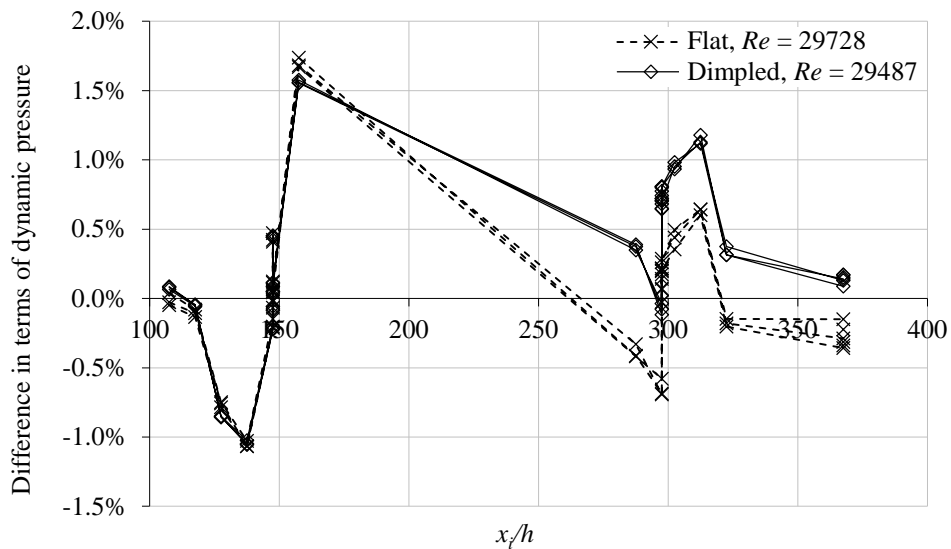


**Figure 16. Variation of difference in measured static pressures from least squares fit for flat and corresponding dimpled wall case.**

Applying equations (7) to (10) to the data used to plot Figure 16 gives a drag reduction of about 0.5% for the dimpled case. It may be noted that Figure 16 actually

shows data taken from three consecutive runs, and very limited scatter is observed in the measurements obtained from these three runs. The same observation about the very limited scatter in the data can also be made for Figure 15, which shows data from three consecutive runs at each Reynolds number, showing the high consistency of the measurements over a range of Reynolds numbers. Although the change in drag is only about 0.5% for the case presented in Figure 16, the vertical shift is clearly prominent and much larger than the scatter in the data.

The magnitude of the non-dimensional vertical shift $\Delta_p = \left|P_2 - P_1\right| \left/ \dfrac{1}{2}\rho U^2\right.$ is mainly affected by the length of the dimpled test section $L_D$, the change in drag due to the dimples $\Delta_d$ and the mean streamwise pressure gradient given by $m$ according to the following equation:

$$\Delta_p = \frac{\Delta_d L_D m}{\dfrac{1}{2}\rho U^2} \tag{11}$$

where $\frac{1}{2}\rho U^2$ is the dynamic pressure, $U$ being the mean centerline velocity. From the Colebrook-White relation shown in Figure 9(b), it may be inferred that the fully developed mean streamwise pressure gradient is related to the dynamic pressure if the density $\rho$ remains constant. Increasing the length of the dimpled test section $L_D$ will result in an increase in the magnitude of the vertical shift for a given change in drag, thus increasing the sensitivity of the experiment and allowing very small changes in drag to be measured confidently. The relatively long dimpled test section of 2.4m in the present channel flow facility thus contributes significantly to the high sensitivity of the present experiment. An estimate was made of the uncertainty of this method based on the pressure transducer used and this was found to vary from about

3% at low Reynolds numbers to 0.2% at the higher Reynolds numbers involved in the present study.

### 3.2.2   Drag results

The described method gives the change in drag due to the dimples in the test section compared to the flat channel sections used as a baseline. The effect on drag by the three different dimple configurations compared to the flat channel case is plotted in Figure 17 up to the maximum Reynolds number of about 37,000 that the present channel set-up can deliver. $d/D$ in the legend of the figure refers to the dimple depth to diameter ratio, while CR refers to the area coverage ratio previously defined in Figure 4. The experiment is repeated several times to obtain confidence in the results. The consistency of the measurements is such that the scatter within the data is small compared to the percentage changes in drag shown by the dimple arrays. It is clear that for the deeper 5% $d/D$ dimples of cases 1 (CR = 40%) and 2 (CR = 90%), their effect on drag varies with the Reynolds number. However, their dependence on Reynolds number decreases as the Reynolds number increases.  In fact for Case 1, beyond $Re$= 20,000, its effect on drag stays almost constant up to the maximum Reynolds number of 37,000. For the shallow 1.5% $d/D$ dimples of Case 3, their effect on drag is almost independent of the Reynolds number. It appears that reducing the dimple depth and the dimple area coverage ratio result in reduced dependence on Reynolds number.

At low Reynolds numbers, Case 1 and 2 dimple configurations show drag increases compared to the flat wall, while the opposite is true at higher Reynolds numbers where both show drag reductions. The cross over point where the dimples begin to show drag reductions vary for the two cases. Case 1 with coverage ratio of 40% have its cross over point at a $Re = 8,000$ while the Case 2 dimples with coverage ratio of

90% crosses over to drag reduction at about $Re = 13{,}000$. Despite the late cross over point for Case 2, the drag reduction steadily increases to almost 3%, which is greater than the other two cases at a Reynolds number of 37,000. Case 1 shows a near constant drag reduction of slightly less than 2% at almost all Reynolds number after its cross over point. Case 3 shows a drag reduction of about 2% over the range of Reynolds numbers studied here. Increasing dimple depth and coverage ratios appear to increase the maximum drag reduction at high Reynolds numbers, possibly due in part to its higher dependence on the Reynolds number. Shallow dimples show drag reduction even at lower Reynolds numbers, and may be favoured if reduced drag is desired at low Reynolds numbers.

Drag increases at the lower Reynolds number range also varies with the three cases. Although Case 2 shows the greatest drag reduction at high Reynolds numbers, it also shows the greatest drag increase at low Reynolds numbers. A maximum of almost 4% increase in drag is observed at the lower Reynolds number range before transition effects make accurate measurements difficult. As the main focus of the present study was for the higher Reynolds number range, further examination of the drag increases at the lower Reynolds numbers was not carried out.
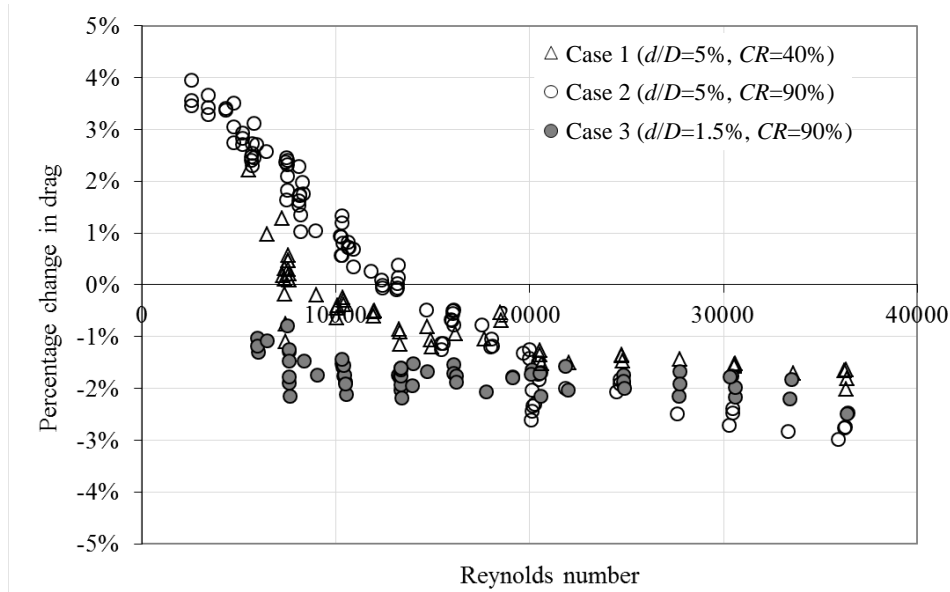
**Figure 17. Effect on drag by various dimple configurations compared to the flat channel without dimples.**

The above measurements were mainly carried out with the static pressure taps and the dimpled array installed on the roof of the channel. This allowed easy access to both the dimpled plate and the static pressure taps during the experiments. Some concern arose whether the dimples being on the same side as the pressure taps, would affect the measured results. If the flow within the channel was not symmetrical about the centerline, the conclusions drawn from the previously measured static pressure variation might be inaccurate.

To investigate this matter, several runs were carried out with the static taps on the roof of the channel while the dimple array was installed on the floor of the channel. This was carried out only for Case 3 to verify this concern. It is assumed that if the result is valid for any one case, it would make the other cases equally valid. The result from this test is shown in Figure 18. It shows that similar results are obtained regardless of whether the pressure taps are located on the same side of the dimples or

43

not. This gives greater confidence in the previous pressure measurements. For a better comparison, the results presented in Figure 18 are also included in Figure 17.
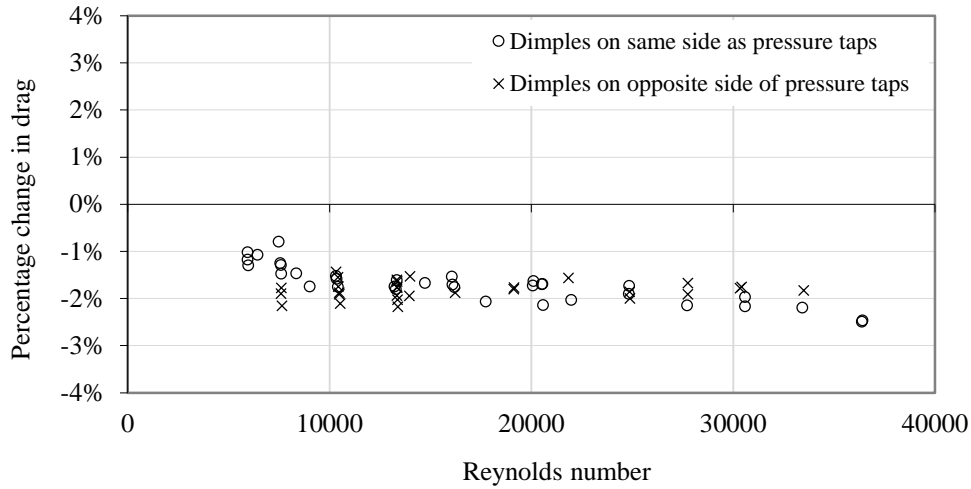


**Figure 18. Effect on drag with dimples installed on different sides of the channels**

## 3.3 Hot-wire velocity measurements

### 3.3.1 Initial hot wire measurements at low spatial resolution

Detailed hot-wire measurements were made for cases 2 and 3 since these show greatest drag reduction at high and low Reynolds numbers respectively. Velocity measurements were made at Reynolds numbers (based on the half channel height and centreline velocity) of about 10,000, 15,000, 23,000 and 35,000. The coordinate system used in these hot-wire measurements has its origin ($x/D = 0$, $z/D = 0$) centered at the center dimple of the $11^{th}$ row of the dimple array. An initial measurement with the hot-wire was sampled at 3,000 Hz for about 80 seconds at ($x/D = 0$, $y/h$=0.05, $z/D = 0$) for all four Reynolds numbers. From this velocity time history, the average velocity $U_{average}$ obtained from $t = 0$ to $t = t_1$ was plotted by varying $t_1$ in steps of 0.1s. This can be expressed mathematically as:

$$U_{average} = \frac{1}{t_1} \int_0^{t_1} u\,dt \qquad (12)$$

The mean velocity $U$ obtained from the complete time history is assumed to be accurate, and the percentage difference between $U_{average}$ and $U$ is plotted against $t_1$ in Figure 21. Because the percentage difference, or error in the sampling time falls rapidly as the sampling time $t_1$ increases, only the portion of the plots for $t_1 \leq 10s$ is shown. With a sampling time of 5s, the percentage difference has reduced to below 0.1% for all Reynolds numbers.
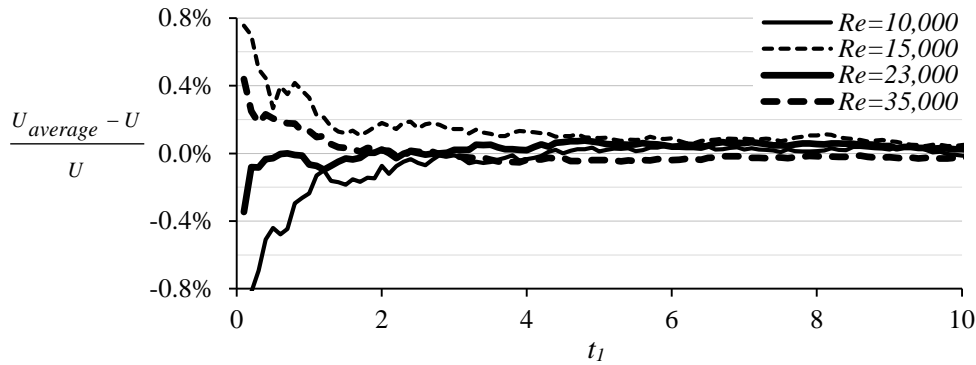


**Figure 19. Error in average velocity with sampling time.**

As such, all the hot-wire measurements were sampled at 3,000 Hz for $2^{14}$ points, giving a sampling duration of about 5.5 seconds at each location. Only those used to subsequently measure the spectral distributions of the velocity fluctuations were sampled at a higher sampling rate and over a longer period. This will be discussed further in the subsequent appropriate section.

Initial measurements were made within the measurement volume $-0.8D \leq x \leq 0.8D$ and $-1.0D \leq z \leq 1.0D$ from near the dimpled surface to the channel centerline to gain a basic idea of the flow and identify any possible areas of interest for a more detailed study. Figure 20 shows the location of the measurement grid relative to the dimples in the array. The dashed circles indicate the position of the dimples.

45
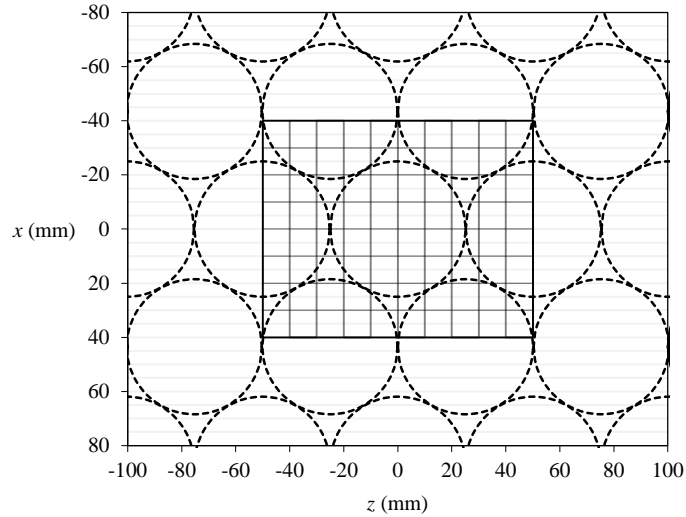
**Figure 20. Hot-wire measurement grid.**

The measurement grid spacing for these early measurements is relatively coarse with $\Delta x \approx 0.20D$ and $\Delta z \approx 0.20D$. The measurement grid spacing in the vertical $y$ direction is not uniform but is smaller near the wall and increases as the measurement location rises above the dimpled surface. As shown in Figure 3 previously, the $y$ coordinate is measured from the flat areas between the dimples. Not too surprisingly, the deeper Case 2 dimples affects the flow up to a greater distance above the wall than the shallower Case 3 dimples. This is shown in Figure 21, where the velocity variation in the spanwise direction for the Case 2 and Case 3 dimples are shown, together with the relative position of the dimples indicated by the black lines. The figure shows that the deeper Case 2 dimples affect the flow up to a height of $y/h = 0.3$, while at a height of $y/h = 0.1$, the velocity is nearly constant for the shallower Case 3 dimples. A velocity peak is observed along the centerline of the shallower Case 3 dimples at all heights below $y/h = 0.1$, but the velocity peak only extends to a height of $y/h = -0.04$ within the dimple depression for the deeper Case 2 dimples. Above this height, a local minimum in the velocity is observed up to at least $y/h = 0.3$. This difference in velocity peaks for these two dimple cases are also similarly observed at the other two Reynolds numbers of 10,000 and 35,000.

46
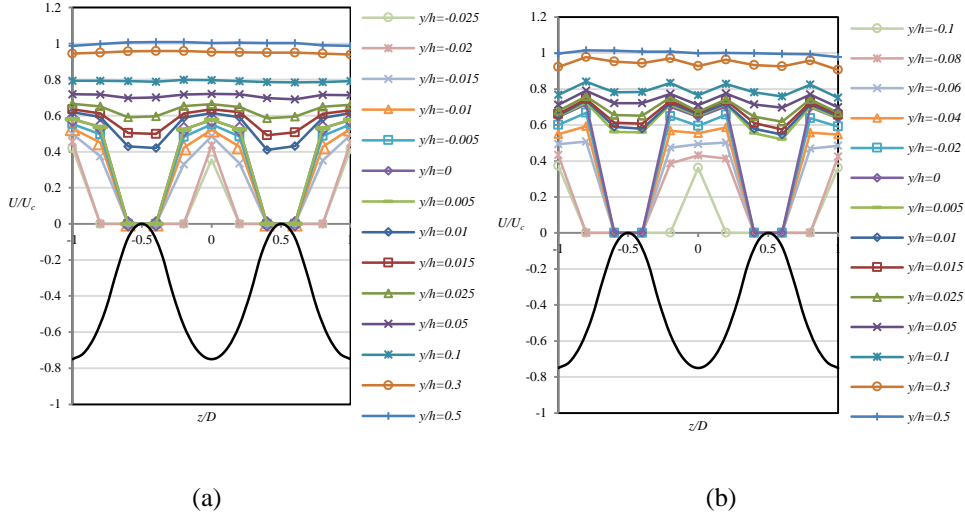
**Figure 21. Normalised mean streamwise velocity plots at various heights over dimple arrays, *Re* ≈ 15,000, *x/D* = 0. (a) Case 3 (*d/D* = 1.5%), (b) Case 2 (*d/D* = 5%). Bold lines show the locations of dimples and are exaggerated to show their relative depth.**

The flow pattern over the dimples may be more easily appreciated if the velocity contours in the *x-z* plane over the dimples are presented. However, one problem is inherent in using the coarse measurement grid shown in Figure 20 for presenting *u*-velocity contours in the *x-z* plane. The grid spacing in Figure 20 is regular at 10mm in both the *x* and *z* directions, resulting in the measurement points being not in phase with the streamwise or spanwise spatial wavelengths of the dimple array. The result of this, together with the coarse measurement grid spacing, on the velocity contours is shown in Figure 22 at *y/h*=0.05. The plot shows the contours of the mean streamwise velocity normalized by the channel centerline velocity. While the velocity contours over the central dimple in Figure 22 appears symmetric about the dimple centerline, a careful observation of the velocity contours for the row of dimples upstream and downstream of this central dimple are not. The reason for this apparent asymmetry is due to the coarse measurement grid not being in phase with the spatial wavelengths of the dimple array and when the contours are interpolated over the coarse grid, the interpolation errors result in the asymmetric contours. The difference in the relative measurement points with respect to each dimple is responsible for the observed difference in the mean interpolated *u*-velocity contours.

47

To confirm this hypothesis and further observe how similar the velocity contours are over adjacent dimples in the array, the measurement grid was expanded to $-0.87 \leq x/D \leq 2.0$ and $-1.50 \leq z/D \leq 1.50$. The spanwise grid spacing was set at $0.1D$, equivalent to $1/10^{th}$ the spanwise wavelength of the dimple array, and the streamwise grid spacing was set to $0.0872D$, equivalent $1/20^{th}$ the streamwise dimple array wavelength. In this way, the measurement points relative to each dimple centre are kept the same for all dimples in the array as shown in Figure 21. This grid spacing effectively also doubles both the spanwise and streamwise spatial resolution compared to that shown in Figure 22. The previous measurements with the coarser grid over the smaller region of $-0.8 \leq x/D \leq 0.8$ and $-1.0 \leq z/D \leq 1.0$ shown in Figure 22 included measurements at various heights above the dimple array. This allowed plots such as Figure 21 to be carried out. However, with the new denser grid with increased spatial resolution, measurements at various heights within the channel would take an impractically long time. Measurements with this denser grid were only carried out at one height, $y/h = 0.05$ to allow comparison with Figure 22.

The result for Case 2, $Re \approx 15,000$ with the denser measurement grid is shown in Figure 23 with the mean streamwise velocity and the root-mean-squares of the streamwise velocity fluctuations normalized by their respective values at the channel centerline. Since the measurement points are the same relative to each dimple center, similar contours are observed over each dimple. Similar general observations can be made for both Figure 22 and Figure 23(a).
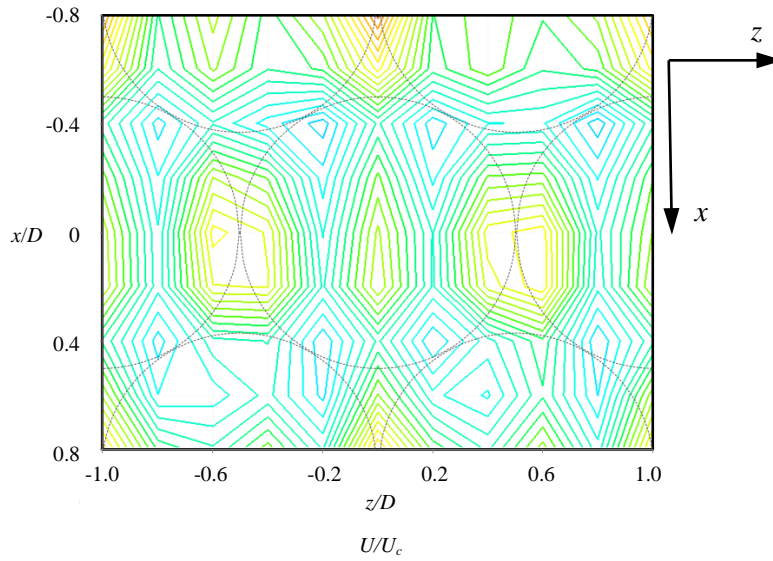
**Figure 22. Normalised mean streamwise velocity contours in the *x-z* plane for Case 2 dimples, *Re* ≈ 15,000, *y/h* = 0.05.**
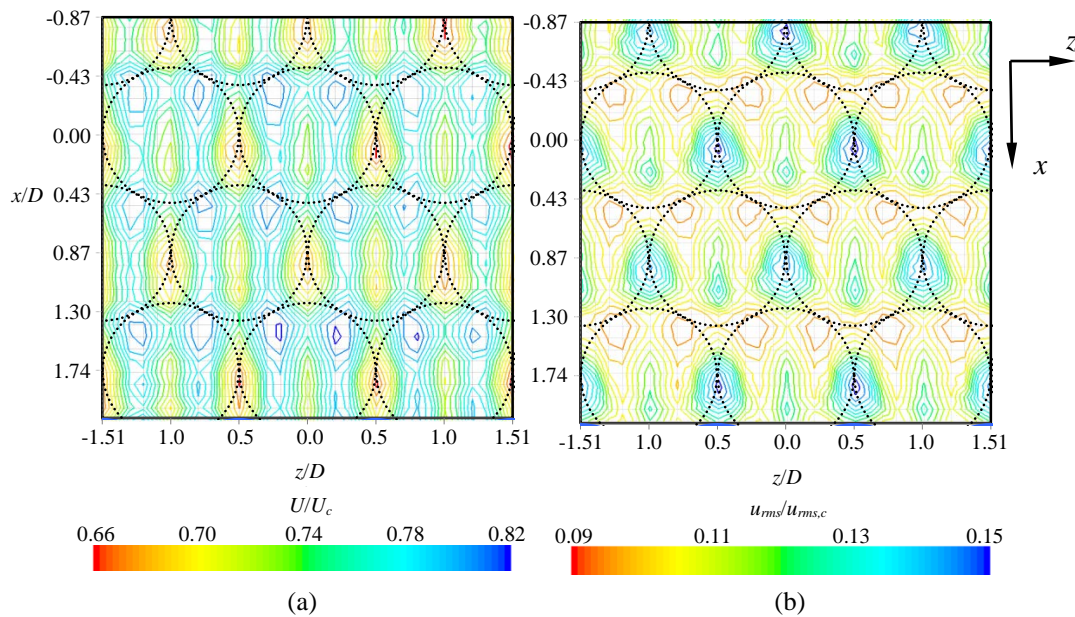


**Figure 23. Normalized mean streamwise velocity contours with expanded measurement grid for *y/h* = 0.05, Case 2 (*d/D* = 5%), *Re* ≈ 15,000. Flow direction is from top to bottom, vertices of grid show measurement locations. (a) Mean streamwise velocity contour, *U*. (b) Root-mean-square of streamwise velocity fluctuations, *u_rms*.**

Both figures show low speed regions at the dimple center as well as at the left and right edges of the dimples. Streaky high speed regions flow between these low speed regions and connect between adjacent dimples. These similarities between Figure 22

49

and Figure 23, the latter being more accurate due to the denser measurement grid resulting in less interpolation errors, serves to confirm what was discussed earlier.

The similarity of contours for both the mean streamwise velocity and root-mean-square (rms) of the velocity fluctuations over all the dimples in the measured area also suggests that the flow has reached an equilibrium state by the time the flow reaches the 11th row of dimples in the array where the measurements were made. The contours over each dimple is similar regardless of its location within the array, allowing the conclusions drawn from the detailed study of the flow over a single dimple to be applicable to the rest of the dimples within the array, except for perhaps the first few rows of dimples, when the flow is transitioning to the dimpled equilibrium state. Since there are 54 rows of dimples within the present channel test section, the flow over most of the dimples within the present array may be considered to be in the equilibrium state. It is worth noting that the "equilibrium" used here does not refer to the fully developed flow state where flow properties do not vary with streamwise position. Instead, the "equilibrium" state used here only refers to the flow properties being the same at the same relative position of each dimple, independent of the actual position of the dimple in the test section.

### 3.3.2   Detailed hot-wire measurements over dimples

### 3.3.2.1 Hot-wire measurements over Case 2 deep dimples

To study the flow over each dimple further, measurements were taken at an even higher spatial resolution again about the dimple located at (0, 0). Measurements were made for $-0.87 \leq x/D \leq 0.87$ and $-0.60 \leq z/D \leq 0.60$ with spatial resolutions in the $x$ and $z$ directions of $0.0432D$ and $0.05D$ respectively. Measurements were made at $Re$ = 10,000, 15,000, 23,000 and 35,000. Figure 24 shows the contours of the mean velocity and the root-mean-squares of the streamwise velocity fluctuations obtained

at $y/h = 0.05$ normalized by their respective values at the channel centerline ($y/h = 0.5$) for the deeper Case 2 dimples.
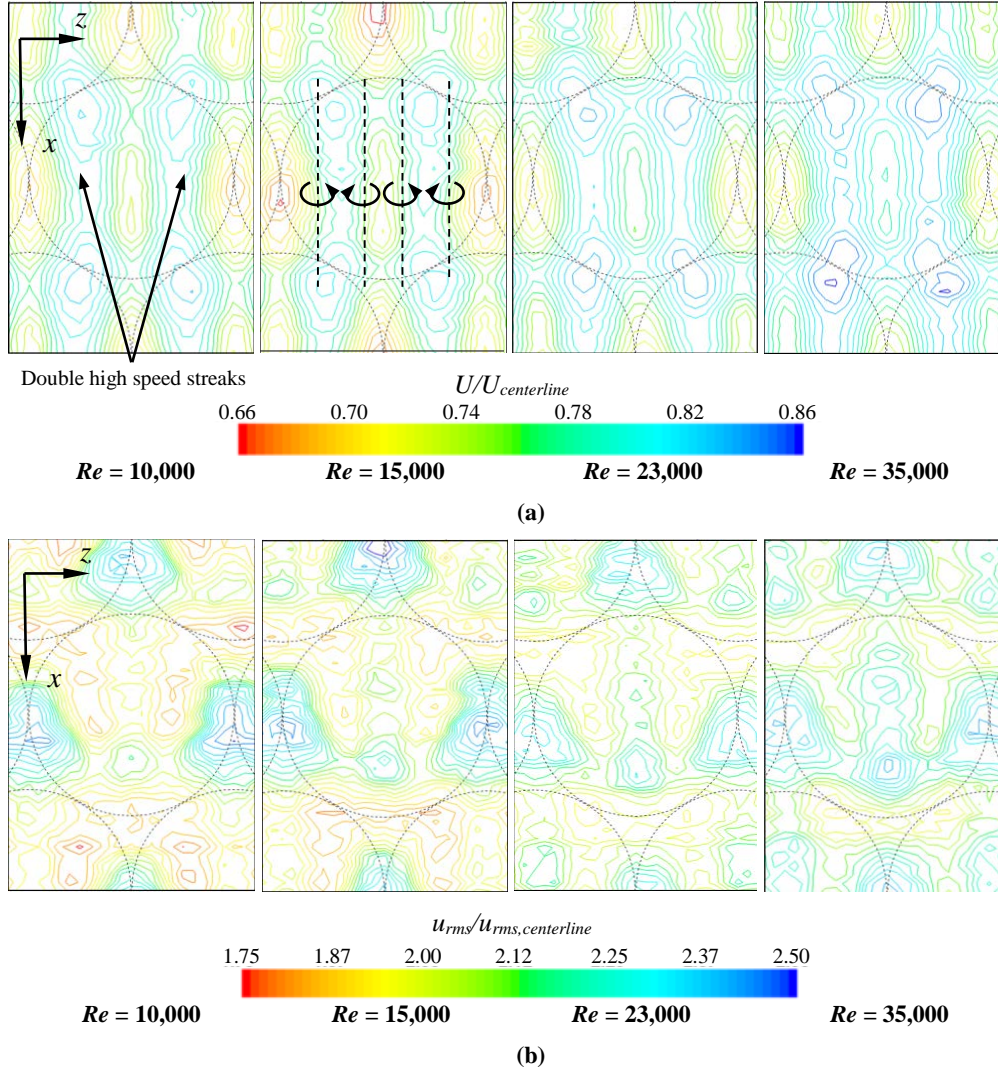


**Figure 24. Contours for Case 2 dimples ($d/D = 5\%$) at $y/h = 0.05$ for Re = 10,000, 15,000, 23,000 and 35,000. (a) Mean streamwise velocity contour, $u$. (b) Root-mean-square of streamwise velocity fluctuations, $u_{rms}$.**

The mean flow over the dimples is generally symmetric about the dimple centerline over the Reynolds number range between 10,000 and 35,000. Two relatively high speed streaks on either side of the dimple centerline are observed at these Reynolds numbers. These high speed streaks are indicated by the arrows in Figure 24(a) for $Re = 10,000$, but are also clearly visible at the other Reynolds numbers. One possible way to interpret these streaks is to attribute the higher speed regions to downward

51

flow bringing high speed fluid down towards the wall and vice versa for the low speed regions (Iuso et al. 2002).

The contours of the rms of the streamwise velocity fluctuations also support such an interpretation, where the regions of low fluctuations are brought about by downward flow bringing low turbulent intensity fluid towards the wall and the regions of high velocity fluctuations are due to upwards flows bringing fluid with higher turbulent intensity near the wall upwards. Interpreted this way, the contours show the presence of two pairs of counter-rotating vortices over the deeper Case 2 dimples. These two pairs of vortices are indicated by dashed lines in Figure 24(a) for $Re$ = 15,000, and the curved arrows show their direction of rotation. Pairs of vortices are also similarly observed at the other Reynolds numbers. Such pairs of streamwise vortices are also observed and reported by Ligrani et $al$. (2001) and Won et $al$. (2005) for much deeper dimples with $d/D$ from 10% to 30%. Their flow visualization results agree well with the vortices implied by the present velocity contours in terms of size, position and direction of rotation as indicated by the velocity contours in Figure 24.

3.3.2.2 Hotwire measurements over Case 3 shallow dimples

Figure 25shows the contours of the mean velocity and the root-mean-squares of the streamwise velocity fluctuations obtained at $y/h$ = 0.05 normalized by their respective values at the channel centerline ($y/h$ = 0.5) for the shallower Case 3 dimples. Similar to the Case 2 dimples, the mean flow over these dimples is also symmetric about the dimple centerline.

However, while the velocity contours in Figure 24 show that the flow over the deeper Case 2 dimples do not vary significantly as the Reynolds number increases from

10,000 to 35,000, the contours in Figure 25 show significant flow changes as the Reynolds number is increased within this range for the shallower Case 3 dimples.
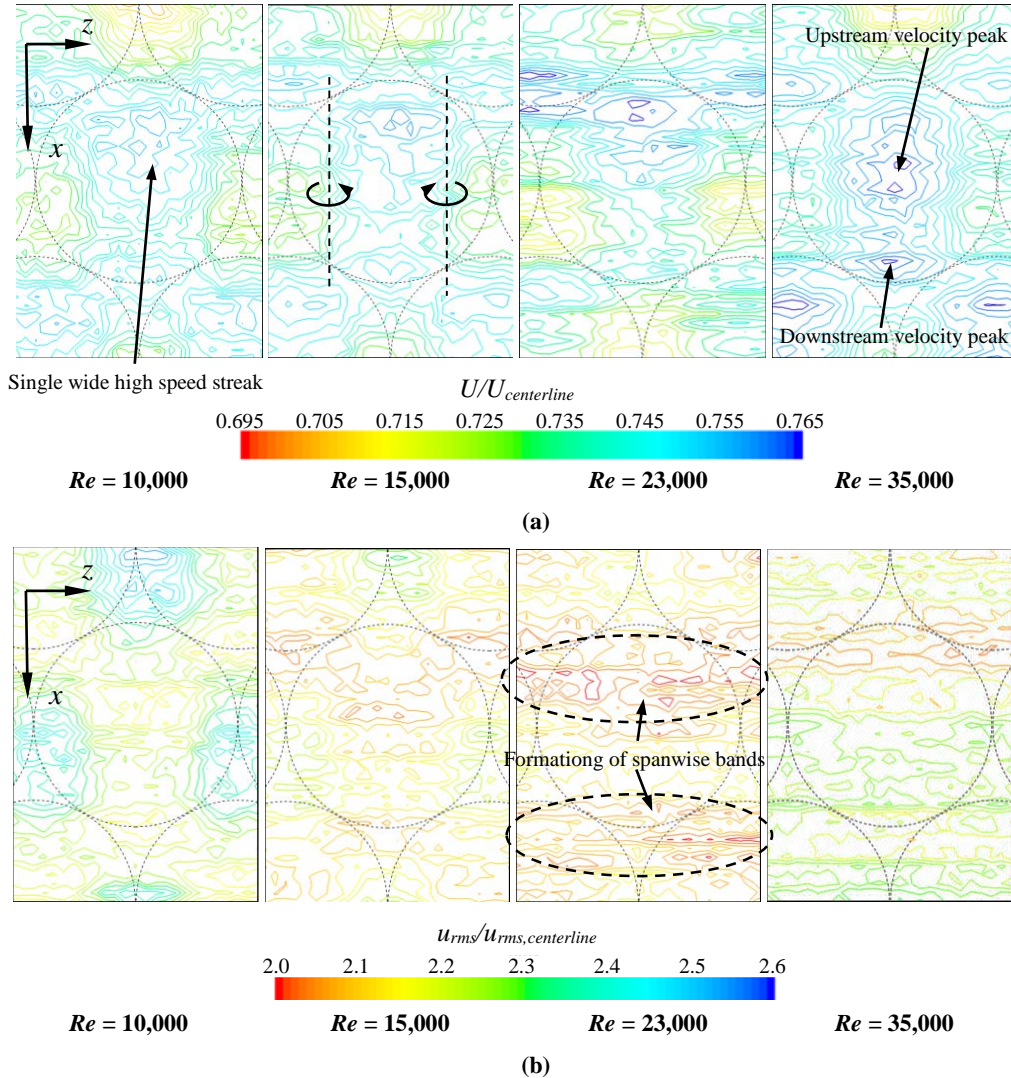


**Figure 25. Contours for Case 3 dimples (*d/D* = 1.5%) at *y/h* = 0.05 for Re = 10,000, 15,000, 23,000 and 35,000. (a) Mean streamwise velocity contour, *u*. (b) Root-mean-square of streamwise velocity fluctuations, *u*$_{rms}$.**

The flow is still generally symmetric about the centerline for the shallower Case 3 dimples, but instead of two high speed streaks and two pairs of counter-rotating vortices that Figure 24 shows for the deeper Case 2 dimples, Figure 25 shows only the presence of a single high speed streak which suggest only a single pair of counter rotating vortices over each dimple. While the presence of the single pair of counter-rotating vortices appears to persist as the Reynolds number increases from 10,000 to

35,000, other minor changes in the velocity contours become evident as the Reynolds number varies in this range. Two peaks in the mean streamwise velocity contours, one upstream of the other along the centerline is observed as the Reynolds number increases to 35,000. These are indicated by the arrows in Figure 25(a) for $Re = 35,000$.

Changes in the contours for the velocity fluctuations are even more obvious as the Reynolds number increases. At $Re = 10,000$, the velocity fluctuations reflect the expected variation with regions of high velocity showing lower fluctuations and regions of lower velocity showing higher velocity fluctuations as fluid is pushed downwards and upwards respectively by the pair of streamwise vortices, similar to the variation seen with the deeper Case 2 dimples as Figure 24 shows. However, as the Reynolds number increases, the contours of the streamwise fluctuations changes and spanwise bands begin to appear. These are indicated by the dashed ovals in Figure 25(b) for $Re = 23,000$ and similar spanwise bands can also be seen at $Re = 35,000$.

Spanwise bands in the flow contours are an indication of spanwise vorticity. Consider the flow over a 2-dimensional backward facing step, where spanwise vorticity is significant. The mean velocity contours in a plane parallel to the wall just downstream of the step would be made up of largely spanwise lines, indicating the strong spanwise vorticity. In the same way, streamwise bands in the contours are an indication of streamwise vorticity. The presence of the dimples serves to introduce streamwise vorticity into the flow, which would otherwise only consist of wall generated spanwise vorticity. This introduction of the streamwise vorticity is also observed by Ligrani et al. (2001) and Won et al. (2005), as well as the streamwise linking of the high speed regions and the presence of the streamwise vortices indicated by the velocity contours in Figure 24 and Figure 25. The greater the dimple

depth, the greater the streamwise vorticity that is added. This streamwise vorticity can be added in terms of stronger vortices or through the presence of more vortices as a comparison between Figure 24 and Figure 25 shows. The velocity contours for the shallow Case 3 dimples only show the presence of a pair of counter-rotating vortices, while the contours for the deeper Case 2 dimples show the presence of two pairs of counter-rotating vortices.

As the Reynolds number increases, so does the average skin friction, leading to a reduction in the physical size of the average wall unit, a wall unit being an inner scale variable defined by $\nu/u_\tau$. Since the measurements for the contours shown in Figure 24 and Figure 25 were made at a constant height $y/h = 0.05$, the measurement height in terms of the wall unit, measured in terms of $y^+$ ($y^+ = yu_\tau/\nu$) increases with the Reynolds number though not proportionally. Thus though the measurements are made at constant $y/h$ as the Reynolds number increases, they are not made at constant $y^+$ as the Reynolds number increases in Figure 24 and Figure 25. If the flow scales with $y^+$, as a plane channel flow does, then the velocity contours, both the mean as well as their fluctuations are expected to change as the Reynolds number increases. This is perhaps what is happening for the shallower Case 3 dimples in Figure 25, where the contours vary as the Reynolds number is increased, suggesting the importance of common flow parameters such as $y^+$ to the flow scaling. The consistency of the velocity contours for the deeper Case 2 dimples as the Reynolds number increases however, suggests that the flow for these deeper dimples scales less significantly with flow parameters such as $y^+$, but more with a parameter such as the dimple depth or diameter which does not change in Figure 24 as the Reynolds number increases from 10,000 to 35,000. This shows that as the dimple to depth diameter increases, the flow scaling shifts from the wall scaling of normal boundary layer flows to geometric parameters of the dimples such as the dimple depth.

55

Although the early measurements made at various heights using the coarse grids allowed the estimated velocity contours at constant $y^+$ for the shallower Case 3 dimples to be plotted, assuming the skin friction of the plane channel case for computation of $y^+$, no clear conclusion could be drawn as the contours obtained still varied with Reynolds number. This could be attributed either to errors arising from using the plane channel skin friction for computing $y^+$, or more likely that the flow scaling even for such shallow dimples is a hybrid of boundary layer wall scales and dimple geometry, the flow being significantly influenced by both.

## 3.4   Power spectral measurements

While the previous hot-wire velocity measurements were sampled at 3,000 Hz for a duration of about 5.5 seconds, further hot-wire measurements used for spectral analysis were sampled at 6,000 Hz for $2^{19}$ sampling points, giving a sampling duration of about 87 seconds. Due to the much longer sampling time, these measurements were only carried out at specifically chosen points. A low pass filter with a cut-off frequency of 3,000 Hz was used for these measurements so that errors due to aliasing are not significant. The time history of the streamwise velocity obtained from the hot-wire in these measurements were then divided into 1024 equal segments, and the power spectra of the velocity fluctuations was calculated for each of these 1024 segments of time histories. The power spectra plots presented here are obtained from the averaged power spectra of these 1024 time history segments using a Hanning type window. The averaged power spectra are then normalized by the signal variance and the frequency $f$ was normalized by the channel height $h$ and the local mean velocity $U_{local}$ at the measured point such that $St = fh/U_{local}$ in the plots. Figure 26(a) shows the normalized power spectra of the streamwise velocity fluctuations for the Case 2 dimples ($d/D = 5\%$) at a Reynolds number of 15,000 for various locations. Their positions relative to the dimple array is shown in Figure

26(b), where the position of the dimples is indicated by dashed circles. These measurements were made at $y/h = 0.05$, the same as the other hot-wire measurements presented in Figure 22 to Figure 25.
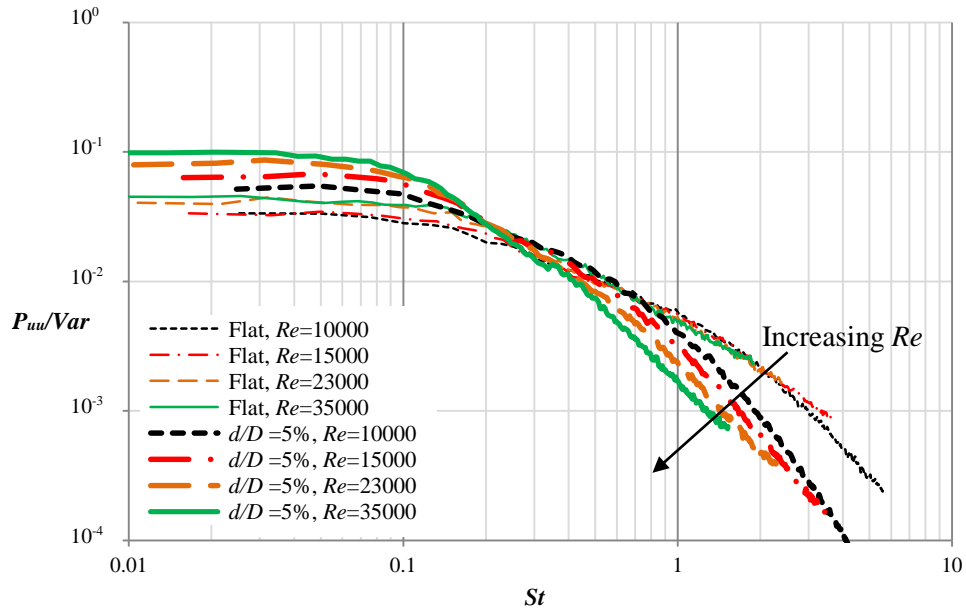


<center>(a)</center>

<center>(b)</center>
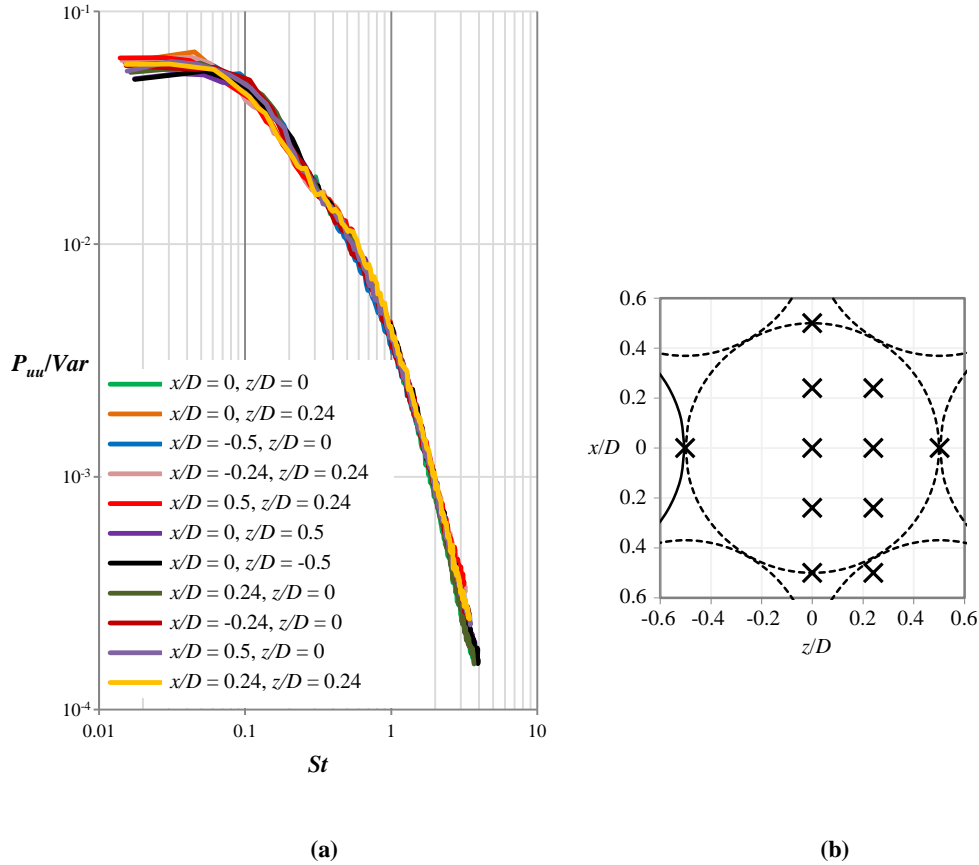
**Figure 26. Normalized power spectra for Case 2 dimples ($d/D=5\%$) at $Re = 15,000$, $y/h = 0.05$. (a) Normalized power spectra. (b) Measurement positions.**

The spectral plot shows that the normalized power spectrum obtained at various points within the dimple is similar. Note that the measured points include those within the high speed streaks, as well as the lower speed regions along the dimple centerline and the spanwise edges of the dimple. Not clearly shown in the plot is the observation that the normalized power spectra obtained for ($x/D = 0$, $z/D = -0.5$) and ($x/D = 0$, $z/D = 0.5$) are very similar, showing the symmetry of the flow about the dimple centerline. The similarity of the normalized power spectra at various locations simplifies the analysis of the flow over the dimples since the position of the measured power spectra is not a significant consideration at $y/h = 0.05$.

<center>57</center>

Figure 27 shows the normalized power spectra for Case 2 dimples ($d/D = 5\%$) measured at ($x/D = 0$, $z/D = 0$, $y/h = 0.05$) at various Reynolds numbers and compared with the normalized power spectra at $y/h = 0.05$ for the flat channel at the same Reynolds numbers. Only the spectra for $x/D = 0$, $z/D = 0$ is shown for the dimple case since the normalised spectra at other positions within the dimples is similar, as Figure 26 has previously shown. In comparison with the flat channel case, the Case 2 dimples cause the normalized power spectra to shift towards lower values of the normalized frequencies. Among the dimple results, there is a clear trend that increasing the Reynolds numbers also shifts the normalized power spectra content towards the lower normalized frequencies. This shift towards the lower normalized frequencies of the dimple cases is also observed for the Case 3 dimples ($d/D = 1.5\%$) as Figure 28 shows. Although a similar trend is observed for these shallower dimples, the shift towards the lower normalized frequencies with respect to the flat channel cases, or among the dimple results as the Reynolds number increases, is not as great as that of the deeper Case 2 dimples ($d/D = 5\%$).

To better understand the changes the dimples cause to the flow around them, the drag reduction results from Figure 17 at the relevant Reynolds numbers are summarized in Table 2. A general observation when comparing Figure 27, Figure 28 and Table 2 is that there appears to be a trend of increasing drag reduction with increasing shifts of the normalized power spectra towards the lower normalized frequencies. This is the case when comparing among each of the dimple cases as the Reynolds number increases, as well as comparing the shallower Case 3 dimples with the flat channel results. A shift towards the lower frequencies is accompanied by a reduction in drag, and the greater these shift of the normalized power spectra towards the lower frequencies, the greater the drag reduction.
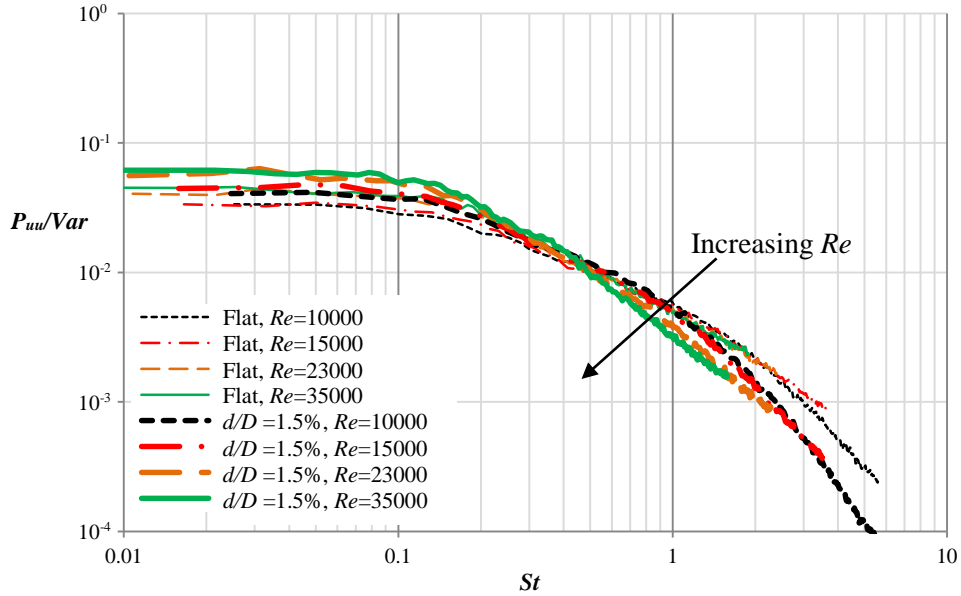
**Figure 27. Normalized power spectra for Case 2 dimples (*d/D*=5%) at (*x/D* = 0, *z/D* = 0, *y/h* = 0.05) and flat channel results.**

This general trend however, is not followed for the Case 2 dimples at a Reynolds number of 10,000 when compared with the flat channel result. Although a marked shift in the normalized power spectra toward the lower frequency is noted for the Case 2 dimples at *Re* = 10,000 when compared to the flat channel result in Figure 27, pressure measurements show a drag increase of 1% for the dimple case when compared to the flat channel. A possible reason for this will be discussed further below.

**Figure 28. Normalized power spectra for Case 3 dimples ($d/D$=1.5%) at ($x/D = 0$, $z/D = 0$, $y/h = 0.05$) and flat channel results.**

**Table 2. Summary of change in average pressure loss**

| Case | $d/D$ | $Re$ | Approximate change in average pressure loss |
|------|-------|--------|---------------------------------------------|
| 2 | 5% | 10,000 | +1% |
| 2 | 5% | 15,000 | –0.5% |
| 2 | 5% | 23,000 | –2% |
| 2 | 5% | 35,000 | –3% |
| 3 | 1.5% | 10,000 | –1.5% |
| 3 | 1.5% | 15,000 | –1.5% |
| 3 | 1.5% | 23,000 | –2% |
| 3 | 1.5% | 35,000 | –2% |

Similar shifts of the power spectra to the lower frequencies coinciding with observed

drag reduction have also been reported in the literature. Iuso et *al*. (2002) conducted

an experiment involving the creation of streamwise vortices within a channel flow

using transverse jets injected through the channel wall. Reduction in skin friction

compared to the plane channel was measured along some positions within the

channel and the spectral distribution of the velocity fluctuations at these positions

also showed a shift of the spectral energy towards the lower frequencies when

60

compared to the plane channel case. The relation between the shift in the spectral distribution and observed drag reduction is also commonly observed in studies involving the use of polymer additives for drag reduction (Den Toonder et al. 1997, Li et al. 2004, Min et al. 2003). This shift of the spectral energy towards the lower frequencies may be interpreted as more energy now being retained by the larger scales within the flow instead of being cascaded down to the smaller scales, or that the turbulence length scales of the streamwise velocity streaks within the boundary layer have increased, implying greater streamwise coherence or an increase in stability of the flow. In their experimental study of drag reduction via polymer additives, Vlachogiannis and Hanratty (2004) further found that the spectral distribution of the streamwise velocity fluctuations for different runs that showed the same drag reduction to be the same, even though the drag reduction was achieved through the use of differing combinations of injected polymer solution and polymer concentration within the test section. These results appear to imply that there is a strong relationship between shifts in the spectral distribution to the lower frequencies and the reduction of skin friction drag. This is not too surprising since the shift in the spectral distribution is evidence of changes in the turbulent near-wall structures which are significant contributors to skin friction and turbulent drag generation.

# Chapter 4

# Detached Eddy Simulation

## 4.1    Motivation for DES

The experiments themselves are unable to give sufficient information for a proper understanding of the flow. Some questions are also not satisfactorily answered by the experimental results. As mentioned before, the result obtained with Case 2 at a Reynolds number of 10,000 does not follow the general trend of a drag reduction occurring with a shift of the spectral distribution to the lower frequencies. Despite the significant shift in the spectral distribution of the streamwise velocity fluctuations when compared to the flat channel case as observed in Figure 27, a drag increase of 1% over that of the flat channel case is measured. To investigate this issue further, a DES was carried out for the same dimple geometry for Case 2 and Case 3. However, due to the huge computational demand for the DES at high Reynolds numbers, the DES will only be carried out at a lower range of Reynolds numbers between 3,300 and 15,000. The availability of experimental $u$ component velocity measurements at these ranges would help to establish the validity of the DES, which can provide additional information about the turbulence kinetic energy budgets, the Reynolds stresses, skin friction and form drag, as well as the vertical and spanwise components of the flow in the dimpled channel that are not easily measured with the hot-wire. Together with the experimental findings, it is hoped that the DES will help build a more complete picture of the flow and give greater confidence in the knowledge and hypothesis made regarding the flow over these relatively shallow dimples.

## 4.2 Governing equations

The same channel geometry is investigated using the DES numerically. The simulated channel has length $l_d$, width $w_d$ and height $h_d$ for consistency with the coordinate system used in the experiments, in the $x$, $z$ and $y$ directions respectively, as shown in Figure 3 and Figure 4. For clarity, the computational domain is also shown in Figure 29.
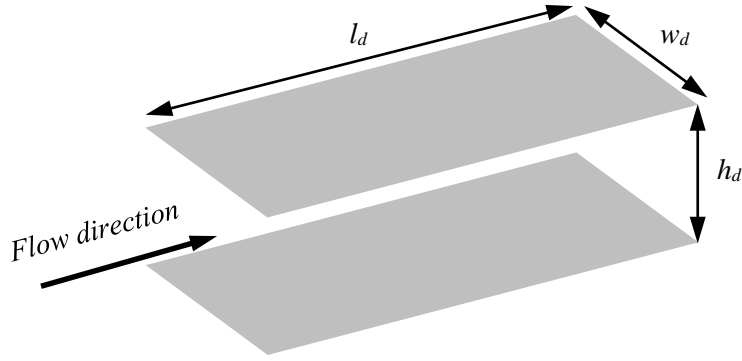


**Figure 29. Computational domain for the channel modelled using DES**

The following dimensional governing equations are used to model the flow:

$$\frac{\partial u_i^*}{\partial x_i^*} = 0 \tag{13}$$

$$\rho^* \left[ \frac{\partial u_i^*}{\partial t^*} + \frac{\partial \left( u_i^* u_j^* \right)}{\partial x_j^*} \right] = -\frac{\partial p^*}{\partial x_i^*} + \mu^* \frac{\partial^2 u_i^*}{\partial x_j^* \partial x_j^*} \tag{14}$$

and the superscript $^*$ indicates dimensional quantities.

Decomposing the pressure variables into its mean and fluctuating components gives:

$$p^*(x, y, z, t) = p_{in}^* - \beta^* x^* + p'^*(x, y, z, t) \tag{15}$$

where $\beta^*$ is the dimensional mean streamwise pressure gradient. The Navier-Stokes equation can then be expressed as:

$$\rho^* \left[ \frac{\partial u_i^*}{\partial t^*} + \frac{\partial \left( u_i^* u_j^* \right)}{\partial x_j^*} \right] = -\frac{\partial p'^*}{\partial x_i^*} + \mu^* \frac{\partial^2 u_i^*}{\partial x_j^* \partial x_j^*} + \beta^* \delta_{i1} \tag{16}$$

where $\delta_{ij}$ is the Kronecker delta. In the present channel, the subscript $j$ is set to 1 to impose a mean pressure gradient in the streamwise direction only.

The friction velocity $u_\tau^*$ is used as the reference velocity, and using the half channel height $h/2$ as the reference length scale, the friction velocity is defined as

$u_\tau^* = \sqrt{\beta^* \dfrac{h^*}{2} / \rho^*}$ , where $\rho^*$ is the density of air since the fluid used in the current study is air. Defining the Reynolds number based on the friction velocity and half channel height $h/2$ as $Re_\tau = \dfrac{u_\tau^* h^*}{2v^*}$ , where $v^*$ is the kinematic viscosity of air, the non-dimensional continuity and momentum equations can then be written as

$$\frac{\partial u_i}{\partial x_i} = 0 \tag{17}$$

$$\frac{\partial u_i}{\partial t} + \frac{\partial (u_i u_j)}{\partial x_j} = -\frac{\partial p'}{\partial x_i} + \frac{1}{Re_\tau} \frac{\partial^2 u_i}{\partial x_j \partial x_j} + \beta \delta_{i1} \tag{18}$$

The non-dimensional decompositions of the pressure variables can also be written as

$$p(x, y, z, t) = p_{in} - \beta x + p'(x, y, z, t) \tag{19}$$

where the non-dimension mean streamwise pressure gradient term $\beta = 1$. A no slip boundary condition, $u_i = 0$ is imposed at the upper and lower walls of the simulated channel, and periodic boundary conditions are applied on the streamwise and spanwise edges of the simulated computational domain for the velocity $u_i$ and pressure $p'$.

To evaluate the hydrodynamic drag due to the dimples, the total streamwise pressure drag $D_p$ and skin friction $D_f$ are given by:

$$\langle D_p \rangle = -\int (p' - \beta x) \vec{i} \cdot \vec{n} dA_w \tag{20}$$

$$\langle D_f \rangle = \int \left( \tau_{xx} \vec{i} + \tau_{xy} \vec{j} + \tau_{xz} \vec{k} \right) \cdot \vec{n} dA_w \qquad (21)$$

where $A_w$ is the surface area of the upper and lower walls, $\vec{n}$ is the outward surface normal vector and $\vec{i}$, $\vec{j}$ and $\vec{k}$ refers to unit vectors in the streamwise, vertical and spanwise directions respectively.

## 4.3    The Detached Eddy Simulation Method

The DES method is a type of zonal approach where the flow field being simulated is separated into two distinct zones. Away from the wall, the grid is relatively large and the large energy carrying eddies are resolved and computed, similar to the Large Eddy Simulation (LES) method (Pope 2000, Sagaut 2001). Nearer the wall, where the flow scale requires very small grid sizes for complete resolution of the small eddies, the flow is modelled to eliminate the need for such small grid sizes and so cut down significantly on the computational resource required for the simulation. Despite this, the computational resource required is still large.

The DES model, introduced by Spalart et al. (1997) originally used the one equation Spalart-Allmaras (S-A) model in which the transport equation for the eddy viscosity is solved. By modifying the model length scale to account for the fine resolution in the LES regions, the production of eddy viscosity is decreased further away from the wall. DES has been successfully implemented on a variety of separated flows (eg. Strelets, 2001), and was chosen for the current study due to the expected flow separation commonly observed in flows over dimples (Won *et al.* 2005, Isaev et *al.* 2003, Tay 2011).

For the current study, the filtered governing equations for the DES of an incompressible flow are:

$$\frac{\partial \tilde{u}_i}{\partial x_i} = 0 \tag{22}$$

$$\frac{\partial \tilde{u}_i}{\partial t} + \frac{\partial \tilde{u}_i \tilde{u}_j}{\partial x_j} = -\frac{\partial \tilde{p}'}{\partial x_i} + \frac{1}{Re_\tau} \frac{\partial^2 \tilde{u}_i}{\partial x_j x_j} + \beta \delta_{i1} - \frac{\partial \tau_{ij}}{\partial x_i} \tag{23}$$

where the script ~ represents the time-space filtering of the variable shown below it, and $\tau_{ij} = \widetilde{u_i u_j} - \tilde{u}_i \tilde{u}_j$ is the subgrid-scale stresses and is modelled using the following eddy viscosity model:

$$\tau_{ij} - \frac{\delta_{ij}}{3} \tau_{kk} = -2\nu_t \tilde{S}_{ij} \tag{24}$$

where

$$\tilde{S}_{ij} = \frac{1}{2} \left( \frac{\partial \tilde{u}_i}{\partial x_j} + \frac{\partial \tilde{u}_j}{\partial x_i} \right) \tag{25}$$

And the eddy viscosity $\nu_t$ is given by $\nu_t = \tilde{\nu} f_{v1}$, with $\tilde{\nu}$ defined according to:

$$\frac{\partial \tilde{\nu}}{\partial t} + \frac{\partial (\tilde{u}_i \tilde{\nu})}{\partial x_i} = \frac{1}{\sigma_\nu} \left\{ \frac{\partial}{\partial x_j} \left[ (\nu + \tilde{\nu}) \frac{\partial \tilde{\nu}}{\partial x_j} \right] + C_{b2} \frac{\partial \tilde{\nu}}{\partial x_j} \frac{\partial \tilde{\nu}}{\partial x_j} \right\} + C_{b1} \tilde{S} \tilde{\nu} - C_{w1} f_w \left( \frac{\tilde{\nu}}{\tilde{d}} \right)^2 \tag{26}$$

And

$$f_{v1} = \frac{\chi^3}{\chi^3 + C_{v1}^3} \tag{27}$$

$$\chi = \frac{\tilde{\nu}}{\nu} \tag{28}$$

$$\tilde{S} = \sqrt{2\tilde{\Omega}_{ij}\tilde{\Omega}_{ij}} + \frac{\tilde{\nu}}{\kappa^2 \tilde{d}^2} f_{v2} \tag{29}$$

$$\tilde{\Omega}_{ij} = \frac{1}{2} \left( \frac{\partial \tilde{u}_i}{\partial x_j} - \frac{\partial \tilde{u}_j}{\partial xi} \right) \tag{30}$$

66

$$f_{v2} = 1 - \frac{\chi}{1 + \chi \cdot f_{v1}} \tag{31}$$

$$C_{w1} = \frac{C_{b1}}{\kappa^2} + \frac{1 + C_{b2}}{\sigma_{\tilde{v}}} \tag{32}$$

$$f_w = g \left( \frac{1 + C_{w3}^6}{g^6 + C_{w3}^6} \right)^{\frac{1}{6}} \tag{33}$$

$$g = r + C_{w2}\left(r^6 - r\right) \tag{34}$$

$$r = \frac{\tilde{v}}{\tilde{S}\kappa^2 \tilde{d}^2} \tag{35}$$

The model constants used are $\sigma_v = \frac{2}{3}$, $C_{b1} = 0.1355$, $C_{b2} = 0.6220$, $\kappa = 0.4187$,

$C_{v1} = 7.10$, $C_{w2} = 0.30$ and $C_{w3} = 2.0$. Similar to Spalart et al. (1997), the length scale

used in the destruction term $\tilde{d}$ is defined as the minimum of the Reynolds Average

Navier-Stokes (RANS) and LES length-scales. Mathematically, it may be stated as:

$$\tilde{d} = \min\left(d_w, C_{DES}\Delta\right) \tag{36}$$

where $d_w$ is the distance from the solid wall and $\Delta$ is the largest grid spacing in the $x$,

$y$ and $z$ directions. A value of 0.65 is used for the constant $C_{DES}$ in the present study,

similar to Shur et al. (1999). This definition of the length scale of the destruction

term $\tilde{d}$ means that near the solid wall, where $d_w < C_{DES}\Delta$, the DES model acts similar

to a RANS model. Far from the wall where $d_w > C_{DES}\Delta$, the DES model acts similar

to a LES model. To improve code convergence, the use of limiters are employed in

the S-A model in accordance to Tu et al. (2009):

$$f_{v1} = \begin{cases} 0, & \chi \le 2.5 \times 10^{-5} \\ \dfrac{\chi^3}{\chi^3 + C_{v1}^3}, & \text{otherwise} \end{cases} \tag{37}$$

$$g = \begin{cases} 250, & r \ge 3.0632301 \\ r + C_{w2}\left(r^6 - r\right), & 0.005 \le r < 3.0632301 \\ \dfrac{g}{C_{w3}\left(1 + C_{w3}^6\right)^{1/6}}, & r < 0.005 \end{cases} \tag{38}$$

$$f_w = \begin{cases} 250\left(\dfrac{1 + C_{w3}^6}{250^6 + C_{w3}^6}\right)^{1/6}, & g \ge 250 \\ g\left(\dfrac{1 + C_{w3}^6}{g^6 + C_{w3}^6}\right)^{1/6}, & 0.005 \le g < 250 \\ \dfrac{g}{C_{w3}\left(1 + C_{w3}^6\right)^{1/6}}, & g < 0.005 \end{cases} \tag{39}$$

Because the highly stiffed differential equation of the S-A model is prone to underflow/overflow of floating point values, a very small positive value of $1 \times 10^{-20}$ is set for the minimum value of the eddy viscosity to avoid the unphysical possibility of a negative eddy viscosity.

For the purpose of the current DES, the finite-volume-based parallel DES code modified from Wang et al. (2006) and subsequently used by Chen et al. (2012, 2013) was used for the current work.

## 4.4 Validation of the DES

### 4.4.1 Validation with plane flat channel flow

The main purpose of the DES was to study the flow over the dimples, and to simulate a flow similar to that studied in the experiments. The simulation domain size normalized by the half channel height is $8.693 \times 2.0 \times 5.019$, and is shown in Figure 30. For simulation of the flow over dimples, this domain includes one central dimple and four quarter-dimples at the four corners. The periodic boundary conditions at the streamwise and spanwise edges allow dimple arrays such as the ones in the experiment to be simulated. The same domain size is used for the DES of the flat channel for code validation and comparisons with the dimple simulation to be made.
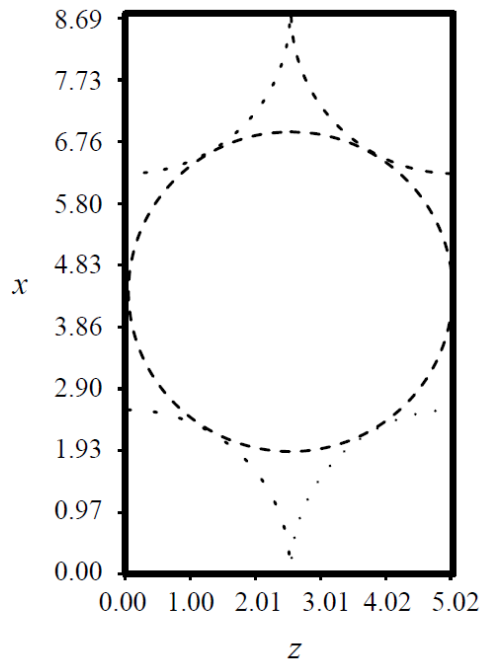


**Figure 30. Plan view of DES computational domain, with dimples shown by dashed lines.**

Six separate runs were made with the code for a flat channel case for the purpose of validation. The parameters used are listed in Table 3 for each run.

69

**Table 3. Parameters used for flat channel validation runs**

| Run | $Re_\tau$ | Number of cells $(N_x \times N_y \times N_z)$ | Domain size | $\Delta x^+$ | $\Delta z^+$ | $\Delta y^+_{min}$ | $\Delta t^+$ |
|---|---|---|---|---|---|---|---|
| 1 | 180 | $128 \times 128 \times 128$ | $8.693 \times 2.0 \times 5.019$ | 12.224 | 7.058 | 0.233 | 0.002 |
| 2 | 395 | $128 \times 128 \times 128$ | $8.693 \times 2.0 \times 5.019$ | 26.826 | 15.488 | 0.512 | 0.002 |
| 3 | 590 | $128 \times 128 \times 128$ | $8.693 \times 2.0 \times 5.019$ | 40.069 | 23.134 | 0.765 | 0.002 |
| 4 | 590 | $128 \times 256 \times 128$ | $8.693 \times 2.0 \times 5.019$ | 40.069 | 23.134 | 0.376 | 0.001 |
| 5 | 590 | $128 \times 256 \times 64$ | $\frac{3}{4}\pi \times 2.0 \times \frac{1}{4}\pi$ | 10.861 | 7.240 | 0.376 | 0.001 |
| 6 | 590 | $128 \times 256 \times 64$ | $4.347 \times 2.0 \times 2.510$ | 20.035 | 23.134 | 0.376 | 0.001 |

Velocity profiles for runs 1 - 6 are compared with the DNS results of Kim et al. (1987) and Moser et al. (1999) and shown in Figure 31.
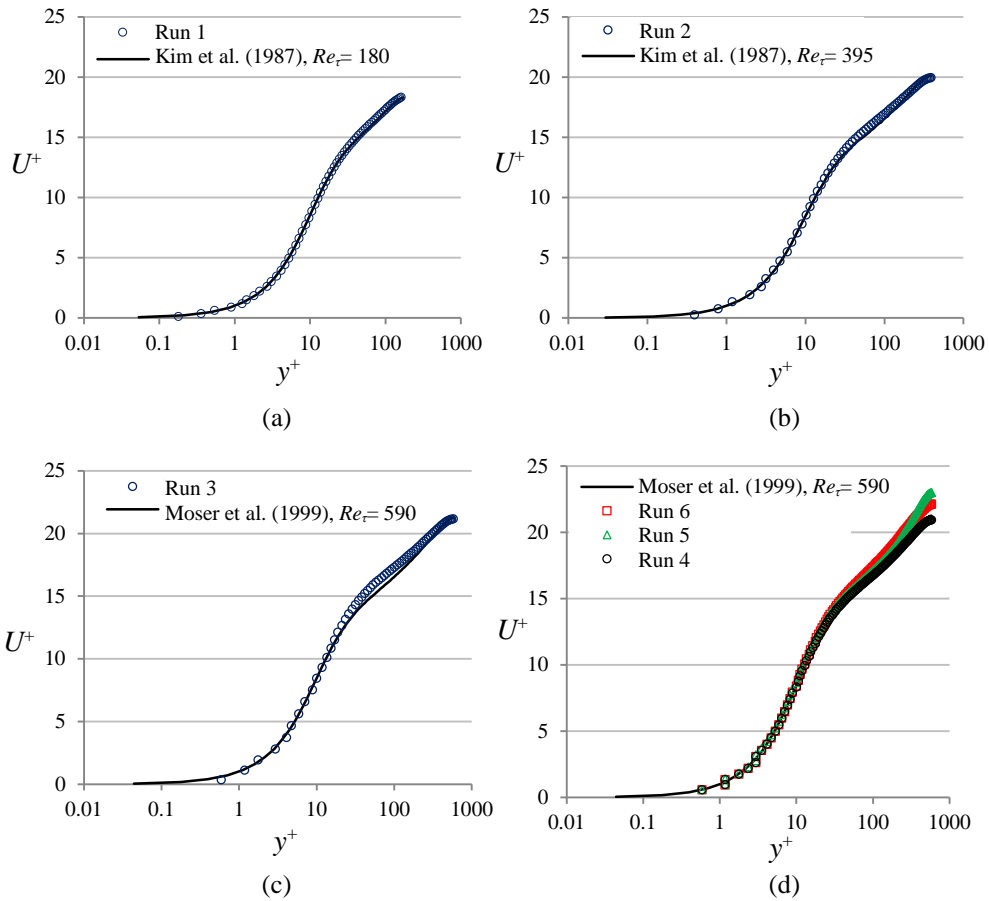


Figure 31. Velocity profiles for flat plate runs. (a) $Re_\tau = 180$, (b) $Re_\tau = 395$, (c) $Re_\tau = 590$, (d) $Re_\tau = 590$

The agreement with the DNS results for run 1 and 2 ($Re_\tau = 180$ and 395) are good, but the agreement with run 3 is less so. This is expected since as the Reynold number increases, the spatial resolution in terms of wall units decreases if the computational

70

grid is unchanged, as Table 3 shows. The reduced resolution means a reduced ability to resolve the flow sufficiently, resulting in reduced accuracy of the DES. Figure 31(d) shows that doubling the cell count in the vertical $y$ direction improves the agreement of the present DES result with the DNS result of Moser et al. (1999). Reducing the size of the domain for runs 5 and 6 leads to poorer agreement with the result of Moser et al. (1999), possibly due to insufficient spatial separation of the edges of the computational domain so that the periodic boundary conditions used in the simulation create a kind of non-physical periodic flow forcing. Thus for the best accuracy, increasing the number of cells while retaining the same domain size (run 4) is most appropriate.

Figure 32 shows the profiles of the RMS of the streamwise velocity fluctuations of the various runs compared also with those of Kim et al. (1987) and Moser et al. (1999). Again the agreement at $Re_\tau = 180$ (run 1) is very good, but the agreement becomes increasingly poor as $Re_\tau$ increases. While run 4 shows the best agreement for the mean streamwise velocity profile for $Re_\tau = 590$, run 5 instead shows the nearest agreement to the $u_{rms}$ profile with those from Moser et al. (1999). Run 5 has the smallest domain size and highest grid density of all the runs and this may contribute to the more accurate $u_{rms}$ profile because it best resolves the velocity fluctuations. However, as mentioned before, the accuracy of the mean velocity suffers when the domain is reduced to this small size.
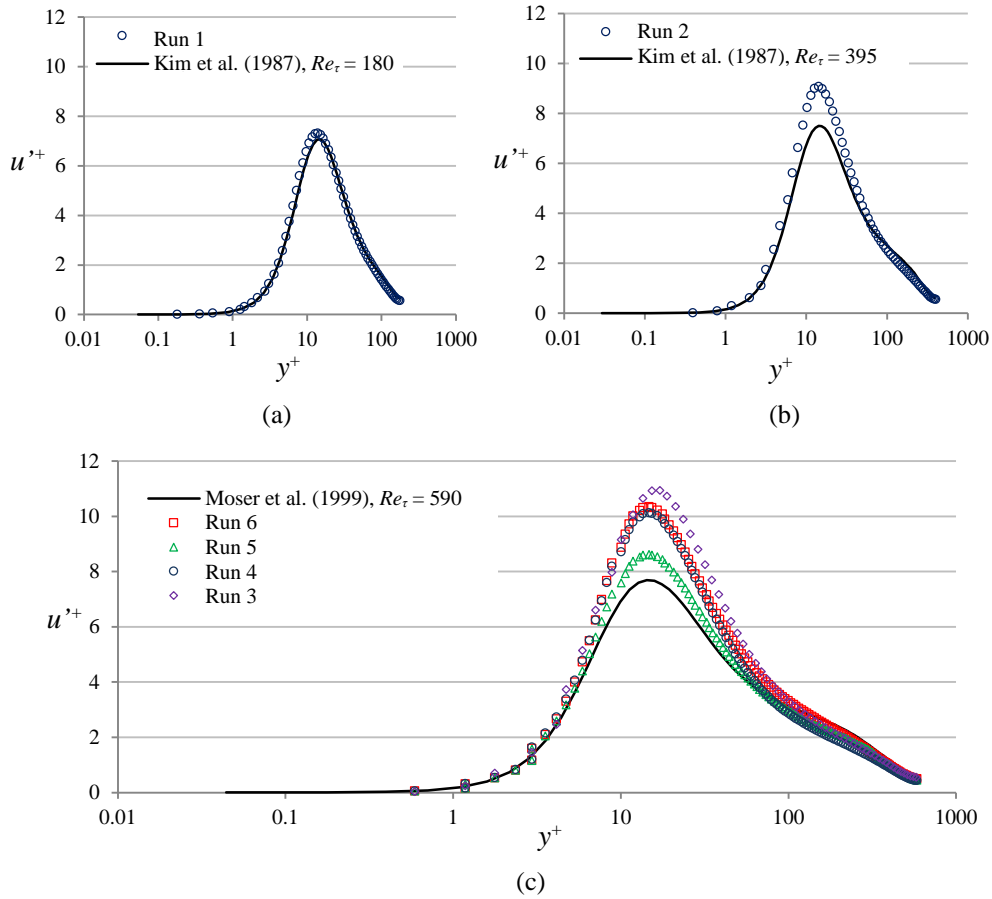
**Figure 32. RMS velocity profiles for flat plate runs. (a) $Re_\tau = 180$, (b) $Re_\tau = 395$, (c) $Re_\tau = 590$**

Comparisons of various components of the turbulent kinetic energy budget have also been made with those of Kim et al. (1987) and Moser et al. (1999). These are shown in Figure 33 for $Re_\tau = 180$, 395 and 590.

A general observation is that as the Reynolds number increases, the agreement between the present DES and the more accurate DNS simulations of Kim et al. (1987) and Moser et al. (1999) becomes poorer, particularly in the region near the wall, most likely due to the increasingly poorer grid resolution as the $Re_\tau$ increases (Table 3). There is also a consistent under-prediction of the dissipation component of the energy budget by the present DES code at all Reynolds numbers near the wall.
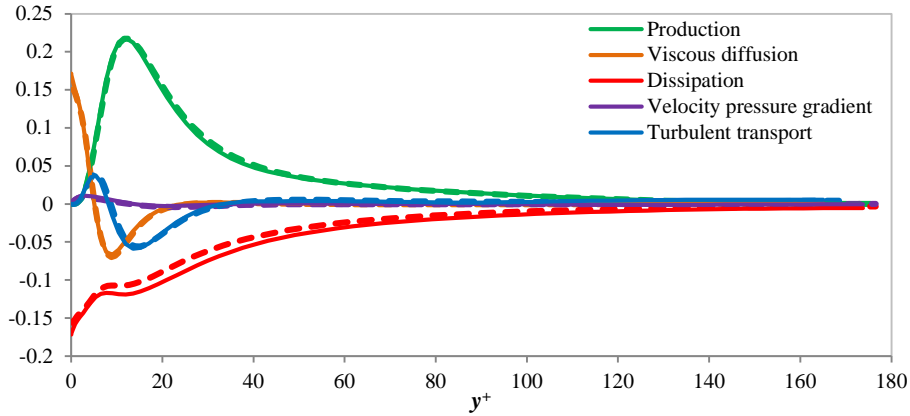
**Figure 33a. Profiles for the turbulent kinetic energy budget terms, at $Re_\tau = 180$. Solid lines: Kim et al. (1987), dashed lines: present DES.**
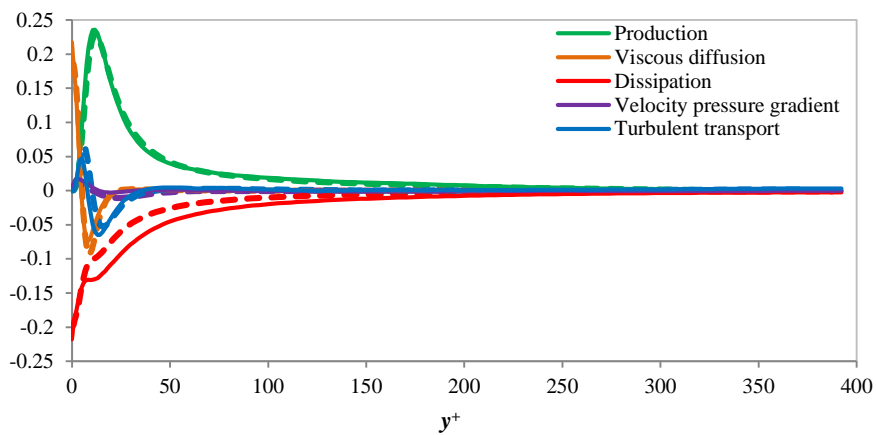


**Figure 33b. Profiles for the turbulent kinetic energy budget terms, at $Re_\tau = 395$. Solid lines: Kim et al. (1987), dashed lines: present DES.**
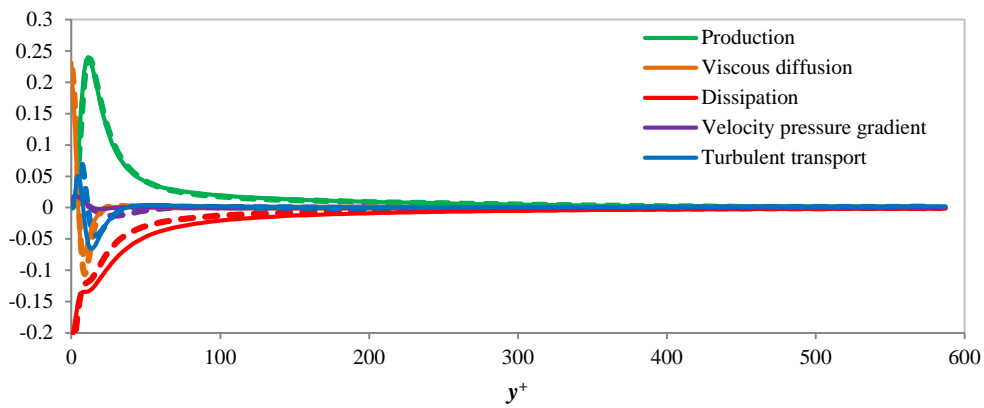


**Figure 33c. Profiles for the turbulent kinetic energy budget terms, at $Re_\tau = 590$. Solid lines: Moser et al. (1999), dashed lines: present DES, run 4.**

The above is not meant to be used to further optimize the grid, as some modelling is involved in the DES simulation, and some inaccuracy must be accepted because of

this. One way to reduce this accuracy is to reduce the already small grid sizes to resolve the length scale further. However, this comes at an increased computational cost. Furthermore the benefits offered by DES being able to simulate a flow accurately using a relatively coarse grid may no longer be the case if the grid is reduced sufficiently small approaching that for a DNS to be run. The accuracy of the mean velocity profile also suffers if the domain is reduced significantly. Further stringent validation of the same DES code has been carried out by Chen et al. (2012, 2013) in their numerical study of dimples and protrusions in a turbulent channel flow. The aim of the above discussion is to identify the possible limitations of the current DES code so that a more accurate analysis can be carried out on the DES results of the simulated dimple flow. While the DES may not be sufficiently accurate in predicting the absolute values due to the flow modelling involved, it is hoped that it can still be useful for comparing trends in the various runs obtained from the use of a single DES code.

### 4.4.2 Validation of dimpled channel flow with hot-wire results

DES runs for the dimpled configuration were made for three different $Re_{h/2}$, namely at 3,300, 10,000 and 15,000. The higher two Reynolds numbers of the DES runs coincide with the lower two Reynolds numbers of the hot-wire runs presented earlier, allowing a direct comparison. For Case 2 dimples ($d/D = 5\%$), the experimental results in Table 2 shows a drag increase of 1% for $Re = 10,000$ and a drag reduction of 0.5% for $Re = 15,000$. This allows us to compare the flow for a case with drag increase and another with a small drag reduction for these deeper Case 2 dimples with the DES which can provide much more flow details than the single hot-wire measurements and allow us to better understand the mechanism of drag reduction in flows over dimples. Figure 17 shows a much larger drag increase of 3.5% for the Case 2 dimples at $Re = 3,300$ experimentally.

All the DES runs with the dimple geometries used the domain and dimple distribution shown in Figure 30. Six separate runs were made with the code for two dimple geometries. Although the earlier analysis (Figure 31 and Figure 32) shows that a coarser grid may be sufficiently accurate for the lower Reynolds number cases, the very small changes in drag observed in the present study caused a concern that it might be inconsistent to compare the various Reynolds number cases using different grid and time step sizes. Thus the mesh for the lower Reynolds number cases were refined and matched to that of the highest Reynolds number cases. Thus all simulated dimple cases use the same fine grid and time step size. Similarly, to yield consistent results, the three flat channel cases used to compare with the dimple results also uses the same grid and time step size. These parameters are listed in Table 4 for each DES run. With this fine mesh and time step size, each run took about one month to complete using 16 CPUs (Intel Xeon E5-2603) in parallel for each computation.

**Table 4. Parameters used for dimpled channel runs**

| Case | $d/D$ | $Re$ | Number of cells $(N_x \times N_y \times N_z)$ | Domain size | $\Delta x^+$ | $\Delta z^+$ | $\Delta y^+_{min}$ | $\Delta t^+$ |
|------|-------|------|------------------------|-------------|--------------|--------------|--------------------|--------------|
| Flat | - | 3,300 | | | 12.224 | 7.058 | 0.115 | |
| Flat | - | 10,000 | | | 33.278 | 19.213 | 0.313 | |
| Flat | - | 15,000 | | | 47.540 | 27.448 | 0.447 | |
| 2 | 5% | 3,300 | | | 12.224 | 7.058 | 0.115 | |
| 2 | 5% | 10,000 | $128 \times 256 \times 128$ | $8.693 \times 2.0 \times 5.019$ | 33.278 | 19.213 | 0.313 | 0.0005 |
| 2 | 5% | 15,000 | | | 47.540 | 27.448 | 0.447 | |
| 3 | 1.5% | 3,300 | | | 12.224 | 7.058 | 0.115 | |
| 3 | 1.5% | 10,000 | | | 33.278 | 19.213 | 0.313 | |
| 3 | 1.5% | 15,000 | | | 47.540 | 27.448 | 0.447 | |

Hot-wire measurements were carried out previously at $y = 0.3$mm, 1mm and 5mm for both Case 2 and 3 dimples at $Re = 10,000$ and 15,000. These measurement heights correspond to $y/h = 0.015$, 0.05 and 0.25 respectively for $y$ measured from the flat regions between the dimples. The velocity contours, normalized by their centerline

values obtained from these hot-wire measurements are then compared against those obtained from the DES. An example is shown in Figure 34 for the Case 2 dimples ($d/D = 5\%$) at $Re = 10,000$. A more complete comparison of the velocity contours for the two dimple cases at various heights and Reynolds numbers between the DES and hot-wire results is included in Appendix A.
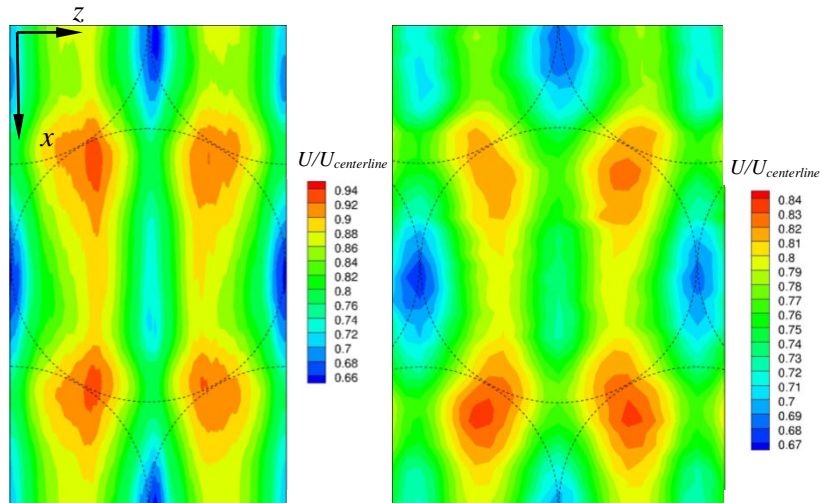


**Figure 34a. Mean streamwise velocity, $d/D$=5% $Re$=10,000, mean, $y/h$=0.05. Flow is from top to bottom. Left: DES. Right: hot-wire. Dashed lines denote position of dimples.**
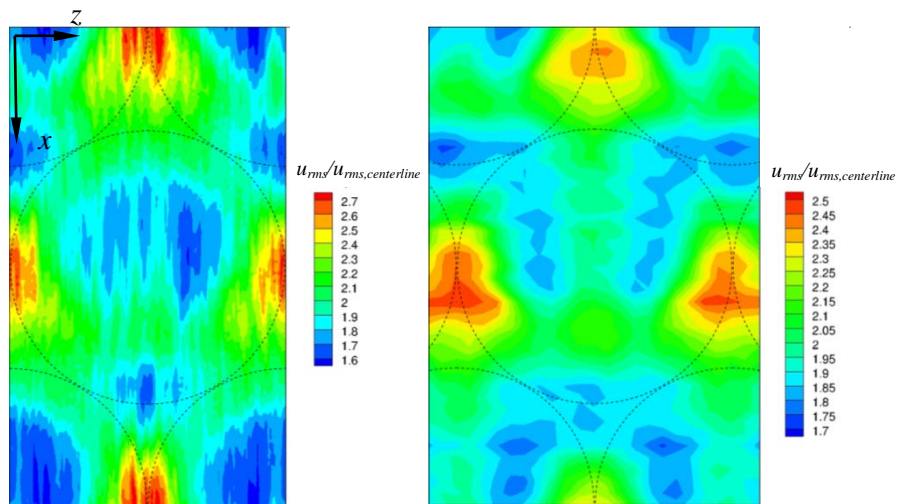


**Figure 34b. Streamwise velocity fluctuations, $d/D$=5% $Re$=10,000, mean, $y/h$=0.05. Flow is from top to bottom. Left: DES. Right: hot-wire. Dashed lines denote position of dimples.**

The agreement between the hot-wire measurements and the DES is generally good, particularly for the deeper Case 2 dimples with $d/D = 5\%$. Both the observed flow patterns and the range of the values of the normalized contours agree well for these

deeper Case 2 dimples. The relatively minor discrepancy in the contour values may be attributed to the flow modelling associated with the DES method, and the spatial resolution errors of the hot-wire probe used in the experimental measurements. Further detailed discussion of the comparison of the various cases is given in the Appendix. The general agreement between the contours from the DES and the hot-wire leads to the conclusion that the DES is sufficiently accurate to reproduce the general flow patterns and features observed in the hot-wire measurements for the entire flow field in the simulated domain.

## 4.5    Skin friction and surface pressure variation

The predicted time averaged skin friction variation on the dimpled surface is shown in Figure 35 for Case 2 ($d/D$ = 5%) at $Re$ = 3,300 and 15,000, and for Case 3 ($d/D$ = 1.5%) at $Re$ = 15,000. The DES shows reduced skin friction at the center of the deeper case 2 dimples at $Re$ = 3,300, compared to the other two cases in Figure 35. However, higher skin friction is observed at the downstream half of these deeper dimples at $Re$ = 3,300. Negative values of skin friction for the Case 2 dimples at both Reynolds number suggest the presence of flow separation for the deeper Case 2 dimples and will be discussed further in a later section.

The time averaged surface pressures are shown in Figure 36 for the same cases as those in Figure 35. The relatively high pressure region at the dimple center is sandwiched between two lower pressure regions upstream and downstream of the dimple center. Such variations in the skin friction and surface pressure are commonly observed in other dimple studies (Lienhart et al. 2008, Veldhuis and Vervoort 2009). However, when the coverage ratio is low and the spacing between dimples is large, the results of Lienhart et al. (2008) shows that the low pressure regions at the upstream and downstream edges of the dimples remain only within the dimple

vicinity. With the large coverage ratio of the dimples in the present work (CR=90%), these low pressure regions link up with those of the surrounding dimples and form continuous low pressure spanwise bands.



(a)                          (b)                          (c)
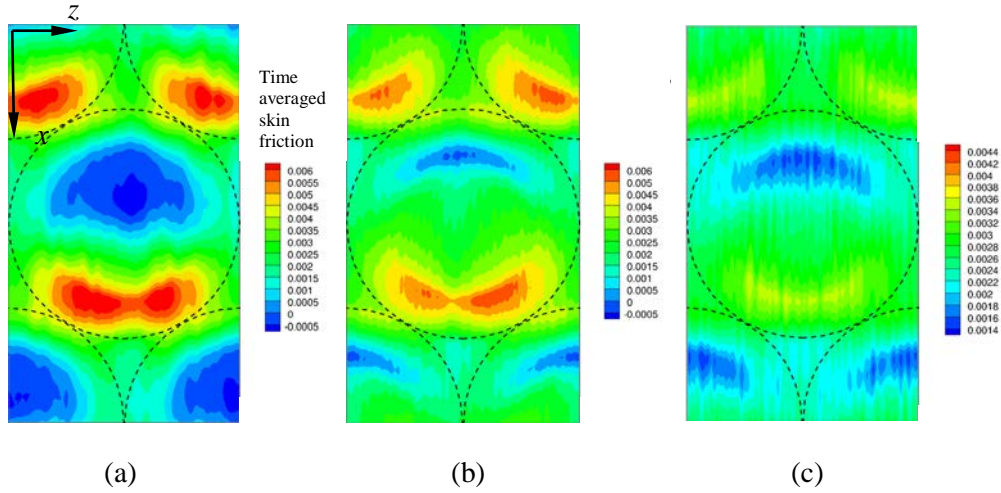
**Figure 35. Time averaged skin friction variation predicted by DES. (a)** $d/D = 5\%$, $Re = 3,300$, **(b)** $d/D = 5\%$, $Re = 15,000$, **(c)** $d/D = 1.5\%$, $Re = 15,000$. **Flow is from top to bottom.**



(a)                          (b)                          (c)
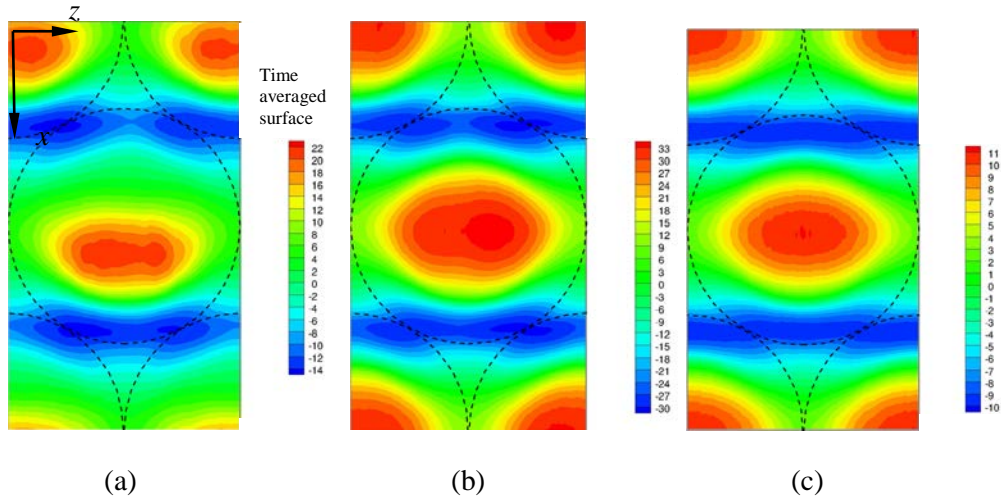
**Figure 36. Time averaged surface pressure predicted by DES. (a)** $d/D = 5\%$, $Re = 3,300$, **(b)** $d/D = 5\%$, $Re = 15,000$, **(c)** $d/D = 1.5\%$, $Re = 15,000$. **Flow is from top to bottom.**

## 4.6    Effect on drag with dimples

Although the velocity contours from the DES matches those of the experiments relatively well (see Figure 34 and Appendix A), the drag predicted by the DES unfortunately do not. Figure 37 shows the total drag as well as the two components that make up the total drag, the skin friction and form drag predicted by the DES. No

drag reduction is observed at any Reynolds number although the experiments shows a small drag reduction for the deeper Case 2 dimples ($d/D$=5%) at $Re = 15,000$ as well as for the shallower Case 3 dimples ($d/D$=1.5%) at $Re = 10,000$ and 15,000.
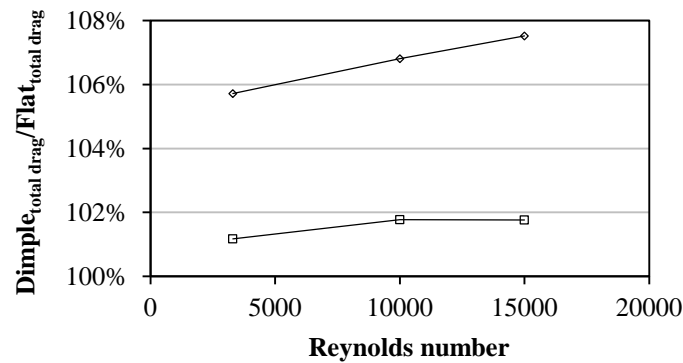


(a)
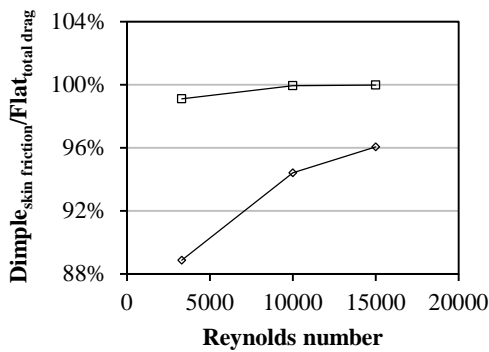


(b)
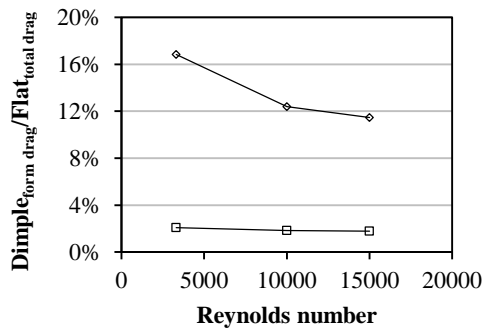


(c)

**Figure 37. (a) Average total drag, (b) skin friction and (c) form drag relative to total drag for flat channel case. Diamonds: Case 2 ($d/D = 5\%$), squares: Case 3 ($d/D = 1.5\%$).**

While further investigation into the DES result may be warranted, because the DES involves some modelling on the flow near the wall, some accuracy is unavoidably lost when compared to a method such as Direct Numerical Simulation (DNS) where no modelling is used. The current DES employs modelling to make investigation of the dimples more practical computationally. Even so, each DES run for each case still takes about one month to complete. The DES shows that the drag increases from about 5.7% to 7.5% from $Re = 3,300$ to 15,000 for the Case 2 dimples ($d/D$=5%) while the shallower Case 3 dimples show a small drag increase from 1.2% to 1.8%

over the same Reynolds number range. These values lie within the errors of the numerical method involved and the inaccuracy involved is made worse by the additional difficulty in predicting the skin friction in the presence of flow separation (Nikitin et al. 2000, Wang et al. 2004, Bozinoski and Davis, 2009). The presence and extent of this flow separation will be discussed in the subsequent section. Because of the known difficulties with DES in skin friction prediction, greater emphasis will be placed on the drag results obtained experimentally in the subsequent discussions.

In the present simulations, both the trend and the absolute values of the total drag with the two dimple configurations do not agree with those of the experiments. While the possibility of inaccuracies in the flow modelling in the current DES offers some explanation for the discrepancy, it is interesting to note that the few claims of drag reduction with dimples known to the author come from experimental studies (Alekseev et al. 1998, Veldhuis and Vervoort 2009, Tay 2011). None of the numerical work carried out on dimples, including the DNS by Lienhart et al. (2008) or the LES by Veldhuis and Vervoort (2009) was able to show the presence of any drag reduction. Similar to the present study, Veldhuis and Vervoort (2009) found that their LES predicted a drag increase with dimples, in contrast to their experiments which showed a drag reduction for the same dimple geometry.

Although the DES has difficulty predicting the skin friction drag accurately, it is useful in predicting the extent of regions of flow separation, usually giving the positions of separation and reattachment with reasonable accuracy (Bozinoski and Davis, 2009, Squires, 2004). Flow separation contributes greatly to the form drag that the dimple surface experience. The trend in the form drag in Figure 37(c) shows a trend very similar to the drag reduction results measured in the experiments. For the deeper Case 2 dimples with $d/D$=5%, the form drag decreases as the Reynolds number increases, but at a decreasing rate. For the shallow Case 3 dimples with

*d*/*D*=1.5%, the form drag is much lower and does not change significantly as the Reynolds number increases from 3,300 to 15,000.

The DES is a hybrid method, where the flow near the solid wall is modelled, in the present case using a derivative of the Spalart-Allmaras one equation RANS model (Nikitin et al. 2000), and the larger eddies in the flow higher up from the wall are resolved and computed using LES. Because of the definition of $\tilde{d}$ in equation

$$\tilde{d} = \min(d_w, C_{DES}\Delta) \qquad\qquad (36, \text{ this switch over from RANS to}$$

LES occurs at *y*/*h* = 0.022 for all cases. This switch over distance is primarily determined by the grid spacing in the *x*-direction in the present study (see equation

$$\tilde{d} = \min(d_w, C_{DES}\Delta) \qquad\qquad (36) \text{ which is constant for all the}$$

different runs listed in Table 4. At *y*/*h* = 0.022, the switch over distance corresponds to $y^+$ values of 4.0, 10.8 and 15.4 at Reynolds numbers of 3,300, 10,000 and 15,000 respectively. Recalling that the events responsible for turbulent skin friction occur mainly near the wall, it may be possible that this RANS modelling occurring near the wall introduces significant errors in the computation of the skin friction. The constants in the RANS model are after all calibrated using the canonical Poiseuille flow and may not be appropriate for the present case where significant spanwise flow components are present near the solid wall. Higher up the wall, where the flow is resolved by the LES, higher accuracy in the predicted flow is obtained. This may allow events such as flow separation and large scale flow patterns higher up above the wall, which are determined more significantly by large scale changes in geometry and relatively large vortices to be predicted more accurately.

## 4.7   Flow separation with dimples

The DES shows the presence of flow separation with the deeper Case 2 dimples (*d*/*D* = 5%) but not for the shallower Case 3 dimples (*d*/*D* = 1.5%). Figure 38 shows the

presence of this flow separation for these Case 2 dimples at Reynolds numbers of 3,300 and 10,000. The locations and full extent of the flow separated regions are shown in Figure 39 for Reynolds numbers 3,300, 10,000 and 15,000.



(a)                                        (b)
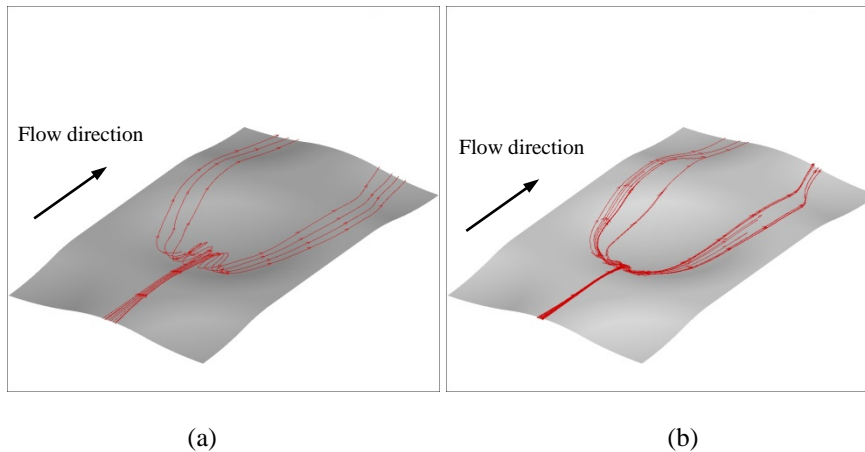
**Figure 38. Streamlines near dimpled surface showing flow separation for Case 2 dimples with *d/D* = 5%. (a) *Re* = 3,300, (b) *Re* = 10,000.**

At all Reynolds numbers, the flow separation region lies near the upstream edge of the dimple. The size of the flow separation region is observed to vary with Reynolds number. The higher the Reynolds number, the smaller the separation region. At *Re* = 15,000, only a small separation region remains. Table 2 shows that a small drag reduction of 0.5% is measured at this Reynolds number. The effect of reducing flow separation with increasing Reynolds number is not unique to dimpled flows, but also occurs in other types of flows such as flows over backward facing steps at sufficiently high Reynolds number (Armaly et al. 1983, Lee and Mateescu 1998) as well as for boundary layer separation bubbles at low Reynolds numbers (Song and Eaton 2004).
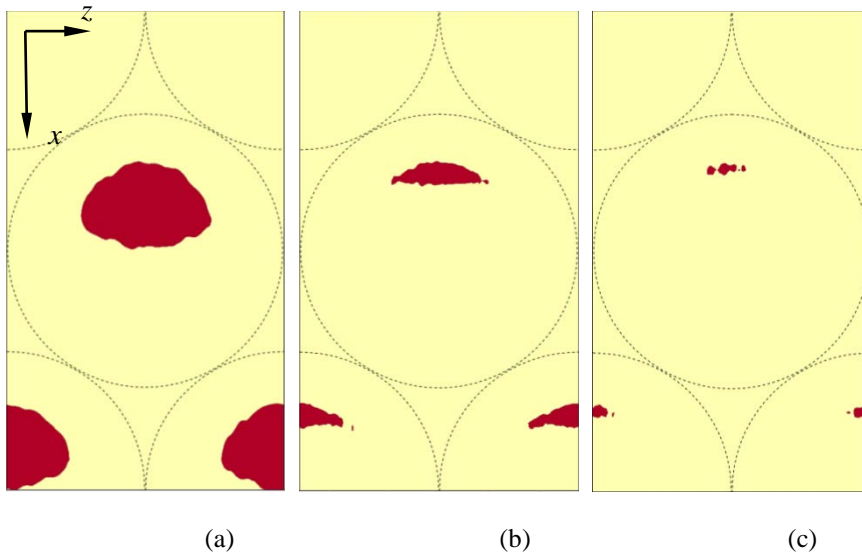
**Figure 39. Dark regions show extent of flow separation regions for Case 2 dimples, *d/D* = 5%. (a) *Re* = 3,300, (b) *Re* = 10,000, (c) *Re* = 15,000. Flow is from top to bottom.**

In an earlier discussion, it was observed that the measured drag reduction by dimpled flows was closely related to shifts in the spectral distribution of the streamwise velocity fluctuations. A shift of the spectral distribution towards the lower frequencies is often accompanied with reduced drag. Observation in drag reducing flows involving long chain polymers also exhibited a similar shift of the spectral distribution towards the lower frequencies when the skin friction drag was reduced. The shift in the spectral distribution of the streamwise velocity fluctuations in the present case is also likely to result in reduced skin friction drag. Dimples however, are three dimensional geometries, which not only exhibit skin friction drag but also form drag, or pressure drag. The reducing flow separation with increasing Reynolds number shown by the DES is able to further explain the earlier observation of the Case 2 dimples (*d/D* = 5%) at *Re* = 10,000. Figure 27 shows that for this case, although a marked shift in its normalized power spectra towards the lower frequencies compared to the flat channel case is observed, it still exhibits a drag increase of about 1% compared to the flat channel (Table 2). The reason for this is most likely due to the presence of form drag. The significance of form drag at lower

Reynolds numbers is also confirmed in Figure 37(c) where the form drag at $Re = 3,300$ is almost 50% higher than that at $Re = 15,000$. At $Re = 3,300$, the DES shows that the form drag is almost 17% of the total drag for a flat channel case.

Figure 39 shows that at all three Reynolds numbers, the flow separation occurs at the upstream portion of the dimple depression. The low pressure within this separated region and its position at the upstream half of the dimple combine to increase the form drag of the flow over the dimples. The larger the extent of the separated region, the greater the additional form drag is added to the flow. The experimental pressure drop method from which Figure 17 is obtained reflects the total flow resistance, which is the combination of the skin friction and the form drag of the three dimensional dimple geometry. If the increase in the form drag is larger than the reduction in skin friction, the total drag increases and hence no drag reduction is observed.

At $Re = 3,300$, the extent of the separated region for Case 2 ($d/D = 5\%$) as shown in Figure 35(a) is significant, and Figure 17 shows that the effect of the dimples is to increase the total flow resistance above that of the basic flat channel flow by about 3.5%. As the Reynolds number increases, the separation region shrinks with a corresponding decrease in the form drag. Since shifts in the power spectra distribution of the fluctuating velocity to the lower frequencies indicate a reduction in the average skin friction as the Reynolds number increases, this together with the reducing form drag leads to drag reduction. The leftward shift of the power spectra distribution to the lower frequencies in Figure 27 suggests that the average skin friction for Case 2 dimples is also lower than that of the flat channel flow even at Reynolds numbers as low as 10,000. Noting that the shallow Case 3 dimples ($d/D = 1.5\%$) show no sign of flow separation and the associated high form drag, the drag reduction observed must be due primarily to the reduction in the skin friction even at

Reynolds numbers as low as 6,000 as Figure 17 shows. The DES shows that the form drag for the shallower Case 3 dimples is indeed much less than that of the deeper Case 2 dimple, with the form drag for the shallow dimples being about 2% of the total drag of the flat channel case and remains almost the same as the Reynolds number is increased from 3,300 to 15,000.

In fact, Figure 17 shows that unlike the deeper Case 2 dimples with $d/D = 5\%$, the increase in drag reduction in the absence of separation-induced form drag for the Case 3 dimples ($d/D = 1.5\%$) to be small as the Reynolds number increases. The change in drag for the Case 3 dimples varies from about -1% at $Re \approx 6,000$ to about -2.5% at $Re \approx 35,000$. The corresponding change in drag for the deeper Case 2 dimples varies between +2.5% to -3% in the same range of Reynolds numbers. Comparing Figure 27 and Figure 28, it can be concluded that the variation in skin friction with Reynolds number is greater for the deeper Case 2 dimples than Case 3 dimples since the magnitude of the shifts in spectra as the Reynolds number varies is greater in Figure 27 than in Figure 28. However, the variation in skin friction alone is unlikely to account for the total net change in flow resistance shown in Figure 17.

The large variation in flow resistance as the Reynolds number varies for the Case 2 dimples ($d/D = 5\%$) is due to the combined effect of reducing skin friction, and decreasing flow separation, both resulting in the overall drag to fall. However, once the region of flow separation shrinks and disappears completely, further reduction in drag will then be determined solely by the reduction in skin friction, assuming total pressure recovery within the dimple. This is supported by the fact that at $Re = 15,000$, Figure 39 shows the region of flow separation to be very small, and Figure 17 shows the flattening of drag reduction with increasing Reynolds number beyond about 20,000 since there is no longer any separation zone to shrink to contribute to the drag reduction. The existence of the separation zone for the deeper Case 2 dimples ($d/D =$

5%) satisfactorily explains the observation of a drag increase at low Reynolds number even with a shift in the power spectra to the lower frequencies, such as that at $Re = 10,000$; and its shrinking and final disappearance with increasing Reynolds number explains the reduction in gradient of the drag reduction with Reynolds number beyond about $Re = 20,000$ for Case 2 in Figure 17.

This competition between the reduced skin friction and the appearance of the form drag is similarly noted by Lienhart et al. (2008), who studied similar shallow dimples with $d/D = 5\%$ and at $Re \approx 10,000$ based on the bulk flow velocity and half channel height. Their DNS show a reduction of about 2% in skin friction, but an increase in form drag by about 5%, resulting in a net increase in the total drag for the dimple geometry they studied. The lower skin friction reduction may be due to the lower dimple area coverage ratio of 22.5% which does not promote strong transverse flow oscillation, and the higher increase in form drag may be due to the use of relatively sharp edged dimples which promote flow separation.

The significant effect of the form drag, which depends very much on the local surface gradients within the dimple suggests that not only is the dimple depth important, but also the particular geometry of the entire dimple on its effect on drag. The fact that the exact dimple geometry is often unreported in the literature may give rise to the various contradicting results reported and make meaningful comparisons between different studies difficult. Factors that are known to affect flow separation such as surface roughness and turbulent intensities are similarly often unreported and may also be the cause of some of the observed contradictions in the reported results. Given that the form drag is dependent on both the dimple geometry and the Reynolds number as well as turbulence intensity and surface roughness, it is postulated that at sufficiently high Reynolds numbers and with careful surface contouring, the drag reduction of 20% obtained by Alekseev *et al.*'s (1998) may also be possible,

particularly since Karniadakis and Choi (2003) have shown that reduction in skin friction of up 40% is possible with the method of introducing transverse flow components to stabilize the flow near the wall. The promise of improved dimple performance at high speeds also opens up possible application in the compressible regime where flow separation is often reduced.

## 4.8 Turbulent kinetic energy budgets

### 4.8.1 Terms of the turbulent kinetic energy budget

The turbulent kinetic energy budget examines the balance and contributions of various energy transport mechanisms and offers greater insight into the flow. For the present channel flow, the turbulent kinetic transport equation may be stated as (Pope, 2000):

$$-\langle u_i u_j\rangle\frac{\partial\langle U_i\rangle}{\partial x_j} - v\left\langle\frac{\partial u_i}{\partial x_j}\frac{\partial u_i}{\partial x_j}\right\rangle + v\frac{d^2}{dy^2}\left(\frac{1}{2}\langle u\cdot u\rangle\right) - \frac{d}{dy}\left\langle\frac{1}{2}vu\cdot u\right\rangle - \frac{1}{\rho}\frac{d}{dy}\langle vp'\rangle = 0 \quad (40)$$

$$\underbrace{\hphantom{-\langle u_i u_j\rangle\frac{\partial\langle U_i\rangle}{\partial x_j}}}_{\textbf{Production}}\ \underbrace{\hphantom{v\left\langle\frac{\partial u_i}{\partial x_j}\frac{\partial u_i}{\partial x_j}\right\rangle}}_{\textbf{Dissipation}}\ \underbrace{\hphantom{v\frac{d^2}{dy^2}\left(\frac{1}{2}\langle u\cdot u\rangle\right)}}_{\substack{\textbf{Viscous}\\\textbf{diffusion}}}\ \underbrace{\hphantom{\frac{d}{dy}\left\langle\frac{1}{2}vu\cdot u\right\rangle}}_{\substack{\textbf{Turbulent}\\\textbf{transport}}}\ \underbrace{\hphantom{\frac{1}{\rho}\frac{d}{dy}\langle vp'\rangle}}_{\substack{\textbf{Pressure}\\\textbf{gradient}}}$$

where the various terms of the energy budget are labeled accordingly. Profiles of these terms in the energy budget for the flow over dimples are presented here in section 4.8 for various locations about the dimple and compared with those for the plane flat channel case as obtained from the DES. These same profiles are also shown in Appendix B in a less cluttered format to allow each profile to be viewed in greater detail.

### 4.8.2 Energy budgets for flow over Case 2 dimples

#### 4.8.2.1 Energy budgets along dimple centerline

Profiles of the energy budget components for the Case 2 dimples are shown in Figure 40 for three different positions, ($x/D$ = -1.04, $z/D$ = 0), ($x/D$ = 0, $z/D$ = 0) and ($x/D$ =

1.04, $z/D = 0$) at various Reynolds numbers. These three points all lie along the dimple centerline and are indicated by the red crosses over their respective mean streamwise velocity contours obtained from the DES, also shown in Figure 40. Note that the results for drag changes ($\Delta_{drag}$) quoted in all following captions refer to those obtained from the experiments, and not from the DES. The profiles shown are plotted against $y^+$ on the horizontal axis, which is the non-dimensionalized wall coordinate measured from the flat surfaces between the dimples, or the dimple horizon. Plotted this way, the profiles at locations within the dimple depression begin at negative values of $y^+$ such as those shown for the profiles at the dimple center ($x/D = 0$, $z/D = 0$) in Figure 40. The shear stress value used to estimate $y^+$ in these plots is the skin friction of the flat channel at the same Reynolds number. Since the drag due to the dimples for these cases does not differ from that of the flat channel by more than a few percent, the skin friction of the flat channel case gives a good estimate of the spatially averaged skin friction for the dimpled cases.

The contours shown in the figures are those of the mean streamwise velocity that lie along the plane $y/h = 0.05$ and are included to indicate the location of the budget profiles relative to the flow patterns over the dimples at each Reynolds number. Also included in the figures are the corresponding budget components from the flat channel simulation at the same Reynolds number for comparison.
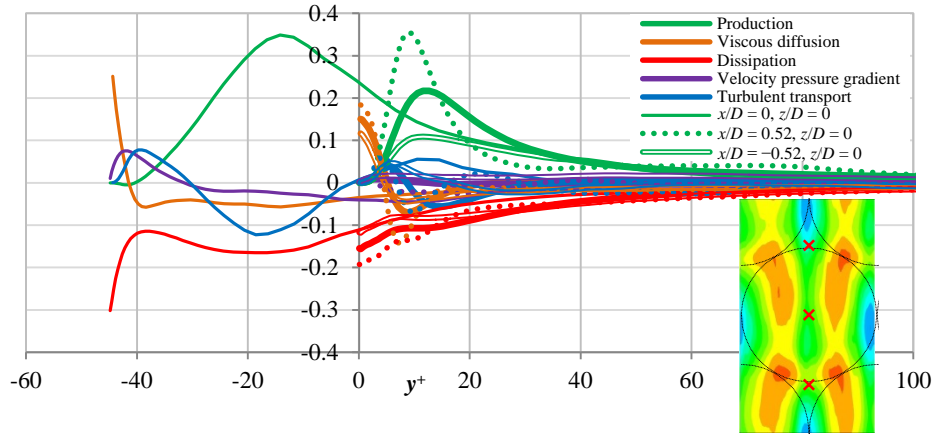
**Figure 40a. Profiles for the turbulent kinetic energy budget terms, Case 2 at *Re* = 3,300, $\Delta_{drag}$=+3.5%. Components of the budget are identified by colour, style of lines indicate position of energy budget profile. Profiles for flat channel are indicated by bold solid lines. Inset contours at lower right are for mean streamwise velocity at *y/h* = 0.05.**
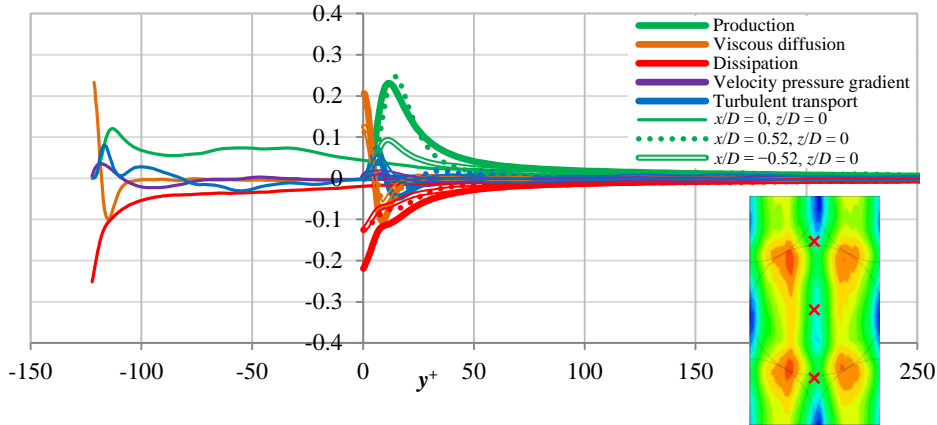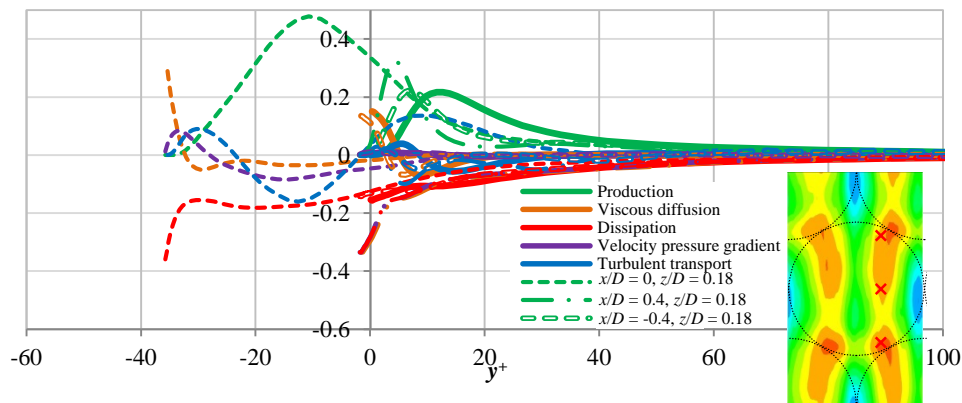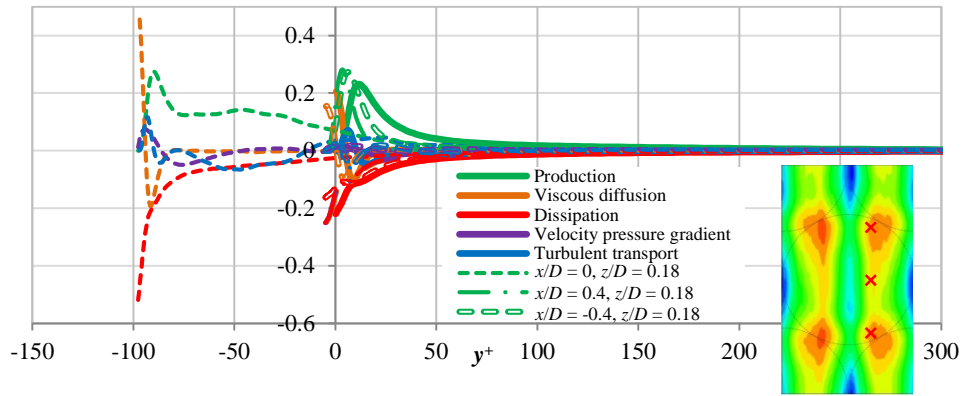


**Figure 40b. Profiles for the turbulent kinetic energy budget terms, Case 2 at *Re* = 10,000, $\Delta_{drag}$=+1%. Components of the budget are identified by colour, style of lines indicate position of energy budget profile. Profiles for flat channel are indicated by bold solid lines. Inset contours at lower right are for mean streamwise velocity at *y/h* = 0.05.**
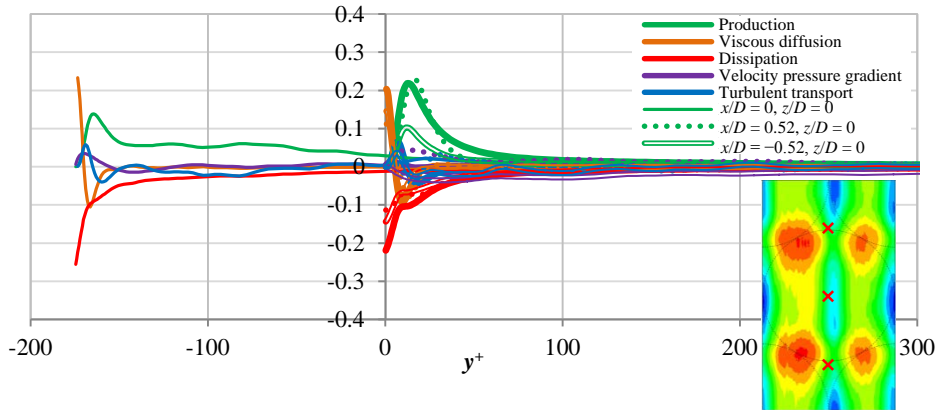


**Figure 40c. Profiles for the turbulent kinetic energy budget terms, Case 2 at *Re* = 15,000, $\Delta_{drag}$=-0.5%. Components of the budget are identified by colour, style of lines indicate position of energy budget profile. Profiles for flat channel are indicated by bold solid lines. Inset contours at lower right are for mean streamwise velocity at *y/h* = 0.05.**
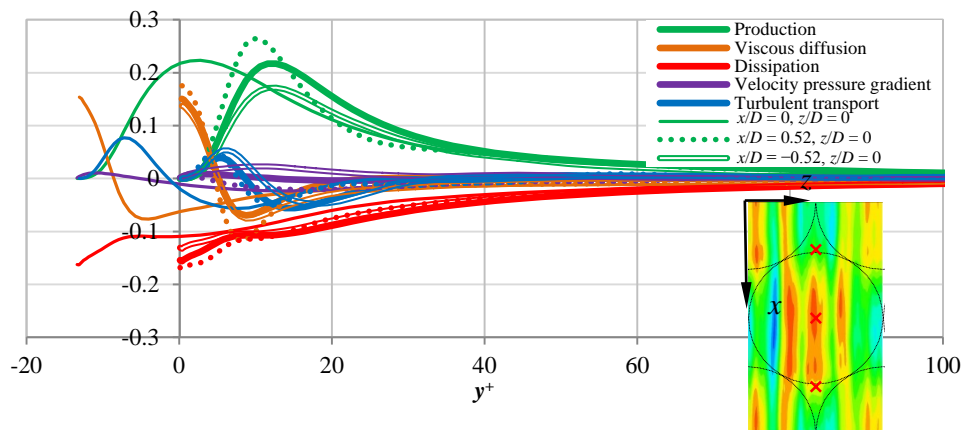
The profiles of the energy budget components show a marked change as the Reynolds number increases for the Case 2 dimples and the drag decreases

89

correspondingly. Significant increase in the production, turbulent transport and the dissipation terms over that of the flat channel case are obvious at $Re = 3,300$ where a drag increase of 3.5% over that of the flat channel was measured. These terms show the greatest increase at the dimple center, followed by the point immediately following the dimple. Referring to Figure 39, we observe that the dimple center lie almost immediately downstream of the flow separation region. Such regions are usually chaotic and is a likely contributor to the significant increase in the turbulent energy budget components. As the Reynolds number increases, the drag decreases and the energy budget components decrease correspondingly. The peaks in the production component of the energy budget lie below that of the flat channel at locations upstream of the dimple and at its center. Immediately downstream of the dimple, it is comparable with that of the flat channel case at $Re = 10,000$ and 15,000.

Unlike the case at $Re = 3,300$ where the peak in the production term is highest at the dimple center, the peaks in the production terms for $Re = 10,000$ and 15,000 exhibit a gradual but steady increase from the most upstream to the most downstream location as the flow flows over the dimple. Closer analysis also reveal that the terms of the energy budget at $Re = 10,000$ with a 1% drag increase, show slightly higher values than those at $Re = 15,000$ where there is a 0.5% drag reduction. These small differences are observed for the production, velocity pressure gradient and turbulent transport terms within the dimple depression where $y^+ < 0$ at the dimple center ($x/D = 0$, $z/D = 0$).

## 4.8.2.2 Energy budgets along spanwise direction from dimple center

Figure 41 shows the same terms of the energy budget but for points located along the spanwise direction from the dimple center for Case 2 dimples ($d/D = 5\%$). The point furthest from the dimple center lies near the dimple edge, while the point in between

90

($x/D = 0$, $z/D = 0.18$) is chosen to coincide with the location of the high speed region on either side of the dimple centerline as shown in the contour plot. The plots of the energy budgets show that at the location of the high speed region, the various terms of the energy budget, particularly the production, dissipation and turbulent transport terms show greater increases compared to the other two locations. This shows the increased energy being generated and dissipated within the high speed streaks over the dimple. The most significant increase is observed at $Re = 3,300$ where the drag is highest. The peaks in the production and dissipation terms at this Reynolds number is about twice those of the flat channel case. As the Reynolds number increases and the drag reduces, these increases in the terms of the energy budget also reduce. At $Re = 10,000$ and $15,000$, a significant increase in the viscous diffusion term is observed very near the wall at the location of the high speed streak. This is balanced by a similar increase in the dissipation term in this near wall region.
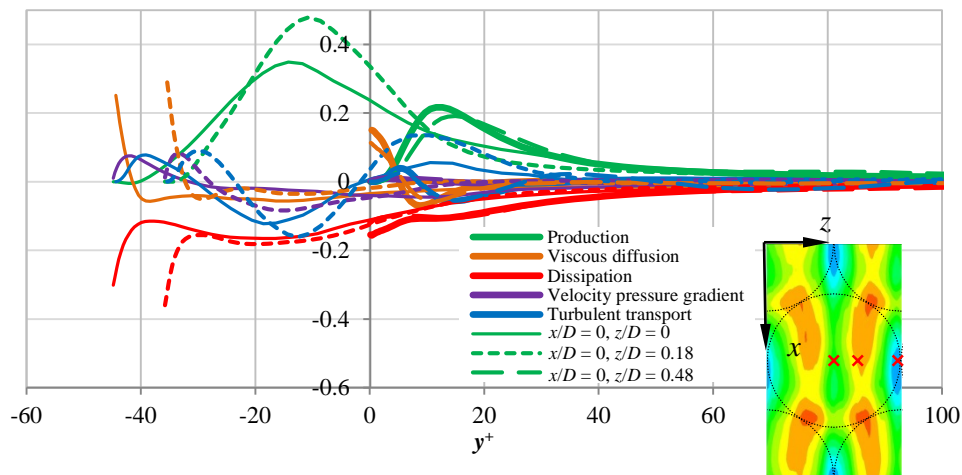


**Figure 41a. Profiles for the turbulent kinetic energy budget terms, Case 2 at $Re = 3,300$, $\Delta_{drag}=+3.5\%$. Components of the budget are identified by colour, style of lines indicate position of energy budget profile. Profiles for flat channel are indicated by bold solid lines. Inset contours at lower right are for mean streamwise velocity at $y/h = 0.05$.**
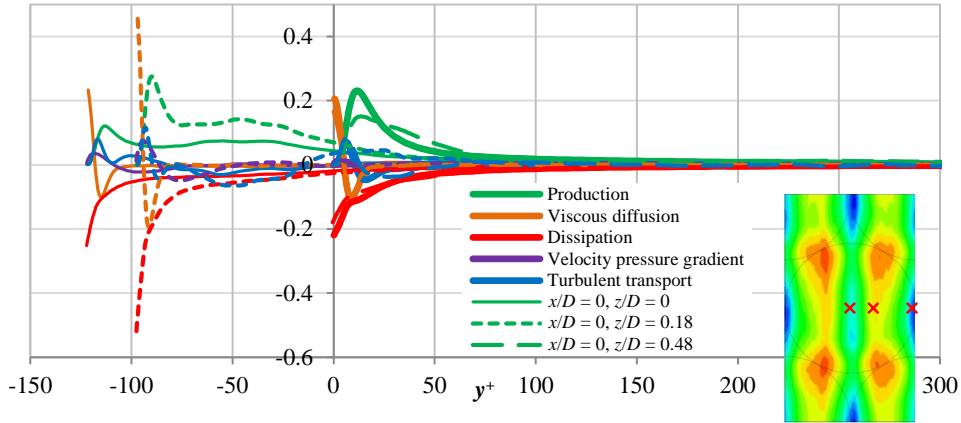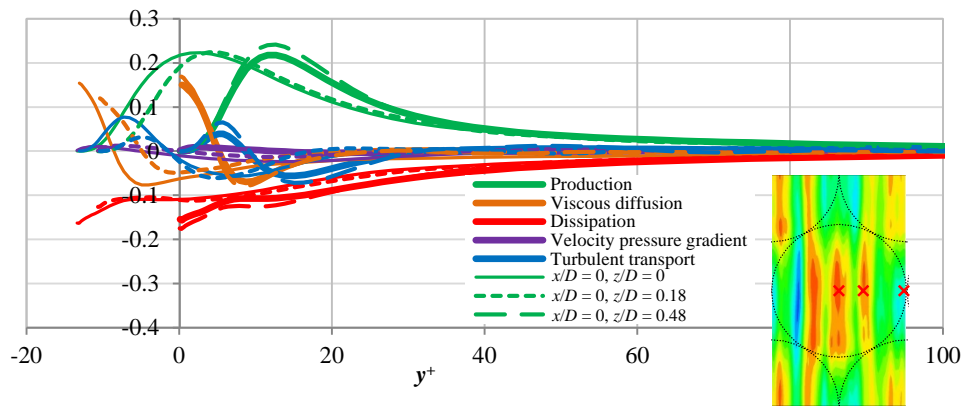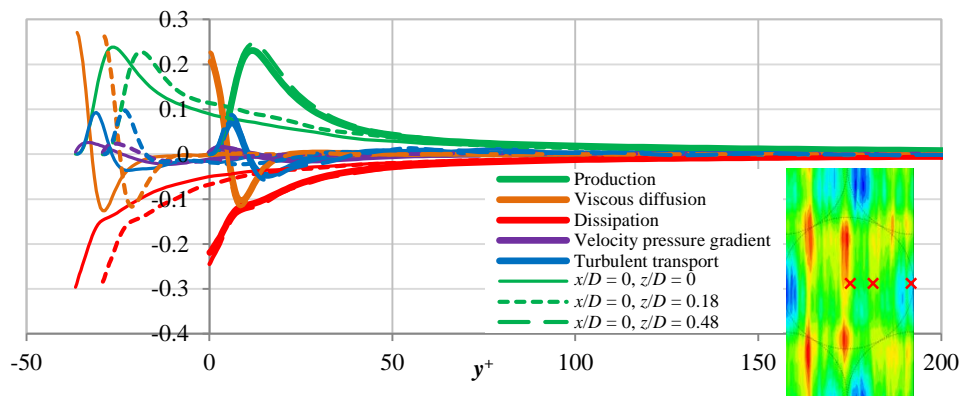
**Figure 41b. Profiles for the turbulent kinetic energy budget terms, Case 2 at *Re* = 10,000, Δ*drag*=+1%. Components of the budget are identified by colour, style of lines indicate position of energy budget profile. Profiles for flat channel are indicated by bold solid lines. Inset contours at lower right are for mean streamwise velocity at *y/h* = 0.05.**
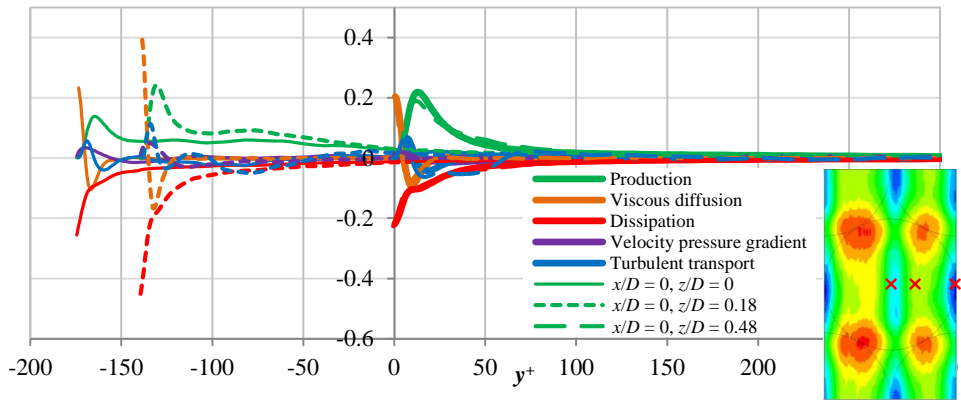


**Figure 41c. Profiles for the turbulent kinetic energy budget terms, Case 2 at *Re* = 15,000, Δ*drag*=-0.5%. Components of the budget are identified by colour, style of lines indicate position of energy budget profile. Profiles for flat channel are indicated by bold solid lines. Inset contours at lower right are for mean streamwise velocity at *y/h* = 0.05.**

### 4.8.2.3 Energy budgets along high speed streak region

A further investigation of the energy budget terms is carried out at the location of the high speed streaks. Figure 42 shows the profiles of the terms of the energy budget at three locations within the high speed streak for the Case 2 dimples (*d/D* = 5%). The general observation that the peaks of the profiles of these energy budget terms is significantly higher at *Re* = 3,300 where the drag is highest compared to the other Reynolds numbers where the drag is reduced is still observed in Figure 42. At *Re* = 3,300, the peak in the production term is lowest at the most upstream location. This increases significantly as the flow moves into the dimple, but again reduces at the most downstream location as the flow leaves the dimple depression. A similar

92

observation is also true for the dissipation, velocity pressure gradient and turbulent transport terms. The viscous diffusion term plays a relatively less significant role except at the region near the wall where it shows a significant increase. The flow structure changes as the Reynolds number increases however, and at $Re = 15,000$ where a small drag reduction is observed, the peak in the production term is highest at the most upstream location and gradually reduces until it is lowest at the most downstream location as the flow leaves the dimple. Unlike the case at $Re = 3,300$ where the highest peak in the terms lie within the dimple, Figure 42c for $Re = 15,000$ appear to suggest that the dimple actually is able to stabilize the flow so that the peaks in the production term is steadily reduced as the flow flows into and then out of the dimple depression. Figure 42b for $Re = 10,000$, which shows a drag value between that at $Re = 3,300$ and 15,000 shows a variation in the production terms between the observations made for $Re = 3,300$ and 15,000.



**Figure 42a. Profiles for the turbulent kinetic energy budget terms, Case 2 at $Re = 3,300$, $\Delta_{drag}$=+3.5%. Components of the budget are identified by colour, style of lines indicate position of energy budget profile. Profiles for flat channel are indicated by bold solid lines. Inset contours at lower right are for mean streamwise velocity at $y/h = 0.05$.**
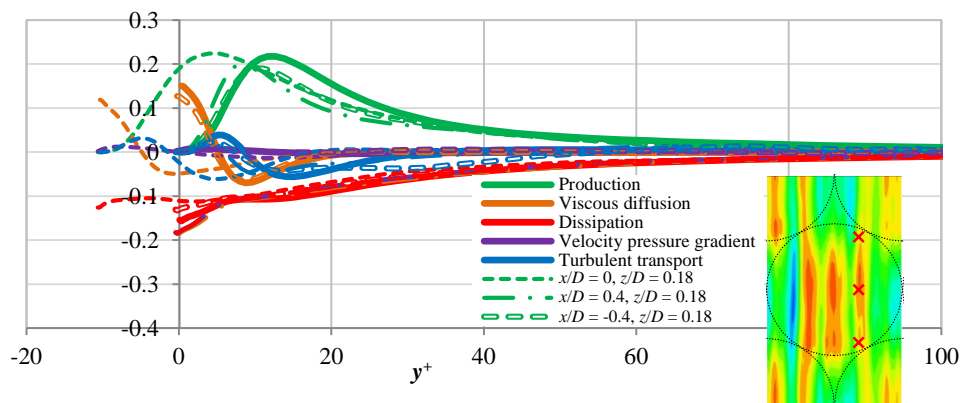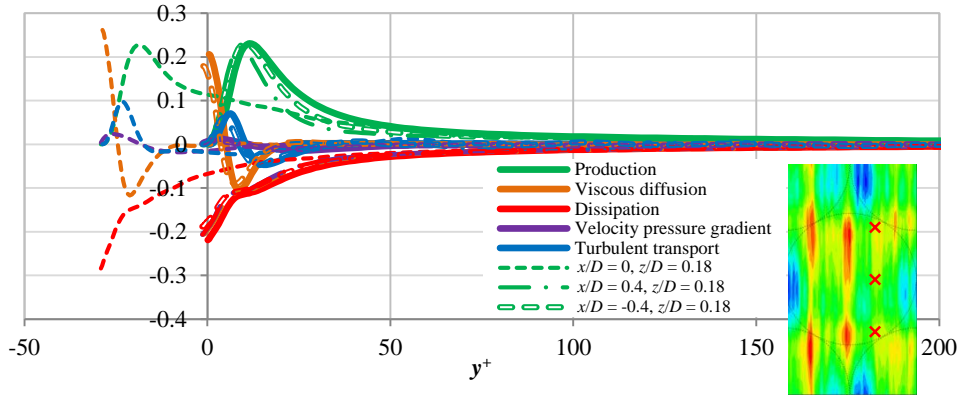
**Figure 42b. Profiles for the turbulent kinetic energy budget terms, Case 2 at *Re* = 10,000, Δ*drag*=+1%. Components of the budget are identified by colour, style of lines indicate position of energy budget profile. Profiles for flat channel are indicated by bold solid lines. Inset contours at lower right are for mean streamwise velocity at *y/h* = 0.05.**
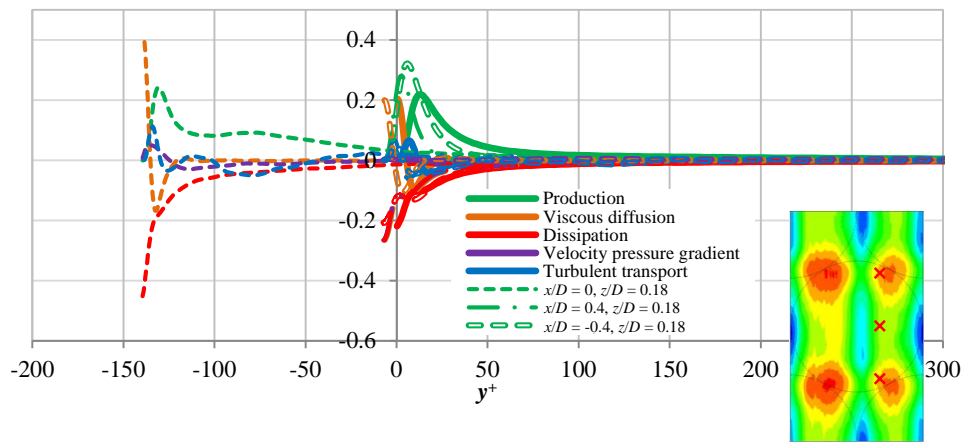


**Figure 42c. Profiles for the turbulent kinetic energy budget terms, Case 2 at *Re* = 15,000, Δ*drag*=-0.5%. Components of the budget are identified by colour, style of lines indicate position of energy budget profile. Profiles for flat channel are indicated by bold solid lines. Inset contours at lower right are for mean streamwise velocity at *y/h* = 0.05.**

### 4.8.3 Energy budgets for flow over Case 3 dimples

#### 4.8.3.1 Energy budgets along dimple centerline

A similar analysis was carried out for the shallow Case 3 dimples (*d/D* = 1.5%). Unlike the Case 2 dimples (*d/D* = 5%) where the relative drag changes from +3.5% to -0.5% as the Reynolds number increases from 3,300 to 15,000, the variation in drag over the same Reynolds number range is much smaller. At *Re* = 3,300, the shallow Case 3 dimples show an estimated drag reduction of about 1%, which increases to only about 1.5% at *Re* = 15,000. This small variation in drag is reflected in the small variation in the terms of the energy budget as the Reynolds number increases. This agreement in the trend between experimental drag measurements and

94

the computational results of these energy budgets adds further credibility to our experimental measurements. Consequently, the variation in the energy budget profiles as the Reynolds number changes is less for Case 3 than the deeper Case 2 dimples. These are shown in Figure 43 to Figure 45 for the shallow Case 3 dimples ($d/D$ = 1.5%). Due to their very shallow depth of 1.5%$D$, the variation in the terms of the energy budget is similar to those of the flat channel case.

The trend in the production term in Figure 43 follows that in Figure 40c for the Case 2 dimples at $Re$ = 15,000, which similarly exhibit a drag reduction like the shallow Case 3 dimples in Figure 43. The peak in the production term is lowest at the upstream edge of the dimple, and progressively increases as the flow flows over the dimple to the downstream edge.



**Figure 43a. Profiles for the turbulent kinetic energy budget terms, Case 3 at *Re* = 3,300, Δ*drag* ≈ -1%. Components of the budget are identified by colour, style of lines indicate position of energy budget profile. Profiles for flat channel are indicated by bold solid lines. Inset contours at lower right are for mean streamwise velocity at *y/h* = 0.05.**
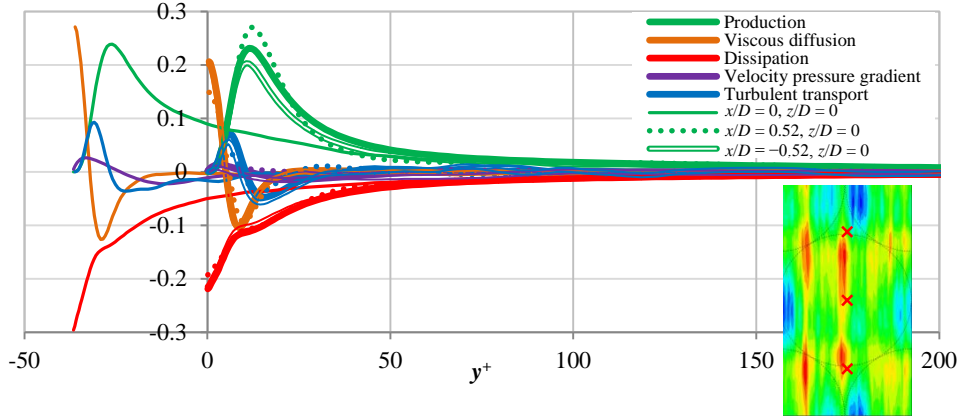
**Figure 43b. Profiles for the turbulent kinetic energy budget terms, Case 3 at *Re* = 10,000, Δ_drag=-1.5%. Components of the budget are identified by colour, style of lines indicate position of energy budget profile. Profiles for flat channel are indicated by bold solid lines. Inset contours at lower right are for mean streamwise velocity at *y/h* = 0.05.**
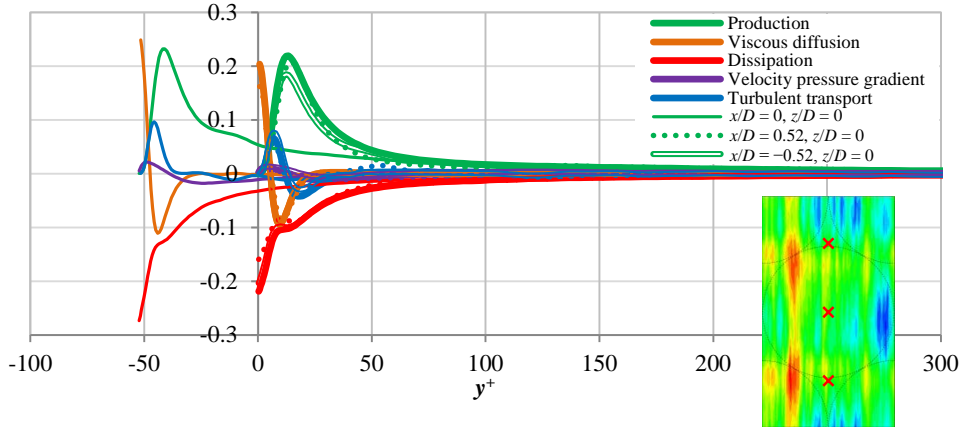


**Figure 43c. Profiles for the turbulent kinetic energy budget terms, Case 3 at *Re* = 15,000, Δ_drag=-1.5%. Components of the budget are identified by colour, style of lines indicate position of energy budget profile. Profiles for flat channel are indicated by bold solid lines. Inset contours at lower right are for mean streamwise velocity at *y/h* = 0.05.**

4.8.3.2 Energy budgets along spanwise direction from dimple center

Figure 44 shows the profiles of the energy budget terms for points located along the spanwise direction from the dimple center. Unlike the Case 2 dimples (*d/D* = 5%) where the position (*x /D* = 0, *z/D* =0.18) corresponds to the high speed streak region, this may not be the case for these shallower Case 3 dimples. The contour plots in Figure 44 suggest that there may be three high speed regions within the dimple. Due to the very shallow depth of the dimple, the presence of these individual high speed streaks are not as clearly defined as those in the deeper Case 2 dimples with *d/D* = 5%. This can be inferred by comparing the range in normalized velocity contours in

96

Figure 24 for the deeper Case 2 dimples with Figure 25 for the shallower Case 3 dimples. The Case 2 dimples exhibit a larger range of velocities than the shallower Case 3 dimples. This smaller variation for the shallower Case 3 dimples also makes it more difficult for the hot-wire to identify the presence of three individual high speed streaks. The hot-wire measurements in Figure 25 show only the presence of a broad high speed region along the dimple centerline. The small variation of the mean velocity in the spanwise variation is likely also a cause for the observation of no clear trends in the variation of the energy budget profiles for the three positions shown in Figure 44.



**Figure 44a. Profiles for the turbulent kinetic energy budget terms, Case 3 at *Re* = 3,300, Δ*drag* ≈ - 1%. Components of the budget are identified by colour, style of lines indicate position of energy budget profile. Profiles for flat channel are indicated by bold solid lines. Inset contours at lower right are for mean streamwise velocity at *y/h* = 0.05.**



**Figure 44b. Profiles for the turbulent kinetic energy budget terms, Case 3 at *Re* = 10,000, Δ*drag*=- 1.5%. Components of the budget are identified by colour, style of lines indicate position of energy budget profile. Profiles for flat channel are indicated by bold solid lines. Inset contours at lower right are for mean streamwise velocity at *y/h* = 0.05.**
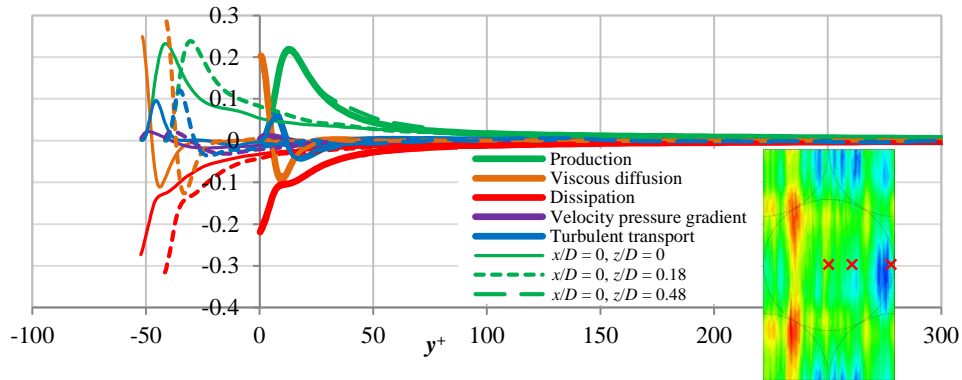
**Figure 44c. Profiles for the turbulent kinetic energy budget terms, Case 3 at *Re* = 15,000, Δ*drag*=-1.5%. Components of the budget are identified by colour, style of lines indicate position of energy budget profile. Profiles for flat channel are indicated by bold solid lines. Inset contours at lower right are for mean streamwise velocity at *y/h* = 0.05.**

### 4.8.3.3 Energy budgets along points offset from centerline

Similarly, no clear trend is observed among the energy budget profiles for the three positions shown in Figure 45 for the Case 3 dimples (*d/D* = 1.5%). Unlike these same points for Case 2, where they correspond to the location of the high speed streak, and where the peaks in the energy budget profiles are higher than those of the flat channel case at the corresponding Reynolds numbers, the peaks of the energy budget profiles for the shallow Case 3 dimples in Figure 45 are comparable to their respective flat channel cases.



**Figure 45a. Profiles for the turbulent kinetic energy budget terms, Case 3 at *Re* = 3,300, Δ*drag* ≈ -1%. Components of the budget are identified by colour, style of lines indicate position of energy budget profile. Profiles for flat channel are indicated by bold solid lines. Inset contours at lower right are for mean streamwise velocity at *y/h* = 0.05.**

**Figure 45b. Profiles for the turbulent kinetic energy budget terms, Case 3 at *Re* = 10,000, Δ_{drag}=-1.5%. Components of the budget are identified by colour, style of lines indicate position of energy budget profile. Profiles for flat channel are indicated by bold solid lines. Inset contours at lower right are for mean streamwise velocity at *y/h* = 0.05.**
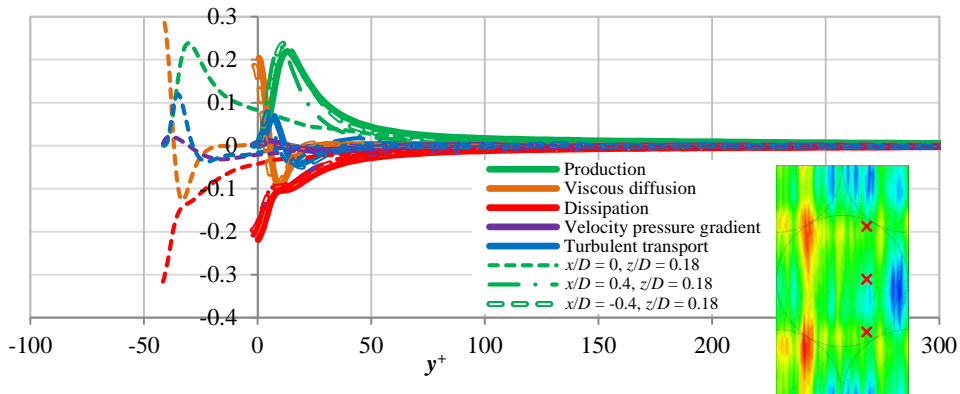


**Figure 45c. Profiles for the turbulent kinetic energy budget terms, Case 3 at *Re* = 15,000, Δ_{drag}=-1.5%. Components of the budget are identified by colour, style of lines indicate position of energy budget profile. Profiles for flat channel are indicated by bold solid lines. Inset contours at lower right are for mean streamwise velocity at *y/h* = 0.05.**

### 4.8.4    Summary of energy budget results

The effect of increased drag on the profiles of the energy budget is clear in general. Significant drag increases are accompanied by significant increases in the terms of the energy budgets. As the drag reduces, so do the terms in the energy budget, showing an increased stability of the flow.

The trends observed in the energy budget profiles in Figure 40 to Figure 45 agree very well with the trends and conclusions drawn from the spectral distribution of the streamwise velocity fluctuations in Figure 27 and Figure 28 as well as the dimple's

99

effect on drag shown in Figure 17. Significant changes in both the profiles of the energy budget obtained computationally and the spectral distribution obtained experimentally are observed as the Reynolds number increases for Case 2 dimples ($d/D$ = 5%). Accompanying this is the relatively significant reduction in drag from +3.5% to -3% as the Reynolds number increases from 3,300 to 37,000. For the Case 3 dimples ($d/D$ = 1.5%), the change in drag as the Reynolds number increases is relatively less significant. The drag only changes from about -1% to -2% over the same Reynolds number range measured experimentally. Both the computational energy budget profiles and the experimental spectral distribution support this by showing a reduction in variation as the Reynolds number varies for the shallower Case 3 dimples compared to the deeper Case 2 dimples. However, unlike the spectral distribution of the streamwise velocity fluctuations, which only reflect changes in the skin friction, the changes in the energy budget profiles reflect changes in the overall drag and are affected by the net effect of both form drag and skin friction drag.

Analysis of the energy budget profiles is clearer when comparing the deeper Case 2 dimples at $Re$ = 3,300, where a drag increase of +3.5% is observed with the same Case 2 dimples at $Re$ = 15,000 where a drag reduction of -0.5% is observed. This relatively large change in the drag is accompanied by significant changes in the energy budget profiles, making analysis of the flow easier. The other cases at intermediate drag levels are found to also follow the same trend, and exhibit changes depending on the drag measured for those cases.

With a relatively large drag increase of +3.5% over the flat channel for Case 2 dimples ($d/D$ = 5%) at $Re$ = 3,300, significant increases in the various terms of the energy budget over those of the flat channel case is observed at several locations about the dimple, and particularly at the dimple center at ($x/D$ = 0, $z/D$ =0). Most significant is the increase in the production term, showing the greatest increase over

the flat channel case within the dimple depression at $y^+ < 0$. The peak in the profile of the production term is about double that of the flat channel case. Significant increases in the dissipation, velocity pressure gradient and turbulent transport terms are also observed within the dimple depression at $y^+ < 0$. At $y^+ > 0$, the various terms including the production term generally falls rapidly towards zero. The viscous diffusion term generally is less significant except in the region very near the wall, where the significant increase in the viscous diffusion term is offset by a similar increase in the dissipation term in this near wall region.

At $Re = 15,000$ and with a small drag reduction of 0.5%, significant changes are observed in the profiles of the energy budget for the same Case 2 dimples. Peaks in the production terms fall to a level comparable to or lower than the flat channel case in almost all the locations about the dimple investigated. Within the dimple depression, the production term does not reduce rapidly to zero after the peak but maintains at a level of about half that of the peak production level for quite a distance above the wall within the dimple depression. It only drops more rapidly to zero above the dimple at $y^+ > 0$. Significant reductions for the other terms in the energy budget are also observed, with their peak values also being comparable to or lower than the flat channel case at this Reynolds number exhibiting drag reduction.

While the drop in the various terms of the energy budget is significant as the Reynolds number increases and the drag reduces, several general observations can also be made that apply both to the drag increase case at $Re = 3,300$ and the drag reduction case at $Re = 15,000$ for the Case 2 dimples. Along the dimple centerline, there is a general increase in the various terms of the budget as the flow flows from the upstream edge to the downstream edge. Significant increase in the viscous diffusion term is observed very near the wall, and this is offset by a comparable increase in the dissipation term in this near wall region. The presence of a high speed

streak within the dimple also causes a significant increase in the various terms of the energy budget. In fact the greatest increase in the terms over the flat channel case is found within the high speed streak region. However, the increase of the peaks, particularly that of the production term, is greatly reduced when drag reduces.

These same trends can also be observed for the shallower Case 3 dimples. However, since the drag reduces only from about -1% at $Re = 3,300$ to -1.5% at $Re = 15,000$, the changes in the profiles of the energy budget terms are not as obvious as those for the deeper Case 2 dimples.

## 4.9    Turbulence kinetic energy

The trends in the turbulence kinetic energy profiles support the previous results. For a more concise presentation of the results, only the turbulent kinetic energy (TKE) profiles for Case 2 ($d/D = 5\%$) at $Re=3,300$ (experimentally highest drag increase), Case 2 at $Re=15,000$ (experimentally highest drag reduction) and Case 3 ($d/D = 1.5\%$) at $Re=3,300$ (comparison with Case 2 at the same Reynolds number but with drag reduction) are presented. Comparisons are made for the TKE profiles at ($x/D=0$, $z/D=0$), ($x/D=0$, $z/D=0.18$) and ($x/D=0$, $z/D=0.48$). These positions are distributed along the spanwise direction from the dimple center and the reader may refer to Figure 41 and Figure 44 for the positions of these locations with respect to the dimples. Compared to points distributed along the streamwise direction, which trace the flow as it evolves and flows downstream, these chosen positions distributed in the spanwise direction show a more complete and concise picture of what is happening to the flow over the dimple array.
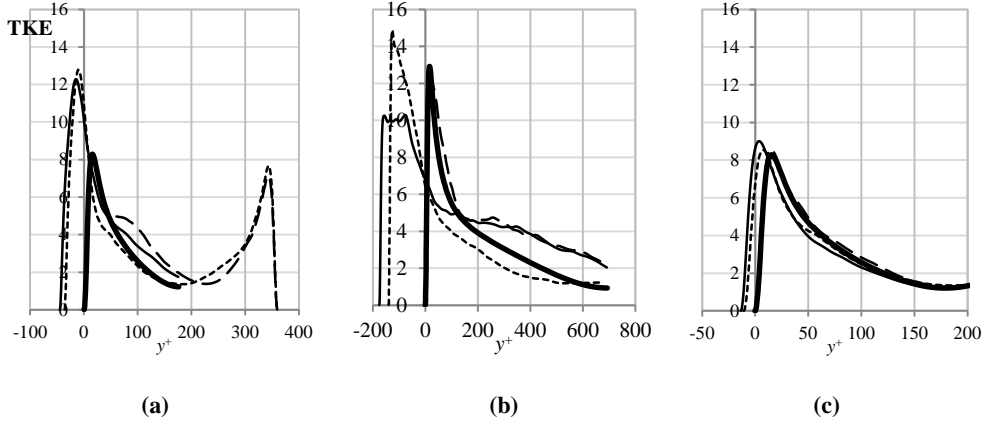
**Figure 46. Profiles of the turbulence kinetic energy. (a) Case 2 at *Re* = 3,300, $\Delta_{drag}$=+3.5%, (b) Case 2 at *Re* = 15,000, $\Delta_{drag}$=-0.5%, (c) Case 3 at *Re* = 3,300, $\Delta_{drag}$=-1%.** ━━━ : **Flat channel reference,** ──── : (*x/D*=0, *z/D*=0), ---------- : (*x/D*=0, *z/D*=0.18), ─ ─ ─ ─ : (*x/D*=0, *z/D*=0.48).

Like the turbulent energy budget terms, significant increases in the magnitude of the TKE are observed with drag increase, and is dependent on the on its position within the dimple. This increases in the peak value of the TKE can be over 50% over that of the flat channel case for the deeper Case 2 dimples (*d/D* = 5%) at *Re*=3,300 where a drag increase of 3.5% is observed. For Case 2 dimples at *Re*=15,000 where a drag reduction of 0.5% is observed, a reduction in the peak value in the TKE is observed. The highest values in the TKE are generally observed for points lying in the high speed region on either side of the dimples. For the shallow dimples (*d/D* = 1.5%) at *Re*=3,300, increases in the TKE is marginal and the profiles tend to be similar to those of the flat channel case due to the small drag reduction they show as well as their relatively shallow dimple depressions. The similarity of the TKE profiles to those of the flat channel case for the shallow Case 3 dimples is also noted for the turbulence energy budget terms previously discussed.

## 4.10   Reynolds stress profiles

Similar to the cases shown in section 4.8, Reynolds stress profiles are presented for the same positions for Case 2 (*d/D* = 5%) at *Re*=3,300 and *Re*=15,000 and Case 3 (*d/D* = 1.5%) at *Re*=3,300 for brevity.

## 4.10.1  Profiles of $u'^2$

Similar observations are made of the $u'^2$ profiles of the Reynolds stress for the deeper Case 2 dimples ($d/D$ = 5%). The most significant increases in the $u'^2$ magnitudes occur in the presence of greatest drag increases, while with drag reduction, the peaks in the $u'^2$ profiles are similar or lower than the corresponding flat channel values. For the shallower Case 3 dimples ($d/D$ = 1.5%), a surprising increase in the $u'^2$ peak is seen in the dimple center, though the magnitude of the peak is still less than those seen for Case 2 dimples ($d/D$ = 5%) at $Re$= 3,300 at the points where $u'^2$ is highest.
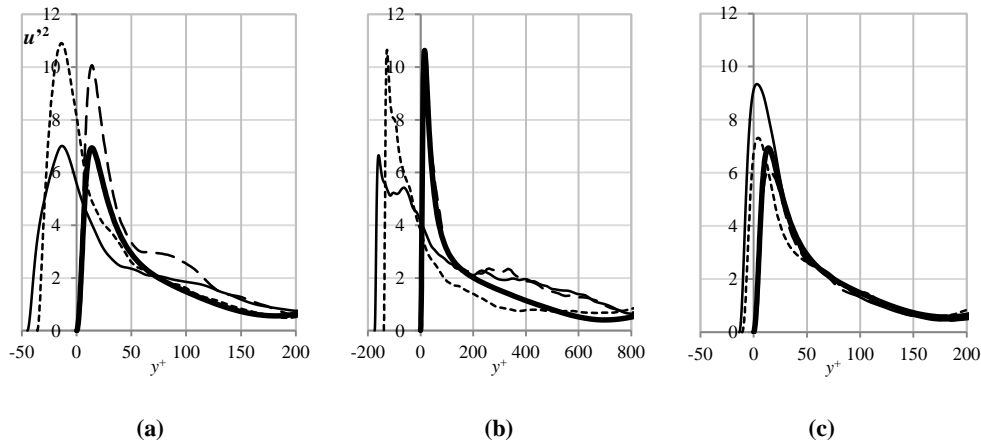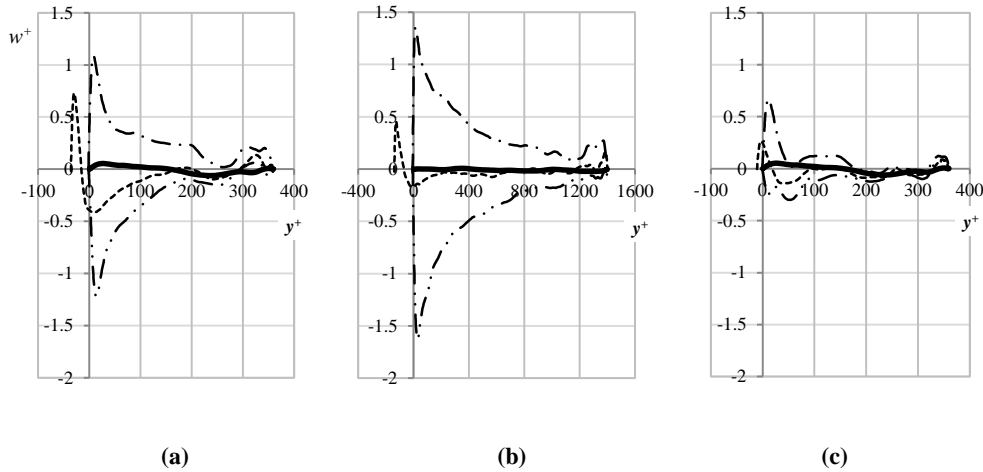


**Figure 47. Profiles of $u'^2$.** (a) Case 2 at $Re$ = 3,300, $\Delta_{drag}$=+3.5%, (b) Case 2 at $Re$ = 15,000, $\Delta_{drag}$=-0.5%, (c) Case 3 at $Re$ = 3,300, $\Delta_{drag}$=-1%.  ——— : **Flat channel reference,** ——— : (*x/D*=0, *z/D*=0), --------- : (*x/D*=0, *z/D*=0.18), − − − − : (*x/D*=0, *z/D*=0.48).

## 4.10.2  Profiles of $u'v'$

Unlike the previous profiles discussed, where changes to the profiles are somewhat limited to the lower half of the channel where the dimples are located, significant changes are observed of profiles of $u'v'$ in the upper half of the channel away from the dimpled wall. This is due to the significant presence of $v'$ introduced by the dimples that would otherwise be absent in the plane Poiseuille flow of the flat channel case.
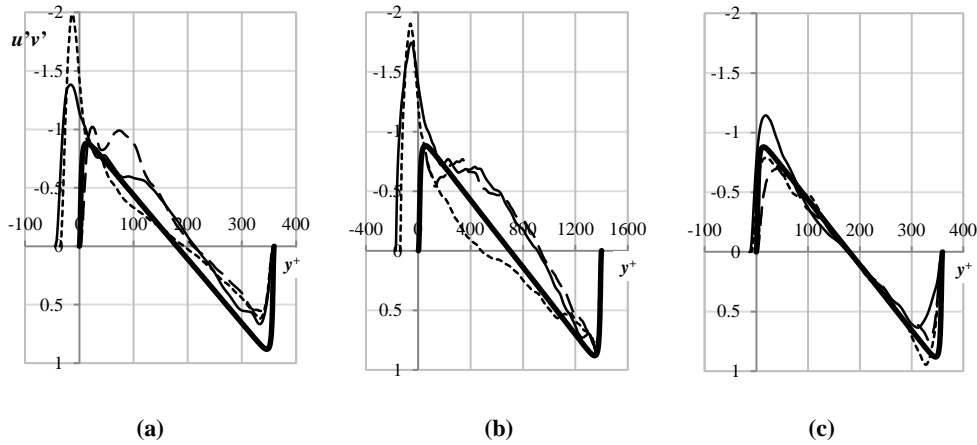
**Figure 48. Profiles of *u'v'*. (a) Case 2 at *Re* = 3,300, Δ_drag=+3.5%, (b) Case 2 at *Re* = 15,000, Δ_drag=-0.5%, (c) Case 3 at *Re* = 3,300, Δ_drag=-1%.** ———— **: Flat channel reference,** ———— **: (*x/D*=0, *z/D*=0), ---------- : (*x/D*=0, *z/D*=0.18), − − − − : (*x/D*=0, *z/D*=0.48).**

Significant increases in *u'v'* are observed for the deeper Case 2 dimples at both Reynolds numbers in Figure 48 despite the drag reduction at *Re*=15,000. Deviations from the flat channel profiles are observed almost to the opposite wall for these deeper dimples. While the peak in *u'v'* for the Case 2 dimples at *Re*=3,300 (with a 3.5% drag increase,) at the high speed region at (*x/D*=0, *z/D*=0.18) is significantly higher than that at the dimple center at (*x/D*=0, *z/D*=0), the peaks at these two locations are comparable at *Re*=15,000 where a drag reduction of 0.5% is observed. Although the peaks are comparable, the magnitude of *u'v'* at the higher Reynolds number (where drag reduction is observed,) rapidly drops below that of the flat channel case and stays below for most of the channel. For the shallower Case 3 dimples, the variation in *u'v'* remains similar to that of the flat channel case. Interestingly, there appears to be a redistribution of the Reynolds stresses where the peak magnitude at the dimple center (*x/D*=0, *z/D*=0) is higher than the flat channel case at the dimple side but lower at the opposite wall while the opposite is observed at (*x/D*=0, *z/D*=0.18) where the peak magnitude is higher at the opposite wall but lower at the dimple wall. At the dimple edge at (*x/D*=0, *z/D*=0.48), the magnitude of *u'v'* is lower than the flat channel case at all heights within the channel.

### 4.10.3 Profiles of $v'^2$

Figure 49 confirms the significant contribution of $v'$ to the magnitude of $u'v'$ in Figure 48. Similar to the $u'v'$ profiles, significant deviations in the $v'^2$ profiles from that of the flat channel flow are observed in the upper half of the channel away from the dimpled wall.
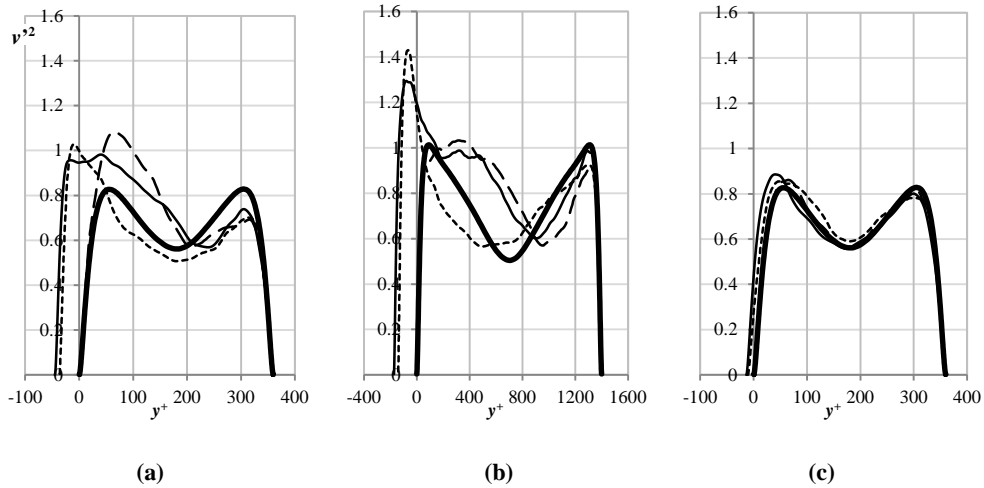


**Figure 49. Profiles of $v'^2$. (a) Case 2 at $Re$ = 3,300, $\Delta_{drag}$=+3.5%, (b) Case 2 at $Re$ = 15,000, $\Delta_{drag}$=-0.5%, (c) Case 3 at $Re$ = 3,300, $\Delta_{drag}$=-1%.** ──── **: Flat channel reference,** ──── **: ($x/D$=0, $z/D$=0),** --------- **: ($x/D$=0, $z/D$=0.18),** − − − − **: ($x/D$=0, $z/D$=0.48).**

The peak in the $v'^2$ profiles for Case 2 ($d/D$ = 5%) at $Re$=15,000 is higher than at $Re$=3,300, even though a drag reduction is observed $Re$=15,000, and a drag increase at $Re$=3,300. This is different from the trend that has been observed where increases in the Reynolds stress is accompanied by a drag increase. Comparing the magnitudes of $u'^2$ and $v'^2$ however, it is noted that the $u'^2$ has a much larger magnitude than $v'^2$ and thus would have a much greater effect on the overall drag than the smaller change in $v'^2$. While $v'^2$ generally increases within the side of the channel where the dimples are located, they are lower than the flat channel case at the other side of the channel away from the dimples. The highest peaks in $v'^2$ for the deeper dimples of Case 2 ($d/D$ = 5%) occur along the high speed region. Only minor changes in the $v'^2$ profiles from the flat channel case are observed for the shallow Case 3 dimples, most likely due to their very shallow depth.

These same observations in the $v'^2$ profiles for these dimple cases can be made of the $w'^2$ profiles, though not shown here for brevity.

### 4.10.4  Profiles of the mean wall normal velocity $v$.

The proposed drag reduction mechanism involves the introduction of streamwise vorticity resulting in spanwise flow near the wall. Spanwise flow components near the wall are found to stabilize the flow and reduce drag. The spectral distribution of the streamwise velocity fluctuations, as well as the turbulent kinetic energy budget terms from the DES shows evidence of the flow stabilization, but the magnitude of the streamwise vorticity added is not sufficient to result in streamline traces showing the presence of spiraling streamlines usually associated with a vortical feature. However, analysis of the mean wall normal and spanwise velocities shows evidence of the presence of the streamwise vorticity introduced by the dimples.

Figure 50 shows the profiles of the mean wall normal velocity normalized by the wall friction velocity for the various cases. At $Re$=3,300, the deeper Case 2 dimples ($d/D$ = 5%) appear to show only a single pair of counter-rotating vortices, unlike at higher Reynolds numbers and similar to the shallow Case 3 dimples ($d/D$ = 1.5%). The contours of the streamwise velocity contours from the DES for this case is shown in the inset in Figure 41a. The flow over most of the dimple is flowing into the dimple depression, though at the dimple center, this downward flow towards the dimple is limited to only a small region directly above the dimple. At the spanwise edge of the dimple, the flow has a strong upward component away from the dimple wall.
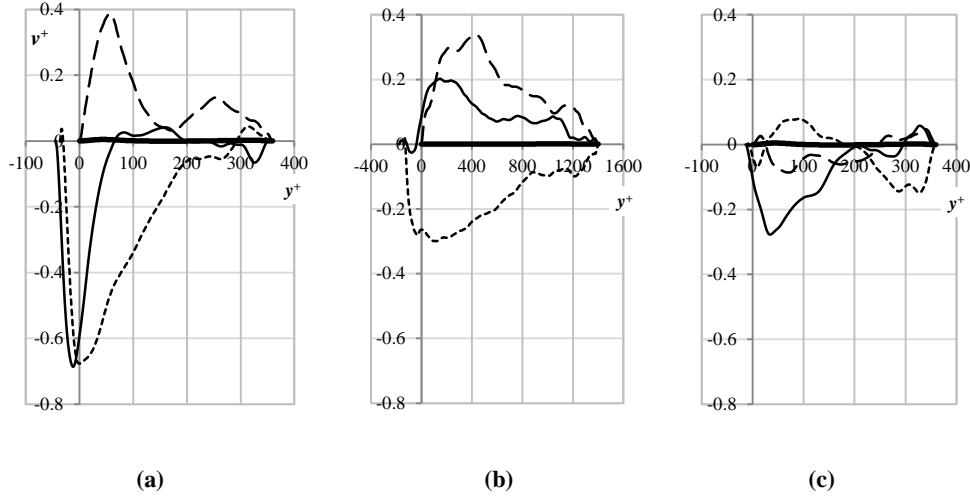
**Figure 50. Profiles of $v^+$ (a) Case 2 at *Re* = 3,300, $\Delta_{drag}$=+3.5%, (b) Case 2 at *Re* = 15,000, $\Delta_{drag}$=-0.5%, (c) Case 3 at *Re* = 3,300, $\Delta_{drag}$=-1%. ———: Flat channel reference, ———: (*x/D*=0, *z/D*=0), ----------: (*x/D*=0, *z/D*=0.18),– – – –: (*x/D*=0, *z/D*=0.48).**

At the higher Reynolds number of 15,000, the $v^+$ profiles of the deeper Case 2 dimples support the presence of two pairs of counter-rotating vortices within the dimple. The profiles show upflow away from the dimple at the dimple center and spanwise edge, and down flow towards the dimple at (*x/D* = 0, *z/D* = 0.18), supporting presence of the streamwise vortex pairs shown in Figure 24(a) and similarly observed by Ligrani et *al*. (2001) and Won et *al*. (2005).

For the shallow Case 3 dimples (*d/D* = 1.5%), only a relatively strong downward flow towards the dimple surface is observed at the dimple center, supporting the streamwise vortices suggested by the hot wire measurements in Figure 25a. Further up the wall at the opposite half of the channel, a relatively strong downward flow away from the flat opposite wall is also observed. Generally though, when both the magnitude and extents of the moving fluid is considered, the shallow Case 3 dimples have less vertical fluid momentum than the deeper Case 2 dimples, and this is expected from the much shallower dimple depth of the Case 3 dimples. Also expected is the practically zero mean wall normal velocity for the flat channel case throughout the channel.

108

4.10.5  Profiles of the mean spanwise velocity *w*.

Further support of the streamwise vorticity added to the dimples can be seen in the profiles of the mean spanwise velocity. The mean spanwise velocity is normalized by the friction velocity and shown in Figure 51.



(a)                                      (b)                                      (c)
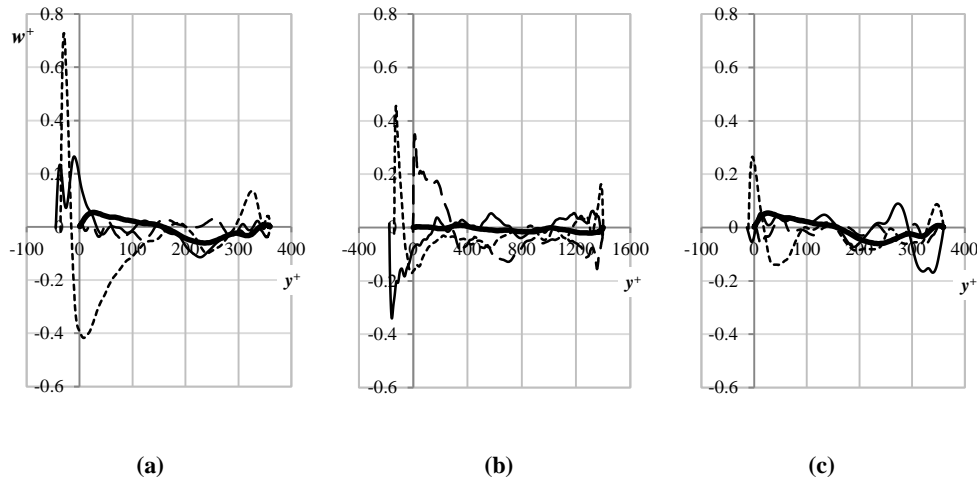
**Figure 51. Profiles of $w^+$. (a) Case 2 at *Re* = 3,300, $\Delta_{drag}$=+3.5%, (b) Case 2 at *Re* = 15,000, $\Delta_{drag}$=-0.5%, (c) Case 3 at *Re* = 3,300, $\Delta_{drag}$=-1%. ———— : Flat channel reference, ——— : (*x/D*=0, *z/D*=0), ·········· : (*x/D*=0, *z/D*=0.18), — — — — : (*x/D*=0, *z/D*=0.48).**

The $w^+$ profiles similarly support the presence of the streamwise vortices previously discussed. The deeper Case 2 dimples (*d/D* = 5%) at *Re*=3,300 shows a relatively strong positive *w* component near the wall at (*x/D* = 0, *z/D* = 0.18) but negative *w* component slightly higher up, showing a strong vorticity in this region. The profiles at the other two positions in Figure 51(a) do not show such sharp changes in *w*, thus supporting the presence of a single vortex pair within the dimple as mentioned previously. At *Re*=15,000, the Case 2 dimples shows sharp changes in *W* at all three positions shown in Figure 51(b) near the dimple surface. At (*x/D* = 0, *z/D* = 0.18) particularly, *w* changes from positive (towards the dimple center) near the dimple surface to negative (away from the dimple center) higher up from the dimple surface. This figure, together with Figure 50(b) supports the observation of Ligrani et *al*.

(2001) and shows the presence of a pair of counter-rotating vortices within each half of the dimple, with the vortex nearer the dimple center located slightly higher above the wall than the vortex nearer the spanwise dimple edge. The sharp change in *w* from positive to negative for the shallow Case 3 dimples (*d/D* = 1.5%) at *Re*=3,300 near the dimple surface also support the presence of a pair of streamwise vortices within the dimple as previously discussed.

It is interesting that all the dimples cases shown in Figure 51 show peaks in the spanwise velocity near the dimple surface, particularly at (*x/D* = 0, *z/D* = 0.18), along the location of the high speed streak for the deeper dimple case. Figure 52 shows the profiles of the spanwise velocity *w* for the same cases along streamwise direction at *z/D* = 0.18. The location of these points relative to the dimple can be seen in the insets of Figure 42 and Figure 45.



|     (a)     |     (b)     |     (c)     |

**Figure 52. Profiles of *w*⁺. (a) Case 2 at *Re* = 3,300, Δ_drag=+3.5%, (b) Case 2 at *Re* = 15,000, Δ_drag=-0.5%, (c) Case 3 at *Re* = 3,300, Δ_drag=-1%.** ──── : **Flat channel reference,** ─··─ : (*x/D*=-0.4, *z/D*=0.18), --------- : (*x/D*=0, *z/D*=0.18), ─·─·─: (*x/D*=0.4, *z/D*=0.18).

The profiles show that large magnitudes of the mean spanwise velocity *w* occur along this spanwise coordinate. In both the deeper and shallow dimple cases (Cases 2 and 3), the peak value of *w* just above the dimple surfaces changes from a negative value at the upstream edge to a positive value at the half way location, and further increases

at the downstream edge. For the deeper Case 2 dimples ($d/D = 5\%$), the maximum magnitude of $w$ occur at the upstream edge, while it occurs at the downstream edge for the shallow Case 3 dimples where $d/D = 1.5\%$. These maximum magnitudes of $w$ are about 7% of the centerline streamwise velocity for the Case 2 ($d/D = 5\%$) dimples at $Re$=3,300. For the same Case 2 dimples at $Re$=15,000, it is about 8%. For the much shallower Case 3 dimples ($d/D = 1.5\%$), the maximum magnitude of $w$ is only about 3.6% that of the streamwise velocity at the channel centerline.

In their DNS study of a channel flow at a Reynolds numbers of 1,800 and 3,200 with spanwise wall jets introduced to achieve drag reduction, Schoppa and Hussain (1998) found that a 50% drag reduction could be achieved with just a wall jet velocity of only 6% that of the channel velocity at the centerline. The experimental work of Choi et al. (1998) further suggests that increasing the spanwise velocity of the jet leads to a monotonic increase in the drag reduction obtained (Figure 1). Analysis of the skin friction distribution on the dimple surface however does not reveal reduced skin friction at these positions (see Figure 35). Further investigation may be needed to establish the limitations of the DES on the skin friction prediction. It may be noted that among the many studies known to the author regarding the effect of transverse flow or wall movement exhibiting drag reduction, all the numerical studies showing the effect of drag reduction use DNS to simulate such flows (eg. Jung et al. 1992, Orlandi and Fatica 1997, Schoppa and Hussain 1998, Choi et al. 2002, Quadrio and Ricco 2004).

Despite the limitations of the current DES to predict the skin friction accurately, it is still able to provide very useful information about the flow within the dimpled channel. The analysis of the various flow profiles further support the hypothesis put forth to explain the cause of the drag reduction being the result of spanwise flow components near the wall. These spanwise flow components arise due to the

streamwise vorticity added to the flow by the dimples, and have the effect of inhibiting the normal energy cascade to the smaller scales by stabilizing the flow at the larger scales.

# Chapter 5
# Conclusions

Three different dimpled configurations have been studied experimentally using hot-wire anemometry and pressure transducers to determine their effect on drag in a channel flow environment. The dimples studied have depth to diameter ($d/D$) ratios of 1.5% and 5% and are arranged in dimple arrays with coverage ratios of 40% and 90%. The study is carried out for a Reynolds number range from 3,300 to 37,000. The relative change in drag of the dimple compared with a flat plane channel is determined by measuring the change in the mean streamwise pressure gradient in the channel due to the dimples in the channel test section. These pressure measurements show that dimples have the ability to reduce drag below that of the flat plane channel flow used as the baseline in the present study. The greatest drag reduction is obtained using the relatively deeper dimples with $d/D$ = 5% and closely packed with a coverage ratio of 90%. These produce a drag reduction of 3% at a Reynolds number of 37,000. The drag generally decreases as the Reynolds number increases. At the lowest Reynolds number studied, these deeper dimples produce a drag increase of 3.5% over that of the flat plane channel. These same dimples with depth to diameter ratios of 5% but arranged with a coverage ratio of 40% show a drag increase of about 1% at $Re$ = 6,000 which becomes a drag reduction of 2% at $Re$ = 37,000. Very shallow dimples with $d/D$ = 1.5% and arranged with a coverage ratio of 90% is also able to produce drag reduction in a channel flow. The drag reduction for these shallow dimples is relatively consistent and varies from 1% at $Re$ = 6,000 to about 2.5% at $Re$ = 37,000.

Further study was carried out on the dimple geometries with $d/D$ = 1.5% and 5% and with coverage ratio of 90% using hot-wire anemometry and DES. Hot-wire

measurements of the streamwise velocity show two high speed streaks on each side of the dimple centerline for the deeper dimples with $d/D = 5\%$ indicating vertical fluid motion as high speed fluid is brought down while low speed fluid is brought up from the wall. The vertical fluid motion introduces vorticity into the flow with associated spanwise motion at the wall. Unlike the deeper dimples, the hot-wire measurements show only a single high speed streak along the dimple centerline for the shallow dimples with $d/D = 1.5\%$.

Analysis of the spectral distribution of the fluctuations of the streamwise velocity shows that the dimples shift the spectral distribution towards the lower frequencies. This shift is greater for the deeper dimples with $d/D = 5\%$ than the shallow dimples with $d/D = 1.5\%$ and is closely linked to reductions in skin friction drag. There is also a general trend of increasing shifts towards the lower frequencies as the Reynolds number increases for both dimple geometries. The shift to the lower frequencies may be interpreted as a lengthening of the near wall streaks, reflecting a greater stability in the flow. A greater shift towards the low frequencies indicates greater stability of the flow, which results in reduced skin friction. The mechanism by which the dimples accomplish this is by introducing streamwise vorticity into the flow, resulting in spanwise flow components near the wall. The spanwise flow motion acts to disrupt the normal energy cascading process of energy transfer towards ever smaller vortices which eventually dissipate the energy through viscosity.

Dimples however, are three dimensional geometries and exhibit both skin friction drag and form drag, with both contributing to the overall drag. Although the shifts in the spectral distribution of the streamwise velocity fluctuation is closely related to the measured drag, some discrepancies are observed when shifts of the spectral distribution towards the lower frequencies occur in the presence of a drag increase, particularly for the deeper dimples with $d/D = 5\%$ at lower Reynolds numbers. This

occurs because shifts in the spectral distribution of the streamwise velocity fluctuations towards the lower frequencies only indicate a greater stability of the flow and an associated reduction in skin friction drag. However, the DES shows that for the deeper dimples with $d/D = 5\%$, significant flow separation occurs at the upstream portion of the dimple at low Reynolds numbers, contributing significantly to form drag. The result is that the form drag dominates over the slightly reduced skin friction drag and causes an overall drag increase. The shallow dimples with $d/D = 1.5\%$ however show no evidence of flow separation over its very shallow depression, so that the small reduction in skin friction inferred from the smaller shifts in the spectral distribution towards the lower frequencies is sufficient to cause an overall drag reduction over the whole Reynolds number range studied. The analysis shows that the overall drag depends very much on the competition between the form drag and the skin friction drag. Deeper dimples which introduce greater streamwise vorticity into the flow leading to reduced skin friction is also shown to exhibit higher form drag due to the presence of significant flow separation. This flow separation occurs in the upstream half of the dimple at low Reynolds numbers and produce a drag increase. However, as the Reynolds number increases, this region of flow separation may reduce and disappear altogether so that the effect of the reduced skin friction dominates and an overall drag reduction results.

Profiles of the various terms in the energy budget and Reynolds stresses obtained from the DES show a clearer picture of the flow and supports the observations from the both the pressure measurements and spectral distribution of the streamwise velocity fluctuations obtained from the hot-wire. The energy budget is affected by both the skin friction and the form drag, and a close relationship is observed in their variation with the variation in drag due to the dimples. Relatively high drag increases are accompanied by significant increases in the various terms in the energy budget, most notably the production, dissipation and turbulent transport terms. Since the flow

is three dimensional, the variations in the energy budget profiles vary with its location about the dimples. When drag reduction occurs, the terms of the energy budget are also observed to reduce accordingly, often to below those of the flat plane channel in many parts over the dimple. In the region of the high speed streak over the deeper dimples with $d/D = 5\%$, significant increases in the terms of the energy budget are observed. There appears to be a redistribution of the energy within the flow into the regions of the high speed streaks when drag reduction occurs as the terms of the energy budget at positions outside the high speed streak region reduces.

Similar observations are also made of the Reynolds stresses. Significant increases in the Reynolds stress terms are observed with drag increases, most notably in the $u'^2$ term. Drag reduction, on the other hand is often accompanied by decreases in the Reynolds stresses below that of the flat channel cases. The three dimensional dimples also introduce significant $v'$ and $w'$ into the flow compared to the flat channel due to the mean $v$ and $w$ components introduced into the flow, so that increases in the peaks of terms involving $v'$ and $w'$ over the plane channel case, such as $u'v'$ occur even in the presence of drag reduction. The increase in these terms however is small compared to the increase in the $u'$ term, resulting in the significance of the $u'^2$ term contributing to the turbulence energy. These observations further support the hypothesis that the flow is stabilized due to the presence of the dimples which then cause the drag reduction.

The DES also shows the vorticity introduced by the dimples through the introduction of mean $v$ and $w$ components near the dimple surface. These $v$ and $w$ components are located at locations within the dimple that support the location of the streamwise vortices observed in the literature and inferred from the present hot-wire measurements. Though the magnitude of the streamwise vorticity introduced by the dimples is low and cannot be easily visualized by spiraling streamlines, the vorticity

116

is concentrated near the surface so that relatively strong spanwise components are generated near the dimple surface. These spanwise components near the wall are the cause of the flow stabilization that is evidenced by both the DES and experimental results.

The present study shows that the flow features within a dimple have opposing effects for drag reduction. With a better understanding of the flow features responsible for the overall flow resistance due to dimples, efforts can be made to tailor the dimples to the flow conditions to optimize its effect for drag reduction applications. The advantage that dimples have for drag reduction over riblets is that large scale motion of the fluid is used to generate drag reduction. This avoids the very small physical sizes encountered in riblets as the Reynolds number is increased to those commonly encountered in engineering applications. The dimples, being circular is also relatively independent on the direction of the incoming flow. While the dimples work in a similar way to produce drag reduction as active methods to introduce streamwise vorticity, such as with spanwise moving walls or jets, the dimples remain a passive method requiring no additional energy or complexity other than the passive contouring of the wall.

# Bibliography

Alekseev, V. V., Gachechiladze, I. A., Kiknadze, G.I. and Oleinikov, V. G., "Tornado-like energy transfer on three-dimensional concavities of reliefs-structure of self-organizing flow, their visualisation, and surface streamlining mechanisms," *Transactions of the 2nd Russian Nat. Conf. of Heat Transfer*, Vol. 6, Heat Transfer Intensification Radiation and Complex Heat Transfer, Publishing House of Moscow Energy Institute (MEI), Moscow, 1998, pp. 33–42.

Armaly, B. F., Durst, F., Pereira, J. C. F. and Schönung, B., **"**Experimental and theoretical investigation of backward-facing step flow," *J. Fluid Mech.* Vol. 127, 1983, pp. 473–496.

Bacher, E. V. and Smith, C. R**., "**Turbulent Boundary‑Layer Modification by Surface Riblets," *AIAA Journal*, Vol. 24, No. 8, 1986, pp. 1382–1385.

Balakumar, P., and Widnall S.E., "Application of Unsteady Aerodynamics to Large-Eddy Breakup Devices in a Turbulent Flow," *Phys. Fluids*, Vol. 29, 1986, pp. 1779–1787.

Barbin, A. R. and Jones, J. B., "Turbulent Flow in the Inlet Region of a Smooth Pipe, *ASME Journal of Basic Engineering*, Vol. 85, 1963, pp. 29–34.

Berchert, D. W., Bartenwerfer, M., Hoppe, G. and Reif, W.-E., "Drag reduction mechanisms derived from shark skin," *Proc. 15th Int. Council of Aeronautical Sciences Congress,* London, UK, 7–12 September 1986, Vol. 2, pp. 1044–1068, paper no. ICAS-86-1.8.3.

Berchert, D. W., Bruse, M., Hage, W., van der Hoeven, J. G. T. and Hoppe, G., "Experiments on drag-reducing surfaces and their optimization with an adjustable geometry," *J. Fluid Mech.* Vol. 338, 1997, pp. 59–87.

Berger, T. W., Kim, J., Lee, C. and Lim, J., "Turbulent boundary layer control utilizing the Lorentz force," *Phys. Fluids* 12, 2000, pp. 631–649.

Bewley, T., Moin, P. and Temam, R., "DNS-based predictive control of turbulence: an optimal benchmark for feedback algorithms," *J. Fluid Mech*. Vol. 447, 2001, pp. 179–225.

Blackwelder, R. F., "The bursting process in turbulent boundary layers," *Lehigh Workshop on Coherent Structure in Turbulent Boundary Layers*. ed. C. R. Smith, D. E. Abbott, 1978, pp. 211-27.

Blackwelder, R. F. and Eekelmann, H., "Streamwise vortices associated with the bursting phenomenon," *J. Fluid Mech*. 94, 1979, pp. 577-594.

Bozinoski, R. and Davis, R. L., RA DES Procedure Applied to a Wall-Mounted Hump," *19th AIAA Computational Fluid Dynamics*, Jun. 2009, San Antonio, AIAA 2009-3667.

Bruun, H. H., "Hot-Wire Anemometry, principles and signal analysis", Oxford University Press, Oxford, UK, 1995.

Burgess, N. K. and Ligrani, P. M., "Effects of dimple depth on channel nusselt numbers and friction factors," *J. Heat Transfer*, Vol. 127, No. 8, 2005, pp. 839–847.

Cantwell, B. J., "Organized motions in turbulent flow," *Ann. Rev. Fluid Mech*. 74, 1981, pp. 251–267.

Chen, J., Leung, J. and Ko, N. W. M., "Drag Reduction in a Longitudinally Grooved Flow Channel," *Ind. Eng. Chem. Fundam*., Vol. 25 (4), 1986, pp. 741–745.

Chen Y., Chew, Y. T. and Khoo, B. C., "Enhancement of heat transfer in turbulent channel flow over dimpled surface," *Int. J. Heat Mass Trans*., Vol. 55, 2012, pp. 8100–8121.

Chen Y., Chew, Y. T. and Khoo, B. C., "Heat transfer and flow structure in turbulent channel flow over protrusions," *Int. J. Heat Mass Trans*., Vol. 66, 2013, pp. 177–191.

Chew, Y. T., Khoo B. C., and Li G. L., "An investigation of wall effects on hot-wire measurements using a bent sublayer probe," *Meas. Sci Tech.*, Vol. 9, 1998, pp. 67–85.

Chew, Y. T., Shi, S. X. and Khoo, B. C., "On the numerical near-wall corrections of single hot-wire measurements," *Int. J. Heat Fluid Flow*, 16, 1995, pp. 471–476.

Choi, H., Moin, P. and Kim, J., "Active turbulence control for drag reduction in wall-bounded flows," *J. Fluid Mech.* Vol. 262, 1994, pp. 75–110.

Choi, K.-S**., "**Near- wall structure of a turbulent boundary layer with riblets**," *J. Fluid Mech.,* Vol. 208, 1989, pp. 417–458.

Choi, K.–S., DeBisschop, J. R. and Clayton, B. R., "Turbulent boundary layer control by means of spanwise-wall oscillation," *AIAA J.* Vol. 36, No. 7, 1998, pp. 1157–1163.

Choi, J. I., Xu, C. X. and Sung, H. J., "Drag reduction by spanwise wall oscillation in wall-bounded turbulent flows," *AIAA J.* Vol. 40, No. 5, 2002, pp. 842–850.

Dean, B. and Bhushan, B., "Shark-skin surfaces for fluid drag reduction in turbulent flow: A review," *Phil. Trans. R.Soc.A* 368, 2010, pp. 4775–4806.

Den Toonder, J. M. J, Hulsen, M. A., Kuiken, G. D. C. and Nieuwstadt, F. T. M., "Drag reduction by polymer additives in a turbulent pipe flow: numerical and laboratory experiments," *J. Fluid Mech.* Vol. 337, 1997, pp. 193–231.

Du, Y and Karniadakis, G. E., "Suppressing wall turbulence via a transverse traveling wave," *Science* Vol. 288, 2000, pp. 1230–1234.

Du, Y. Q., Symeonidis, V. and Karniadakis, G. E., "Drag reduction in wall-bounded turbulence via a transverse travelling wave," *J Fluid Mech*, Vol. 457, 2002, pp. 1–34.

García-Mayoral, R. and Jiménez, J., "Drag reduction by riblets," *Phil. Trans. R. Soc. A* 369, 2012, pp. 1412–1427.

Graham, J. M. R., "The effect of a two-dimensional cascade of thin streamwise plates on homogeneous turbulence," *J. Fluid Mech.* Vol. 356, 1998, pp. 125–147.

Grüneberger, R. and Hage, W., "Drag characteristics of longitudinal and transverse riblets at low dimensionless spacings," *Exp. Fluids* Vol. 50, No. 2, 2011, pp. 363–373.

Guezennec, Y. G. and Choi, W. C., "Stochastic estimation of coherent structures in turbulent boundary layers," In *Proc. Zoran P. Zaric Memorial International Seminar on Near Wall Turbulence*, May 1988 (ed. Kline, S. J. and Afgan, N. H.), 1989, pp. 420–436.

Head, M. R. and Bandyopadhyay, P., "New aspects of turbulent boundary layer structure," *J. Fluid Mech*. Vol. 107, 1981, pp. 297–338.

Isaev, S. A., Kornev, N. V., Leontiev A. I. and Hassel E., "Influence of the Reynolds number and the spherical dimple depth on turbulent heat transfer and hydraulic loss in a narrow channel," International Journal of Heat and Mass Transfer, vol. 53, no. 1–3, 2010, pp. 178–197.

Isaev, S. A., Leont'ev, A. I. and Baranov, P. A., "Identification of self-organized vortexlike structures in numerically simulated turbulent flow of a viscous incompressible liquid streaming around a well on a plane," *Technical Physics Letters*, Vol. 26, No. 1, 2000, pp. 15–18.

Isaev, S. A., Leontiev, A. I., Kudryavtsev, N. A. and Pyshnyi, I. A., "The Effect of Rearrangement of the Vortex Structure on Heat Transfer under Conditions of Increasing Depth of a Spherical Dimple on the Wall of a Narrow Channel," *High Temp.,* Vol. 41 (2), 2003, pp. 229–232.

Itoh, M., Iguchi, R., Yokota, K., Akino, N., Hino, R. and Kubo, S., "Turbulent drag reduction by the seal fur surface," *Phys. Fluids* Vol. 18, 065102, 2006.

Iuso, G., Onorato, M., Spazzini, P. G. and Di Cicca, G. M., "Wall turbulence manipulation by large scale streamwise vortices," *J. Fluid Mech*. Vol. 473, 2002, pp. 23–58.

Jimenez, J. and Moin, P., "The minimal flow unit in near wall turbulence," *J. Fluid Mech*. Vol. 225, 1991, pp. 221–240.

Johansson, A., V. and Alfredsson, P., H., "On the structure of turbulent channel flow," *J. Fluid Mech.,* 122, 1982, pp. 295–314.

Jung, W. J., Mangiavacchi, N. and Akhavan, R., "Suppression of turbulence in wall-bounded flows by high frequency spanwise oscillations," *Phys. Fluids A* 4, 1992, pp. 1605–1607.

Karniadakis, G. E. and Choi, K.-S., "Mechanisms on transverse motions in turbulent wall flows**,"** *Annual Review of Fluid Mechanics* Vol. 35, 2003, pp. 45–62.

Kerho, M., "Active reduction of skin friction drag using low-speed streak control", AIAA paper, 2002-0271, 2002.

Khoo, B. C., Chew, Y. T. and Li G. L., "Effects of imperfect spatial resolution on turbulence measurements in the very near-wall viscous sublayer," *Exp. Fluids* Vol. 22, 1997, pp. 327–335.

Khoo, B. C., Chew, Y. T., Lim, C. P. and Teo, C. J., "Dynamic response of hot-wire anemometer, Part I: A marginally-elevated hot-wire probe for near-wall velocity measurements," *Meas. Sci. Technol*, Vol. 9 (5), 1998, pp. 751–763.

Kim, J., Moin, P. and Moser, R. D., "Turbulence statistics in fully developed channel flow at low Reynolds number," *J. Fluid Mech.* Vol. 177, 1987, pp. 133–166.

Kline, S. J., Reynolds, W. C., Schraub, F. A. and Runstadler, P. W., "The structure of turbulent boundary layers," *J. Fluid Mech.* Vol. 30, 1967, pp. 741–773.

Kovalenko, G. V., Terekhov, V. I. and Khalatov, A. A., "Flow regimes in a single dimple on the channel surface," *J. Applied Mech and Tech Phys*, Vol. 51, 2010, pp. 839–848.

Kwon, H. G., Hwang, S. D. and Cho, H., H., "Measurement of local heat/mass transfer coefficients on a dimple using naphthalene sublimation," Int. *J. Heat and Mass transfer, Applied Mech and Tech Phys*, Vol. 54, 2011, pp. 1071–1080.

Lee, T. and Mateescu, D., "Experimental and numerical investigation of 2D backward‐facing step flow," *J. of Fluids & Structures*, Vol. 12, 1998, pp. 703–716.

Li, F. –C., Kawaguchi, Y. and Hishida, K., "Investigation on the characteristics of turbulence transport for momentum and heat in a drag-reducing surfactant solution flow," *Phys. Fluids,* Vol. 16, No. 9, 2004, pp. 3281–3295.

Lien, K., Monty, J. P., Chong, M. S. and Ooi, A., "The entrance length for fully developed turbulent channel flow," *15th Australian Fluid Mechanics Conference*, The University of Sydney, Australia, 2004, pp. 356–363.

Lienhart, H., Breuer, M. and Köksoy, C., "Drag reduction by dimples? – A complementary experimental/numerical investigation," *Int' J. Heat and Fluid Flow*, Vol. 29, No. 3, 2008, pp. 783–791.

Ligrani, P. M., Burgess, N. K. and S. Y. Won, "Nusselt numbers and flow structure on and above a shallow dimpled surface within a channel including effects of inlet turbulence intensity level," *J. Turbomachinery* Vol. 127, no. 2, 2005, pp. 321–330.

Ligrani, P. M., Harrison, J. L., Mahmood, G. I., and Hill, M. L., "Flow structure due to dimple depression on a channel surface," *Phys. Fluids*, Vol. 13, No. 11, 2001, pp. 3442–3451.

Lim, J., Choi, H. and Kim, J., "Control of streamwise vortices with uniform magnetic fluxes," *Phys. Fluids*, 10, No. 8, 1998, pp. 1997–2005.

Lu, S. S. and Willmarth, W. W., "Measurements of the structure of the Reynolds stress in a turbulent boundary layer," *J. Fluid Mech.* Vol. 60, 1973, pp. 481–511.

Mahmood, G. I. and Ligrani, P. M., "Heat Transfer in a dimpled channel: combined influences of aspect ratio, temperature ratio, Reynolds number, and flow structure," *Int. J. heat Mass Transfer* Vol. 45, 2002, pp. 2011–2020.

Min, T., Yoo, J. Y., Choi, H. and Joseph, D. D., "Drag reduction by polymer additives in a turbulent channel flow," *J. Fluid Mech.*, Vol. 486, 2003, pp. 213–238.

Mitsudharmadi, H., Tay, C. M. J and Tsai, H. M., "Effect of rounded edged dimple arrays on the boundary layer Development," *J. Visualization*, Vol. 12, 2009, pp. 17–25.

Moser, R. D., Kim, J. and Mansour, N. N., "Direct numerical simulations of turbulent channel flow up to $Re_\tau = 590$," *Phys. Fluids* 11, 1999, pp. 943–945.

Mott, R. L., *Applied fluid mechanics, 4th* Ed., Merrill, New York, 1994.

Nikitin, N. V., Nicoud, F., Wasistho, B., Squires, K. D. and Spalart, P.R., "An approach to wall modeling in large-eddy simulations," *Phys Fluids*, Vol. 12, 2000, pp. 1629–1632.

Orlandi, P. and Fatica, M., "Direct simulations of turbulent flow in a pipe rotating about its axis," *J. Fluid Mech*. Vol. 343, 1997, pp. 43–72.

Orlandi, P. and Jimenez, J., "On the generation of turbulent wall friction," *Phys Fluids A* Vol. 6, 1994, pp. 634–641.

Pope, S. B., 2000 *Turbulent Flows* (Cambridge: Cambridge University Press)

Potter, M. C. and Foss, J. F., *Fluid Mechanics, 2nd* ed., Great Lakes Press, Inc., Michigan, 1983.

Quadrio, M. and Ricco, P., "Critical assessment of turbulent drag reduction through spanwise wall oscillations," *J. Fluid Mech*. Vol. 521, 2004, pp. 251–271.

Quadrio, M. and Sibilla, S., "Numerical simulation of turbulent flow in a pipe oscillating around its axis," *J. Fluid Mech*. Vol. 424, 2000, pp. 217–241.

Rathnasingham, R. and Breuer, K. S., "Active control of turbulent boundary layers," *J. Fluid Mech*. Vol. 495, 2003, pp. 209–233.

Reneaux, J., "Overview on drag reduction technologies for civil transport aircraft" European Congress on Computational Methods in Applied Sciences and Engineering (ECCOMAS), P. Neittaanmäki, T. Rossi, S. Korotov, E. Oñate, J. Périaux, and D. Knörzer (eds.) Jyväskylä, 24-28, July 2004.

Robinson, S. K., "Coherent motions in the turbulent boundary layer," *Ann. Rev. Fluid Mech*. 23, 1991, pp. 601–639.

Sagaut, P., *Large Eddy Simulation for Incompressible Flows* (Berlin: Springer) 2001.

Sahlin, A., Alfredsson H. and Johansson A. V., "Direct drag measurements for a flat plate with passive boundary layer manipulators," *Phys. Fluid* 29, 1986, pp. 696–700.

Sahlin, A., Johansson A. V., and Alfredsson H., "The possibility of drag reduction by outer layer manipulators in turbulent boundary layer," *Phys. Fluid* 31, 1988, pp. 2814–2823.

Savill, A., M. and Mumford, J., C., "Manipulation of Turbulent Boundary Layers by Outer Layer Devices : Skin-Friction and Flow Visualization Results," *J. Fluid Mech*. Vol. 191, 1988, pp. 389–418.

Schoppa, W. and Hussain, F., "A large-scale control strategy for drag reduction in turbulent boundary layers," *Phys. Fluids* 10, 1998, pp. 1049–1051.

Shur, M., Spalart, P., Strelets, M. and Travin, A., "Detached eddy simulation of an airfoil at high angle of attack," In: *Fourth International Symposium on Engineering Turbulence Modelling and Experiments*, May 24–26, 1999, Elsevier, Corsica, pp. 669–678.

Song, S. and Eaton, J. K., "Reynolds number effects on a turbulent boundary layer with separation, reattachment, and recovery," *Exp. Fluids*, Vol. 36, 2004, pp. 246–258.

Spalart, P. R., Jou, W. H., Strelets, M. and Allmaras S. R., "Comments on the feasibility of LES for wings and on a hybrid RANS/LES approach," In *Advances in DNS/LES*, ed., Liu. C. and Liu, Z., Columbus, OH, Greyden, 1997, pp. 137–148.

Squires, K. D., "Detached-eddy simulation: current status and perspectives," In *Direct and Large-Eddy Simulation V*, ed., Friedrich, R., Geurts, B. J., Metais, O., Kluwer Academic Publishers, Dordrecht, 2004, pp. 465–480.

Strelets, M., "Detached eddy simulation of massively separated flows," AIAA Paper 2001-0879, 2001.

Sumer, B. M. and Fredsøe, J., *Hydrodynamics around Cylindrical Structures*, World Scientific Publishing, London, 1997.

Tay, C. M., "Determining the Effect of Dimples on Drag in a Turbulent Channel Flow," *49th AIAA Aerospace Sciences Meeting and Exhibit*, Jan. 2011, Orlando, AIAA paper 2011–0682.

Tay, C. M., Chew, Y. T. and Khoo, B. C., "Development of flow structures over dimples," *Exp. Thermal Fluid Sci.*, Vol. 52, 2014, pp. 278–287.

Tay, C. M. J., Khoo, B. C. and Chew, Y. T., "Determination of hot-wire position from a solid wall in an opaque channel," *Meas. Science and Tech.*, 23, 2012, pp. 085305-1–085305-8.

Tu, S., Aliabadi, S., Patel, R. and Watts, M., "An implementation of the Spalart–Allmaras DES model in an implicit unstructured hybrid finite volume/element solver for incompressible turbulent flow," I*nt. J. Numerical Methods Fluids*, Vol. 59 (9), 2009, pp. 1051–1062.

Turan, O. and Azad, D. S., "Wall effects on the hot-wire signal without flow", *Journal of Physics E: Scientific Instruments,* Vol. 20, 1987, pp. 1278-1280.

Veldhuis, L. L. M. and Vervoort, E., "Drag effect of a dented surface in a turbulent flow," *27th AIAA Applied Aerodynamics Conference*, June 2009, San Antonio, Texas, AIAA paper 2009–3950.

Vlachogiannis, M. and Hanratty, T. J., "Influence of wavy structured surfaces and large scale polymer structures on drag reduction," *Exp. Fluids*, Vol. 36, 2004, pp. 685–700.

Wallace, J. M., "On the structure of bounded turbulent shear flow: a personal view," In *Developments in Theoretical and Applied Mechanics, XI*, ed. Chung, T. J. and Karr, G. R., University of Alabama, Huntsville, Alabama, 1982, pp. 509–521.

Wallace, J. M., Eckelmann, H. and Brodkey, R. S., "The wall region in turbulent shear flow," *J. Fluid Mech.* Vol. 54, 1972, pp. 39–48.

Walsh, M. J., "Drag characteristics of V-groove and transverse curvature riblets," In *Viscous Drag Reduction*, ed. GR Hough, 1980, pp. 168–184, AIAA, Washington, DC.

Walsh, M. J., "Turbulent boundary layer drag reduction using riblets," *AIAA Pap. 82-0169*, 1982, AIAA, Reston, VA.

Walsh, M. J., "Riblets," In *Viscous Drag Reduction in Boundary Layers, Progress in Astronautics and Aeronautics*, ed. Bushnell, D. and Hefner, J., Vol. 123, AIAA Reston, VA, 1990, pp. 203–262

Wang, Z. J., Chi, X. K., Shih, T. and Bons, J., "Direct Simulation of Surface Roughness Effects with RANS and DES Approaches in Viscous Adaptive Cartesian Grids," *AIAA Flow Conference*, Jun. 2004, Portland, AIAA paper 2004-2420.

Wang, Z. Y., Yeo, K. S. and Khoo, B. C., "DNS of low Reynolds number turbulent flows in dimpled channels" *J. Turbulence*, Vol. 7, 2006, pp. 1–31.

Willmarth, W. W. and Lu, S. S., "Structure of the Reynolds stress near the wall," *J. Fluid Mech.* Vol. 55, 1972, pp. 65–92.

Won, S. Y., Zhang, Q. and Ligrani, P. M., "Comparisons of flow structure above dimpled surfaces with different dimple depths in a channel," *Phys. Fluids*, Vol. 17, 045105, 2005.

Wu, J. & Yeo, K.S., "Flow past Dimpled Surfaces; Part 2: Computational Study for Turbulent Flow in Dimpled Channels," *Annual report on the NUS-Airbus collaboration under project R-265-000-272-597*, December 2011.

Zhang, W. G., Zhou, Y. and Bai, H. L., "Turbulent Drag Reduction Using an Array of Piezo-ceramic Actuators," In: *the 17th Australasian Fluid Mechanics Conference*, Auckland, New Zealand, 2010. Paper No. 64

Zhou, J., Adrian, R. J., Balachandar, S. and Kendall, T. M., "Mechanisms for generating coherent packets of hairpin vortices in channel flow," *J. Fluid Mech.* Vol. 387, 1999, pp. 353–396.

# Appendix A

## Comparison of DES with hot-wire measurements in dimpled channel

A comparison between of the DES results and the hot-wire velocity measurements was carried as a validation of the DES method. The velocity predictions from the DES were compared with the hot-wire measurements carried out at $y = 0.3$mm, 1mm and 5mm for both Case 2 and 3 dimples at $Re = 10,000$ and $15,000$. These measurement heights correspond to $y/h = 0.015$, $0.05$ and $0.25$ respectively, with $y$ measured from the flat regions between the dimples. The velocity contours are normalized by their centerline values and shown in Figure 53 to Figure 60. Table 5 lists the parameters for each of these figures. The complete list of figures is presented here to provide a clearer picture of the similarities between the experimental measurements and the predicted DES results.

**Table 5. List of figures presented with their associated parameters**

| Figure No. | $d/D$ | $Re$ | Contour values | $y/h$ |
|---|---|---|---|---|
| Figure 53a | | | | 0.015 |
| Figure 53b | | | $U/U_{centerline}$ | 0.05 |
| Figure 53c | | 10,000 | | 0.25 |
| Figure 54a | | | | 0.015 |
| Figure 54b | | | $u_{rms}/u_{rms,centerline}$ | 0.05 |
| Figure 54c | 5% | | | 0.25 |
| Figure 55a | | | | 0.015 |
| Figure 55b | | | $U/U_{centerline}$ | 0.05 |
| Figure 55c | | 15,000 | | 0.25 |
| Figure 56a | | | | 0.015 |
| Figure 56b | | | $u_{rms}/u_{rms,centerline}$ | 0.05 |
| Figure 56c | | | | 0.25 |
| Figure 57a | | | | 0.015 |
| Figure 57b | | | $U/U_{centerline}$ | 0.05 |
| Figure 57c | | 10,000 | | 0.25 |
| Figure 58a | | | | 0.015 |
| Figure 58b | | | $u_{rms}/u_{rms,centerline}$ | 0.05 |
| Figure 58c | 1.5% | | | 0.25 |
| Figure 59a | | | | 0.015 |
| Figure 59b | | | $U/U_{centerline}$ | 0.05 |
| Figure 59c | | 15,000 | | 0.25 |
| Figure 60a | | | | 0.015 |
| Figure 60b | | | $u_{rms}/u_{rms,centerline}$ | 0.05 |
| Figure 60c | | | | 0.25 |

**Figure 53a.** *d/D*=5% *Re*=10,000, *U*, *y/h*=0.015. Flow is from top to bottom.
Left: DES. Right: hot-wire. Dashed lines denote position of dimples.
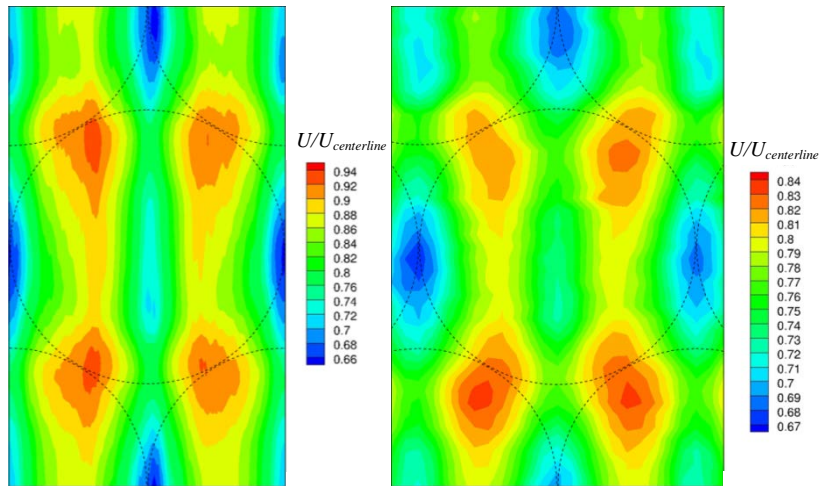


**Figure 53b.** *d/D*=5% *Re*=10,000, *U*, *y/h*=0.05. Flow is from top to bottom.
Left: DES. Right: hot-wire. Dashed lines denote position of dimples.
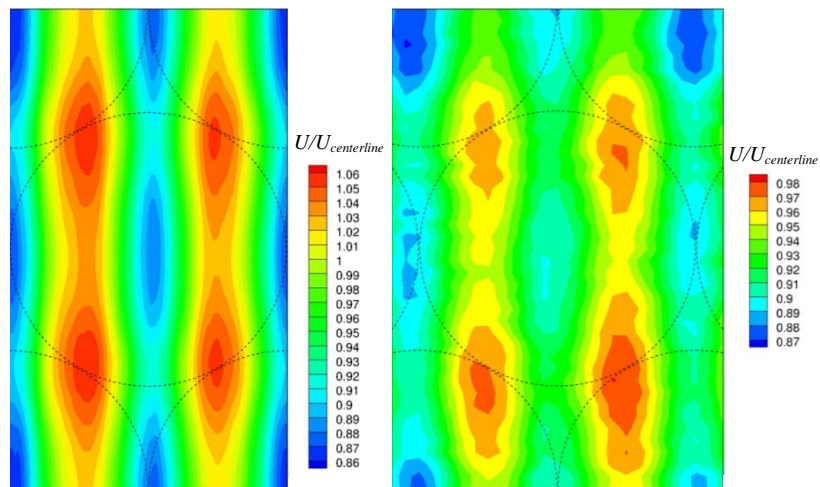


**Figure 53c.** *d/D*=5% *Re*=10,000, *U*, *y/h*=0.25. Flow is from top to bottom.
Left: DES. Right: hot-wire. Dashed lines denote position of dimples.
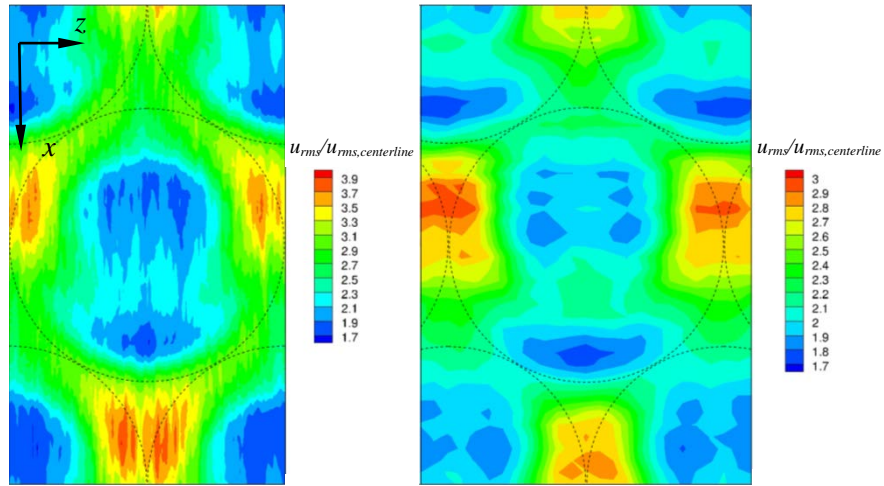
**Figure 54a.** *d/D*=5% *Re*=10,000, *u_rms*, *y/h*=0.015. Flow is from top to bottom.
Left: DES. Right: hot-wire. Dashed lines denote position of dimples.
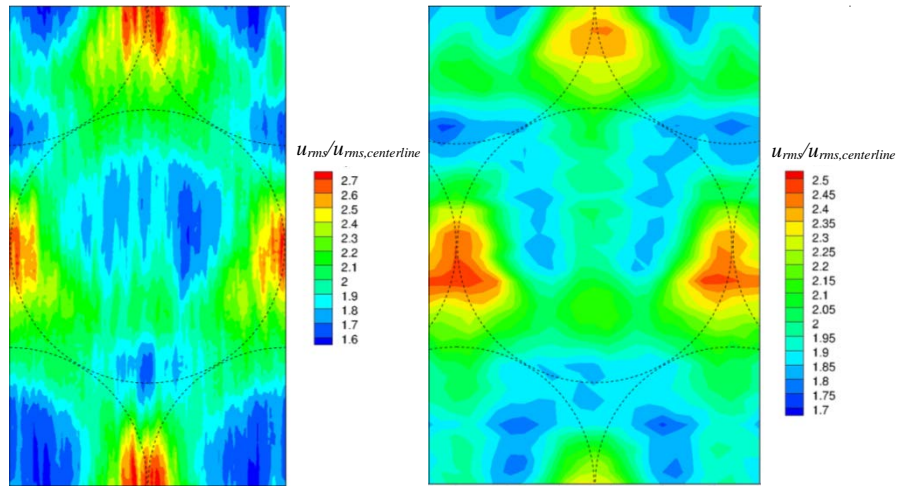


**Figure 54b.** *d/D*=5% *Re*=10,000, *u_rms*, *y/h*=0.05. Flow is from top to bottom.
Left: DES. Right: hot-wire. Dashed lines denote position of dimples.
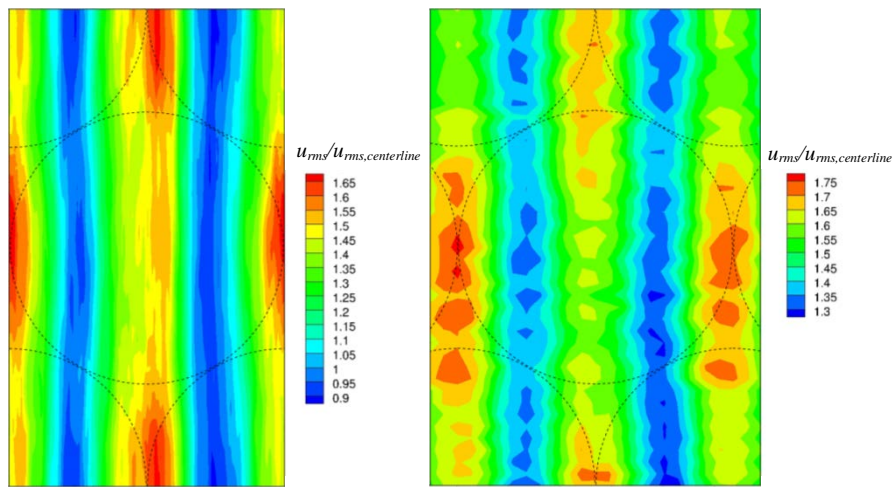


**Figure 54c.** *d/D*=5% *Re*=10,000, *u_rms*, *y/h*=0.25. Flow is from top to bottom.
Left: DES. Right: hot-wire. Dashed lines denote position of dimples.

130
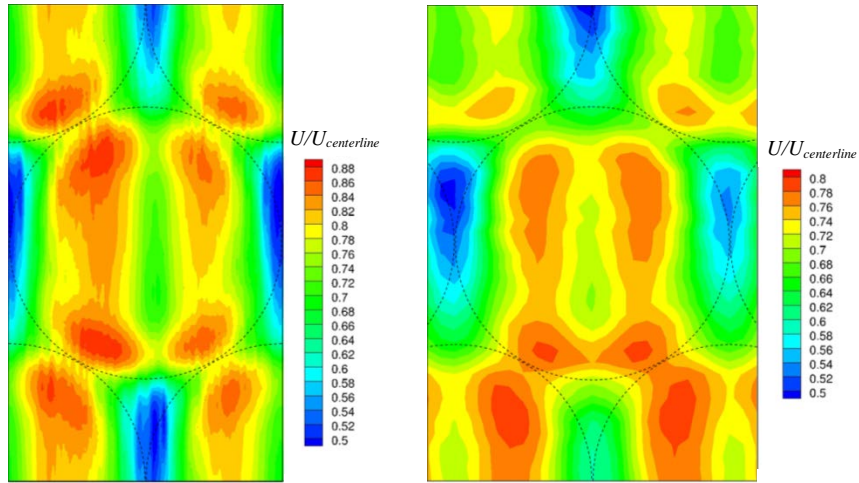
**Figure 55a.** *d/D*=5% *Re*=15,000, *U*, *y/h*=0.015. Flow is from top to bottom.
**Left: DES. Right: hot-wire. Dashed lines denote position of dimples.**
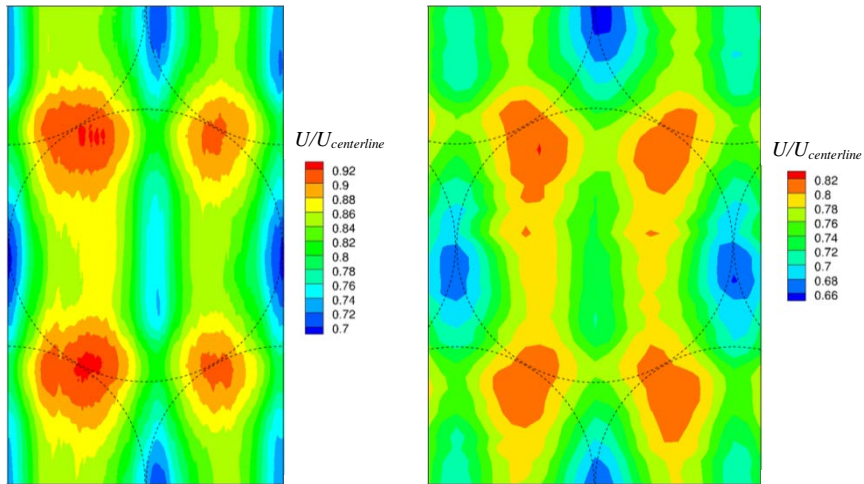


**Figure 55b.** *d/D*=5% *Re*=15,000, *U*, *y/h*=0.05. Flow is from top to bottom.
**Left: DES. Right: hot-wire. Dashed lines denote position of dimples.**
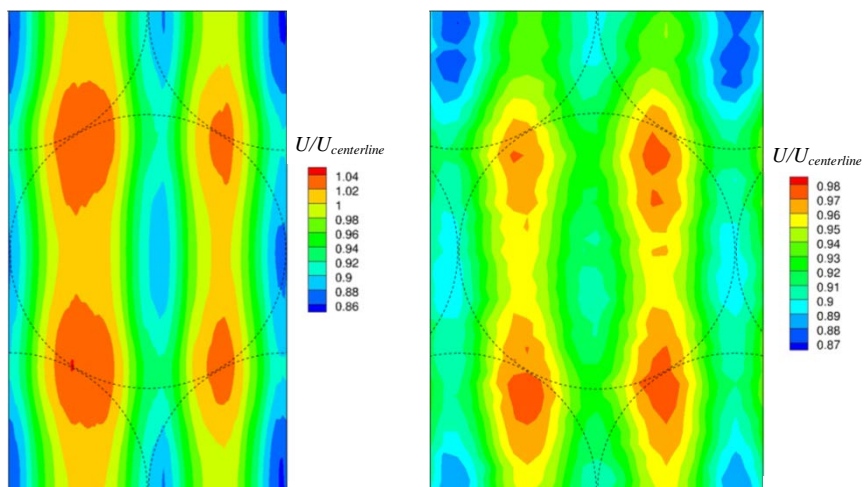


**Figure 55c.** *d/D*=5% *Re*=15,000, *U*, *y/h*=0.25. Flow is from top to bottom.
**Left: DES. Right: hot-wire. Dashed lines denote position of dimples.**

131
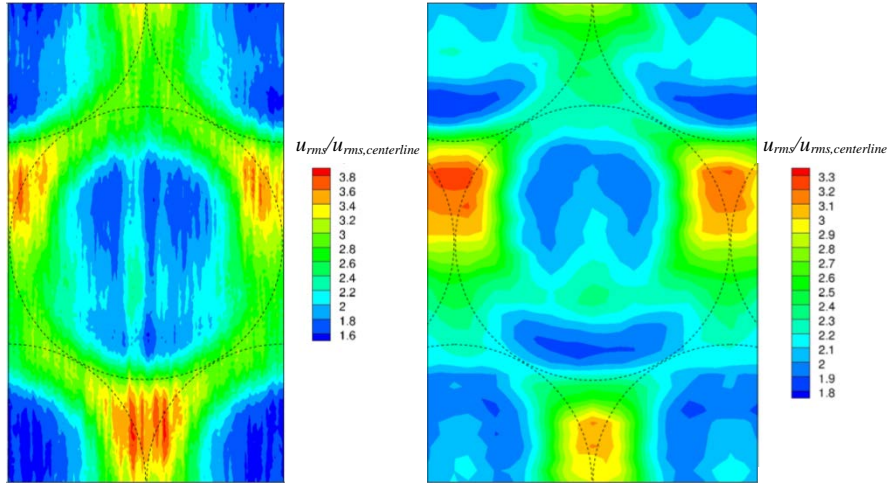
**Figure 56a.** *d/D*=5% *Re*=15,000, *u_rms*, *y/h*=0.015. Flow is from top to bottom.
**Left: DES. Right: hot-wire. Dashed lines denote position of dimples.**
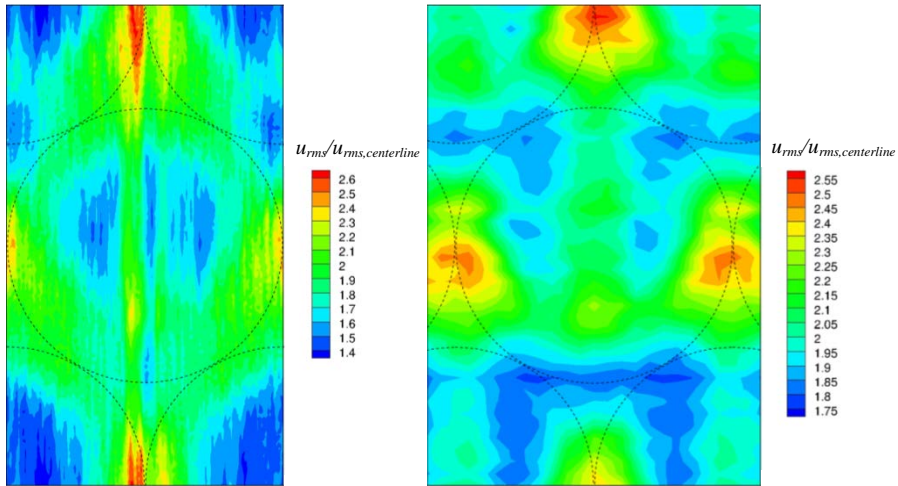


**Figure 56b.** *d/D*=5% *Re*=15,000, *u_rms*, *y/h*=0.05. Flow is from top to bottom.
**Left: DES. Right: hot-wire. Dashed lines denote position of dimples.**
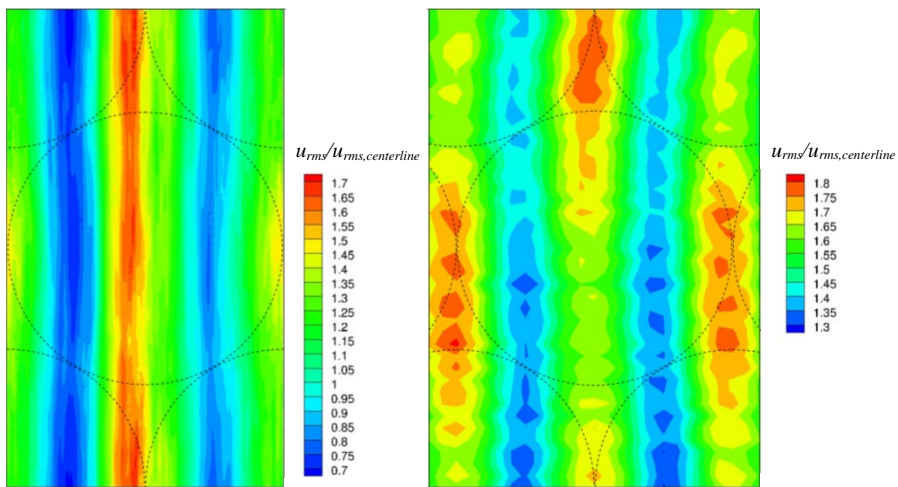


**Figure 56c.** *d/D*=5% *Re*=15,000, *u_rms*, *y/h*=0.25. Flow is from top to bottom.
**Left: DES. Right: hot-wire. Dashed lines denote position of dimples.**

132
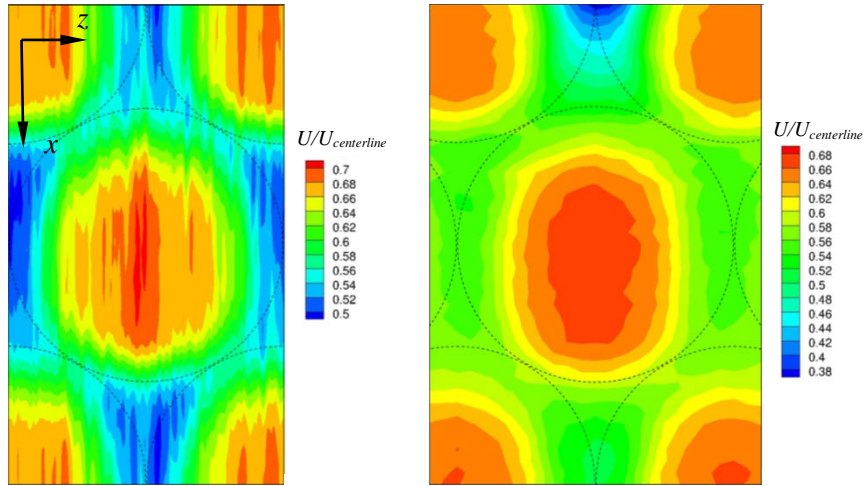
**Figure 57a.** *d/D*=1.5% *Re*=10,000, *U*, *y/h*=0.015. Flow is from top to bottom.
**Left: DES. Right: hot-wire. Dashed lines denote position of dimples.**
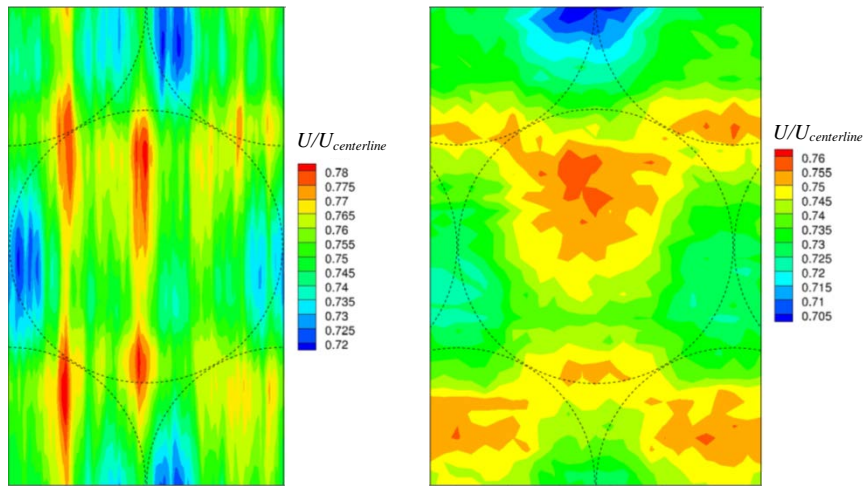


**Figure 57b.** *d/D*=1.5% *Re*=10,000, *U*, *y/h*=0.05. Flow is from top to bottom.
**Left: DES. Right: hot-wire. Dashed lines denote position of dimples.**
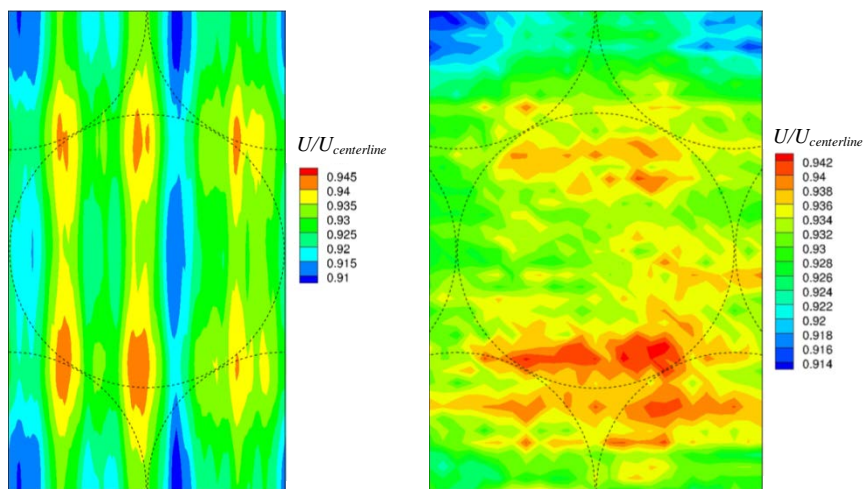


**Figure 57c.** *d/D*=1.5% *Re*=10,000, *U*, *y/h*=0.25. Flow is from top to bottom.
**Left: DES. Right: hot-wire. Dashed lines denote position of dimples.**

133
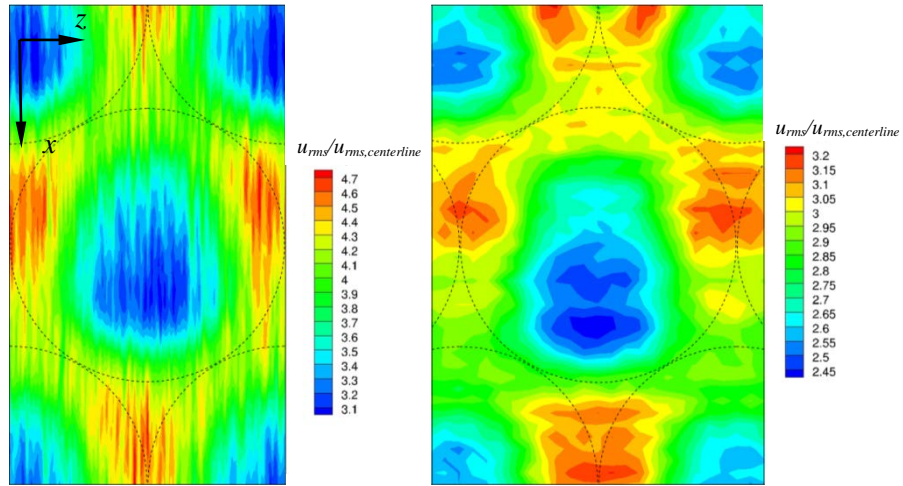
**Figure 58a.** *d/D*=1.5% *Re*=10,000, *u*$_{rms}$, *y/h*=0.015. Flow is from top to bottom.
**Left: DES. Right: hot-wire. Dashed lines denote position of dimples.**
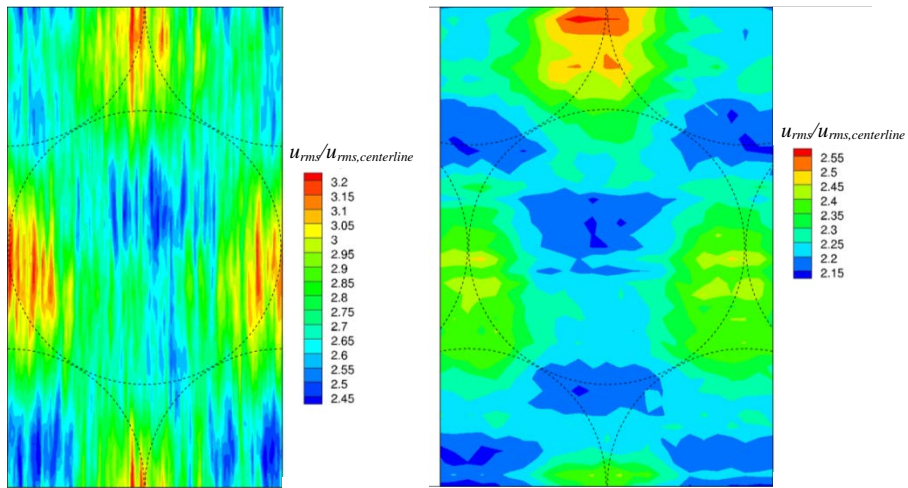


**Figure 58b.** *d/D*=1.5% *Re*=10,000, *u*$_{rms}$, *y/h*=0.05. Flow is from top to bottom.
**Left: DES. Right: hot-wire. Dashed lines denote position of dimples.**
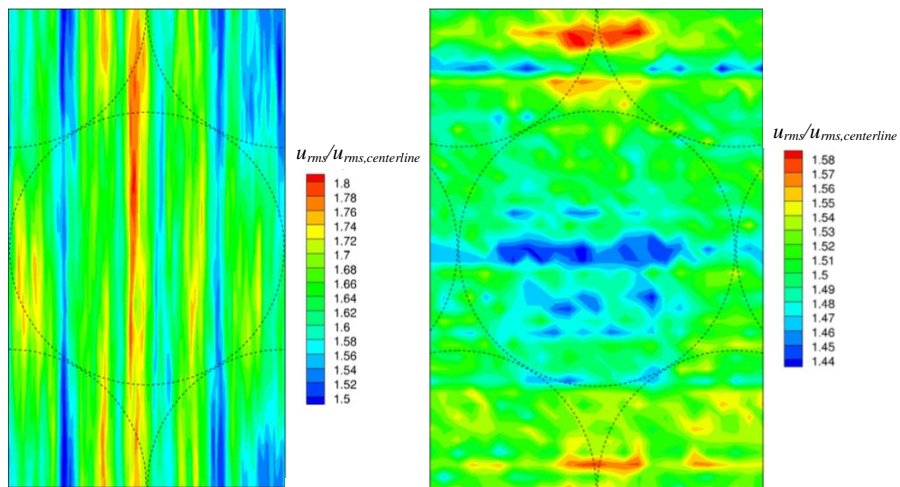


**Figure 58c.** *d/D*=1.5% *Re*=10,000, *u*$_{rms}$, *y/h*=0.25. Flow is from top to bottom.
**Left: DES. Right: hot-wire. Dashed lines denote position of dimples.**

134
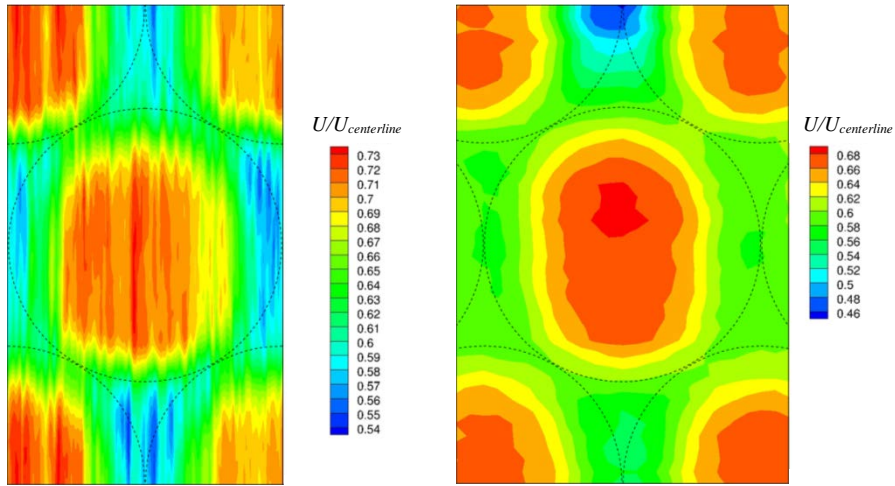
**Figure 59a.** *d/D*=1.5% *Re*=15,000, *U*, *y/h*=0.015. Flow is from top to bottom.
**Left: DES. Right: hot-wire. Dashed lines denote position of dimples.**
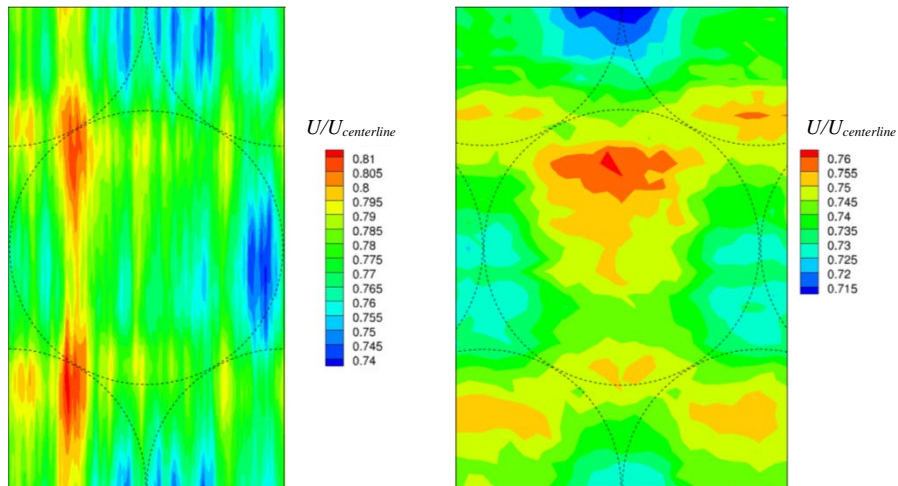


**Figure 59b.** *d/D*=1.5% *Re*=15,000, *U*, *y/h*=0.05. Flow is from top to bottom.
**Left: DES. Right: hot-wire. Dashed lines denote position of dimples.**
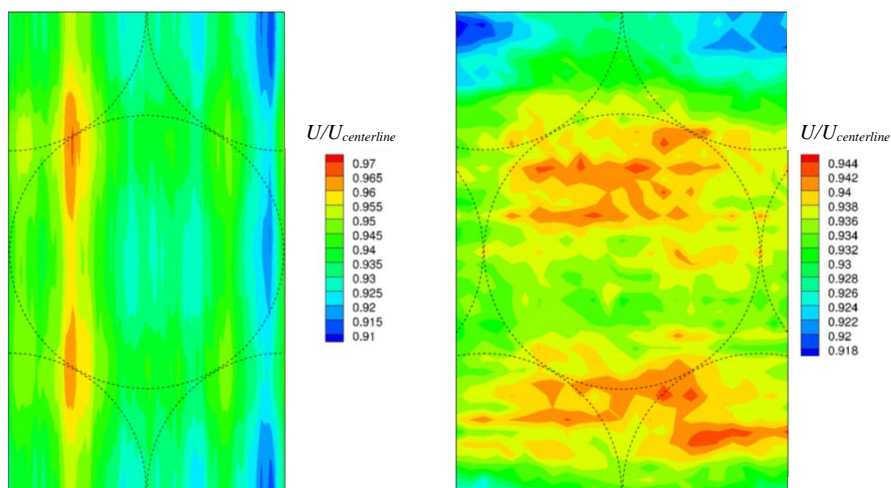


**Figure 59c.** *d/D*=1.5% *Re*=15,000, *U*, *y/h*=0.25. Flow is from top to bottom.
**Left: DES. Right: hot-wire. Dashed lines denote position of dimples.**

135
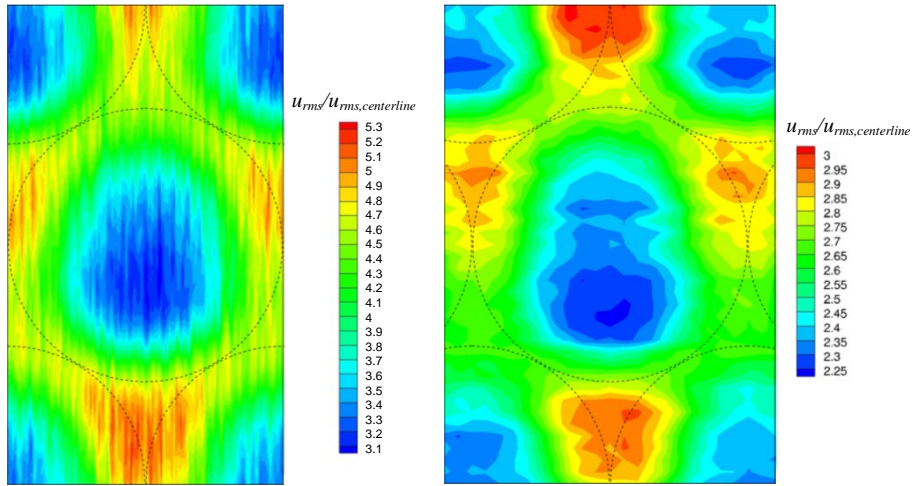
**Figure 60a.** *d/D*=1.5% *Re*=15,000, $u_{rms}$, *y/h*=0.015. Flow is from top to bottom.
**Left: DES. Right: hot-wire. Dashed lines denote position of dimples.**
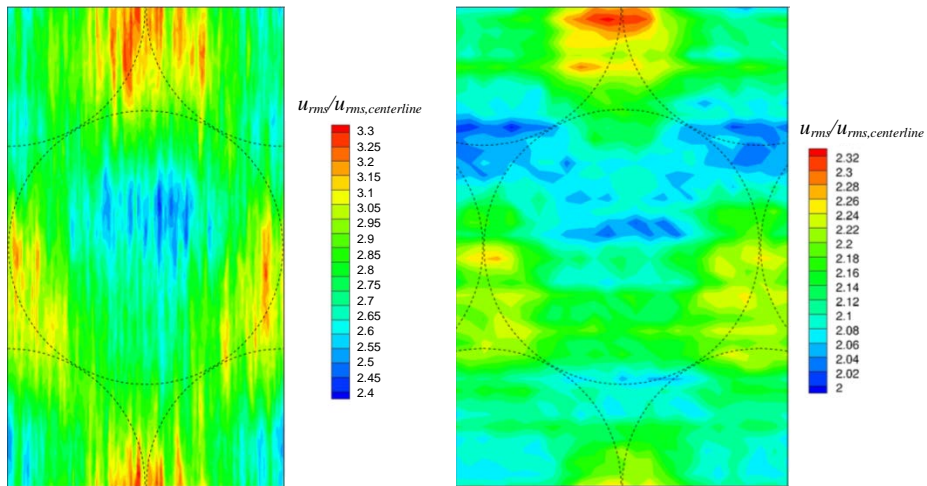


**Figure 60b.** *d/D*=1.5% *Re*=15,000, $u_{rms}$, *y/h*=0.05. Flow is from top to bottom.
**Left: DES. Right: hot-wire. Dashed lines denote position of dimples.**
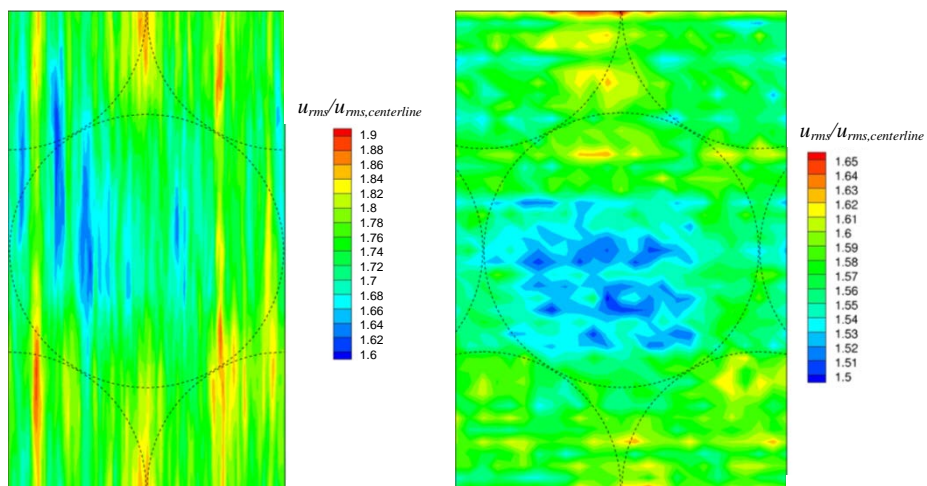


**Figure 60c.** *d/D*=1.5% *Re*=15,000, $u_{rms}$, *y/h*=0.25. Flow is from top to bottom.
**Left: DES. Right: hot-wire. Dashed lines denote position of dimples.**

136

The agreement between the hot-wire measurements and the DES is generally good, particularly for the deeper Case 2 dimples with $d/D = 5\%$ (Figure 53 to Figure 56). Both the observed flow patterns and the range of the values of the normalized contours agree well for these deeper Case 2 dimples. Some asymmetry of the flow about the centerline can be seen in the DES for Case 2 ($d/D = 5\%$) at $Re = 15,000$, though this is small and the general flow pattern is still clearly reproduced accurately.

While the agreement between the DES and the hot-wire measurements for the deeper Case 2 dimples ($d/D = 5\%$) is relatively good, the agreement between the hot-wire measurements and the DES for the shallow Case 3 dimples with $d/D = 1.5\%$ (Figure 57 to Figure 60) is generally slightly poorer when compared to the deeper Case 2 dimples. The main reason for this is that with these very shallow dimples with $d/D = 1.5\%$, the resultant flow manipulation by the dimples is relatively weak. The shallow dimples cause only small variations to the flow, which are not as easily picked up by the hot-wire measurements. Comparing the hot-wire measurements in Figure 53b with those of Figure 57b, both measured at the same Reynolds number and at the same height, but for the two different dimple depths, it is observed that the ratio between the maximum and minimum contours values in Figure 53b is about 125% compared to just 108% for the shallower Case 3 dimples in Figure 57b. The best agreement between the hot-wire measurements and the DES for these shallow Case 3 dimples with $d/D = 1.5\%$ are those obtained nearest the wall ($y/h = 0.015$) where the effect of the dimples on the flow is the greatest and the variation in the maximum and minimum contour values are correspondingly greatest. As the variation in the contour values decrease further up the wall, the measurement of any flow patterns higher up the wall at $y/h = 0.25$ becomes increasingly difficult. These small variations due to the dimples are also of the same order as the small variations that naturally occur as the flow passes the dimples. The result is that apparent flow asymmetry is observed

137

in the DES if an unusually long averaging time is not used. Again this issue manifests itself most obviously higher up above the dimples where the variation in the velocity contours is smallest.

Another observation for these shallow dimples is that the normalized contour values for $u_{rms}$ is significantly higher in the DES compared to the hot-wire measurements. One possible reason for this is due to the finite spatial resolution of the hot-wire probe used. This results in the measured $u_{rms}$ being lower than the actual $u_{rms}$ in the flow. Since the hot-wire length is not changed for the different runs at different Reynolds numbers, one would expect that due to the finite spatial resolution of the hot-wire probe used, the discrepancy of the $u_{rms}$ measured by the hot-wire is greater as the Reynolds number increases since the hot-wire length in terms of $y^+$ would increase as the Reynolds number increases. This is confirmed by the difference in the DES values being greater than those measured by the hot-wire as the Reynolds number increases (cf. Figure 58 and Figure 60). The mean contour values however are similar for both the DES and the hot-wire measurements since spatial resolution of a hot-wire probe is less of an issue when mean velocity contours are concerned for such relatively large scale geometries (Figure 57 and Figure 59). Despite these minor differences traced to the small variations of the flow and the finite spatial resolution of the hot-wire probe used, the DES is still able to reproduce the general flow patterns as observed in the hot-wire measurements for the entire flow field in the simulated domain.

# Appendix B

## Detailed turbulent kinetic energy budget with dimples

The energy budgets shown and discussed in section 4.8 is shown here in greater detail. Each figure contains plots of each term of the budget according to equation (40) for each dimple geometry. The figures for the turbulent kinetic budget terms here are organized according to Table 6.

**Table 6. List of figures for turbulent kinetic energy budget terms**

| Figure No. | Case | $d/D$ | Reynolds number | Profile positions |
|:---:|:---:|:---:|:---:|:---:|
| 61 | | | 3,300 | $x/D=0, z/D = 0$ |
| 62 | | | 10,000 | $x/D=0.52, z/D = 0$ |
| 63 | | | 15,000 | $x/D=-0.52, z/D = 0$ |
| 64 | | | 3,300 | $x/D=0, z/D = 0$ |
| 65 | 2 | 5% | 10,000 | $x/D=0, z/D = 0.18$ |
| 66 | | | 15,000 | $x/D=0, z/D = 0.48$ |
| 67 | | | 3,300 | $x/D=0, z/D = 0$ |
| 68 | | | 10,000 | $x/D=0.4, z/D = 0.18$ |
| 69 | | | 15,000 | $x/D=-0.4, z/D = 0.18$ |
| 70 | | | 3,300 | $x/D=0, z/D = 0$ |
| 71 | | | 10,000 | $x/D=0.52, z/D = 0$ |
| 72 | | | 15,000 | $x/D=-0.52, z/D = 0$ |
| 73 | | | 3,300 | $x/D=0, z/D = 0$ |
| 74 | 3 | 1.5% | 10,000 | $x/D=0, z/D = 0.18$ |
| 75 | | | 15,000 | $x/D=0, z/D = 0.48$ |
| 76 | | | 3,300 | $x/D=0, z/D = 0$ |
| 77 | | | 10,000 | $x/D=0.4, z/D = 0.18$ |
| 78 | | | 15,000 | $x/D=-0.4, z/D = 0.18$ |
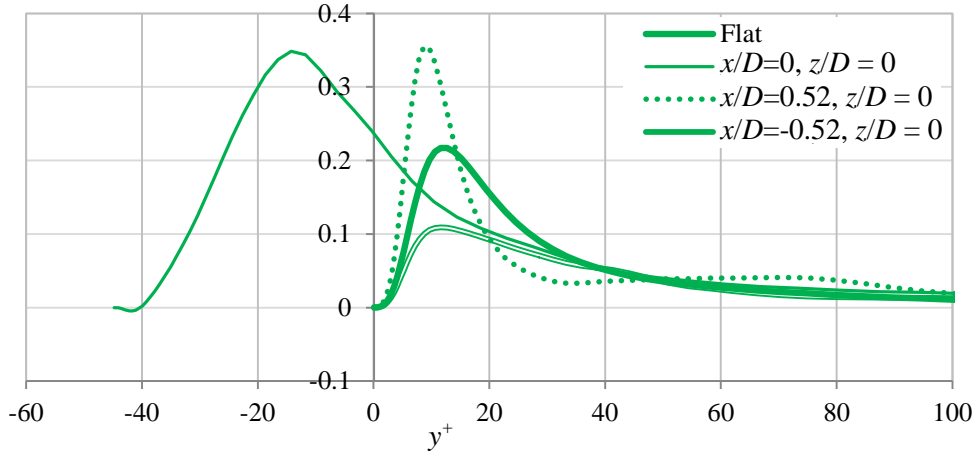
**Figure 61a. Profiles for the production term in the turbulent kinetic energy budget for Case 2 at** $Re = 3,300$, $\Delta_{drag}=+3.5\%$.
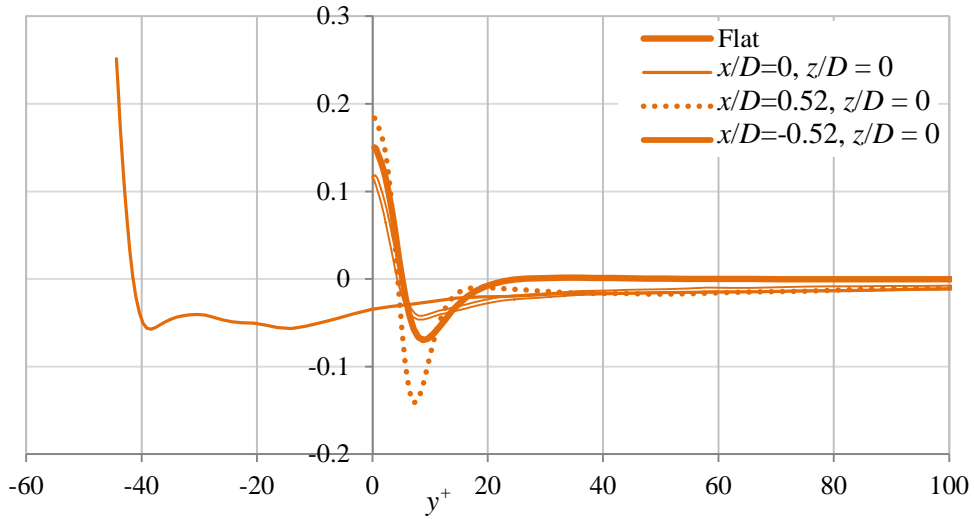


**Figure 61b. Profiles for the viscous diffusion term in the turbulent kinetic energy budget for Case 2 at** $Re = 3,300$, $\Delta_{drag}=+3.5\%$.
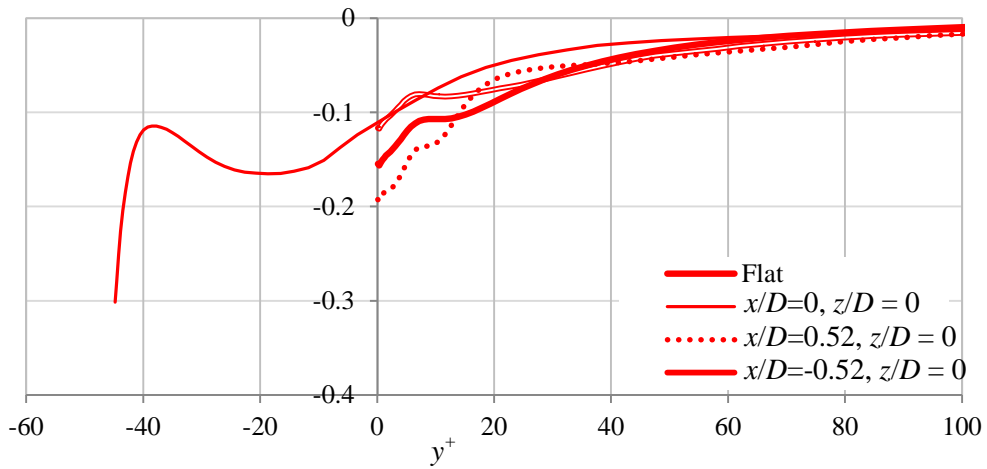


**Figure 61c. Profiles for the dissipation term in the turbulent kinetic energy budget for Case 2 at** $Re = 3,300$, $\Delta_{drag}=+3.5\%$.
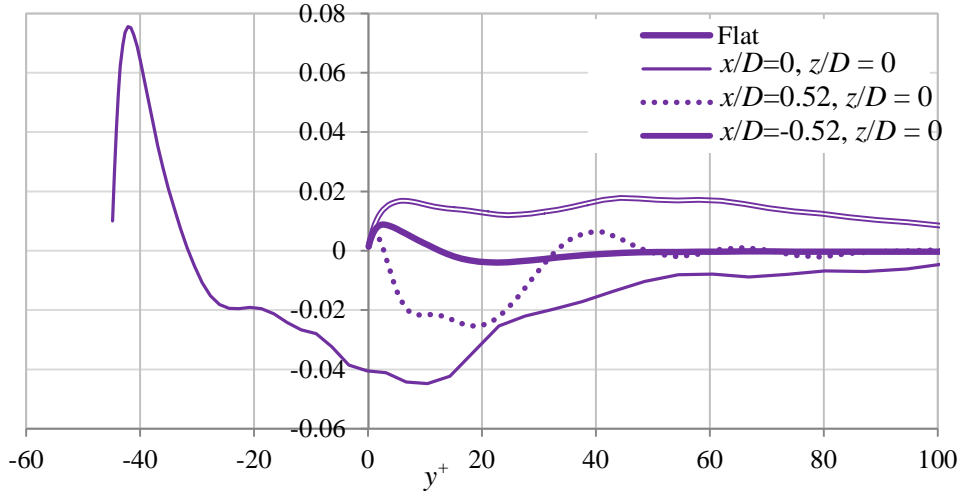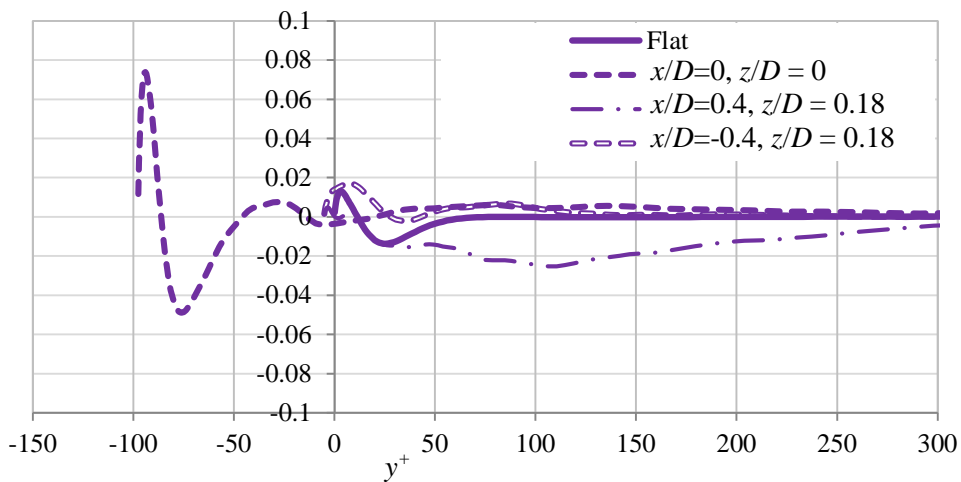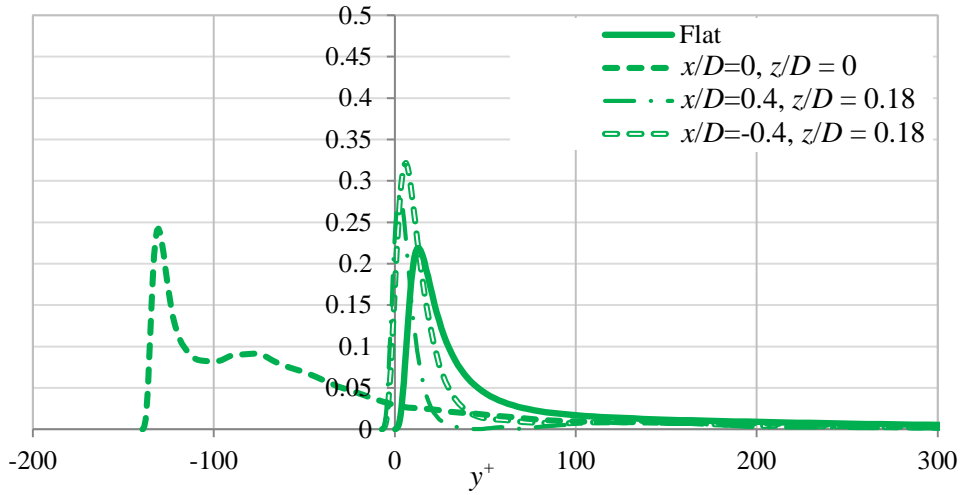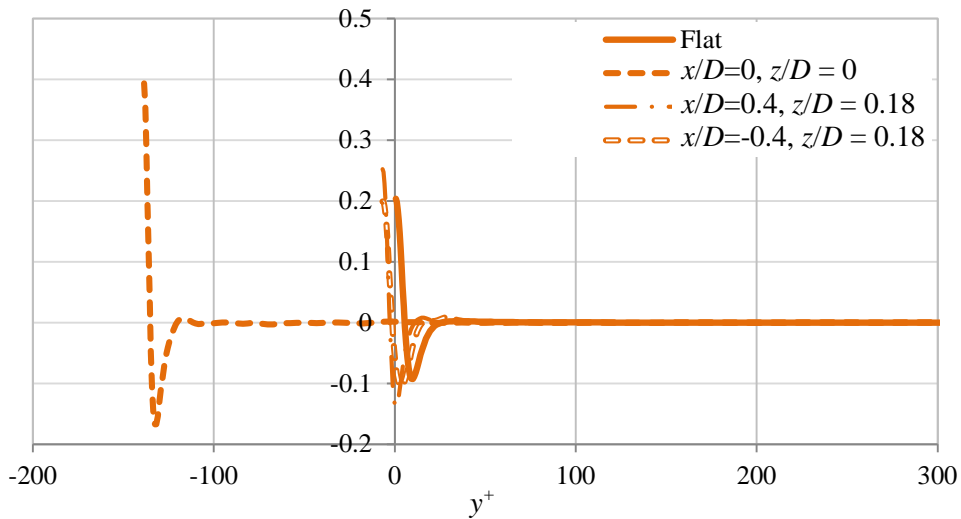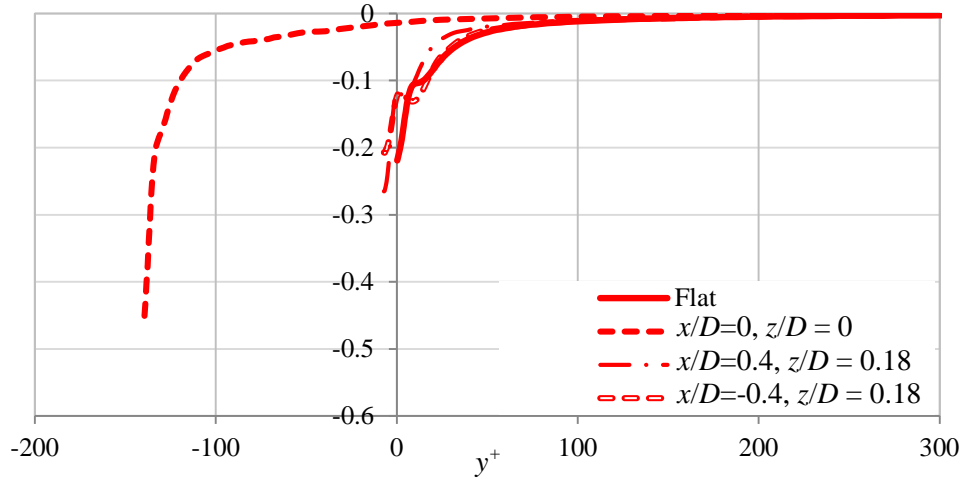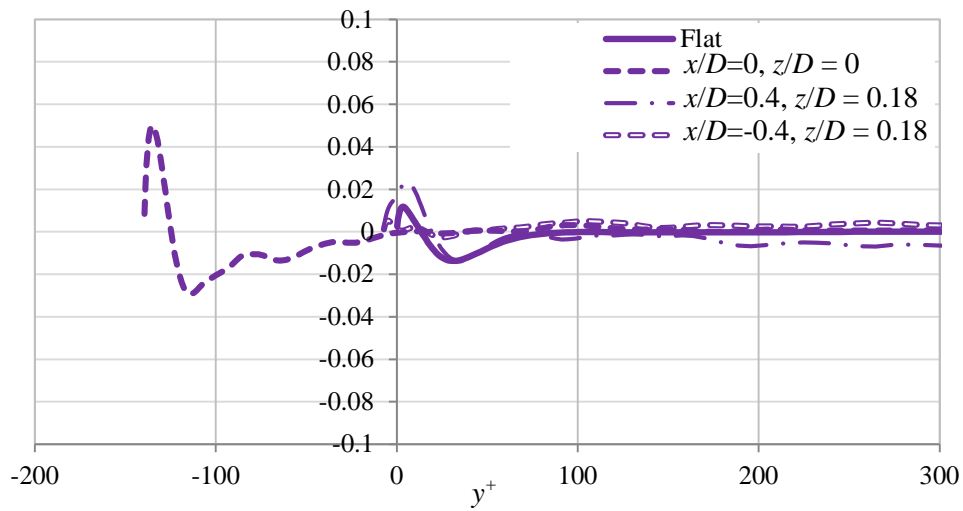
**Figure 61d. Profiles for the velocity pressure gradient term in the turbulent kinetic energy budget for Case 2 at *Re* = 3,300, Δ*drag*=+3.5%.**
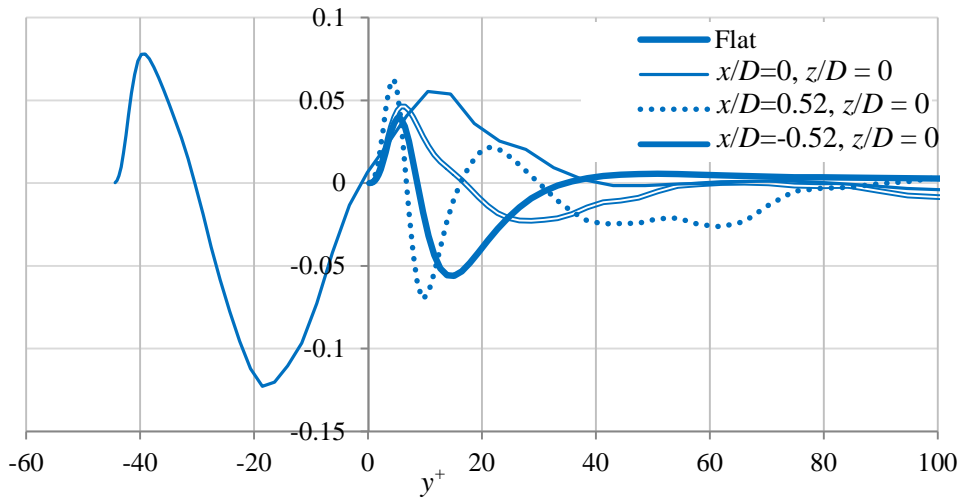


**Figure 61e. Profiles for the turbulent transport term in the turbulent kinetic energy budget for Case 2 at *Re* = 3,300, Δ*drag*=+3.5%.**
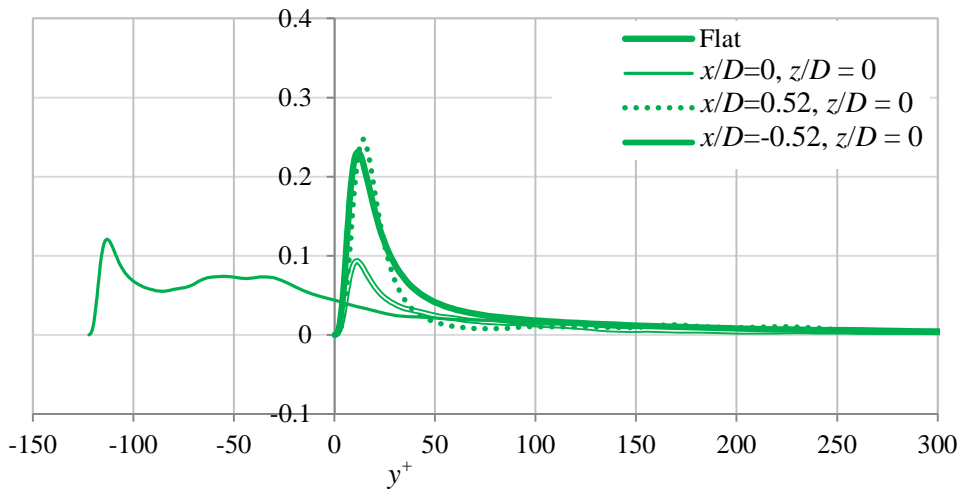


**Figure 62a. Profiles for the production term in the turbulent kinetic energy budget for Case 2 at *Re* = 10,000, Δ*drag*=+1%.**
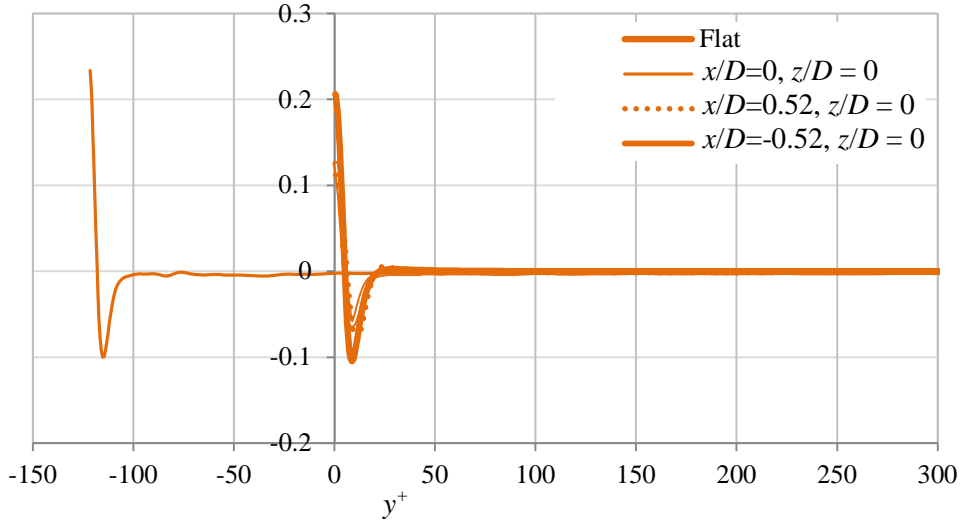
**Figure 62b. Profiles for the viscous diffusion term in the turbulent kinetic energy budget for Case 2 at *Re* = 10,000, $\Delta_{drag}$=+1%.**
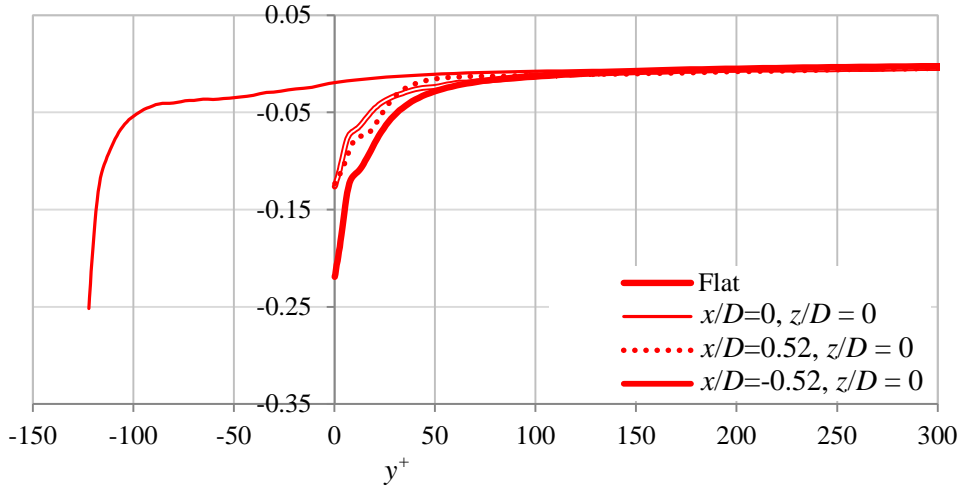


**Figure 62c. Profiles for the dissipation term in the turbulent kinetic energy budget for Case 2 at *Re* = 10,000, $\Delta_{drag}$=+1%.**
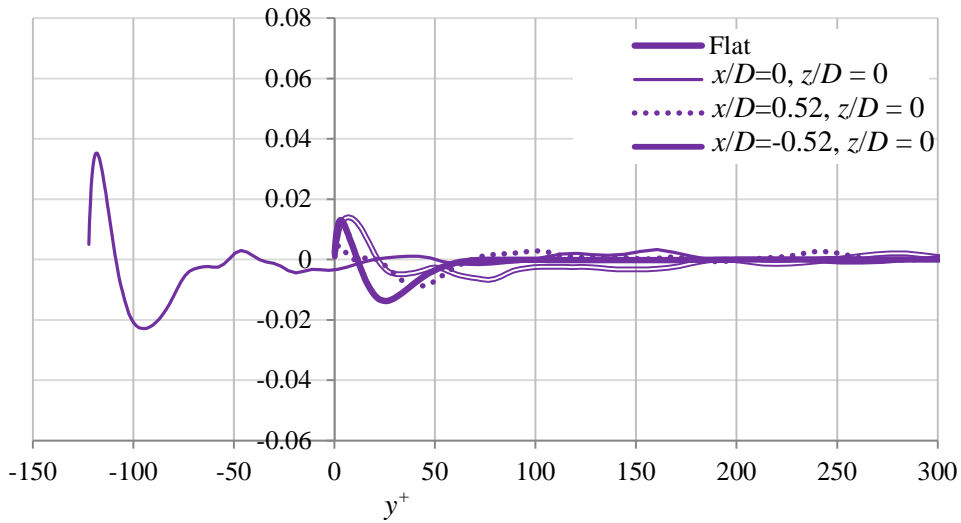


**Figure 62d. Profiles for the velocity pressure gradient term in the turbulent kinetic energy budget for Case 2 at *Re* = 10,000, $\Delta_{drag}$=+1%.**
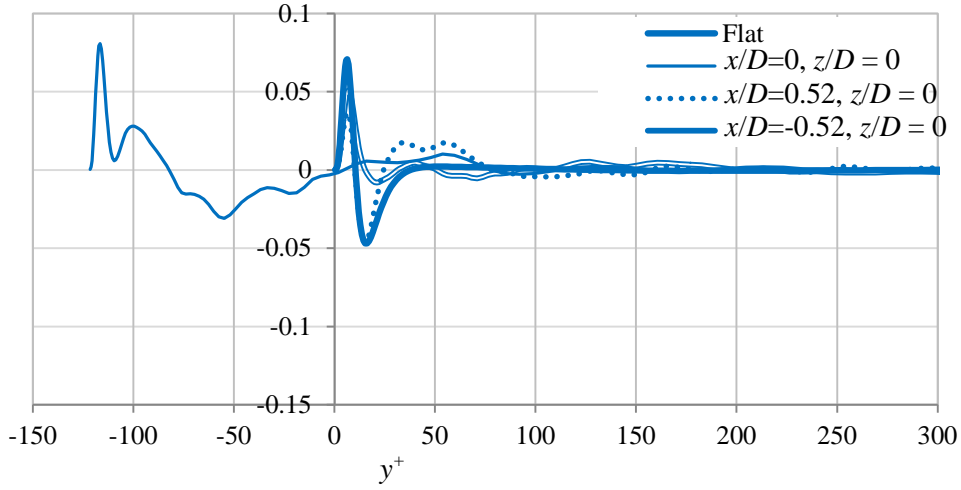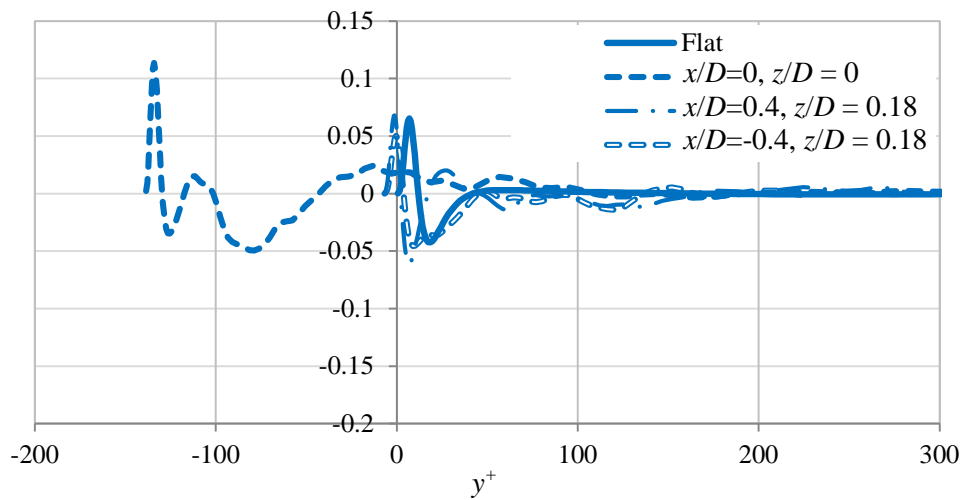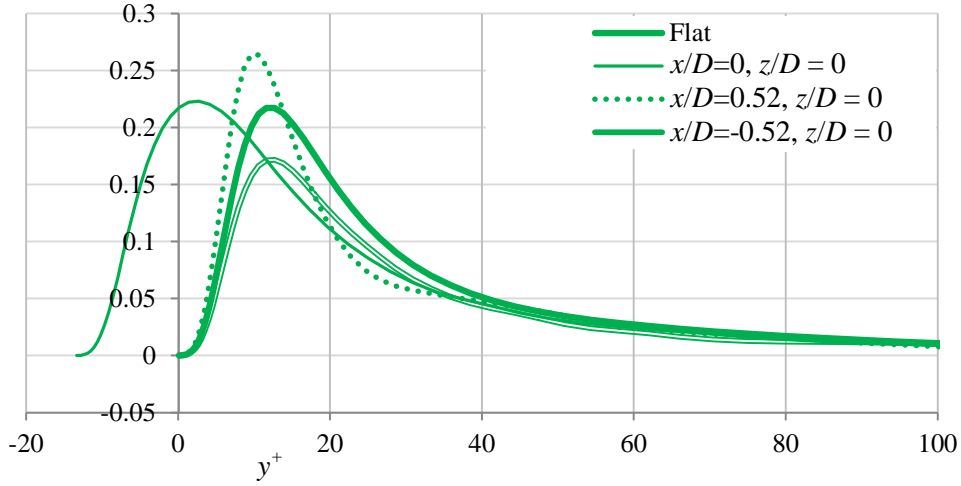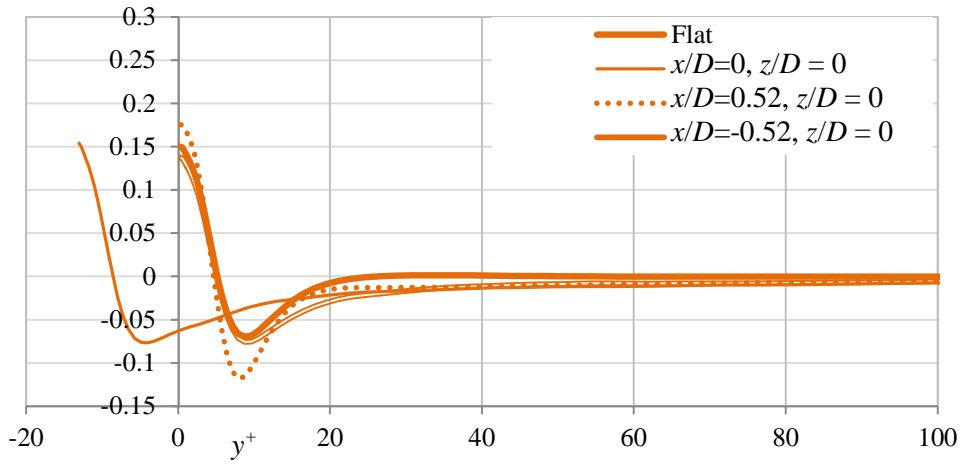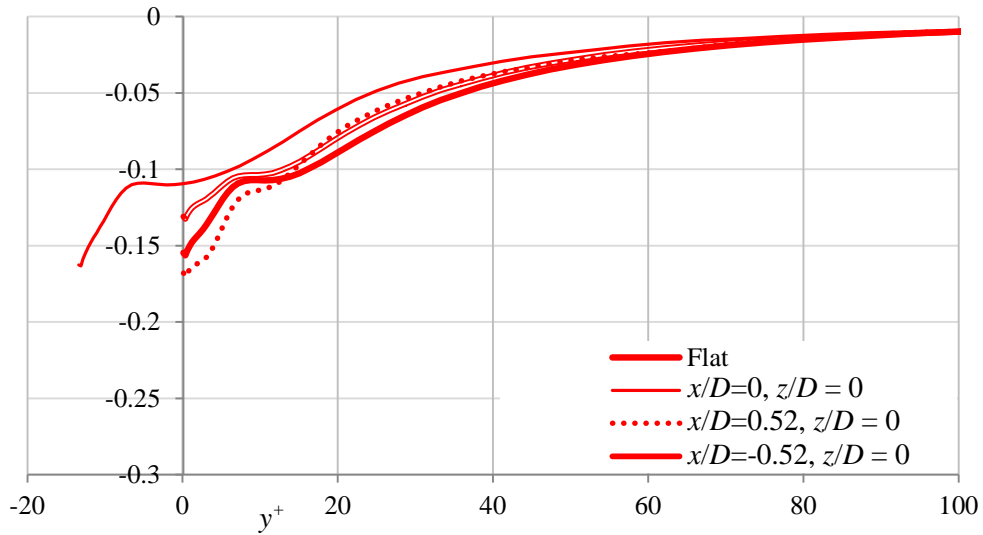
**Figure 62e. Profiles for the turbulent transport term in the turbulent kinetic energy budget for Case 2 at *Re* = 10,000, Δ*drag*=+1%.**
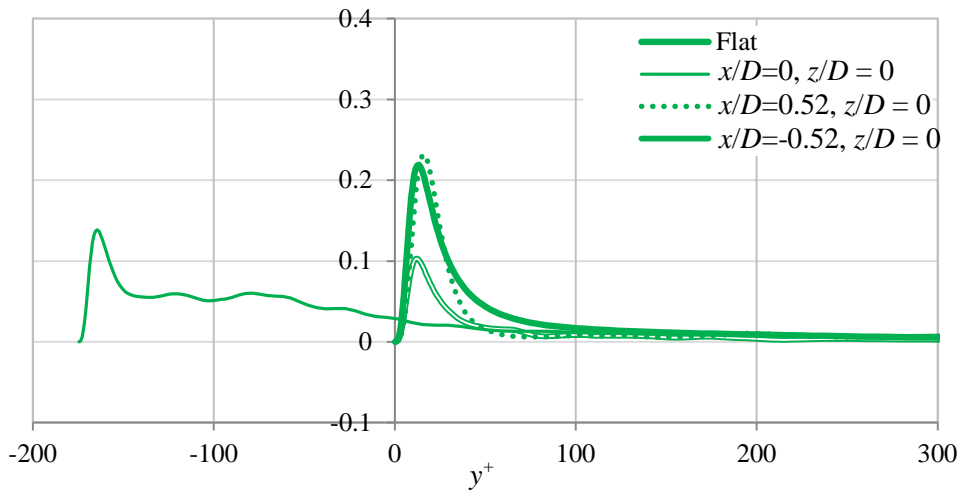


**Figure 63a. Profiles for the production term in the turbulent kinetic energy budget for Case 2 at *Re* = 15,000, Δ*drag*=-0.5%.**
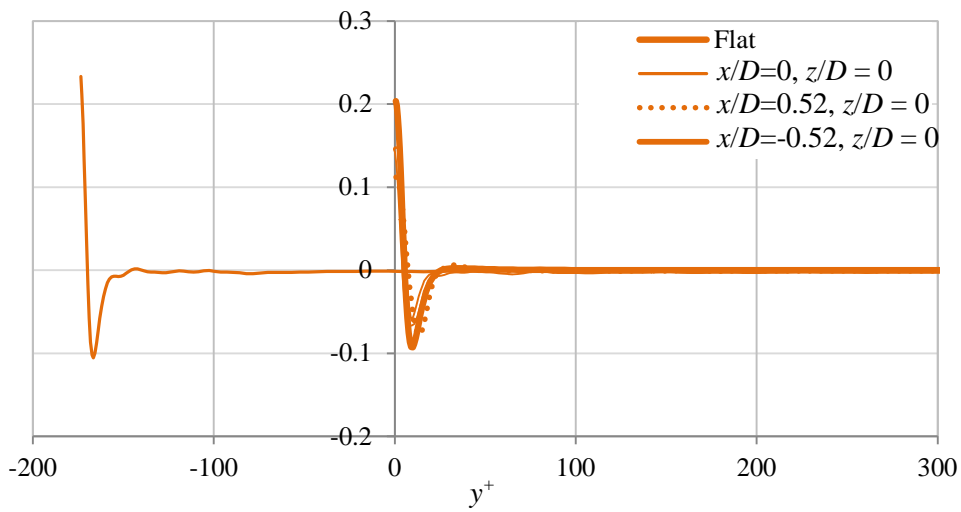


**Figure 63b. Profiles for the viscous diffusion term in the turbulent kinetic energy budget for Case 2 at *Re* = 15,000, Δ*drag*=-0.5%.**
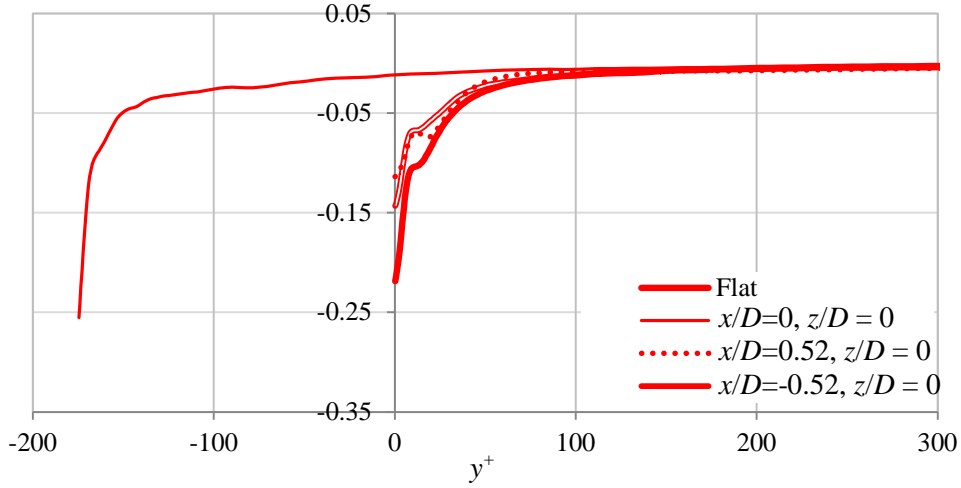
**Figure 63c. Profiles for the dissipation term in the turbulent kinetic energy budget for Case 2 at $Re = 15,000$, $\Delta_{drag}=-0.5\%$.**
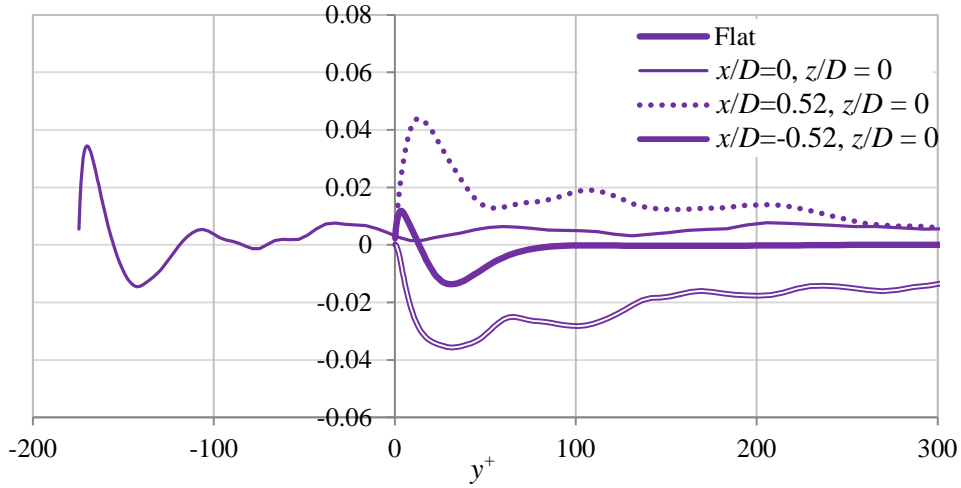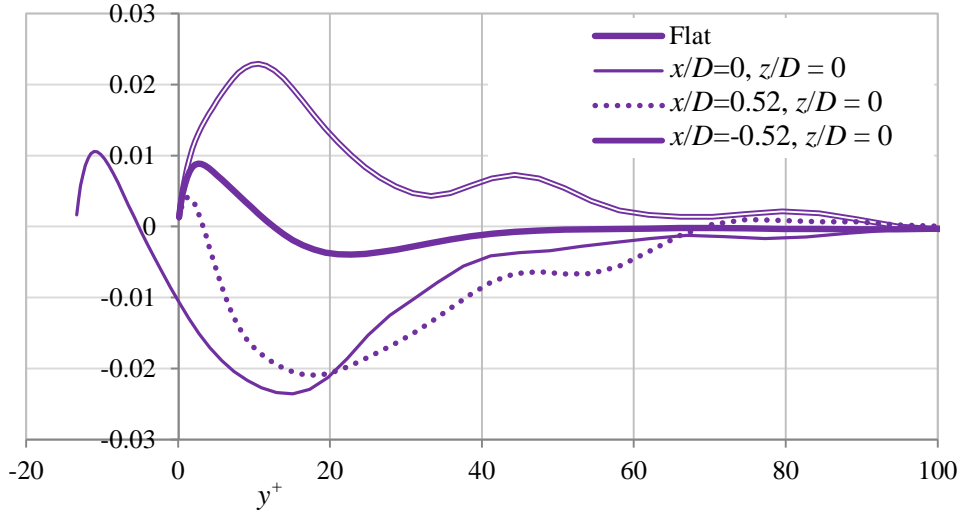


**Figure 63d. Profiles for the velocity pressure gradient term in the turbulent kinetic energy budget for Case 2 at $Re = 15,000$, $\Delta_{drag}=-0.5\%$.**
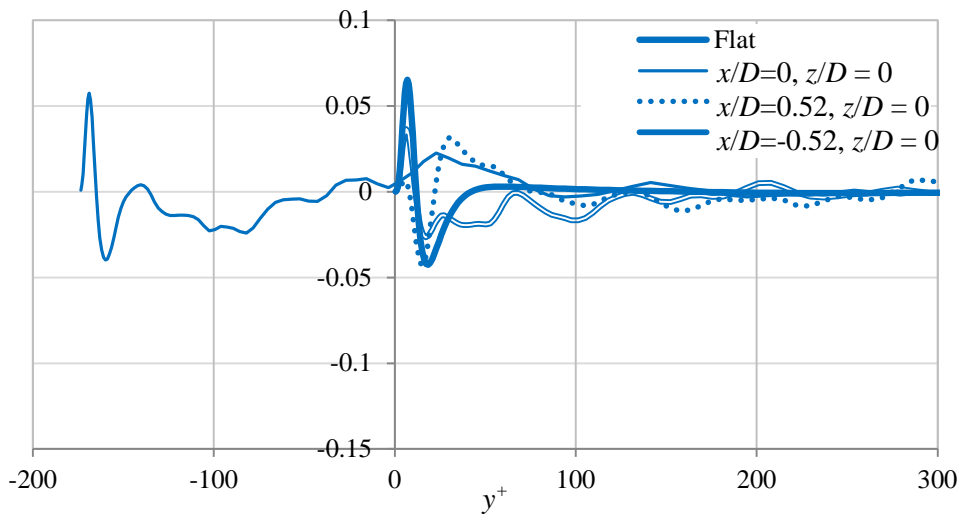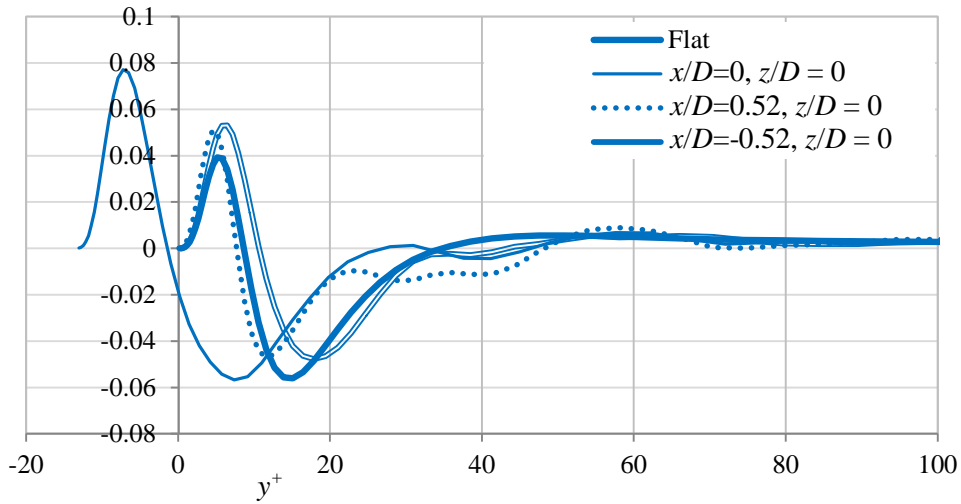


**Figure 63e. Profiles for the turbulent transport term in the turbulent kinetic energy budget for Case 2 at $Re = 15,000$, $\Delta_{drag}=-0.5\%$.**
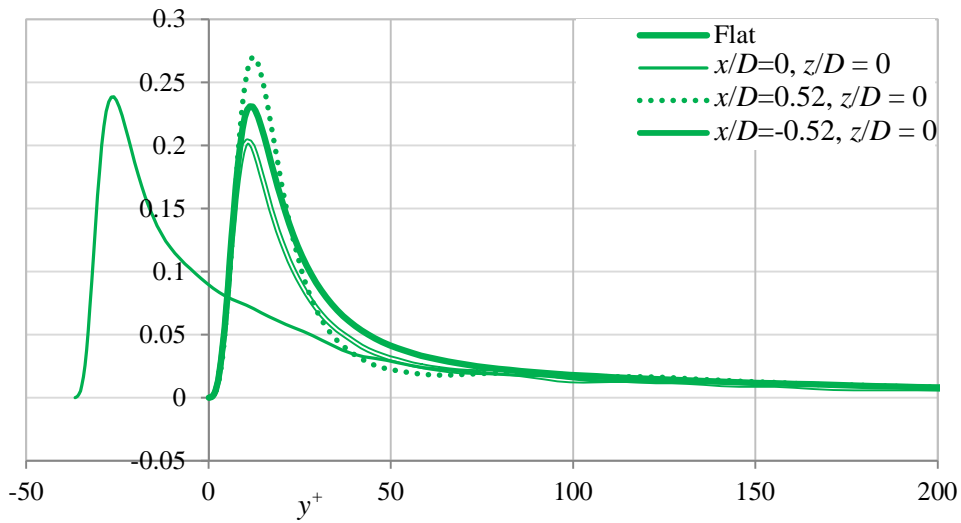
144
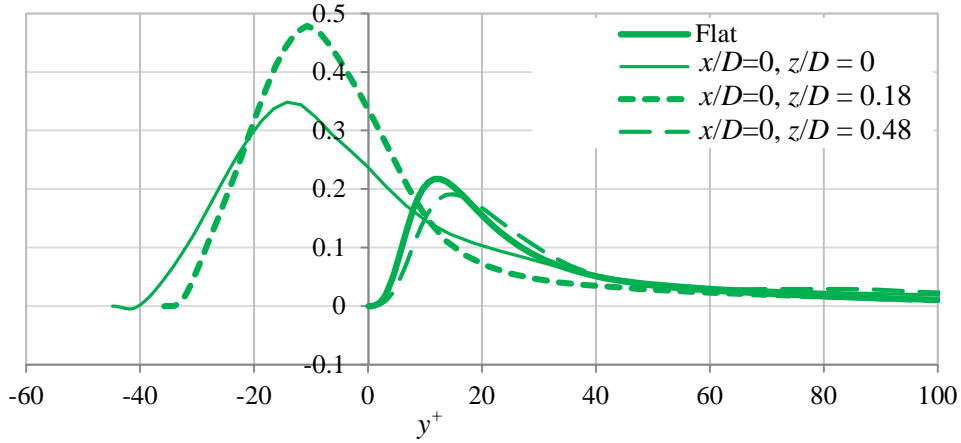
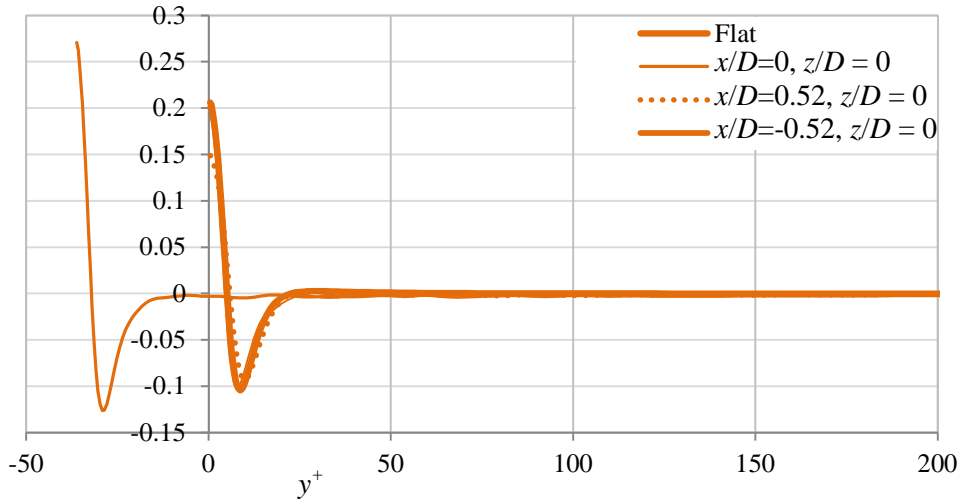**Figure 64a. Profiles for the production term in the turbulent kinetic energy budget for Case 2 at Re = 3,300, Δ_drag=+3.5%.**
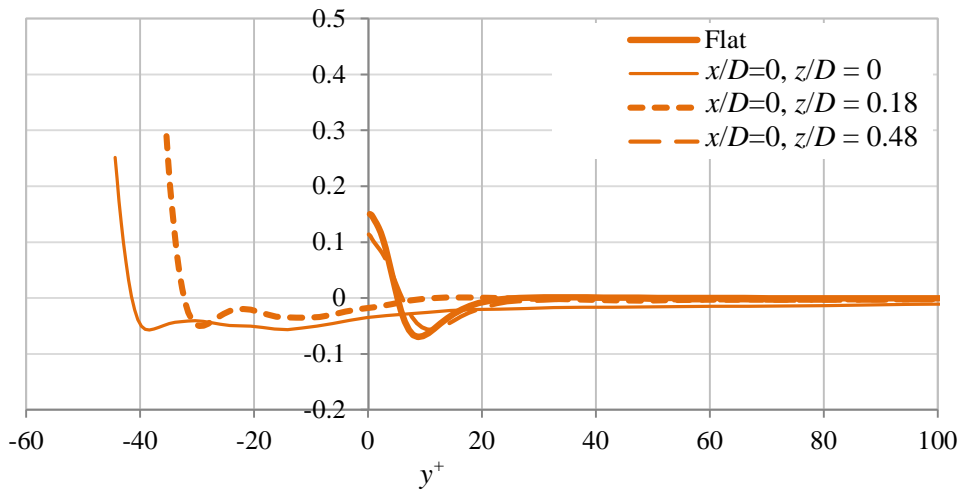


**Figure 64b. Profiles for the viscous diffusion term in the turbulent kinetic energy budget for Case 2 at Re = 3,300, Δ_drag=+3.5%.**
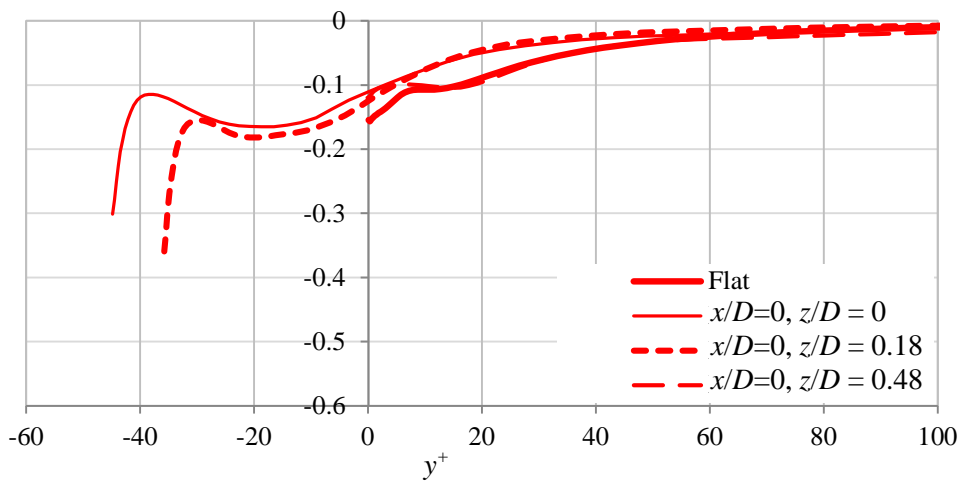


**Figure 64c. Profiles for the dissipation term in the turbulent kinetic energy budget for Case 2 at Re = 3,300, Δ_drag=+3.5%.**
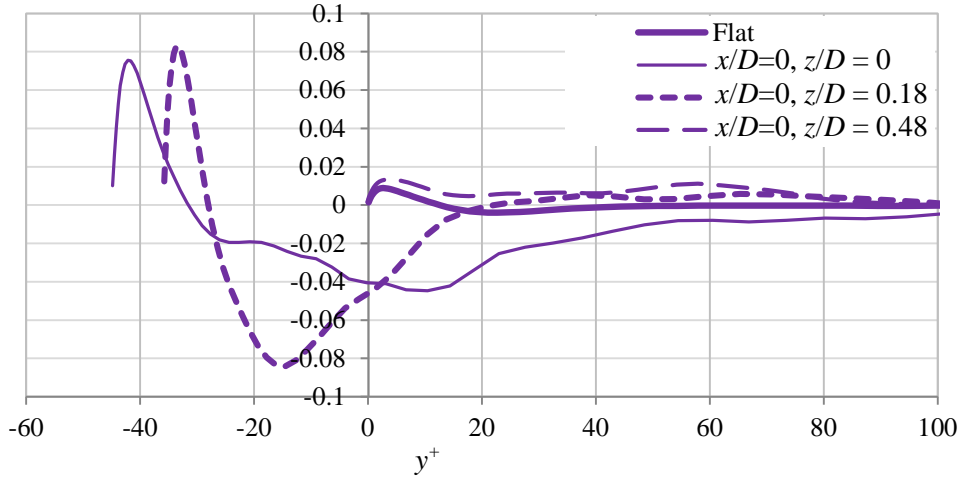
**Figure 64d. Profiles for the velocity pressure gradient term in the turbulent kinetic energy budget for Case 2 at *Re* = 3,300, Δ*drag*=+3.5%.**
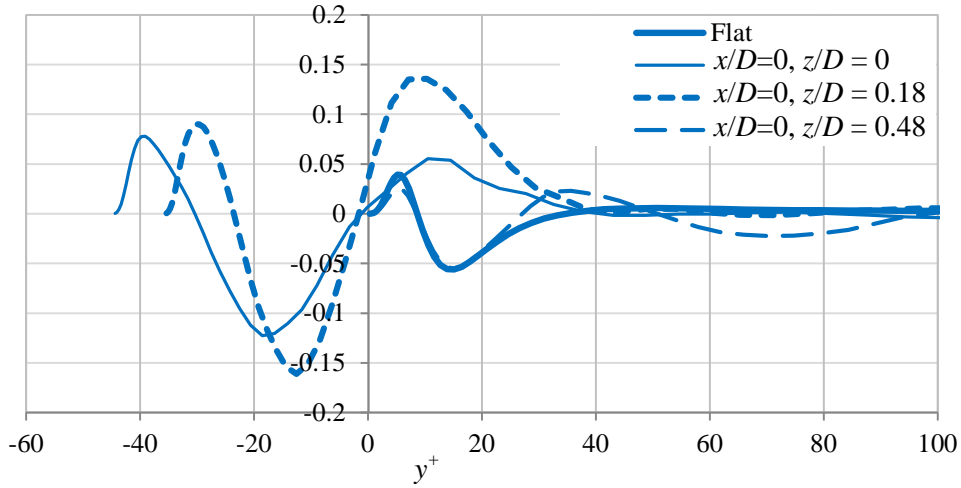


**Figure 64e. Profiles for the turbulent transport term in the turbulent kinetic energy budget for Case 2 at *Re* = 3,300, Δ*drag*=+3.5%.**
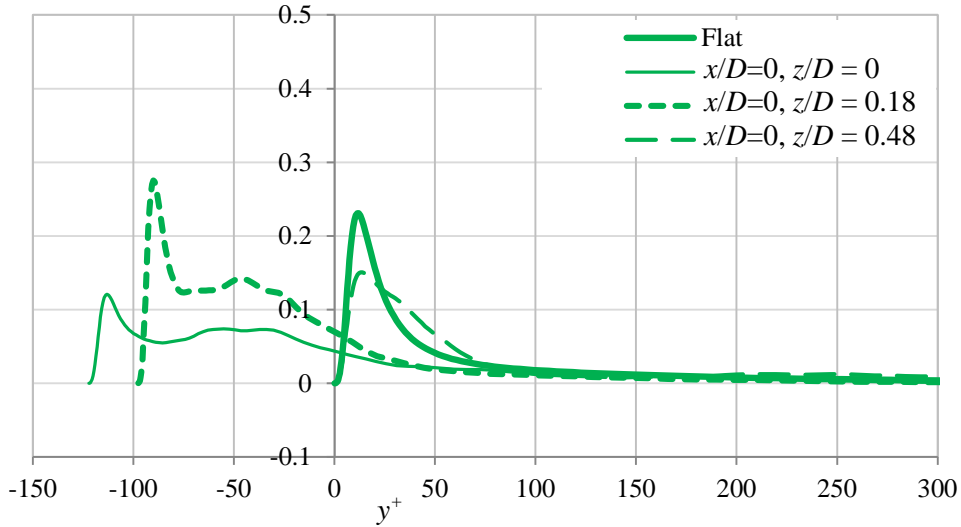


**Figure 65a. Profiles for the production term in the turbulent kinetic energy budget for Case 2 at 10,000, Δ*drag*=+1%.**

146
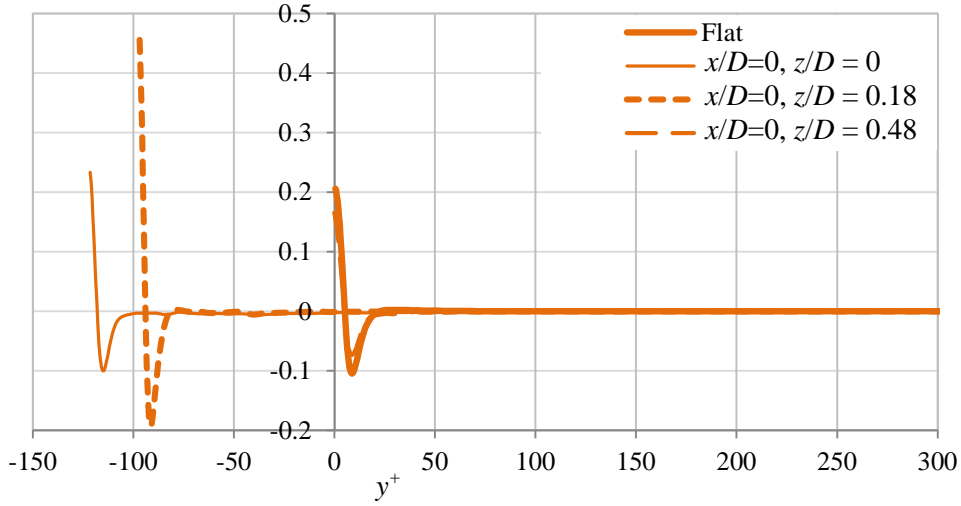
**Figure 65b. Profiles for the viscous diffusion term in the turbulent kinetic energy budget for Case 2 at *Re* = 10,000, Δ*drag*=+1%.**
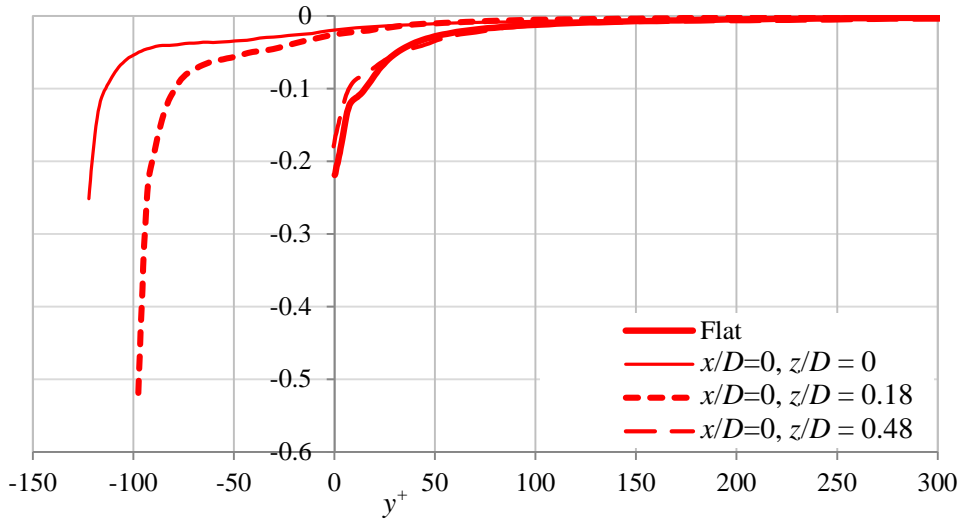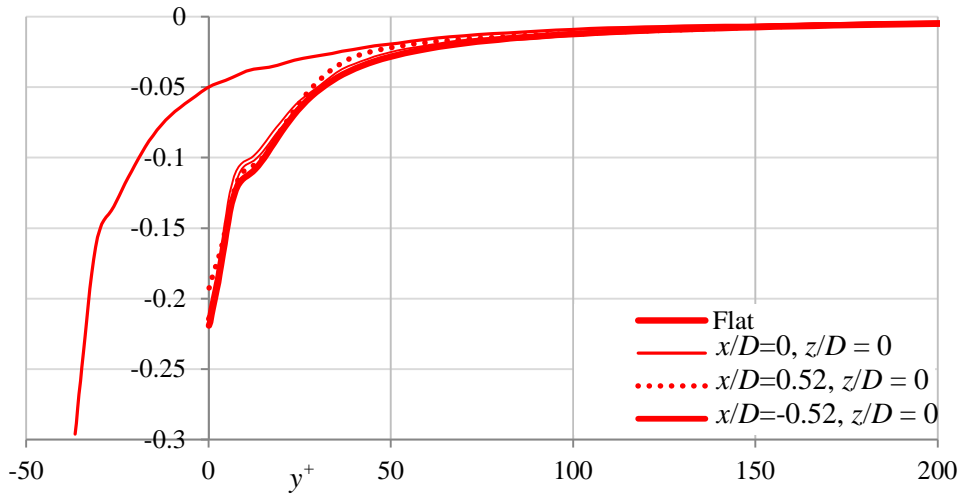


**Figure 65c. Profiles for the dissipation term in the turbulent kinetic energy budget for Case at *Re* = 10,000, Δ*drag*=+1%.**
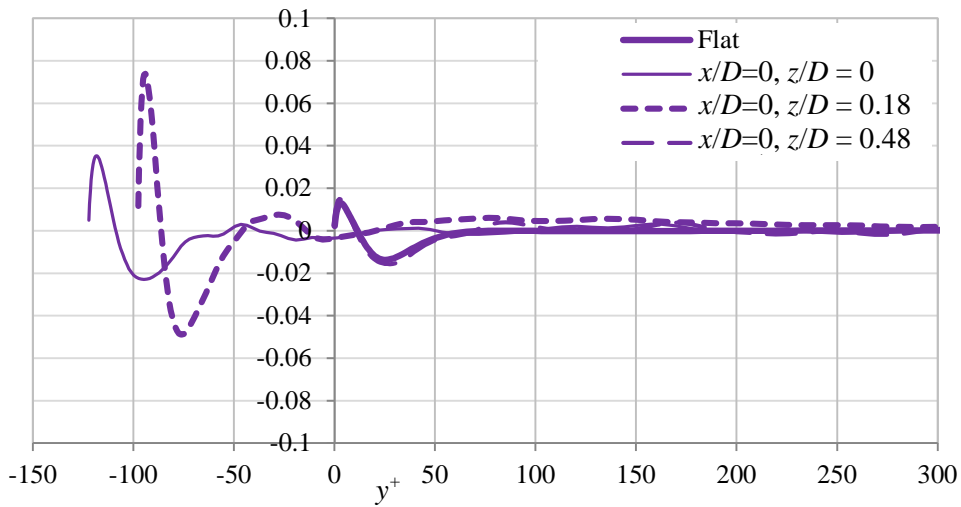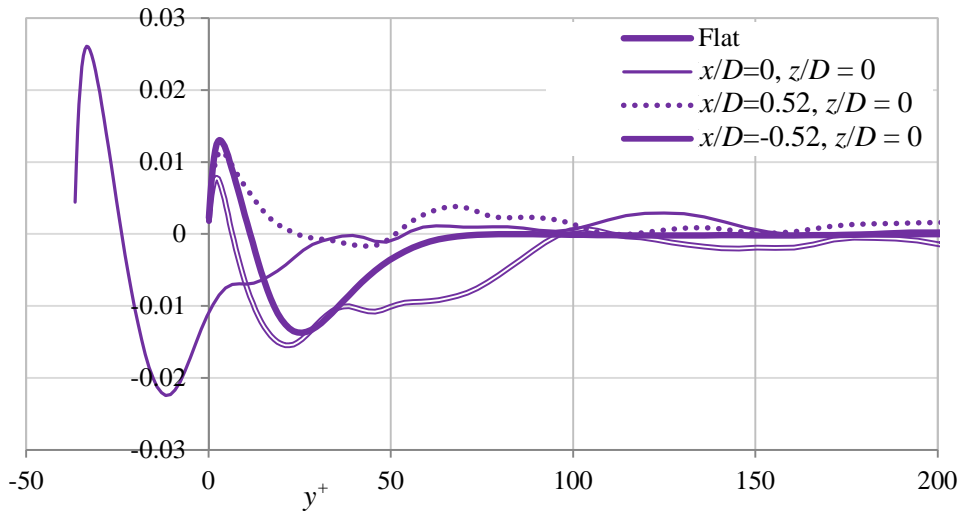


**Figure 65d. Profiles for the velocity pressure gradient term in the turbulent kinetic energy budget for Case 2 at *Re* = 10,000, Δ*drag*=+1%.**
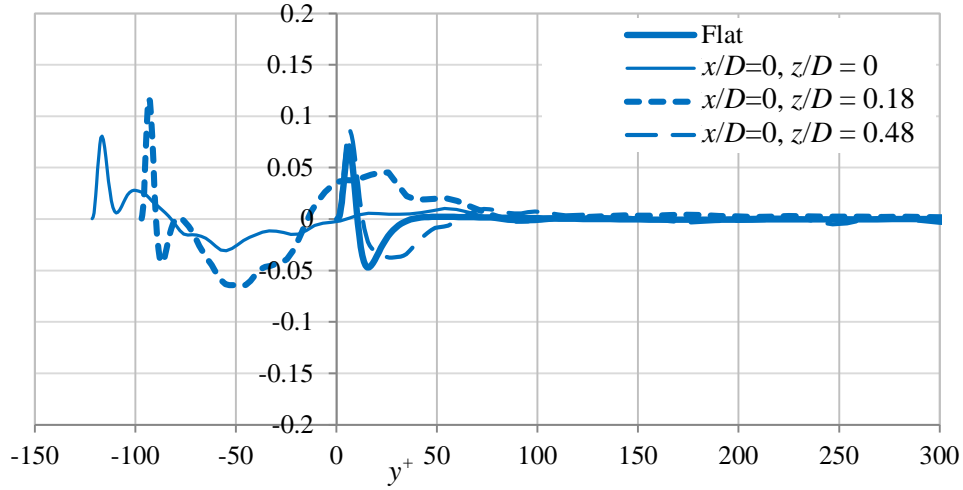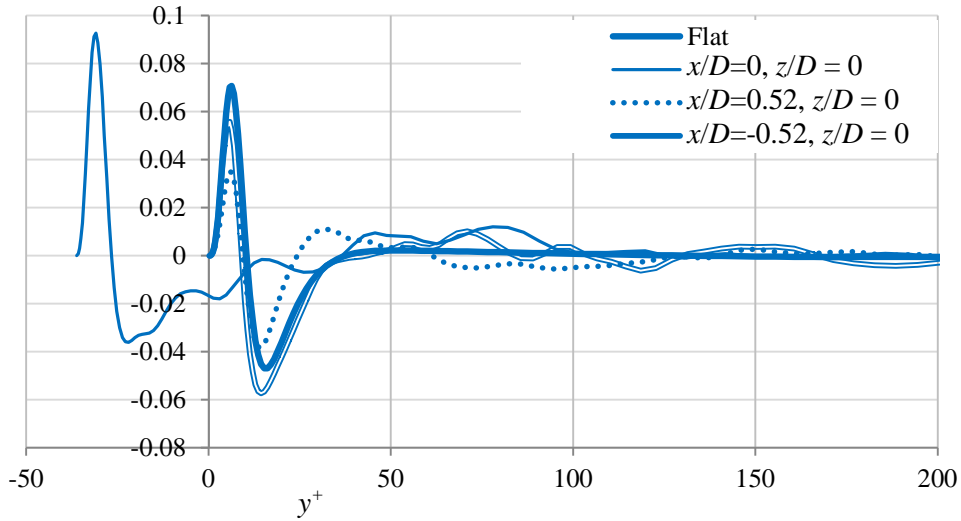
**Figure 65e. Profiles for the turbulent transport term in the turbulent kinetic energy budget for Case 2 at $Re$ = 10,000, $\Delta_{drag}$=+1%.**
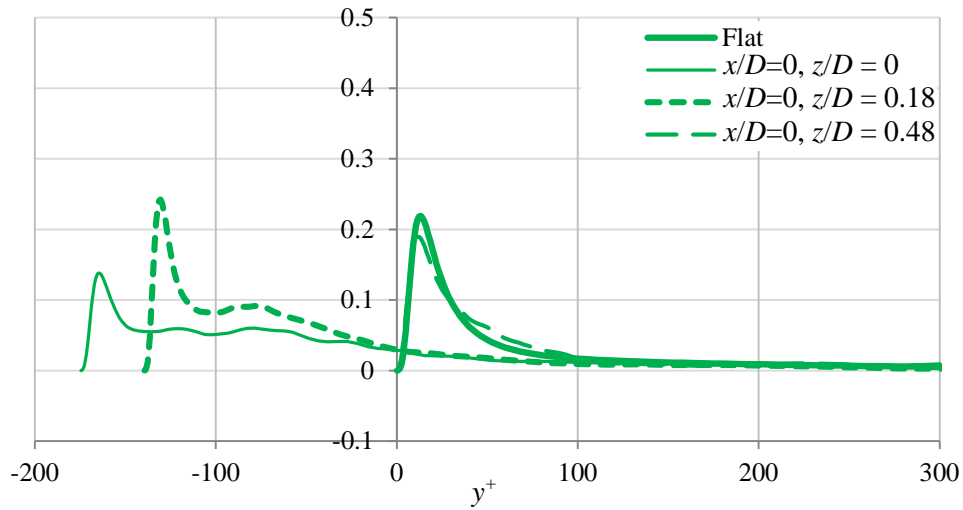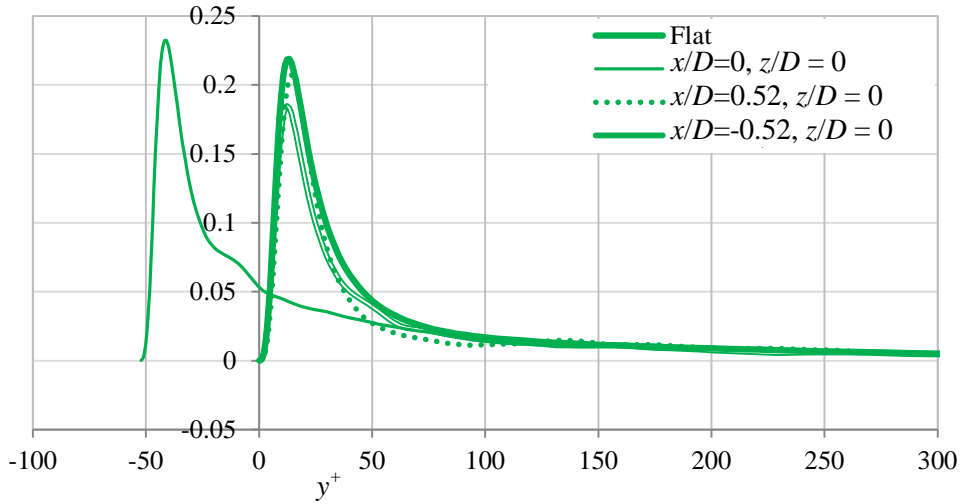


**Figure 66a. Profiles for the production term in the turbulent kinetic energy budget for Case 2 at $Re$ = 15,000, $\Delta_{drag}$=-0.5%.**
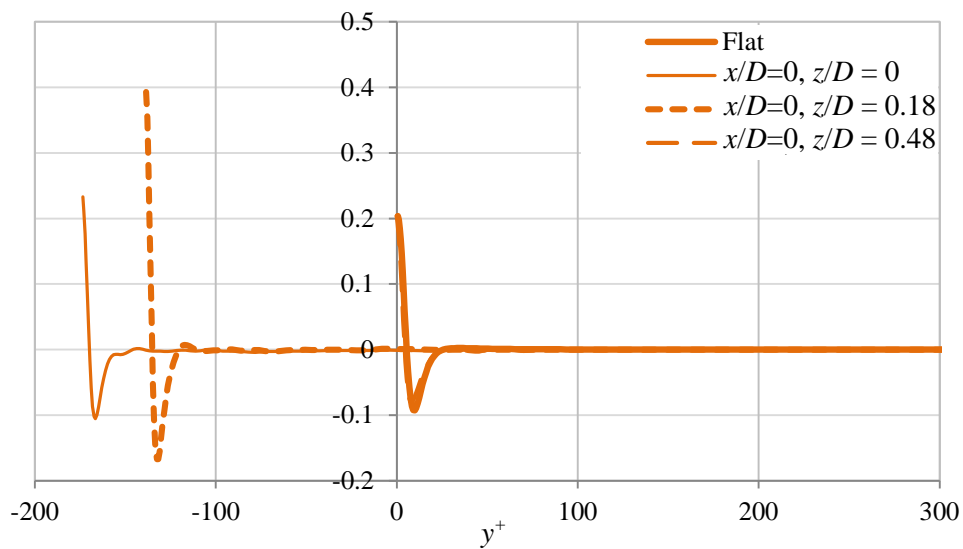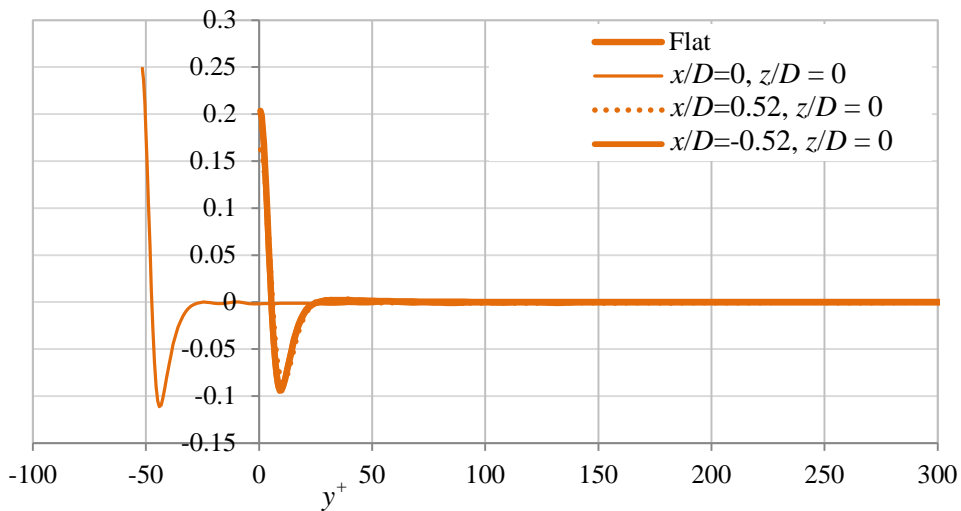


**Figure 66b. Profiles for the viscous diffusion term in the turbulent kinetic energy budget for Case 2 at $Re$ = 15,000, $\Delta_{drag}$=-0.5%.**
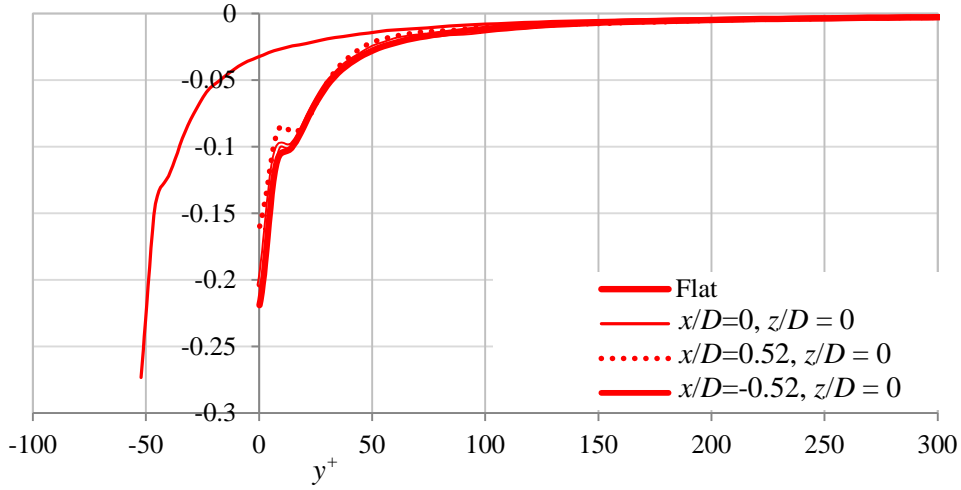
148
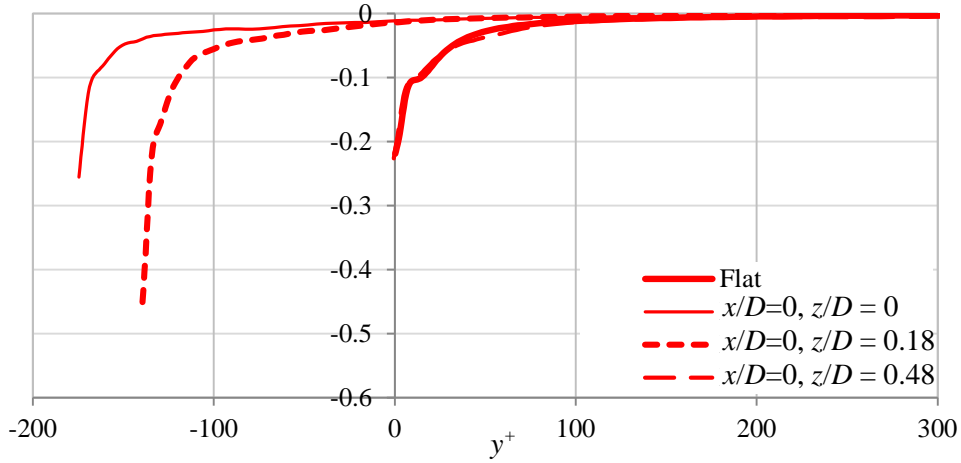
**Figure 66c. Profiles for the dissipation term in the turbulent kinetic energy budget for Case 2 at $Re = 15{,}000$, $\Delta_{drag}$=-0.5%.**
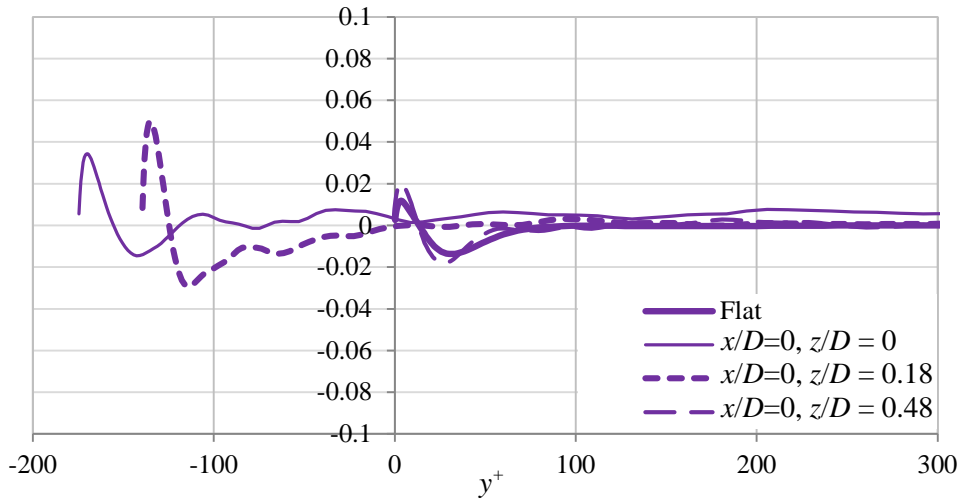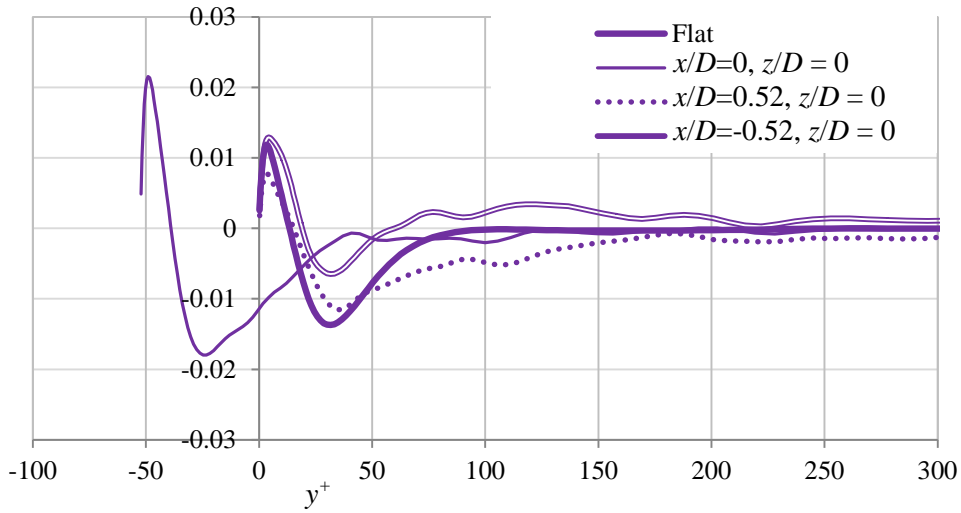


**Figure 66d. Profiles for the velocity pressure gradient term in the turbulent kinetic energy budget for Case 2 at $Re = 15{,}000$, $\Delta_{drag}$=-0.5%.**
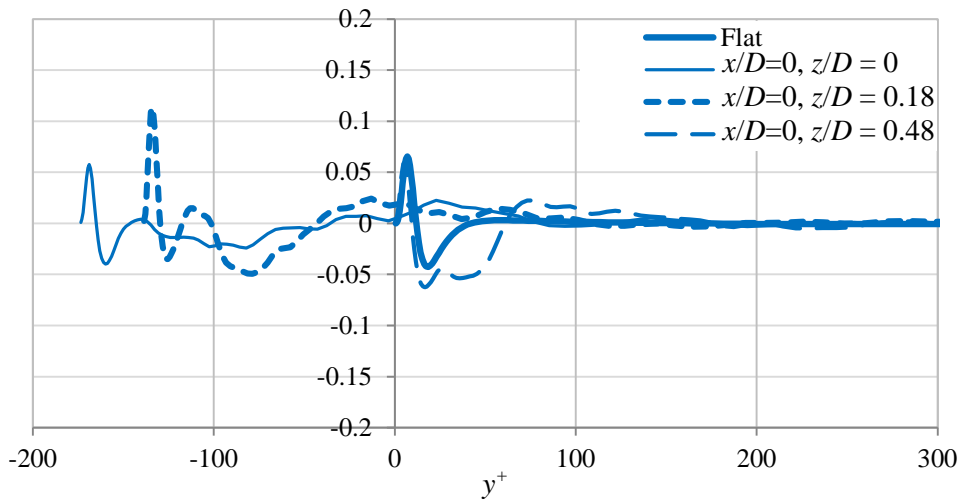


**Figure 66e. Profiles for the turbulent transport term in the turbulent kinetic energy budget for Case 2 at $Re = 15{,}000$, $\Delta_{drag}$=-0.5%.**
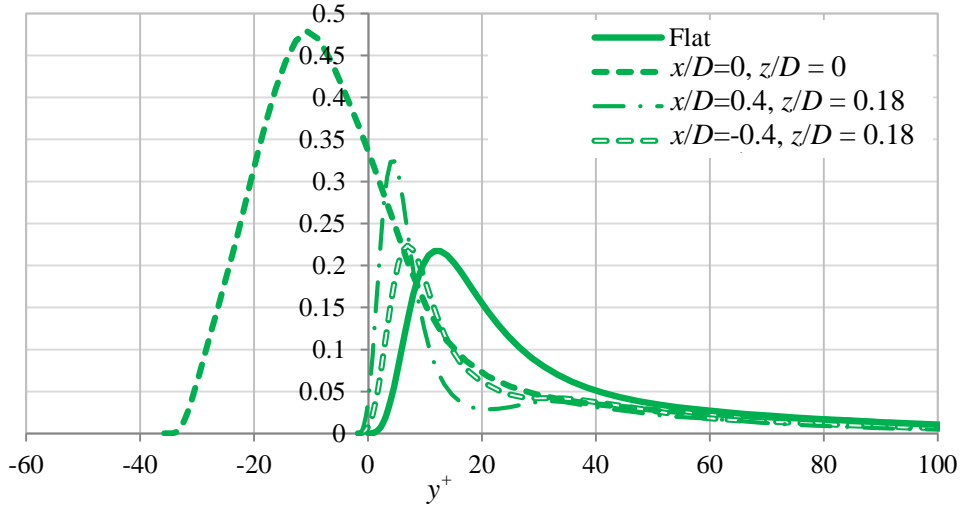
**Figure 67a. Profiles for the production term in the turbulent kinetic energy budget for Case 2 at** *Re* **= 3,300, Δ**_drag_**=+3.5%.**
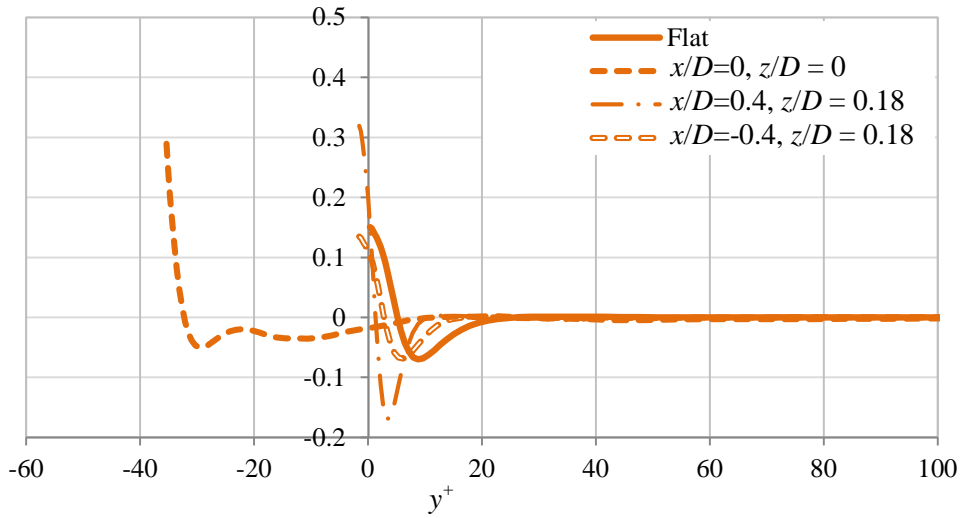


**Figure 67b. Profiles for the viscous diffusion term in the turbulent kinetic energy budget for Case 2 at** *Re* **= 3,300, Δ**_drag_**=+3.5%.**
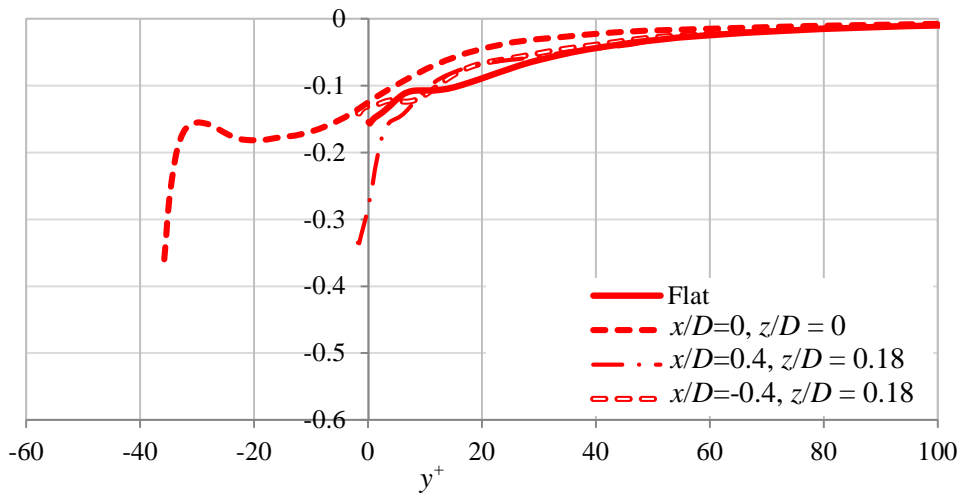


**Figure 67c. Profiles for the dissipation term in the turbulent kinetic energy budget for Case 2 at** *Re* **= 3,300, Δ**_drag_**=+3.5%.**
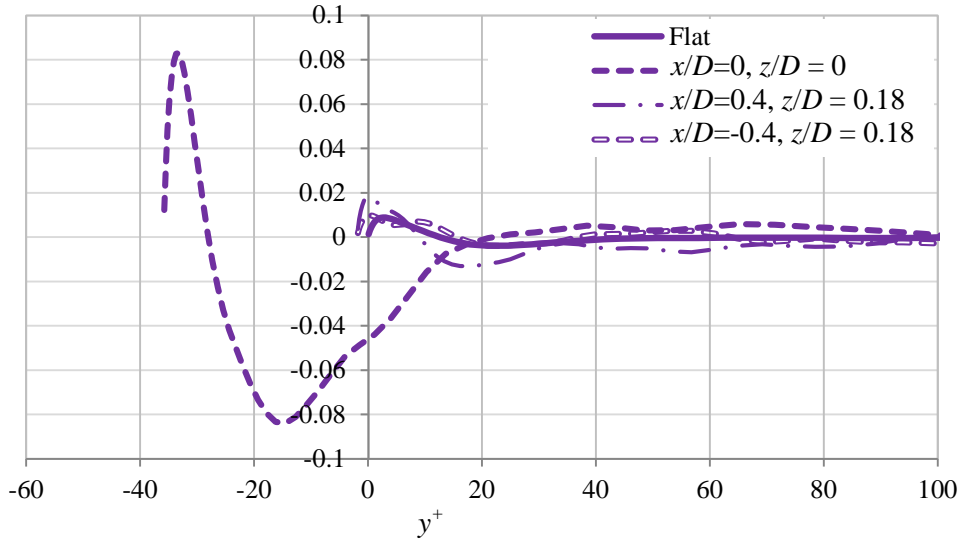
**Figure 67d. Profiles for the velocity pressure gradient term in the turbulent kinetic energy budget for Case 2 at $Re = 3,300$, $\Delta_{drag}$=+3.5%.**
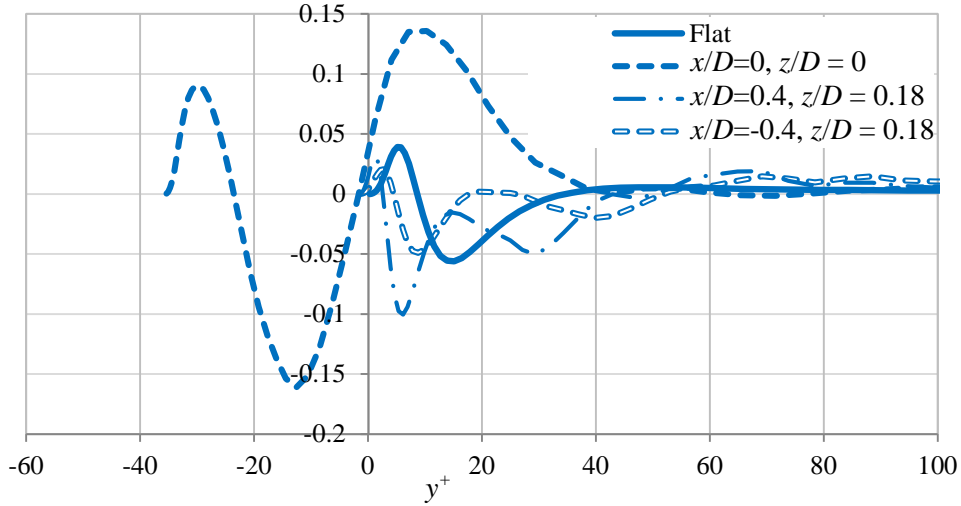


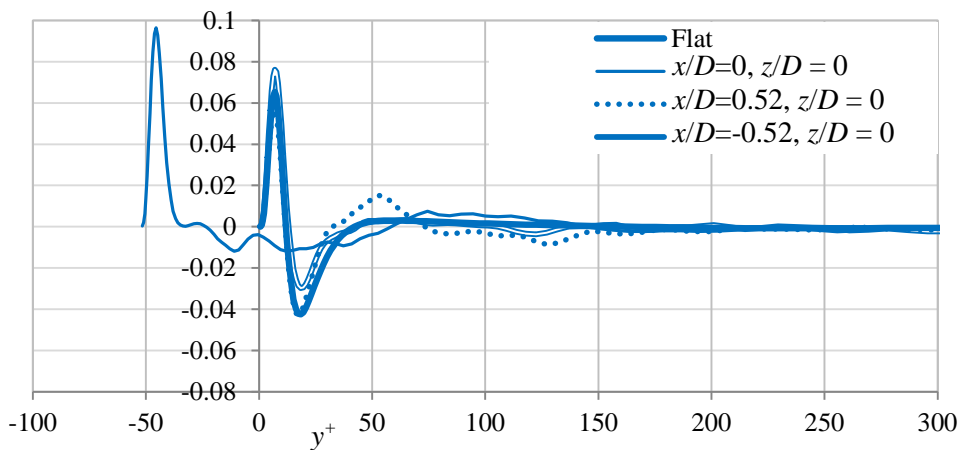**Figure 67e. Profiles for the turbulent transport term in the turbulent kinetic energy budget for Case 2 at $Re = 3,300$, $\Delta_{drag}$=+3.5%.**
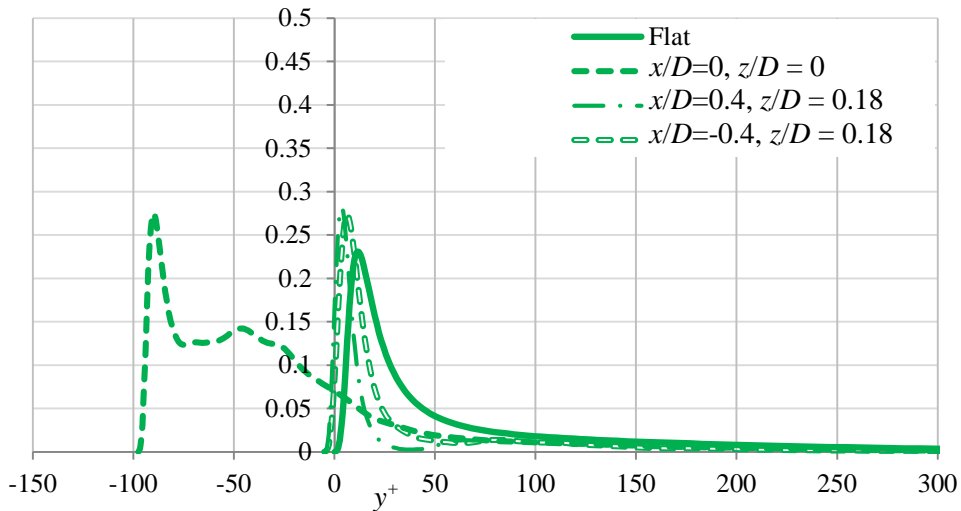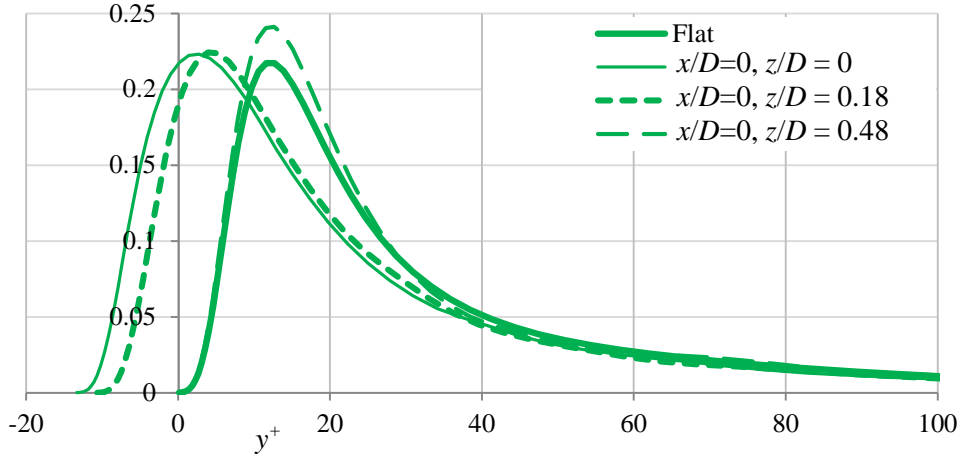


**Figure 68a. Profiles for the production term in the turbulent kinetic energy budget for Case 2 at 10,000, $\Delta_{drag}$=+1%.**
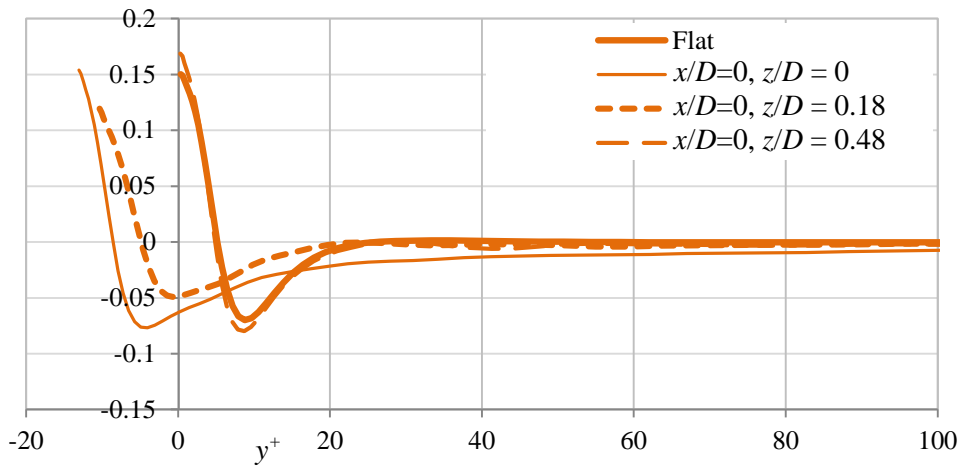
151
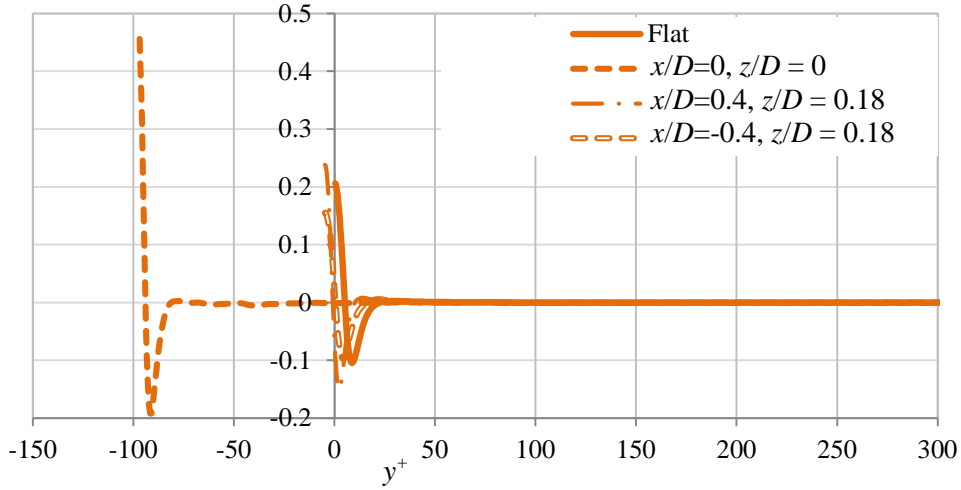
**Figure 68b. Profiles for the viscous diffusion term in the turbulent kinetic energy budget for Case 2 at 10,000, $\Delta_{drag}$=+1%.**
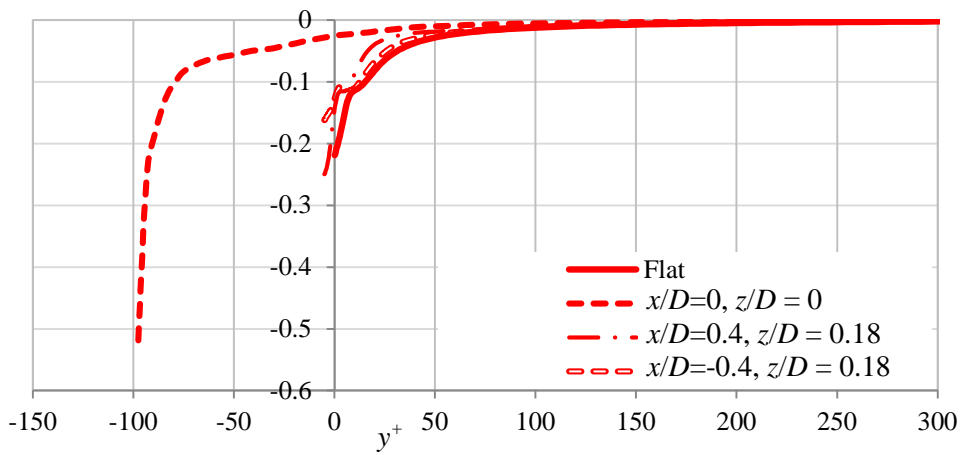


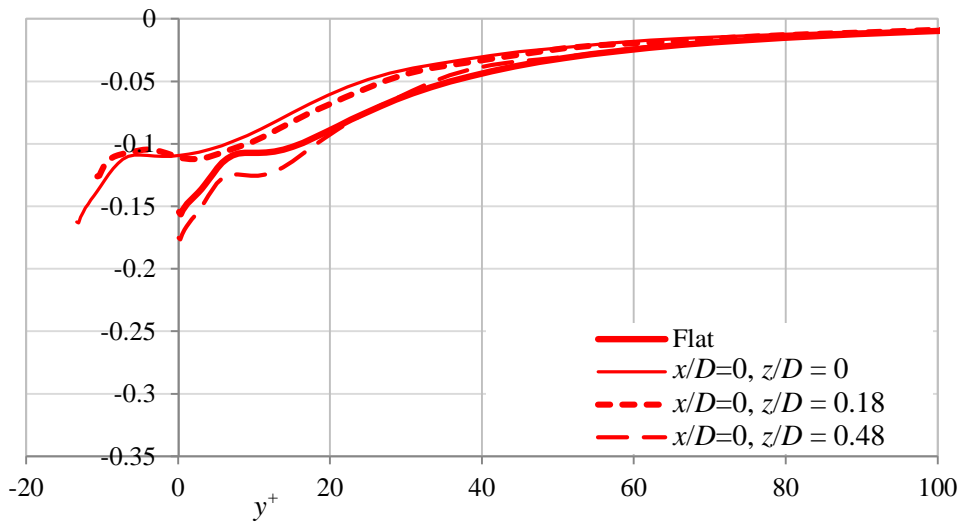**Figure 68c. Profiles for the dissipation term in the turbulent kinetic energy budget for Case 2 at 10,000, $\Delta_{drag}$=+1%.**
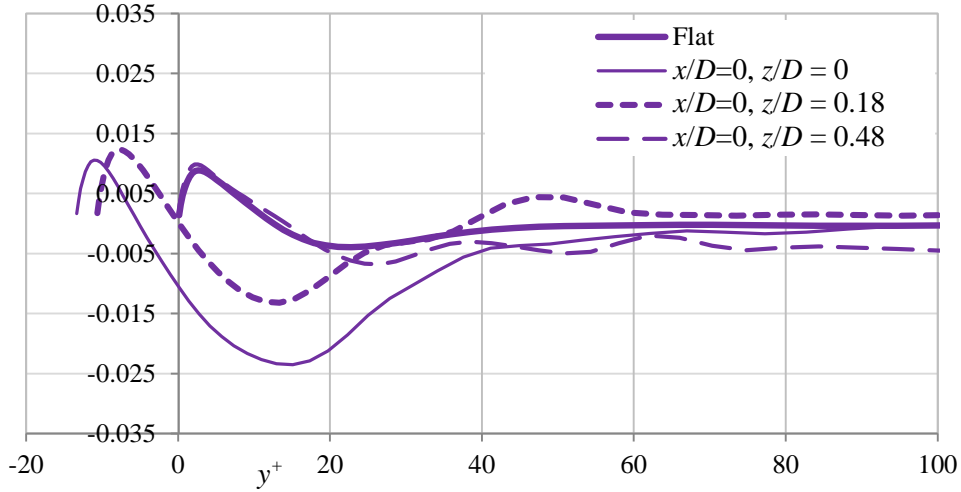


**Figure 68d. Profiles for the velocity pressure gradient term in the turbulent kinetic energy budget for Case 2 at 10,000, $\Delta_{drag}$=+1%.**

152
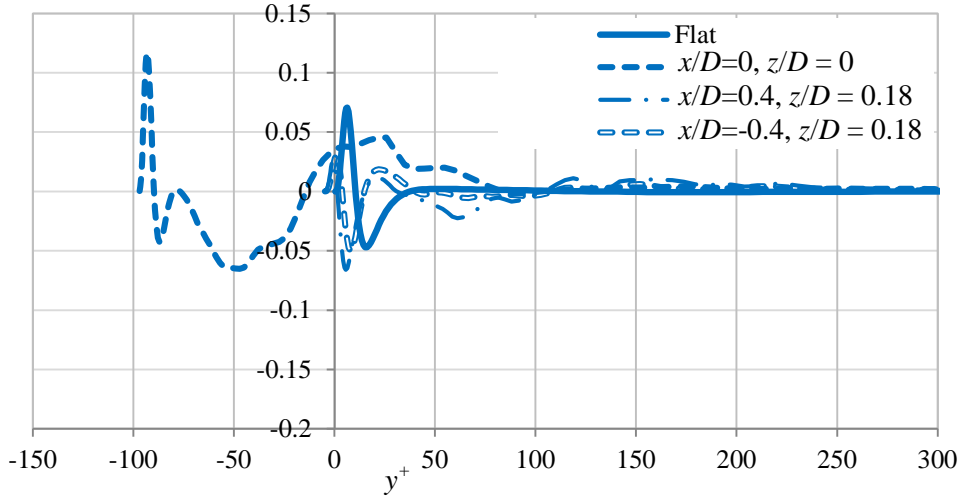
**Figure 68e. Profiles for the turbulent transport term in the turbulent kinetic energy budget for Case 2 at 10,000, Δ_drag=+1%.**



**Figure 69a. Profiles for the production term in the turbulent kinetic energy budget for Case 2 at Re = 15,000, Δ_drag=-0.5%.**



**Figure 69b. Profiles for the viscous diffusion term in the turbulent kinetic energy budget for Case 2 at Re = 15,000, Δ_drag=-0.5%.**

**Figure 69c. Profiles for the dissipation term in the turbulent kinetic energy budget for Case 2 at**
$Re$ = 15,000, $\Delta_{drag}$=-0.5%.



**Figure 69d. Profiles for the velocity pressure gradient term in the turbulent kinetic energy budget for Case 2 at $Re$ = 15,000, $\Delta_{drag}$=-0.5%.**
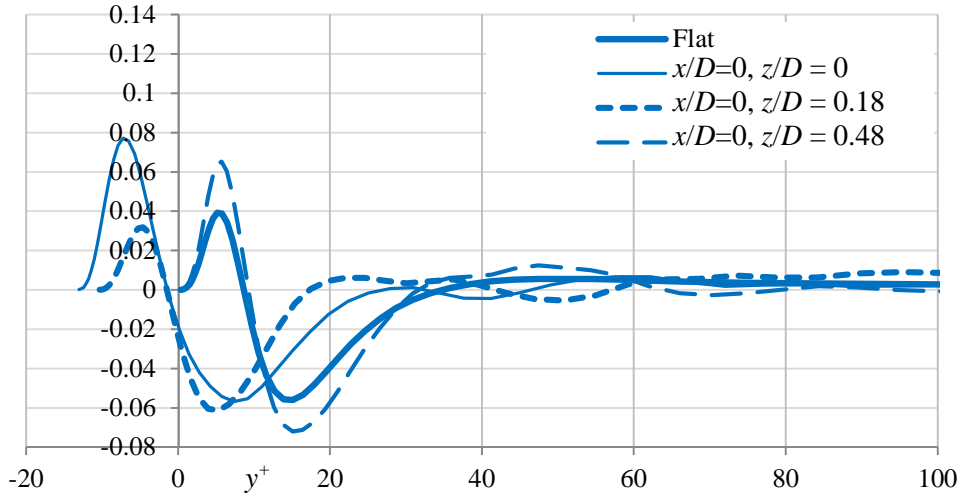


**Figure 69e. Profiles for the turbulent transport term in the turbulent kinetic energy budget for Case 2 at $Re$ = 15,000, $\Delta_{drag}$=-0.5%.**
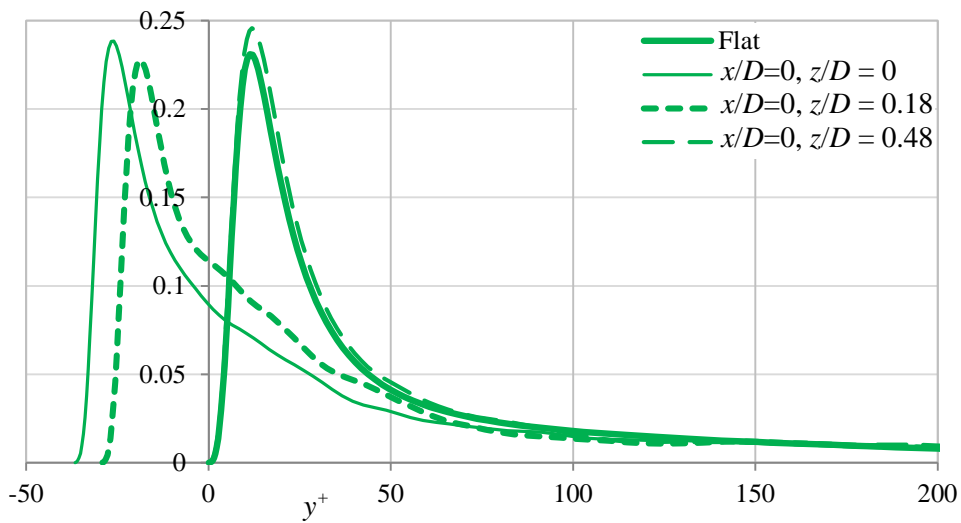
154

**Figure 70a. Profiles for the production term in the turbulent kinetic energy budget for Case 3 at** $Re = 3,300$, $\Delta_{drag}$=-1%.
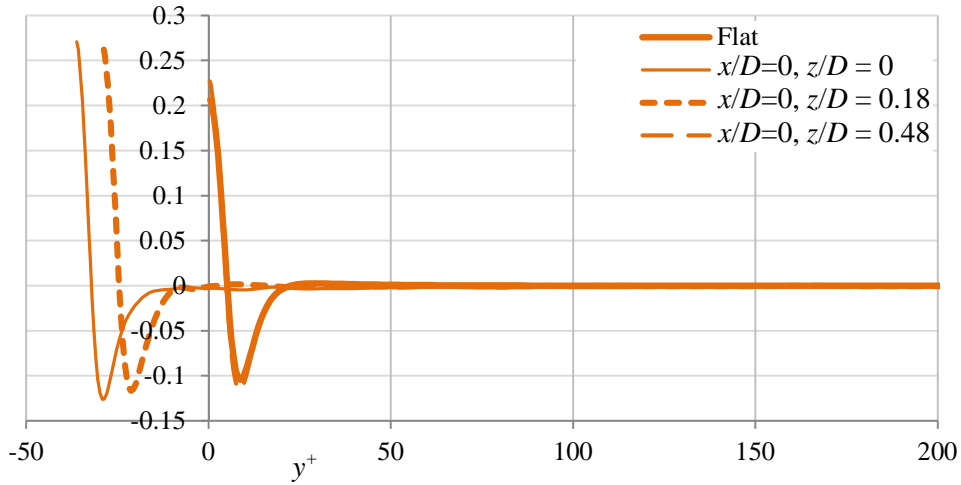


**Figure 70b. Profiles for the viscous diffusion term in the turbulent kinetic energy budget for Case 3 at** $Re = 3,300$, $\Delta_{drag}$=-1%.



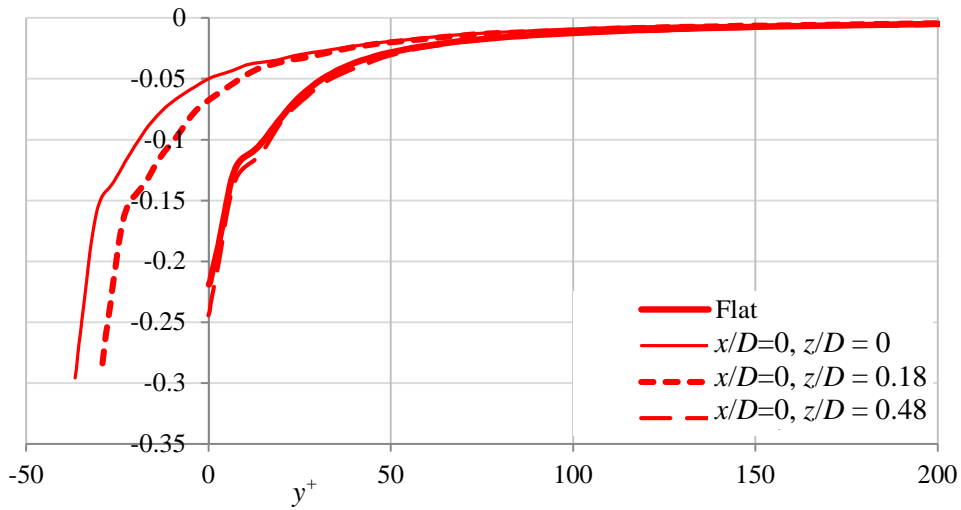**Figure 70c. Profiles for the dissipation term in the turbulent kinetic energy budget for Case 3 at** $Re = 3,300$, $\Delta_{drag}$=-1%.
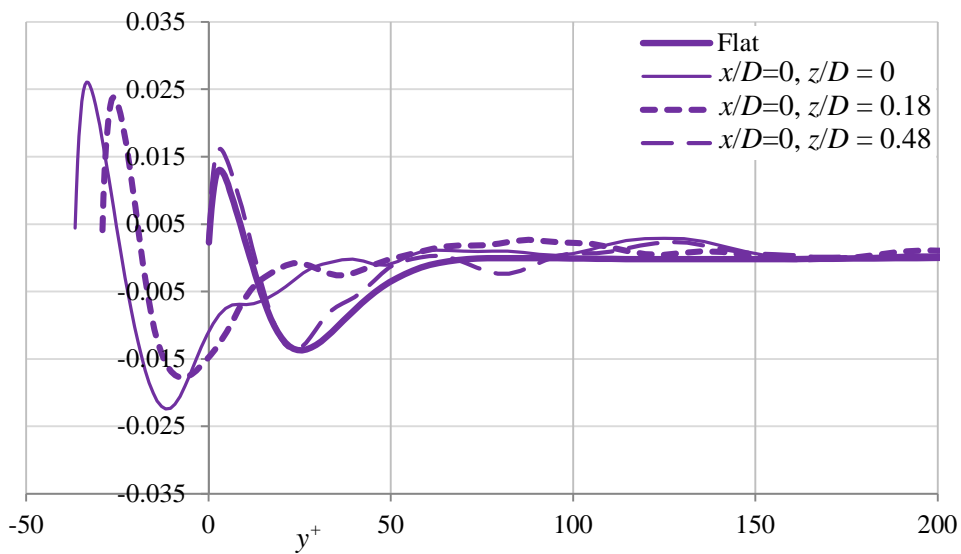
**Figure 70d. Profiles for the velocity pressure gradient term in the turbulent kinetic energy budget for Case 3 at *Re* = 3,300, Δ*drag*=-1%.**



**Figure 70e. Profiles for the turbulent transport term in the turbulent kinetic energy budget for Case 3 at *Re* = 3,300, Δ*drag*=-1%.**



**Figure 71a. Profiles for the production term in the turbulent kinetic energy budget for Case 3 at *Re* = 10,000, Δ*drag*=-1.5%.**

156

**Figure 71b. Profiles for the viscous diffusion term in the turbulent kinetic energy budget for Case 3 at *Re* = 10,000, Δ*drag*=-1.5%.**



**Figure 71c. Profiles for the dissipation term in the turbulent kinetic energy budget for Case 3 at *Re* = 10,000, Δ*drag*=-1.5%.**



**Figure 71d. Profiles for the velocity pressure gradient term in the turbulent kinetic energy budget for Case 3 at *Re* = 10,000, Δ*drag*=-1.5%.**
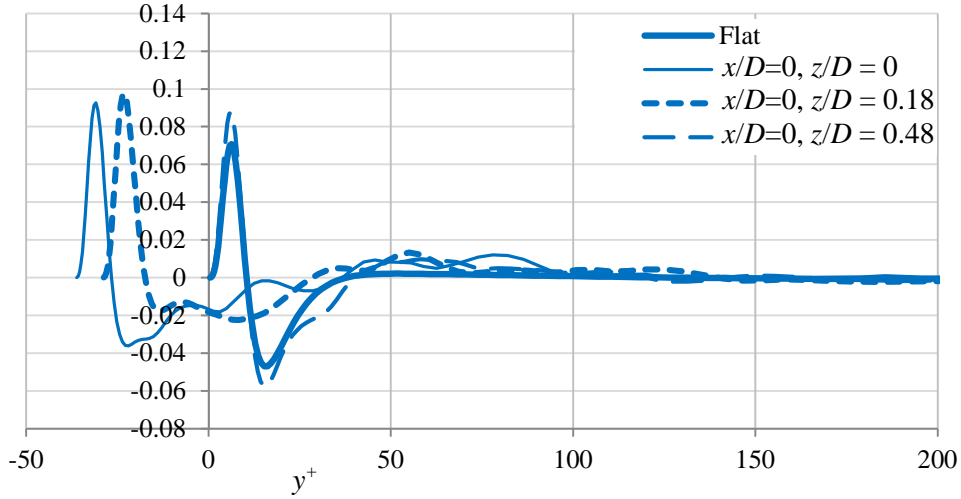
**Figure 71e. Profiles for the turbulent transport term in the turbulent kinetic energy budget for Case 3 at *Re* = 10,000, Δ*drag*=-1.5%.**
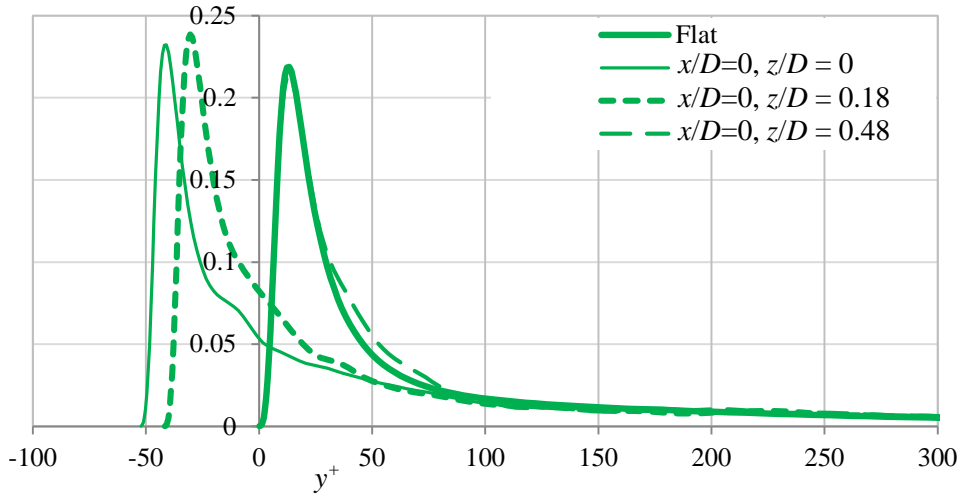


**Figure 72a. Profiles for the production term in the turbulent kinetic energy budget for Case 3 at *Re* = 15,000, Δ*drag*=-1.5%.**



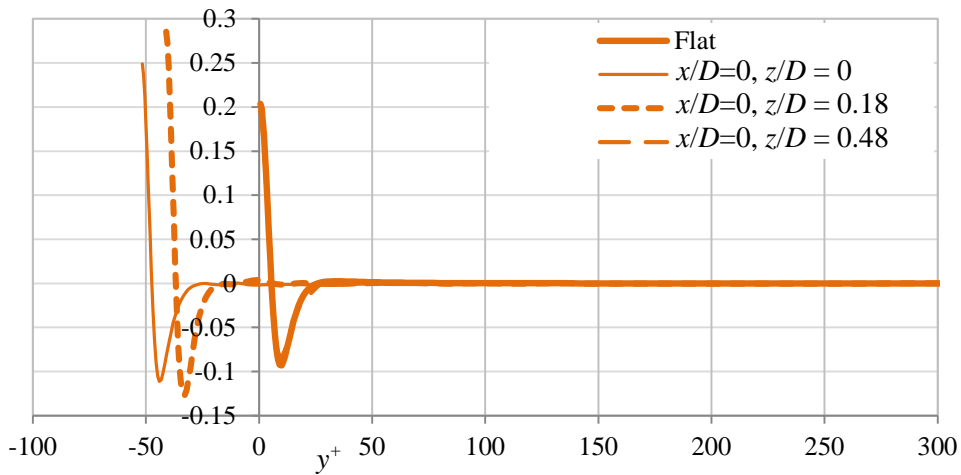**Figure 72b. Profiles for the viscous diffusion term in the turbulent kinetic energy budget for Case 3 at *Re* = 15,000, Δ*drag*=-1.5%.**
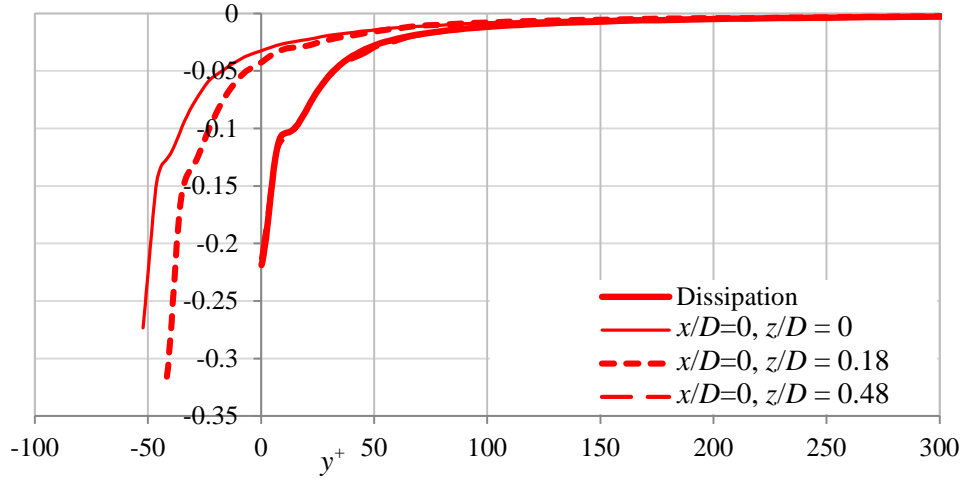
**Figure 72c. Profiles for the dissipation term in the turbulent kinetic energy budget for Case 3 at $Re = 15,000$, $\Delta_{drag}$=-1.5%.**
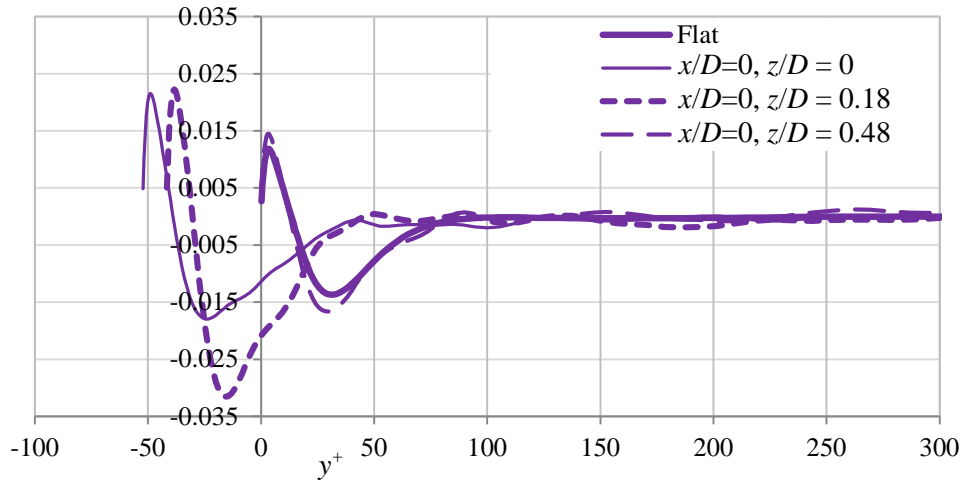


**Figure 72d. Profiles for the velocity pressure gradient term in the turbulent kinetic energy budget for Case 3 at $Re = 15,000$, $\Delta_{drag}$=-1.5%.**
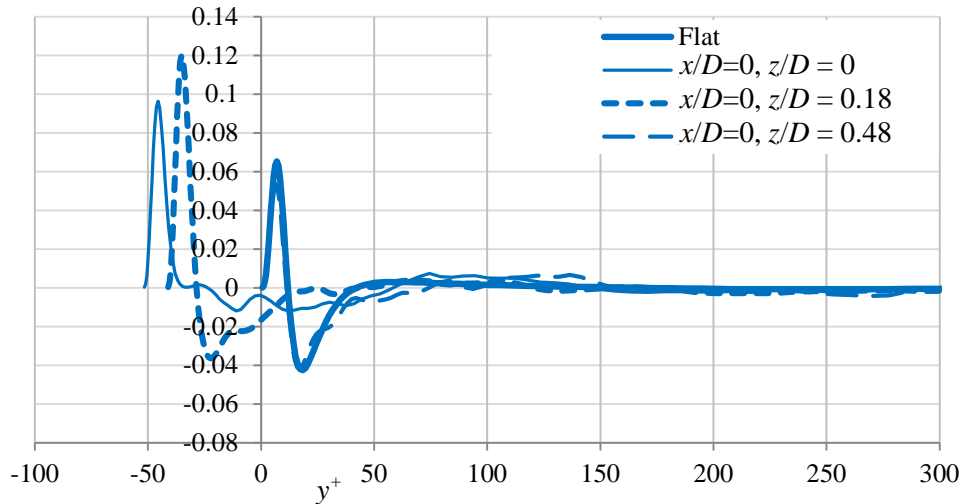


**Figure 72e. Profiles for the turbulent transport term in the turbulent kinetic energy budget for Case 3 at $Re = 15,000$, $\Delta_{drag}$=-1.5%.**
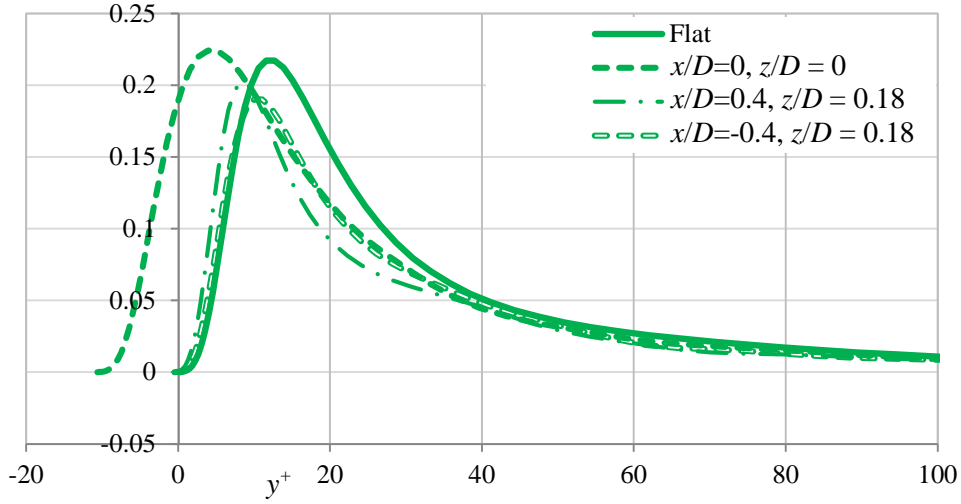
**Figure 73a. Profiles for the production term in the turbulent kinetic energy budget for Case 3 at $Re = 3{,}300$, $\Delta_{drag}=-1\%$.**



**Figure 73b. Profiles for the viscous diffusion term in the turbulent kinetic energy budget for Case 3 at $Re = 3{,}300$, $\Delta_{drag}=-1\%$.**



**Figure 73c. Profiles for the dissipation term in the turbulent kinetic energy budget for Case 3 at $Re = 3{,}300$, $\Delta_{drag}=-1\%$.**

**Figure 73d. Profiles for the velocity pressure gradient term in the turbulent kinetic energy budget for Case 3 at *Re* = 3,300, $\Delta_{drag}$=-1%.**



**Figure 73e. Profiles for the turbulent transport term in the turbulent kinetic energy budget for Case 3 at *Re* = 3,300, $\Delta_{drag}$=-1%.**



**Figure 74a. Profiles for the production term in the turbulent kinetic energy budget for Case 3 at *Re* = 10,000, $\Delta_{drag}$=-1.5%.**
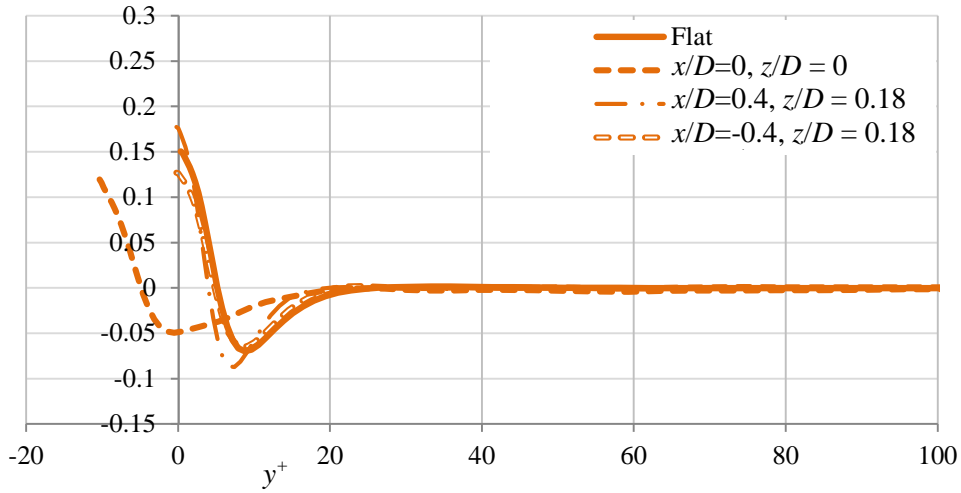
**Figure 74b. Profiles for the viscous diffusion term in the turbulent kinetic energy budget for Case 3 at $Re = 10,000$, $\Delta_{drag}$=-1.5%.**



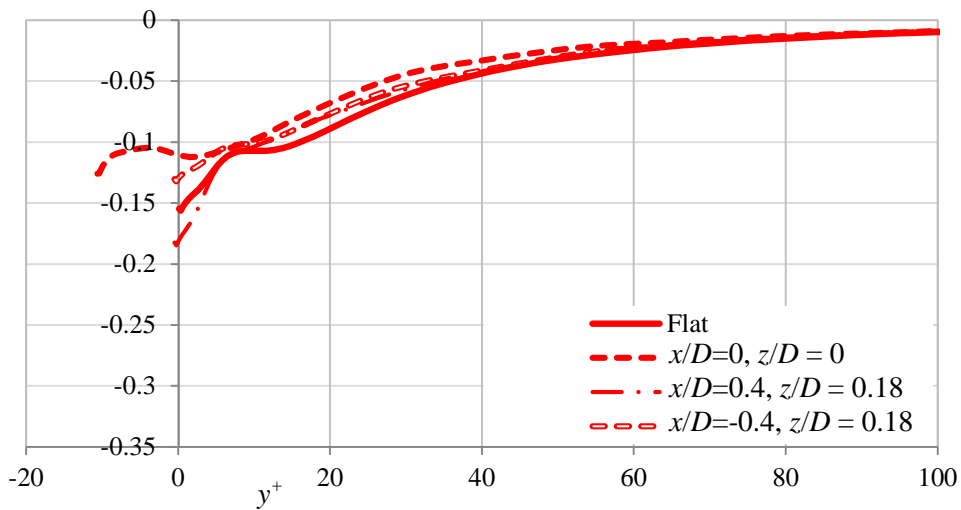**Figure 74c. Profiles for the dissipation term in the turbulent kinetic energy budget for Case 3 at $Re = 10,000$, $\Delta_{drag}$=-1.5%.**
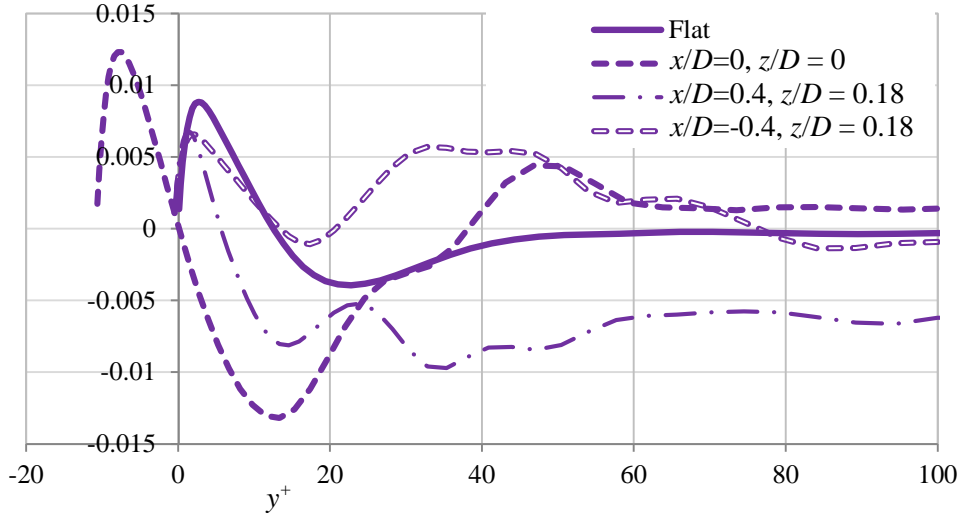


**Figure 74d. Profiles for the velocity pressure gradient term in the turbulent kinetic energy budget for Case 3 at $Re = 10,000$, $\Delta_{drag}$=-1.5%.**
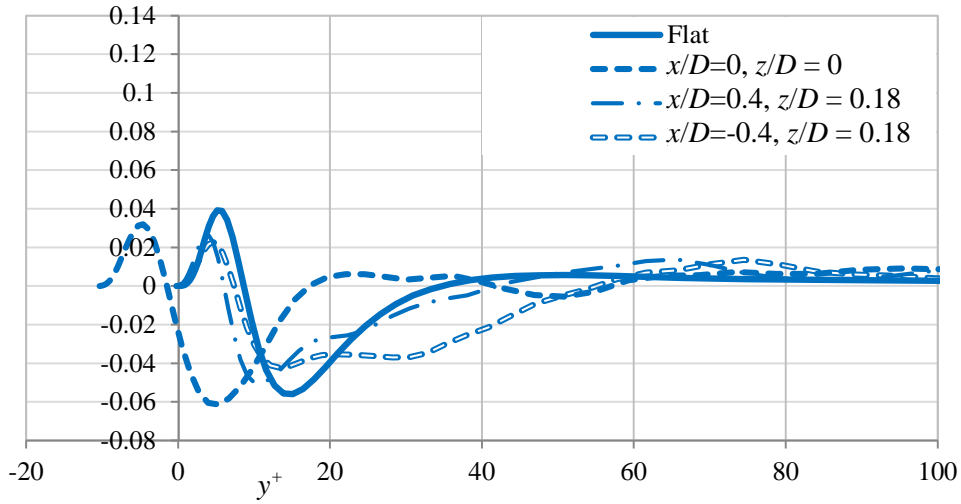
162

**Figure 74e. Profiles for the turbulent transport term in the turbulent kinetic energy budget for Case 3 at *Re* = 10,000, $\Delta_{drag}$=-1.5%.**



**Figure 75a. Profiles for the production term in the turbulent kinetic energy budget for Case 3 at *Re* = 15,000, $\Delta_{drag}$=-1.5%.**



**Figure 75b. Profiles for the viscous diffusion term in the turbulent kinetic energy budget for Case 3 at *Re* = 15,000, $\Delta_{drag}$=-1.5%.**

**Figure 75c. Profiles for the dissipation term in the turbulent kinetic energy budget for Case 3 at** $Re = 15,000$, $\Delta_{drag}$=-1.5%.



**Figure 75d. Profiles for the velocity pressure gradient term in the turbulent kinetic energy budget for Case 3 at** $Re = 15,000$, $\Delta_{drag}$=-1.5%.



**Figure 75e. Profiles for the turbulent transport term in the turbulent kinetic energy budget for Case 3 at** $Re = 15,000$, $\Delta_{drag}$=-1.5%.
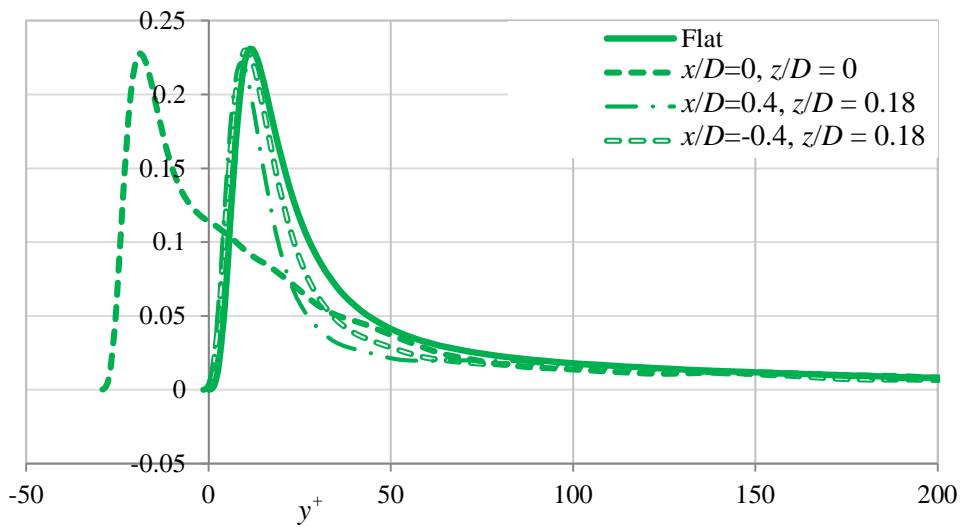
164

**Figure 76a. Profiles for the production term in the turbulent kinetic energy budget for Case 3 at $Re = 3,300$, $\Delta_{drag}$=-1%.**
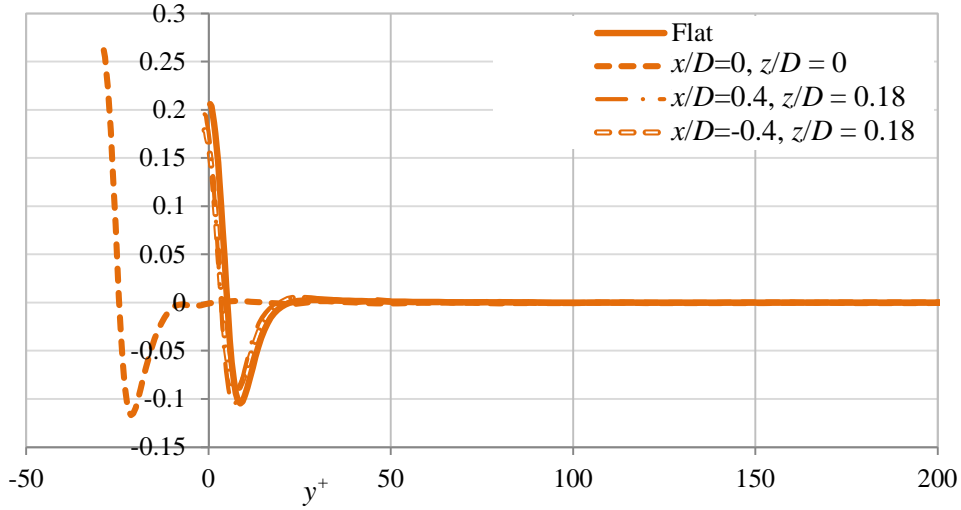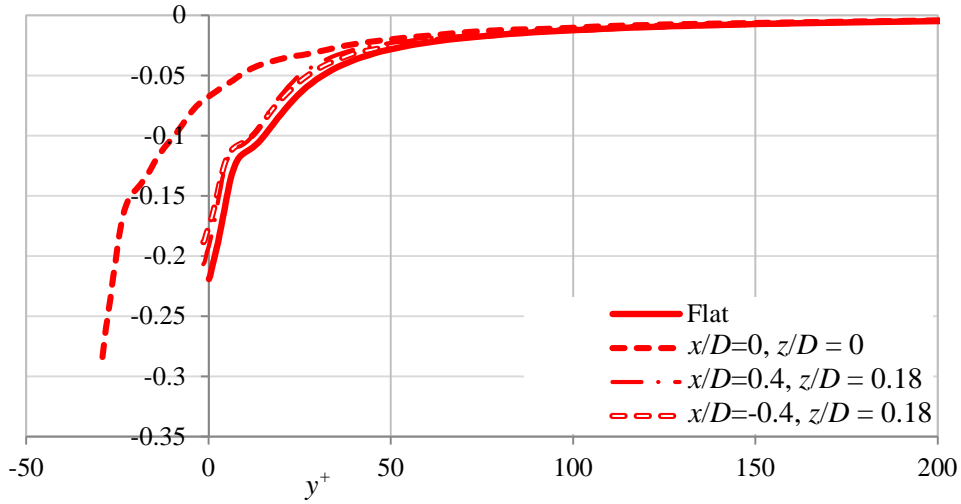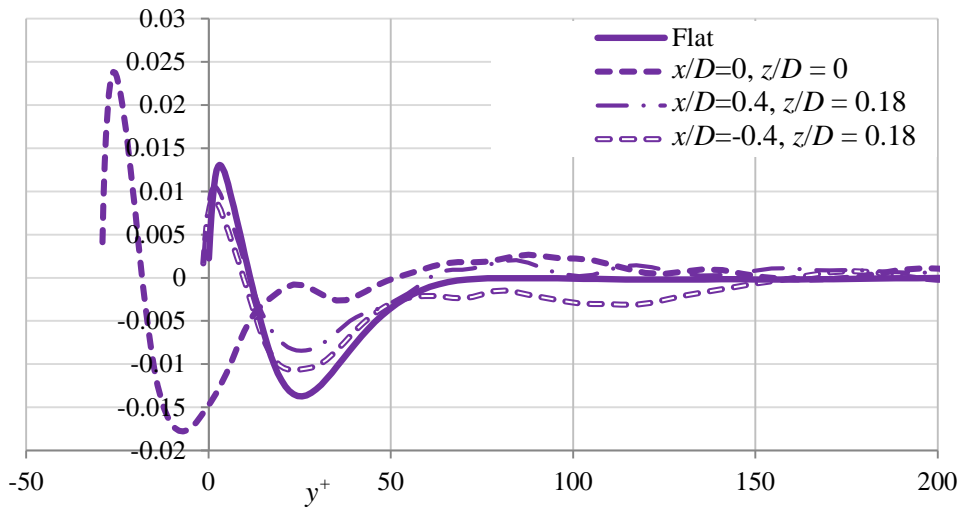


**Figure 76b. Profiles for the viscous diffusion term in the turbulent kinetic energy budget for Case 3 at $Re = 3,300$, $\Delta_{drag}$=-1%.**



**Figure 76c. Profiles for the dissipation term in the turbulent kinetic energy budget for Case 3 at $Re = 3,300$, $\Delta_{drag}$=-1%.**

165

**Figure 76d. Profiles for the velocity pressure gradient term in the turbulent kinetic energy budget for Case 3 at *Re* = 3,300, Δ*drag*=-1%.**
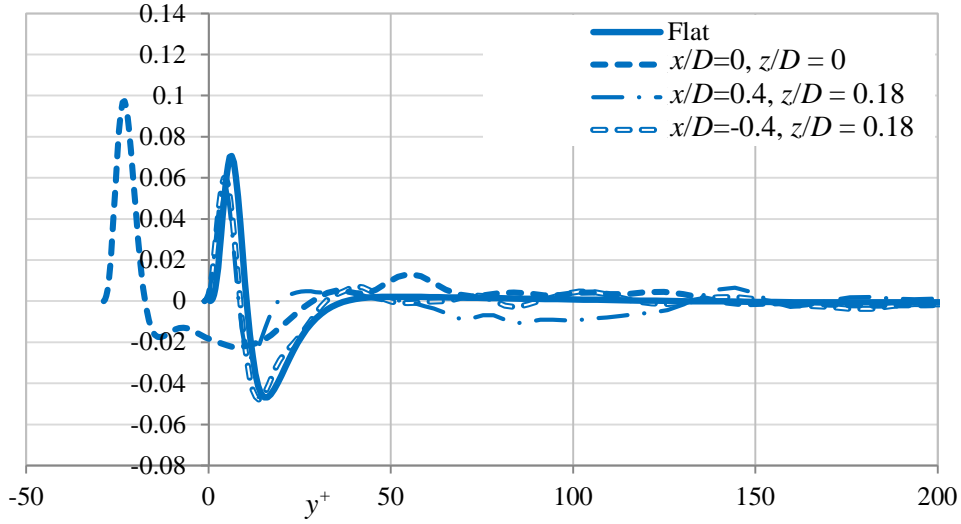


**Figure 76e. Profiles for the turbulent transport term in the turbulent kinetic energy budget for Case 3 at *Re* = 3,300, Δ*drag*=-1%.**



**Figure 77a. Profiles for the production term in the turbulent kinetic energy budget for Case 3 at *Re* = 10,000, Δ*drag*=-1.5%.**

**Figure 77b.** Profiles for the viscous diffusion term in the turbulent kinetic energy budget for Case 3 at $Re = 10,000$, $\Delta_{drag} = -1.5\%$.
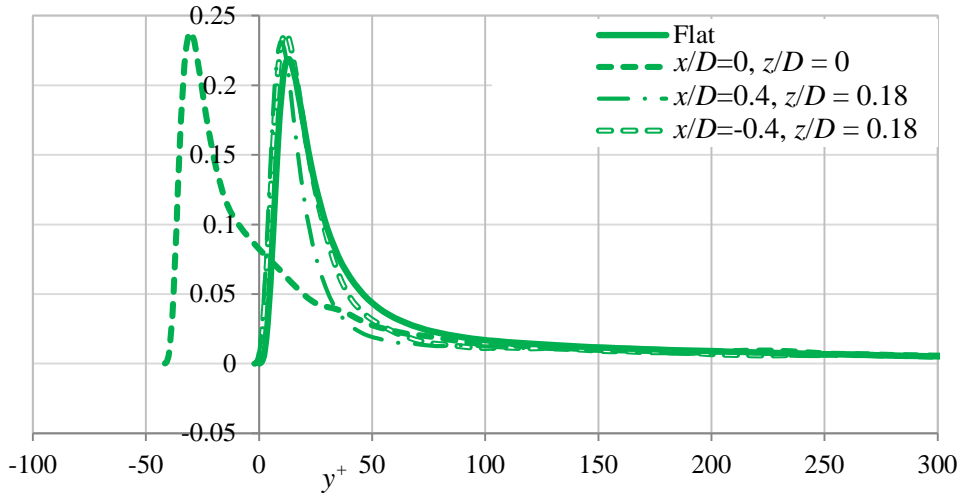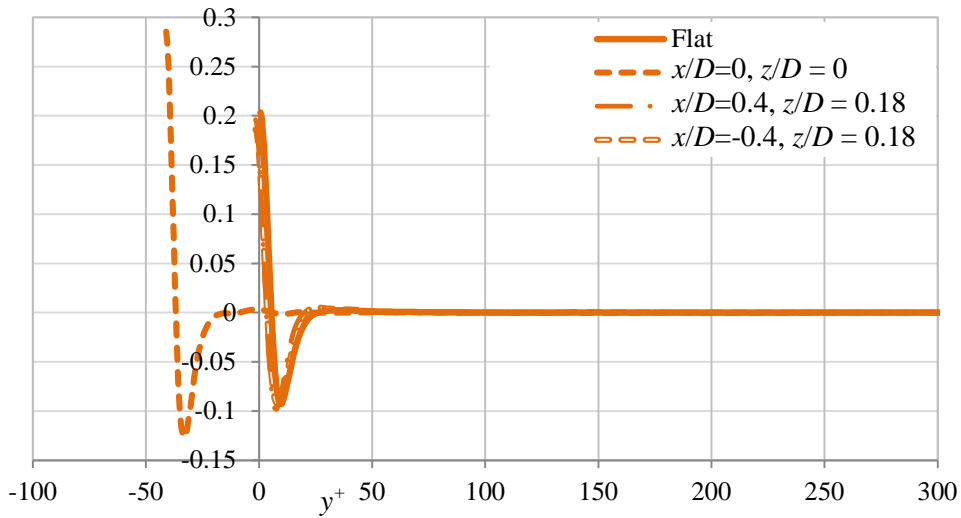


**Figure 77c.** Profiles for the dissipation term in the turbulent kinetic energy budget for Case 3 at $Re = 10,000$, $\Delta_{drag} = -1.5\%$.



**Figure 77d.** Profiles for the velocity pressure gradient term in the turbulent kinetic energy budget for Case 3 at $Re = 10,000$, $\Delta_{drag} = -1.5\%$.

167

**Figure 77e. Profiles for the turbulent transport term in the turbulent kinetic energy budget for Case 3 at *Re* = 10,000, Δ*drag*=-1.5%.**



**Figure 78a. Profiles for the production term in the turbulent kinetic energy budget for Case 3 at *Re* = 15,000, Δ*drag*=-1.5%.**



**Figure 78b. Profiles for the viscous diffusion term in the turbulent kinetic energy budget for Case 3 at *Re* = 15,000, Δ*drag*=-1.5%.**
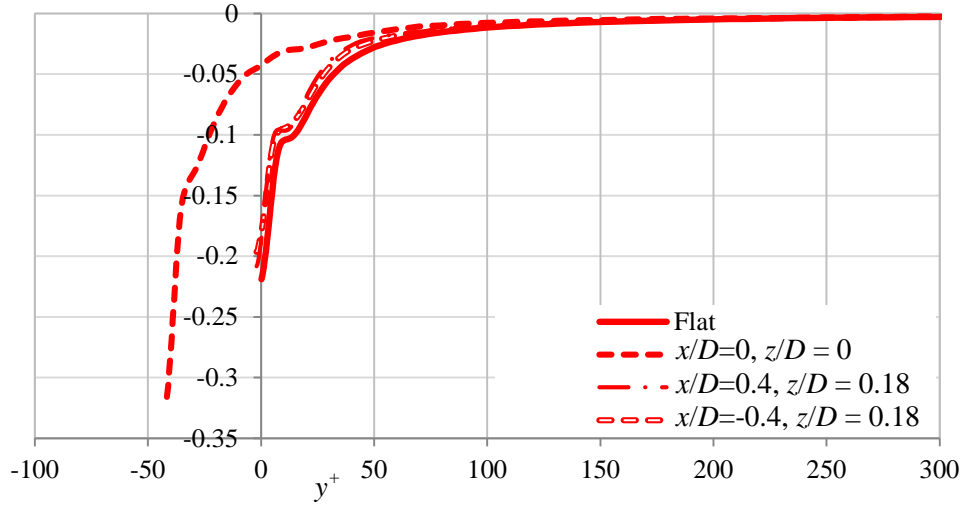
**Figure 78c. Profiles for the dissipation term in the turbulent kinetic energy budget for Case 3 at $Re = 15,000$, $\Delta_{drag}$=-1.5%.**
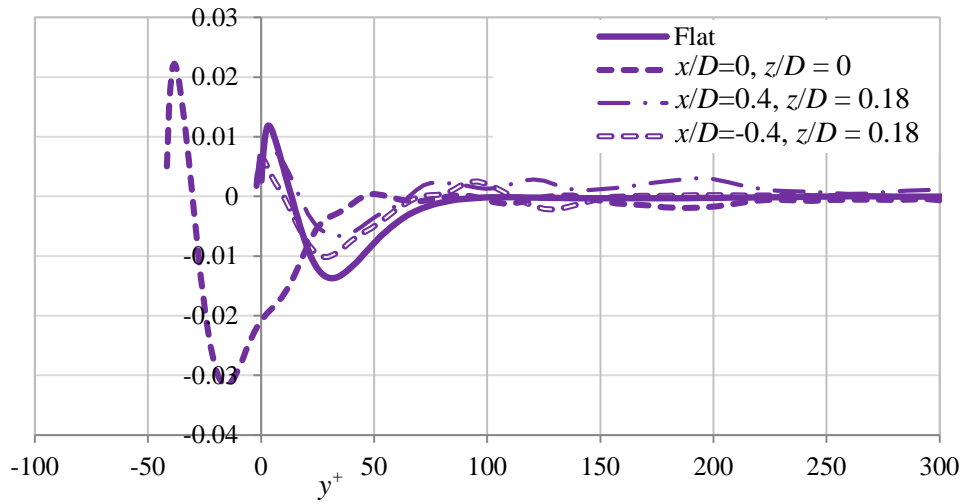


**Figure 78d. Profiles for the velocity pressure gradient term in the turbulent kinetic energy budget for Case 3 at $Re = 15,000$, $\Delta_{drag}$=-1.5%.**
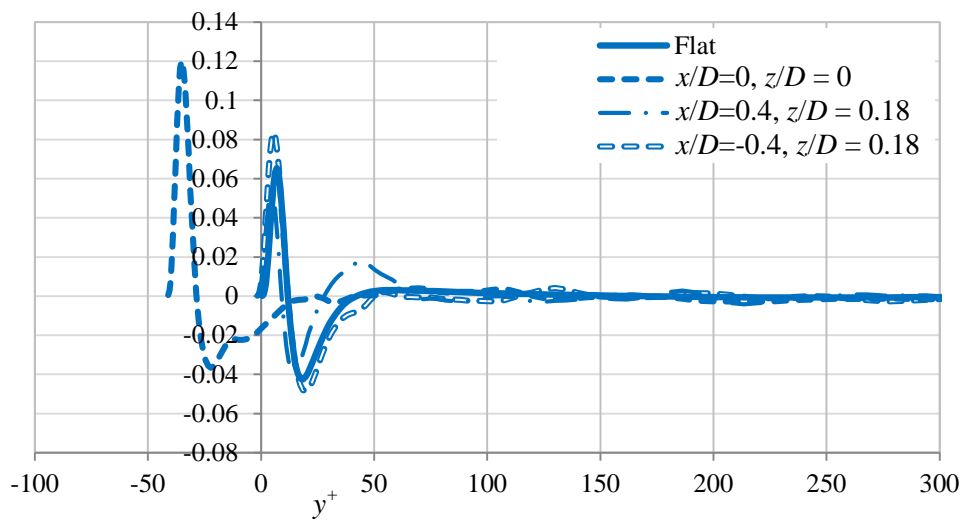


**Figure 78e. Profiles for the turbulent transport term in the turbulent kinetic energy budget for Case 3 at $Re = 15,000$, $\Delta_{drag}$=-1.5%.**